acta mechanica et automatica

vol. 6, no. 3 (21)

Bialystok University of Technology Publishing Office

Białystok 2012

The articles published in „Acta Mechanica et Automatica"
have been given a favourable opinion by reviewers designated by Editorial/Scientific Board

ISSN 1898-4088

The original version of the journal is a printed version

THE ADDRESS FOR THE CORRESPONDENCE:
„Acta Mechanica et Automatica"
Faculty of Mechanical Engineering
Bialystok University of Technology
ul. Wiejska 45C, 15-351 Białystok, Poland
tel. +48 85 746 92 04, fax +48 85 746 92 10
e-mail: acta.mechanica@pb.edu.pl
www.acta.mechanica.pb.edu.pl

Guidlines for the authors and conditions of subscription you can find on website www.acta.mechanica.pb.edu.pl

Project of the cover: Małgorzata Zdrodowska
Published by: Bialystok University of Technology Publishing Office
Edition: 200 copies

CONTENTS

ANALYSIS OF VISCOPLASTIC PROPERTIES OF A MAGNETORHEOLOGICAL FLUID IN A DAMPER

Jerzy BAJKOWSKI[*], Paweł SKALSKI[**]

[*]Institute of Machine Design Fundamentals, Warsaw University of Technology, ul. Narbutta 84, 00-524 Warszawa, Poland
[**]Institute of Aviation, Al. Krakowska 110/114, 02-256 Warszawa, Poland

jba@simr.pw.edu.pl, pawel.skalski@ilot.edu.pl

Abstract: The aim of presented paper is a mathematical description and an analysis of viscoplastic properties of a magnetorehological fluid in operational conditions of a damper's work. The authors consider the possibility of use the viscoplastic law, typically for metals, to describe the behaviour of device with a magnethorheological fluid.

Key words: Magnetorheological Fluid, Bodner-Partom Model, Numerical Simulations

1. INTRODUCTION

Magnetorheological fluids, beside ferromagnetic and electrorheological fluids, belong to the non-Newtonian rheostable fluids, which are characterized by a yield point (Haake, 1998). Magnetic, ferromagnetic and electrorheological fluids are colloidal suspension of microscopic solids in the liquid carrier, and their main characteristic is rapid grouping of particles into a dense grid under the influence of an external stimulus (Carlson & Weiss, 1994).

Magnetorheological fluids (MRF) are very useful in solving damping problems which are one of main engineering dilemmas of construction and exploitation of machines and devices. Magnetorheological fluids change their rheological properties under the influence of a magnetic field. These properties of MR fluids couldn't be fully used until the age of the computer steering equipment.

MRF are used e.g. in: dampers, shock absorbers, clutches and brakes (Goncalves, 2005; Lee et al., 1999). MR dampers and MR shock absorbers are applied e.g. in damping control, in operation of buildings and bridges (Dyke et al., 1996), as well as in damping of high-tension wires (Wu, 2006). Actually, MR fluids are used, in large scale production in the car industry and military industry (Poynor, 2001).

In the development and production area of MR fluids, LORD Company is a dominating figure on the global market, producing fluids and devices, it contributes to their development. Despite plenty of works being currently led at universities and research centres, still the need of a better and more extensive knowledge of particular properties of these liquids is noticed, their behaviour in exploitative conditions, as well as learning all possibilities to control their rheological properties.

The authors of presented paper took the attempt to describe the MR fluid's behaviour, by using constitutive equations which are generally applied for metals. Before taking such a decision one should think and answer following question: whether and why, and which constitutive equations, proper for metals, can be used in the mathematical description of MR fluid's properties and behaviour?

Responding to the question, we should note that in certain operational conditions an MR fluid changes its density, becoming semi-solid, or even solid. It is one of an MR fluid's most significant features.

Therefore, it was decided to undertake an analysis of magnetorheological fluid's viscoplastic properties in operational conditions of a damper's work, to be able to apply the Bodner-Partom law, for description of properties and behaviour of MR fluids.

2. RESEARCH OBJECT

The range of experiments was limited to the T-MR SiMR 132 DG damper prototype (Fig. 1) with a MRF 132 DG from the LORD company. In the presented damper prototype, a gas spring was neglected in its construction. The research program was carried out in the test stand with kinematic excitation (Bajkowski, 2005) at the Faculty of Automobile and Construction Machinery Engineering at the Warsaw University of Technology.

Tab. 1. Fundamental properties of MRF 132 DG fluid (www.lord.com)

Properties	**MRF 132 DG**
Viscosity, temperature 40 [°C]	0.092±0.015 [Pa·s]
Density	2.98÷3.18 [g/cm^3]
Solids content by weight	80.98%
Operating temperature	-40÷130 [°C]
Flash point	>150 [°C]
Appearance	Dark grey

Fig. 1. View of the T-MR SiMR 132 DG damper prototype

In presented work, MR fluid is the research object, which is a work base in the smart dampers. Selected to the analysis, MRF 132 DG, its based on hydrocarbon. Major properties of MRF 132 DG fluid are shown in Tab. 1, while detailed information are available on the producer's website – www.lord.com.

3. RESULTS OF EXPERIMENTAL RESEARCH

During the implementation of studies, using sensors of: displacement, force, temperature and speed, following physical parameters were recorded:

- the force acting on the piston rod of the test device;
- the movement of a piston housing;
- the temperature of the outer casing of device;
- the rotational speed of the movement.

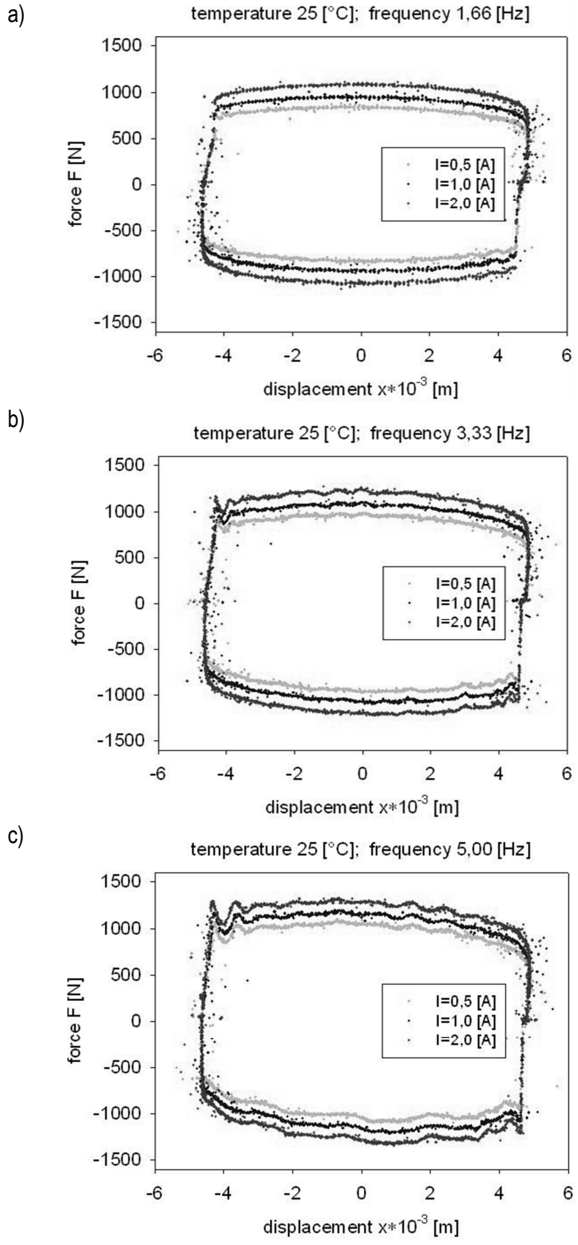

Fig. 2. Impact of the current intensity on the damping force in function of a displacement of the piston, for three oscillation frequencies: (a) 1.66; (b) 3.33; (c) 5.00 Hz

As intended, and pursued in the research program, the impact of changes of oscillation frequency of rod's kinematic excitation, current intensity in the coil winding head mounted in the test sample; effects of changing temperature of the test subject and the gap's height, by which the fluid flows through, were all considered when determining the characteristics of work of examined devices. The final result of research is estimated by the courses of damping force of tested device in function of displacement its piston's rod. All efforts were made to register and record the results as accurate and precise as possible, and the obtained results are burdened with possibly smallest errors.

Constant input signal in such prepared research programme, was a harmonic function $x(t) = A\sin(\omega t)$ for the displacement of the damper's piston, where the amplitude was $A = 10$ mm and rotation speed of circular cam $\omega = 100$; 200; 300 (400) rpm; response to this signal was a function $F(t)$. Time of recording a single experiment was set to $t = 5$ s, and the sampling frequency to 400 Hz. Investigations were conducted for three values of the piston oscillation frequency: $f = 1.66$; 3.33; 5.00 Hz, and three current values: $I = 0.5$; 1.0; 2.0 A. The gap's height was $h = 7$x10-4 m.

The important issue is to determine the impact of frequency oscillation of a piston in the damper and shock absorbers, on characteristics of tested devices. Changing the velocity of a piston movement, changes the speed of fluid flow through the gap in a head, it turns into the value of the damping force. Oscillation frequencies of the piston were selected by evaluating the capabilities of the test stand and the damper prototype.

Oscillation frequencies of the piston were selected by evaluating the capabilities of the test stand and installed object for tests. Three values of oscillation frequencies of the piston, converted to the corresponding values of shear rate of the liquid in the gap, is the minimum value in the identification of parameters of viscoplastic constitutive equations.

Fig. 2 shows the impact of the current intensity, flowing in a solenoid, on the damping force, with oscillation values: (a) 1.66; (b) 3.33; (c) 5.00 Hz. Used on the test stand measuring equipment have been chosen so that, to minimize the error of the method of measurement.

4. ANALYSIS OF MR FLUID

The results of the cyclic experimental tests of the damper and the shock absorber, became a base for an analysis of viscoplastic properties of a magnetorheological fluid under influence of a magnetic field, in operational conditions of a damper's work. The authors of this paper decided to examine yield point in MR fluid, when the fluid flows through the working gap in the head of the damper.

Analysis of these parameters of MR fluid, will be subjected to the influence of shear parameter of fluid flowing through the gap, as well as changes in the value of current flowing in a solenoid and changes of the temperature of the liquid.

Fig. 3a shows an example of graph illustrating the change in force value acting on the piston rod of the tested damper in function of the displacement of the rod. The curve shown in Fig. 3a was a base to obtain the graph in Fig. 3b.

The curve in Fig. 3b was created by cutting a portion of the curve from Fig. 3a, where the force begins to rise. Next, to make analysis easier, cut curve was shifted to position zero of displacement.

The authors estimated the impact of dry friction's work on the total value of force operating on the rod. Empty damper (without MR liquid) resisted 9 N, which is max. 2% of the total value of a resistance force on the piston rod. This variable has been intentionally omitted, due to its very small value. Because of such small influence of friction force, when the damper is not filled with MR fluid and because of the lack of a gas spring, the authors, on that basis, appealed directly to the MR fluid in its operational conditions, so that measurement could be maximally real.

a)

b)

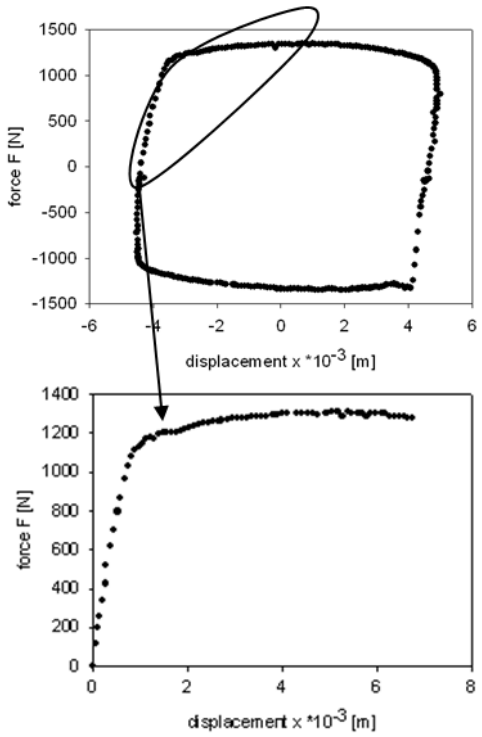

Fig. 3. Characteristic of a work force acting on the piston rod in function of a displacement(a); characteristic of the selected part of Fig. 3a (b)

Such prepared curve in Fig. 3b, allowed to prepare data for analysis on MR fluid, and it enabled the calculation of fluid shear stress τ, fluid shear strain γ, plastic shear strain γ^I, which have been designated in accordance with equations (1), (2), (3) described below:

$$\tau = \frac{F}{A}, \tau = \frac{\Delta x}{h} \tag{1}$$

$$\gamma^I = \gamma - \frac{\tau}{G} \tag{2}$$

$$r = r_1 + \frac{2}{3}(r_2 - r_1), A = 2\pi r l \tag{3}$$

where indicated: A – field shear surface of fluid in the gap, h – the value of the gap's height, Δx – increase of displacement, G – unit value of Kirchoff's modulus, r_1 – the value of the internal radius of the gap, r_2 – the value of the outer gap's radius, r – the radius value calculated from equation (3), l – the length of the piston's head.

In Fig. 4a the working gap of damper's head was indicated, and in Fig. 4b radiuses r_1, r_2 determining the height of the gap, and *l* the length of the head.

To determine the shear rate, it was necessary to know the value of a shear strain in a function of time. The value of a shear strain was calculated from the formula (1), and time t was recorded during the experiment. When carrying out the process to determine the shear rate, a graph was prepared (Fig. 5), illustrating the growth of a shear strain in a function of time. The value of a strain rate was determined based on the slope of the line passing through a section of the curve on which shear stress reached maximum value. Straight line whose slope corresponds to the value of a shear rate was marked in Fig. 5.

a)

b)

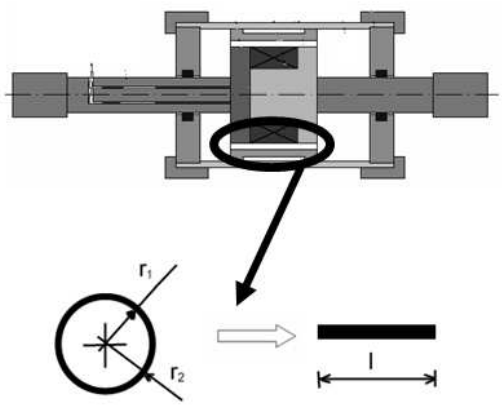

Fig. 4. Scheme of the damper with selected working gap (a); „view" of the working gap (b)

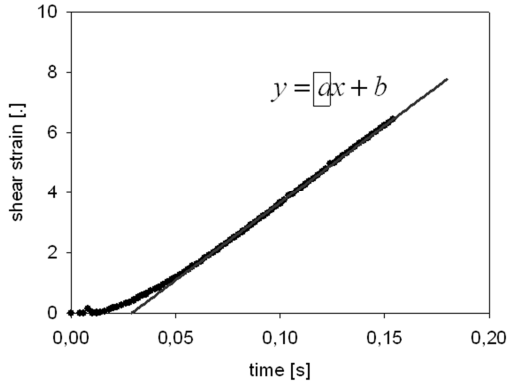

Fig. 5. Determination of a shear rate value

This way was used to estimate the value of shear rate for each rate of the frequencies of rod's oscillation. For a gap's value of h=7x10^{-4} [m], the value of the piston oscillation frequency were 1.66; 3.33; 5.00 Hz, values of shear rate are, respectively 73; 144; 217 [1/s].

In order to estimate the value of a conventional yield point of a magnetorheological fluid under magnetic field, working in the test device, it was necessary to draw a chart (Fig. 6), which presents the course of shear stress in function of strain. The values of shear stress were calculated from equations (1). The yield point, in this case, is designated by the intersection of two lines, one approximately reproducing the elastic part of shear stress in a function of non-dilatational strain and the order, illustrates roughly, the change of plastic values.

Another parameter, which describes the properties of an MR fluid in the magnetic field is a Kirchoff's modulus, also called the shear modulus. In carrying out the process of designating the Kirchoff's modulus, a chart was made (Fig. 7), illustrating the change in a reproducing approximately the elastic part of the curve to the abscissa, on which non-dilatational strain values were marked, expresses the value of the Kirchoff's modulus.

Eliminating the elastic deformation from the total value of non-dilatational strain, the course representing the viscoplastic properties of an MR fluid in operational conditions of the damper's work was obtained.

Extremely important thing is the value of the yield point, beyond which, as shown in Fig. 8, in the next phase of a plastic deformation, viscoplastic course of the MR fluid is determined.

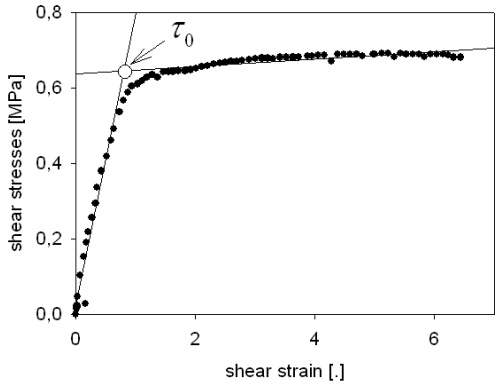

Fig. 6. Evaluation of a yield point τ_0 of an MR fluid

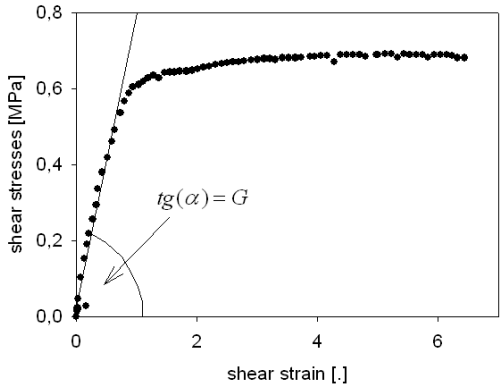

Fig. 7. Evaluation of a Kirchoff's modulus

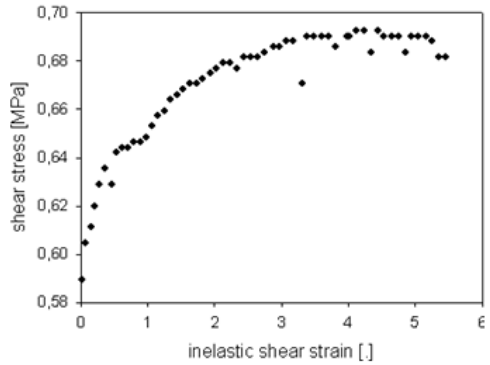

Fig. 8. The change in the value of a shear stress versus a plastic shear strain

Explained above, methodology of presentation of shear stress, non-dilatational strain, its plastic part, estimation of the yield point and the Kirchoff's modulus, obtained results of the fluid MRF 132 DG. The results are summarized in Tab. 2.

The Kirchoff's modulus was 0.95 MPa and was constant for different shear rate and the current value of the variable in the analyzed area.

Tab. 2. Yield point of fluid MR 132 DG

current intensity [A]		0.5	1.0	2.0
yield point [MPa]		τ_0		
shear rate [[1/s]]	102	0.29	0.32	0.37
	202	0.33	0.36	0.41
	304	0.35	0.39	0.45

Fig. 9 illustrates the changes of yield point, obtained for three values of current intensity 0,5; 1,0; 2,0 A and three values of shear rate 73; 144; 217 [1/s]. The increase of shear rate and the increase of current intensity causes the increase of the yield point.

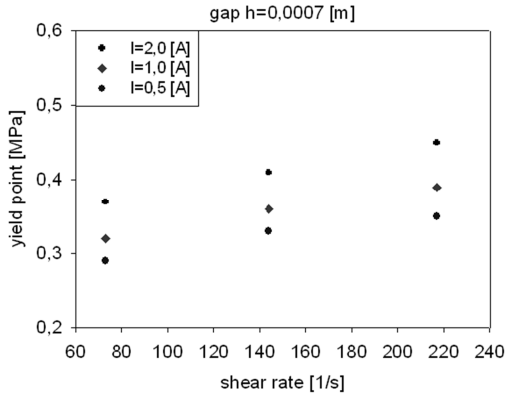

Fig. 9. Impact of shear rate and a current intensity on the yield point, for the gap h=7x10^{-4} m

5. BODNER-PARTOM LAW

The Bodner-Partom law is a typical law for metals. Equations of this model allow to describe a viscoplastic behaviour of analysed material. The constitutive formulation of Bodner-Partom can be expressed in the following form (Skalski, 2010):

$$\dot{\varepsilon}^{\prime ij} = \frac{3}{2}\dot{p}\frac{\sigma^{\prime ij}}{J(\sigma^{\prime rs})} \tag{4}$$

where $\dot{p}$ – the accumulated inelastic strain rate, $\dot{\varepsilon}^{\prime ij}$ – the deviatoric plastic strain rate tensor, $\sigma^{\prime ij}$ – the deviatoric stress tensor, and $J(\sigma^{\prime rs})$ – the invariant of the plastic strain rate tensor.

The constitutive equation of the Bodner-Partom law was written in the form (Skalski, 2010):

$$\dot{\gamma}^I = 2D_0 \exp[-\frac{1}{2}(\frac{R_0}{\sqrt{3}\tau})^{2n}\frac{n+1}{n}]\mathrm{sgn}(\tau) \tag{5}$$

where $\dot{\gamma}^I$ – plastic strain rate, τ – shear stress, n, R_0, D_0 – model parameters.

A large number of parameters describing the constitutive equations, makes considerable problems with their identification.

Identification methods of the Bodner-Partom model parameters are described well in (Chan et al., 1988). In this paper, the methodology and the identification of parameters of the B-P law, based on the scheme given in (Kłosowski and Woźnica, 2007). Parameters estimation was performed using the Marquardt-Levenberg algorithm (Marquardt, 1963) for the objective function, which was adopted as the difference of least squares.

Carried out analysis of yield point value changes of an MR flu-

id, working in a damper, forms the basis for the parameters identification of the Bodner-Partom model. The values obtained at different shear rates, allow to determine the main parameters of viscoplastic models.

For small values of inelastic deformation, the impact of the isotropic hardening is $\mathrm{R} = \mathrm{R}_0$, and kinematic hardening in negligible, and can be omitted. Formula (6) can be treated in a law as the Bonder-Partom contractual definition of a yield point and can be presented in the following form:

$$\tau_0 = \frac{R_0}{\sqrt{3}[\frac{2n}{n+1}\ln(\frac{2D_0}{\dot{\gamma}^I})]^{\frac{1}{2n}}} \tag{6}$$

Fig. 10 shows the initial yield limit (yield point) values τ_0, corresponding to three values of a shear rate. Then, using the method of least squares and using the formula (6), plotted curve and the values of the parameters n and R_0. Parameter D_0 is chosen arbitrary (Kłosowski and Woźnica, 2007).

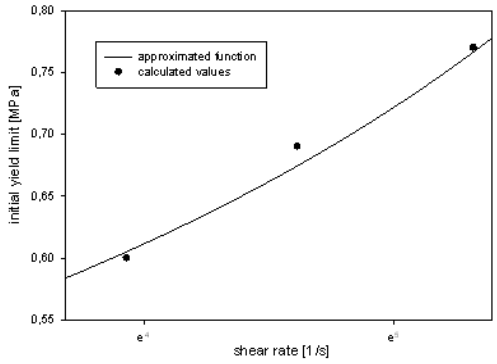

Fig. 10. Evaluation of n and R_0 parameters of the B-P model

At the current values: 0.5; 1.0; 2.0 A, parameters values obtained respectively: $n = 0.21$; 0.23; 0,27 [.] and $\mathrm{R}_0 = 9.4$; 9.4; 8.9 MPa. The value of the D_0 parameter was 1000000 [1/s], related to the shear rate 102; 202; 304 [1/s] (Kłosowski and Woźnica, 2007).

6. NUMERICAL SIMULATIONS AND CONCLUSIONS

Identified viscoplastic model was used to develop numerical simulations to verify the proposed mathematical model to describe the behaviour of MR fluid in the working gap of the head, with data from the experiment. The equation (5) was used to solve the numerical simulation. Obtained results are shown in Fig. 11 – 13.

A comparison between computer simulations of presented viscoplastic model and results of investigations, show that proposed viscoplastic model describes the behaviour of the damper with an MR fluid, very well.

The realized investigations allowed to estimate the yield point and then to evaluate the parameters of Bodner-Partom model. This is a big advantage of this type of identification which refers to the physical phenomena.

The study aimed to explore the possibilities of viscoplastic laws application, usually used to describe a metal behaviour in the decription of devices with a magnetorheological fluid.

Further work will be included in the mathematical model not only the influence of shear rate, and current intensity, but also an impact of a temperature and a gap's height.

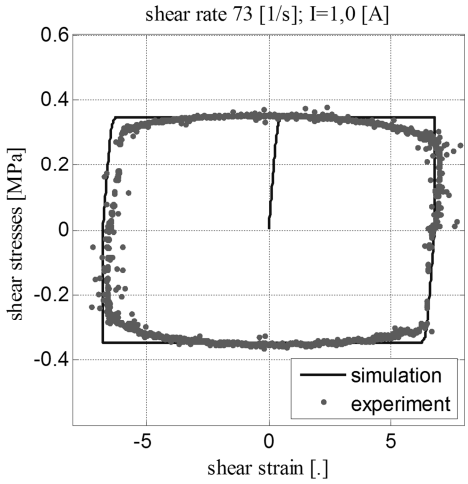

Fig. 11. Comparison of a numerical simulation of the Bodner-Partom law with results of research, when experiment's parameters are: current intensity 1.0 A; gap's height 7x10^{-4} m; shear rate 73 [1/s]

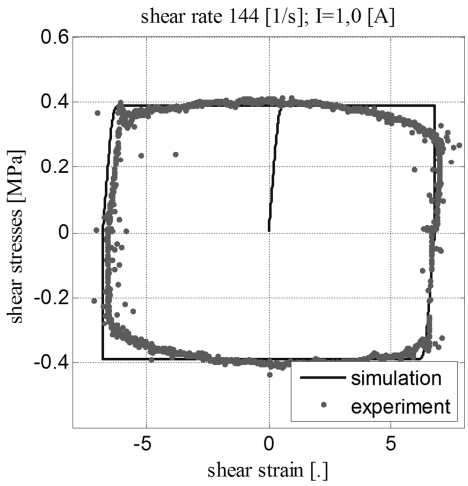

Fig. 12. Comparison of a numerical simulation of the Bodner-Partom law with results of research, when experiment's parameters are: current intensity 1.0 A; gap's height 7x10^{-4} m; shear rate:144 [1/s]

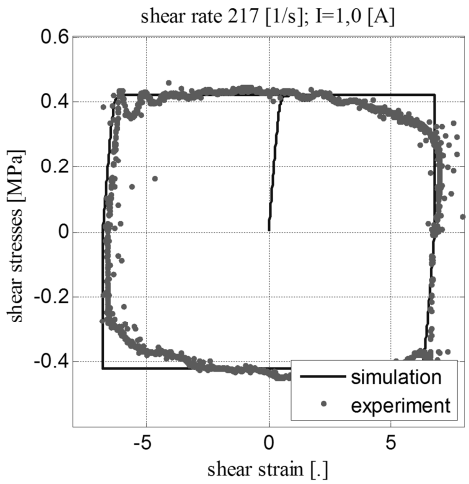

Fig. 13. Comparison of a numerical simulation of the Bodner-Partom l aw with results of research, when experiment's parameters are: current intensity 1.0 A; gap's height 7x10^{-4} m; shear rate 217 [1/s]

REFERENCES

1. **Bajkowski J.** (2005), Research and educational stands for the determination of selected characteristics of a magnetorheological damper or a shock absorber, *XXII Sympozium PKM*, Gdynia-Jurata, 47-56.
2. **Bodner S. R., Partom Y.** (1975), Constitutive equations for elastic-viscoplastic strain-hardening materials, *Journal of Applied Mechanics*, Vol. 42, 385-389.
3. **Carlson J. D., Weiss K. D.** (1994), A growing attraction to magnetic fluids, *Machine Design*, 61-66.
4. **Chan S. C., Bodner S. R., Lindholm U.S.** (1988), Phenomenological Modeling of Hardening and Thermal Recover in Metals, *J. Eng. Mater. & Tech.*, Vol. 11, 1-8.
5. **Dyke S. J., Spencer B. F., Sain M. K., Carlson J. D.** (1996), Modeling and control of magnetorheological dampers for seismic response reduction, *Smart Materials and Structures*, Vol. 5, No. 5, 565-575.
6. **Goncalves F. D.** (2005), Characterizing the behavior of magnetorheological fluids at high velocities and high shear rates, *PhD thesis*, Virginia Polytechnic, Blacksburg.
7. **Haake G. S.** (1998), Rheology. Fundamentals and applications, *Center of Scientific Publications PAN*, Poznań.
8. **Kłosowski P., Woźnica K.** (2007), Non-linear viscoplastic constitutive laws in some structural analysis, Publishing House of Gdansk University of Technology, Gdańsk.
9. **Lee U., Kim D., Jeon D.** (1999), Design analysis and experimental evaluation of an MR clutch, *Journal of Intelligent Materials and Structers,* Vol. 10, 701-707.
10. **Marquardt D. W.** (1963), An algorithm for least square of parameters, *Indust. Math.*, Vol. 11, 431-441.
11. **Poynor J. C.** (2001), Innovative designs for magneto-rheological dampers, *master thesis*, Virginia Polytechnic, Blacksburg.
12. **Skalski P.** (2010), Analysis of viscoplastic properties of a magnetorheological fluid in operational conditions of a dampers work, *PhD thesis*, Warszawa.
13. **Wu W.** (2006), Theoretical and experimental study on cable vibration reduction with tmd-mr damper, *PhD thesis*, Luisiana State University.

NUMERICAL MODELLING AND EXPERIMENTAL VERIFICATION OF GLASS–POLYESTER MIXED LAMINATE BEAM BENDING TEST

Agnieszka BONDYRA[*], Marian KLASZTORNY[*], Piotr SZURGOTT[*], Paweł GOTOWICKI[*]

[*]Department of Mechanics and Applied Computer Science, Faculty of Mechanical Engineering, Military University of Technology, ul. Gen. S. Kaliskiego 2, 00-908 Warszawa, Poland

abondyra@wat.edu.pl, mklasztorny@wat.edu.pl, pszurgott@wat.edu.pl, pgotowicki@wat.edu.pl

Abstract: The subject undertaken in the study is a glass (fibre) – polyester (matrix) layered composite, of the mixed sequence, composed alternately of laminas reinforced with E-glass plain weave fabric (WR600) and E-glass mat (CSM450). The laminate is manufactured on Polimal 104 polyester matrix. The aim of the study is to determine the options/values of parameters for numerical modelling and simulation of static processes in shell structures made of glass-polyester composites undertaken, in MSC.Marc system, recommended in engineering calculations. The effective elastic and strength constants of homogeneous laminas have been determined experimentally according to the standard procedures. The bending test of composite beams has been conducted experimentally and simulated numerically. Numerical investigations have been focused on selection of options/values of the numerical modelling and simulation parameters. The experimental verification of numerical modelling of the bending test is positive in both the quasi-linear range and in the catastrophic – progressive failure zone.

Key words: GRRP Shells, Beam Bending Test, FEM Numerical Modelling, Experimental Verification

1. INTRODUCTION

Wide practical applications of layered polymer-matrix composites first of all result from high relative strength and high relative stiffness of these materials which also exhibit high environmental and chemical resistance. Composite covers of tanks and canals, including wastewater purification plants, are one of the most important areas of practical applications of glass–polyester laminates (see product catalogues of Meier, 2006; Glaplast, 2010).

Numerical modelling and simulation of polymer-matrix composite structures using commercial CAE systems is at early stage of research and development. CAE systems, e.g. MSC.Marc (2008a, 2008b, 2008c) or LS-Dyna (2009), indicate wide possibilities for laminates modelling but, up-to-date, scientists have not developed sets of options/values of parameters recommended in engineering calculations for numerical modelling and simulation of static, rheological, dynamic or impact processes. Special attention should be put onto laminates which exhibit multiple modes of damage and fracture due to their heterogeneity and microstructure.

In problem-oriented references, one can find contributions which develop numerical modelling of polymer-matrix composite structural elements, but the data and descriptions incorporated in those papers are not satisfactory. For example, Vacĭk et al., (2010) presented numerical modelling of the three-point bending test of composite beams using MSC.Marc system. The considerations have been limited to adequacy assessment of various FE types and their combinations (Element_149, Element_22 i Element_75 among the others). Part of the contribution by Zemčĭk et al., (2011) is devoted to numerical analysis of the bending tests for laminates reinforced with glass mat and glass fabric. Modelling methodology description has been limited to giving the material constants, the failure criterion (Hashin) and the residual stiffness factor.

FEM numerical modelling, engineering calculations and design of composite covers of engineering structures is a topical theme in civil engineering. The reasons are collected below:

- a large quantity of serviced composite covers;
- a large quantity of tanks, pools, canals, objects in wastewater treatment plants, and other objects which require composite covers;
- a large quantity of geometric, material, and structural solutions in reference to composite covers;
- no standards and engineering handbooks for design of composite covers and demand for such contributions in design offices;
- rare catastrophic failures of composite covers especially in winter conditions;
- potential military applications of composite covers.

The study develops numerical modelling and experimental verification related to the bending test of beams made of mixed glass–polyester layered composite applied for manufacturing of shell segments for the Klimzowiec wastewater purification plant. The structural material has a mixed symmetric stacking sequence and is manufactured using the contact technology.

The general concept of this study is presented below. The effective elastic and strength constants of uniform laminas have been determined experimentally according to standards PN-EN ISO (1997, 2000, 2001b, 2002) and ASTM (1998). The composite beam bending test has been executed experimentally according to the standard procedure. FEM numerical modelling related to the static bending test of the mixed laminate beam has been developed using FE code MSC.Marc/Mentat. The numerical research has been focussed on selection of options/values of the numerical modelling and simulation parameters. The simulation results have been compared to the respective experimental results (verification). Finally, a set of options/values of numerical modelling and simulation parameters in reference to static pro-

cesses up to total failure in glass–polyester laminate shell structures has been proposed. This set, corresponding to FE code MSC.Marc, is recommended in engineering calculations.

2. DESCRIPTION OF THE COMPOSITE AND EXPERIMENTAL BENDING TEST

The subject of the research is a mixed GFRP structural laminate, denoted with MT code, manufactured using the following components: Polimal 104 polyester resin as the matrix (produced by Organika-Sarzyna Co., Poland), CSM450 E-glass mat and WRF600 E-glass fabric as reinforcement (produced by Krosglass Co., Poland). The laminate has the following stacking sequence: [(CSM450/WRF600)$_3$/CSM450]. WRF600 two-directional balanced plain weave fabric is characterized by 600 g/m^2 G.S.M. and orientation [0/90] with respect to the beam principal axes. The MT laminate has thickness h = 6.1 mm (the average value) and the average thicknesses of laminas are 1.0/0.7/1.0/ 0.7/1.0/0.7/1.0 mm, respectively.

Uniform laminas are denoted as M (mat reinforcement) and T (fabric reinforcement). In order to determine the effective material constants of uniform laminas, the following uniform plate semi-finished products have been manufactured: M (5CSM450) and T (4WR600). The plate semi-finished products MT, M, and T, of overall dimensions 500×500 mm, have been manufactured in ROMA Ltd., Grabowiec, Poland, using the contact technology with technological parameters compatible with the Polimal 104 resin card (2008). This card points out the following properties: good processing properties, good wettability of glass fibre, high strength parameters, good resistance to atmospheric factors.

The effective material constants of uniform laminas, i.e. M lamina reinforced with CSM450 E-glass mat and T lamina reinforced with WRF600 E-glass fabric, have been derived experimentally using respective standard specimens. In the modelling, the average values of those constants have been applied. The following standard tests have been examined:

– in–plane unidirectional static compression according to PN-EN ISO 14126:2002 standard;
– out–of–plane static shear according to PN-EN ISO 14130:2001 standard;
– in–plane unidirectional static tension according to PN-EN ISO 527:2000 standard;
– in–plane static shear according to PN-EN ISO 14129:1997 and ASTM D5379 / D5379M - 98 standards.

The principal directions of M, T, and MT composites are denoted as 1, 2, 3, with the 1-2 lamina plane.

The in–plane unidirectional static compression test, according to PN-EN ISO 14126:2002, enables determining the following constants: X_c – compressive strength in direction 1, e_{1c} – ultimate normal strain at compression in direction 1, E_{1c}– Young's modulus at compression in direction 1, ν_{12c} – Poisson's ratio at compression in direction 1 in the 1-2 plane, ν_{13c} – Poisson's ratio at compression in direction 1 in the 1-3 plane.

PN-EN ISO 14130:2001 standard determines the nominal interlaminar shear strength S_{13}. For this test one can calculate approximately shear strain γ_{13} close to the beam horizontal central plane based on the deflection of the short beam (with dominant shear) and calculate the following constants: G_{13} – shear modulus in the 1-3 plane, g_{13} – ultimate shear strain in the 1-3 plane.

The in–plane unidirectional static tension test, according to PN-EN ISO 527:2000, enables determining the following constants: X_t – tensile strength in direction 1, e_{1t} – ultimate normal strain at tension in direction 1, E_{1t} – Young's modulus at tension in direction 1, ν_{12t} – Poisson's ratio at tension in direction 1 in the 1-2 plane.

The in–plane static shear test for T laminate is performed by tension at angle ±45° in reference to principal direction 1 (PN-EN ISO 14129:1997), whereas for M laminates Iosipescu method is applied (ASTM D5379 / D5379M - 98). The following material constants are determined: S_{12} – in-plane shear strength, G_{12} – in-plane shear modulus, g_{12} – ultimate shear strain in the 1-2 plane.

In addition, non-standard unidirectional compression test in direction 3 has been performed in order to derive the following constants: Z_c – out-of-plane compressive strength, e_{3c} – ultimate normal strain at compression in direction 3, E_{3c} – Young's modulus at compression in direction 3. In this test requirements related to the in–plane unidirectional static compression were followed. Specimens used in the out-of- plane compression test were shaped via sticky of three 10×10 mm plates of M or T type.

The examined specimens of dimensions, dimensional tolerances and final processing determined in standards PN-EN ISO (1997, 2000, 2001b, 2002) were conditioned over 88 hours at 23±2°C temperature and 50±10% relative humidity. The experiments were performed at the same atmospheric conditions.

Independently of the identification tests performed on M and T uniform laminates, the standard tensile test for Polimal 104 polyester resin plastic has been done. The matrix was modelled as isotropic and linear elastic–short material, described by the classic constants: E – Young's modulus, ν – Poisson's ratio, R – tensile strength, e – ultimate normal strain.

Uniform composites M, T are homogenized and modelled as linearly elastic – short orthotropic materials, described by the following material constants:

a) elasticity constants:

$$E_1, E_2, E_3, \nu_{12}, \nu_{23}, \nu_{31}, G_{12}, G_{23}, G_{31} \tag{1}$$

b) ultimate strengths:

$$X_t, X_c, Y_t, Y_c, Z_t, Z_c, S_{12}, S_{23}, S_{31} \tag{2}$$

c) ultimate strains:

$$e_{1t}, e_{1c}, e_{2t}, e_{2c}, e_{3t}, e_{3c}, g_{12}, g_{23}, g_{31} \tag{3}$$

with:

$$E_1 = 0.5(E_{1t} + E_{1c}),\ \ E_2 = E_1\ ,\ \ E_3 = E_{3c} \tag{4}$$

$$\nu_{12} = 0.5(\nu_{12t} + \nu_{12c}),\ \ \nu_{13} = \nu_{13c} \quad \nu_{23} = \nu_{13},\ \ \nu_{31} = \nu_{13}E_3/E_1 \tag{5}$$

$$G_{23} = G_{13}\ ,\ \ G_{31} = G_{13} \tag{6}$$

$$Y_t = X_t\ ,\ \ Y_c = X_c\ ,\ \ Z_t = R\ ,\ \ S_{23} = S_{13}\ ,\ \ S_{31} = S_{13} \tag{7}$$

$$e_{2t} = e_{1t}\ ,\ \ e_{2c} = e_{1c}\ ,\ \ e_{3t} = e \tag{8}$$

$$g_{23} = g_{13}\ ,\ \ g_{31} = g_{13} \tag{9}$$

The average values of the material constants of uniform laminates M and T, based on five specimens in each test, are set up in Tab. 1. The standard deviations did not exceed 5% of the respective average values.

Tab. 1. The material constants of uniform composites M and T (the average values)

Parameter	M	T
E_1 [MPa]	8250	16550
E_2 [MPa]	8250	16550
E_3 [MPa]	4150	5000
ν_{12} [–]	0.390	0.155
ν_{23} [–]	0.235	0.234
ν_{31} [–]	0.118	0.0707
G_{12} [MPa]	3040	2300
G_{23} [MPa]	3100	2400
G_{31} [MPa]	3100	2400
X_t [MPa]	95.7	269
X_c [MPa]	216	202
Y_t [MPa]	95.7	269
Y_c [MPa]	216	202
Z_t [MPa]	70	70
Z_c [MPa]	231	344
S_{12} [MPa]	91.0	32.6
S_{23} [MPa]	35.9	22.5
S_{31} [MPa]	35.9	22.5
e_{1t} [–]	0.021	0.021
e_{1c} [–]	0.031	0.011
e_{2t} [–]	0.021	0.021
e_{2c} [–]	0.031	0.011
e_{3t} [–]	0.017	0.020
e_{3c} [–]	0.061	0.100
g_{12} [–]	0.043	0.050
g_{23} [–]	0.040	0.045
g_{31} [–]	0.040	0.045
μ[1)] [–]	0.29	0.29

1) Coulomb friction coefficient for steel–composite pair determined using the inclined plane method

The 3-point bending test, performed according to standard PN-EN ISO 14125:2001, is depicted in Fig. 1. The beam specimens had overall dimensions 80×15×6.1 mm. The initial theoretical span length of beam specimens equals to 64 mm. The central cylindrical mandrel and cylindrical supporting mandrels, of radius r = 5 mm, were parallel to each other. The vertical velocity of the test machine traverse was equal 1 mm/min. There were registered the vertical pressure force F of the central mandrel and the vertical displacement s of the traverse, with sampling frequency 10 Hz. Five specimens were examined.

Bending test examination for the selected specimen is illustrated in Fig. 2, whereas the test results for five specimens are presented in Fig. 3. Good conformity, both qualitative and quantitative, of quasi-linear relationship $F – s$ in the elastic range is observed in Fig. 3 for the examined samples. The failure process started from the bottom lamina M working in tension first of all, which has its tensile strength smaller twice compared to its compressive strength (Tab. 1, Fig. 2). Next, subsequent laminas fractured in correlation with respective strengths. Thus, progressive – catastrophic damage process is observed. Conformity of the $F – s$ curves in the failure zone for five examined specimens is assessed as good from the qualitative point of view. The deviations result from the manufacturing technology first of all, which leads to non-uniform laminas in microscale (spread in ultimate strengths and strains).

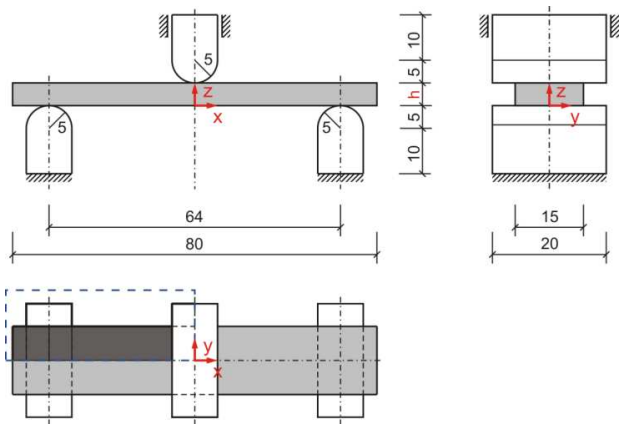

Fig. 1. A scheme of the 3-point bending test of layered composites (a bisymmetric system) with the marked quarter selected for numerical modelling (h=6.1 mm), according to PN-EN ISO 14125:2001

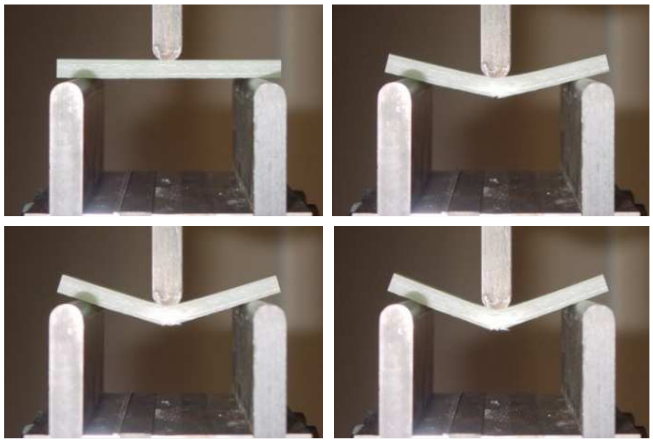

Fig. 2. Photos illustrating the 3-point bending test of the selected MT beam specimen

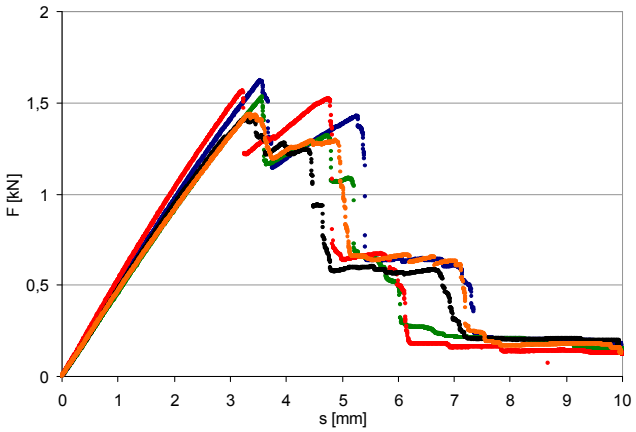

Fig. 3. The $F – s$ diagrams for five examined MT beam specimens in the 3-point bending test

Within the framework of the bending test the material constants characteristic for the 3-point beam bending test have been determined using the classic dependences from standard PN-EN ISO 14125:2001. The ultimate normal stress at bending is calculated for the bottom fibres at the midspan, according to the formula:

$$\sigma_f = \frac{3F_{\max}L}{2bh^2} \tag{10}$$

where: σ_f [MPa] – ultimate normal stress at bending, $F_{\max}$ [N] – load capacity, *L* [mm] – theoretical span length, *h* [mm] – specimen thickness, *b* [mm] – specimen width.

The ultimate normal strain for the bottom fibres is calculated from the formula:

$$e_f = \frac{6 s_{\max} h}{L^2} \tag{11}$$

where: $s_{\max}$ [mm] – deflection corresponding to $F_{\max}$ at the mid-span.

The average values for five specimens amount to:

– the load capacity and the ultimate normal stress: $F_{\max} = 1.51\ \text{kN}, \sigma_f = 264\ \text{MPa}$;
– deflection at the load $F_{\max}$ and the ultimate normal strain at the same conditions: $s_{\max} = 3.43\ \text{mm},\ e_f = 0.03$.

3. NUMERICAL RESEARCH RELATED TO THE MT COMPOSITE BAEM BENDING TEST

Numerical modelling of the 3-point static bending test of the MF composite beam has been conducted using FE code MSC.Marc. The input data have been declared using the following units system: [mm, s, N, K, MPa]. The orthotropy directions 1, 2, 3 for the laminate coincide with the symmetry *x, y, z* axes of the cubicoidal specimen (Fig. 1). Owing to bisymmetry, the FE modelling was limited to a quarter of the system, putting respective boundary conditions. The following assumptions have been adopted:

1. the beam is in static simple bending and shear at bending;
2. the laminas are homogenized and modelled as linearly elastic–short orthotropic materials;
3. each lamina has [0/90] orientation with respect to the beam axis and behaves like an orthotropic material up to short falilure;
4. the central and supporting steel mandrels are modelled as cylindrical rigid surfaces;
5. the central mandrel moves vertically at constant velocity up to 10 mm; at constant geometric increment in the nonlinear process simulation one obtains *ds* = 0.01 mm for 1000 increments;
6. single-side contact and Coulomb friction between steel and composite parts are taken into consideration;
7. the process is physically and geometrically nonlinear (linear elastic–short material, large displacements, small strains).

A discrete model of the system and its components creating respective contact pairs are shown in Fig. 4. The symmetry conditions are reflected by two planes of symmetry defined in the contact options. Taking into consideration the characteristic overall dimensions of laminate beams investigated in the study, a 3D 8-node solid shell element (element type 185 with brick topology), has been chosen, with 24 DOFs (3 translations at each node) and selective reduced integration. This element is based on the second-order laminate theory and is recommended in MSC.Marc system for laminates (2008a, 2008b, 2008c). The element uses the enhanced assumed strain formulation for transverse (through the laminate thickness) normal component and the assumed strain formulation for transverse shear components. These options enable meshing with one layer of finite elements through the laminate thickness (MSC.Marc/Mentat, 2008b).

The stiffness of this element is formed using one integration point in the element plane and three integration points in every lamina (using Simpson's rule). In the case of homogeneous materials five integration points are applied. An additional variationally consistent stiffness term is automatically included to eliminate the hourglass modes. Topology and Gauss points location in Element_185 are depicted in Fig. 5.

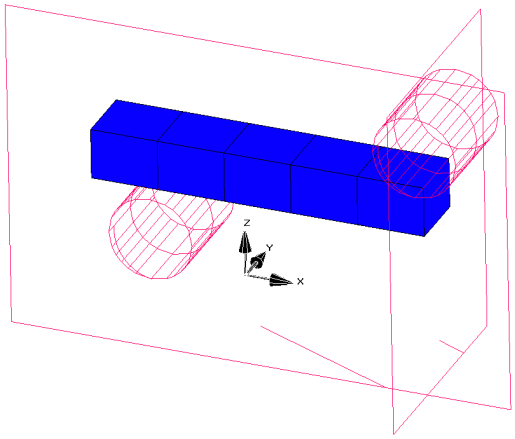

Fig. 4. An FE model of the quarter of the system and components creating contact pairs

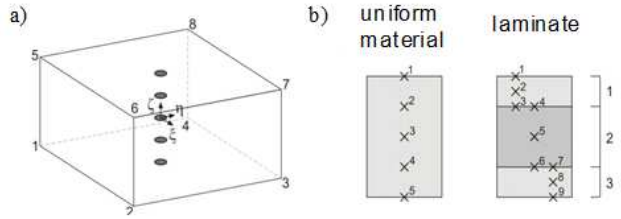

Fig. 5. Element_185 (Solid Shell): a) topology; b) Gauss points (MSC.Marc/Mentat, 2008b)

For comparative purposes finite elements No. 75 and 149 were also tested. Element_75 is a 2D 4-node bilinear thick shell element with 24 DOFs (three translations and three rotations at each node). Element_149 (*Composite Brick Element*) has 8 nodes and corresponds to the orthotropic continuum theory. Laminas are to be parallel to each other. The element is integrated using a numerical scheme based on Gauss quadrature; each lamina contains 4 integration points. The strain-stress relations take into account normal and shear deformations.

The touching contact was tested at 0.05–0.25 mm distance tolerance and 0.95 bias factor. Contact is solved with the direct constraint procedure. The motion of the bodies is tracked, and when contact occurs, direct constraints are placed on the motion using boundary conditions, both kinematic constraints on transformed degrees of freedom and nodal forces. A Coulomb bilinear friction model was used with ultimate stress σ_u=91 MPa.

The preliminary numerical experiments have indicated appropriate failure models. For E-glass mat reinforced homogeneous laminate *Max Strain* failure criterion has been chosen, for which 6 failure indices (FI1–FI6) are calculated at each integration point. The FI values belong to 0–1 interval and are calculated from the following formulas (MSC.Marc/Mentat, 2008b):

$$\begin{aligned}
&\text{FI1} = \left(\frac{\varepsilon_1}{e_{1t}}\right) \text{ for } \varepsilon_1 > 0\,, \quad \text{FI1} = \left(-\frac{\varepsilon_1}{e_{1c}}\right) \text{ for } \varepsilon_1 < 0 \\
&\text{FI2} = \left(\frac{\varepsilon_2}{e_{2t}}\right) \text{ for } \varepsilon_2 > 0\,, \quad \text{FI2} = \left(-\frac{\varepsilon_2}{e_{2c}}\right) \text{ for } \varepsilon_2 < 0 \\
&\text{FI3} = \left(\frac{\varepsilon_3}{e_{3t}}\right) \text{ for } \varepsilon_3 > 0\,, \quad \text{FI3} = \left(-\frac{\varepsilon_3}{e_{3c}}\right) \text{ for } \varepsilon_3 < 0 \\
&\text{FI4} = \left(\frac{\gamma_{12}}{g_{12}}\right)\,, \quad \text{FI5} = \left(\frac{\gamma_{23}}{g_{23}}\right)\,, \quad \text{FI6} = \left(\frac{\gamma_{31}}{g_{31}}\right)
\end{aligned} \tag{12}$$

where: $\varepsilon_1, \varepsilon_2, \varepsilon_3$ – normal strains, $\gamma_{12}, \gamma_{23}, \gamma_{31}$ – shear strains.

For E-glass fabric reinforced homogeneous laminate *Hashin Fabric* failure criterion has been chosen, for which 6 failure indices (FI1–FI6) are calculated at each integration point. These indices reflect the experimentally supported relationships among components of the stress tensor at any point of a T lamina. Indices FI1, FI2 describe material effort with dominant tension/compression of the fibres in direction 1, respectively. Similarly, indices FI3, FI4 describe material effort with dominant tension /compression of the fibres in direction 2, respectively. Indices FI5, FI6 describe material effort with dominant tension /compression of the matrix. The FI values belong to 0-1 interval and are calculated from the following formulas (MSC.Marc/Mentat, 2008b):

$$\begin{aligned}
\mathrm{FI1} &= \left[\left(\frac{\sigma_1}{X_t}\right)^2 + \left(\frac{\sigma_{12}}{S_{12}}\right)^2 + \left(\frac{\sigma_{13}}{S_{13}}\right)^2\right] \text{ for } \sigma_1 > 0 \\
\mathrm{FI2} &= \left[\left(\frac{\sigma_1}{X_c}\right)^2 + \left(\frac{\sigma_{12}}{S_{12}}\right)^2 + \left(\frac{\sigma_{13}}{S_{13}}\right)^2\right] \text{ for } \sigma_1 < 0 \\
\mathrm{FI3} &= \left[\left(\frac{\sigma_2}{Y_t}\right)^2 + \left(\frac{\sigma_{12}}{S_{12}}\right)^2 + \left(\frac{\sigma_{13}}{S_{13}}\right)^2\right] \text{ for } \sigma_2 > 0 \\
\mathrm{FI4} &= \left[\left(\frac{\sigma_2}{Y_c}\right)^2 + \left(\frac{\sigma_{12}}{S_{12}}\right)^2 + \left(\frac{\sigma_{13}}{S_{13}}\right)^2\right] \text{ for } \sigma_2 < 0 \qquad (13) \\
\mathrm{FI5} &= \left[\left(\frac{\sigma_3}{Z_t}\right)^2 + \left(\frac{\sigma_{12}}{S_{12}}\right)^2 + \left(\frac{\sigma_{13}}{S_{13}}\right)^2 + \left(\frac{\sigma_{23}}{S_{23}}\right)^2\right] \text{ for } \sigma_3 > 0 \\
\mathrm{FI6} &= \left[\left(\frac{\sigma_3}{Z_c}\right)^2 + \left(\frac{\sigma_{12}}{S_{12}}\right)^2 + \left(\frac{\sigma_{13}}{S_{13}}\right)^2 + \left(\frac{\sigma_{23}}{S_{23}}\right)^2\right] \text{ for } \sigma_3 < 0
\end{aligned}$$

where: $\sigma_1, \sigma_2, \sigma_3$ – normal stresses, $\sigma_{12}, \sigma_{13}, \sigma_{23}$ – shear stresses.

In both failure models *Progressive Damage* option was used, what results in respective stiffness degradation in laminas. *Selective Gradual Degradation* model that decreases gradually the elasticity constants was selected. The *Full Newton-Raphson* procedure was used to simulate nonlinear processes at the displacement and force convergence criteria with 0.02 tolerance. The time increment is transformed into the geometrical increment (the nominal time of the static process duration is 1 sec).

The simulations were conducted in Department of Mechanics & Applied Computer Science, Military University of Technology, Poland. Each series consumed 5-60 minutes of CPU time. The numerical research has resulted in a set of options/values of the parameters recommended in numerical modelling and simulation of static processes, including progressive failure, in glass-polyester mixed layered composite structures. Tab. 2 gives the recommended values of the parameters related to an adaptive time step, whereas Tab. 3 collects the recommended options/values of the numerical modelling and simulation parameters.

Tab. 2. The recommended values of parameters related to an adaptive time step (MSC.Marc 2008a)

Parameter	Default	Recommended
Initial Fraction of Loadcase Time	0.01	0.001
Minimum Fraction of Loadcase Time	10^{-5}	10^{-6}
Maximum Fraction of Loadcase Time	0.5	0.1
Desired #Recycles / Increment	5	20
Time Step Scale Factor	1.2	1.01

Figs. 7–11 depict diagrams of the central mandrel pressure force *F* vs. the traverse vertical displacement *s*, reflecting selected final numerical tests that constitute the base for determination of the options/values of numerical modelling and simulation parameters, recommended in engineering calculations. The simulated diagrams (in colour) are presented against a background of experimental curves for five specimens (in grey). The simulated curve in red corresponds to the option/values collected in Tab. 3, recommended for modelling and simulation of static processes, including failure, in beam/plate/shell GFRP composite structures.

Tab. 3. The recommended options/values of numerical modelling and simulation parameters

Parameter	Option/value
Element Types	185 (*Solid Shell*)
Element Dimensions	close to laminate thickness
FAILURE	
Failure Criteria	*Hashin Fabric, Max Strain*
Failure	*Progresive Failure*
Stiffness Degradation Method	*Gragual Selective*
Residual Stiffness Factor	0.005
CONTACT	
Support, Mandrel	*Rigid*
Laminate Beam	*Deformable*
Separation Force	0.1
Distance Tolerance	0.15
Bias Factor	0.95
FRICTION	
Type	*Coulomb*
Numerical Model	*Bilinear* (*Displacement*)
Friction Force Tolerance	0.05
Slip Threshold	*Automatic*
ANALYSIS OPTIONS	
Max # Recycles	30
Min # Recycles	2
Iterative Procedure	*Full Newton-Raphson*
Convergence Testing	*Residual and Displacement*
Relative Force Tolerance	0.02
Relative Displacement Tolerance	0.02
Time Step	*Adaptive*
Nonlinear Procedure	*Small Strain* *Assumed Strain* *Large Rotation*
Composite Integration Method	*Full Layer Integration*

The numerical *F–s* diagram obtained for the recommended options/values of numerical modelling and simulation parameters is presented in Fig. 6. Good conformity, both qualitative and quantitative, of the simulation and the experiment is observed in both elastic quasi-linear and catastrophic–progressive failure zones. Values of the ultimate pressure force and corresponding vertical displacement of the pressure mandrel amount to: $F_{\max} = 1.56$ kN, $s_{\max} = 3.21$ mm. The simulated force levels corresponding to catastrophic failure of the subsequent laminas are close to the experimental results.

Fig. 7 compares the numerical diagrams obtained for a 3D 8-node solid shell element (185) and for two other FE types, i.e. an isoparametric 3D 8-node composite brick element (149) and a 2D 4-node 24 DOF bilinear thick shell element (75). Ele-

ment 185 gives the diagram which is very close to the average experimental response.

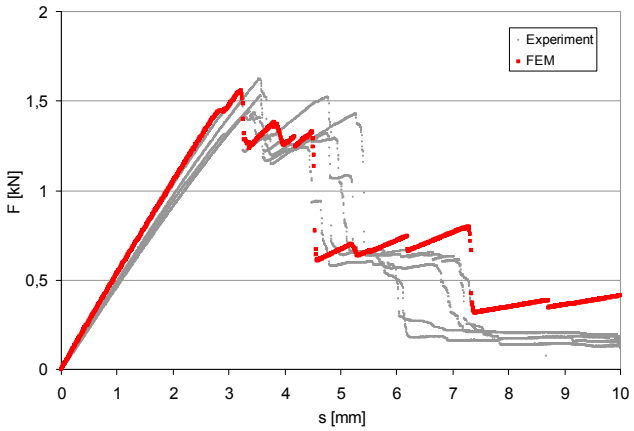

Fig. 6. The simulated *F – s* diagram against a background of the experimental diagrams for five specimens. The most correct numerical solution

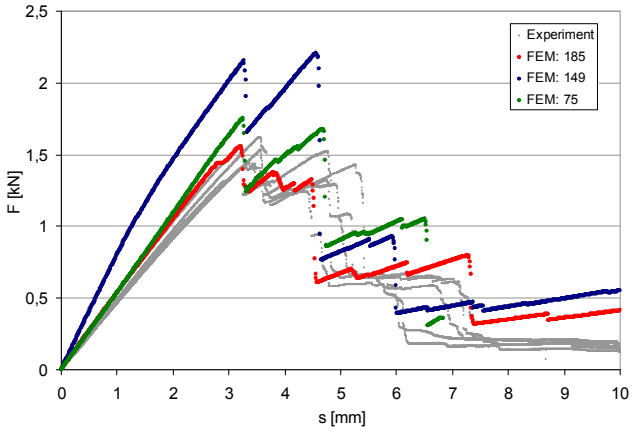

Fig. 7. The simulated curves for selected FE types against a background of the experimental curves

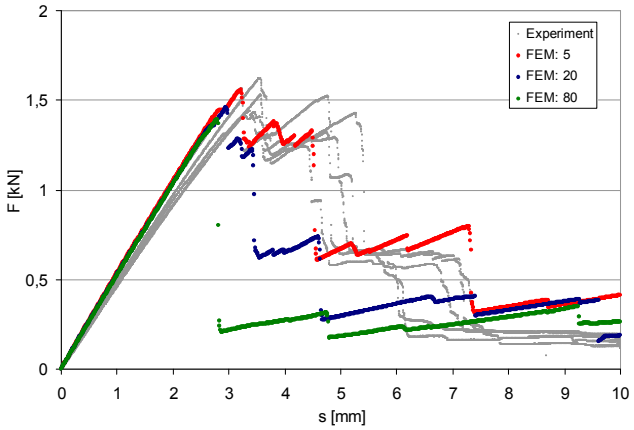

Fig. 8. The simulated curves for selected FE mesh densities against a background of the experimental curves

Fig. 8 presents the *F–s* curves for three FE mesh densities (5, 20, 80 FEs for the quarter of the examined system). Diagrams presented in Fig. 9 reflect the influence of small or large deformations assumption. Fig. 10 shows the results related to testing Residual Stiffness Factor (RSF). It reflects the initial stiffness part below which the laminate stiffness will not be reduced. For RSF=0.005 progressive failure is the most close to reality (smaller values of RSF do not lead to better results). The results reflecting testing a time step (adaptive; 0.001; 0.02) are presented in Fig. 11. The diagrams for an adaptive step and a constant 0.001 mm step are identical.

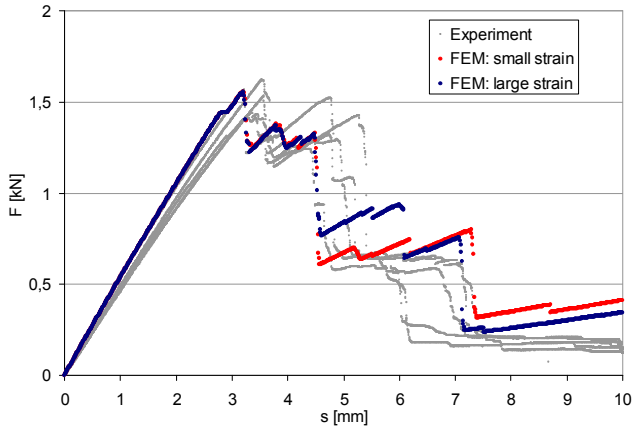

Fig. 9. The simulated curves under small / large strains assumption against a background of the experimental curves

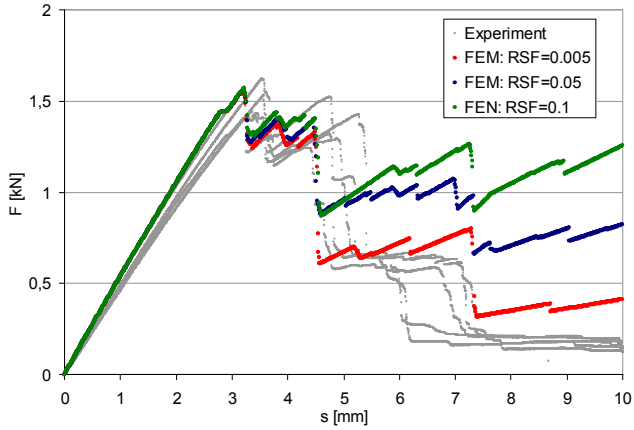

Fig. 10. The simulated curves for selected values of RSF against a background of the experimental curves

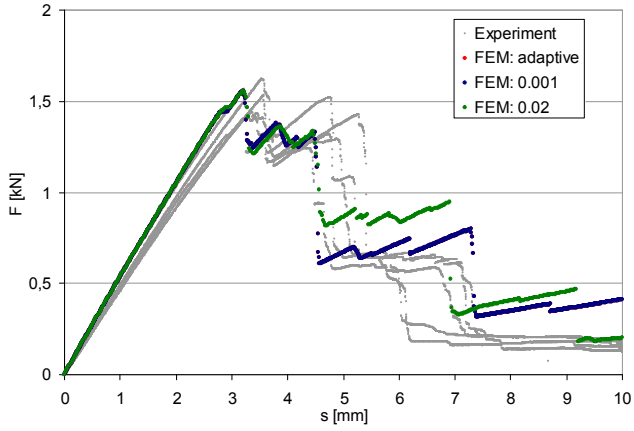

Fig. 11. The simulated curves for selected variants of the displacement increment against a background of the experimental curves

It has been proved that the overall dimensions of FEs in the *xy* plane (the laminate plane) should be close to the laminate thickness, the small strain assumption is correct for linearly elastic–short materials with progressive stiffness degradation beyond the ultimate strains, and an adaptive time step is recommended in the simulations.

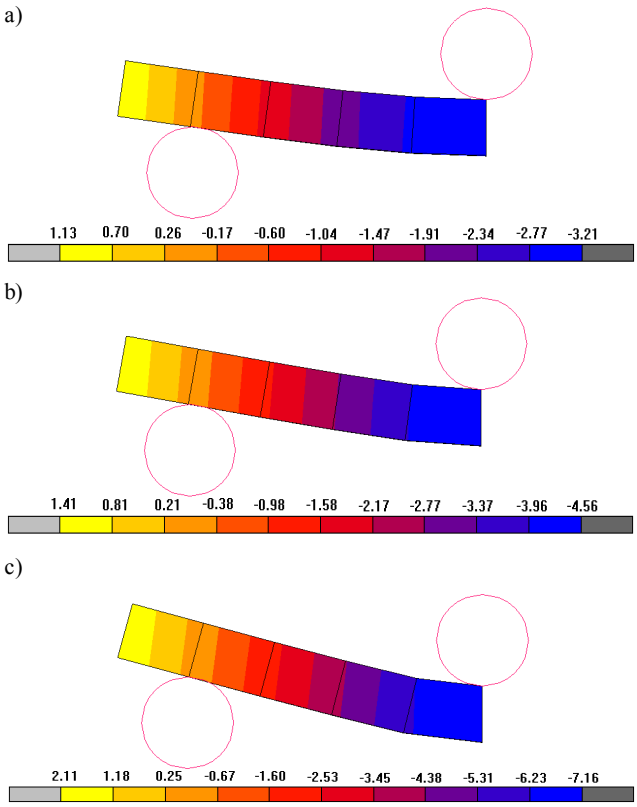

Fig. 12. Vertical displacement contours of the beam quarter (a side view) for selected punch displacements: a) 3.21 mm (the state closely before failure initiation); b) 4.56 mm; c) 7.16 mm

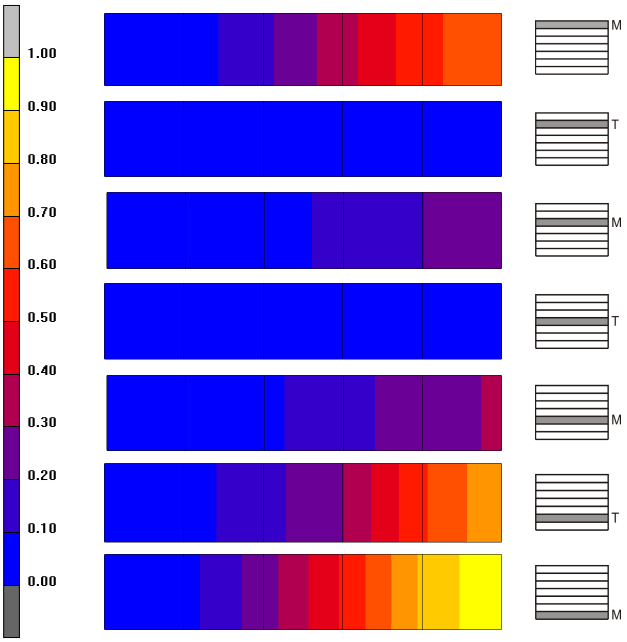

Fig. 13. Contours of the 1st failure index closely before progressive damage initiation in subsequent laminas (a top view onto the beam quarter)

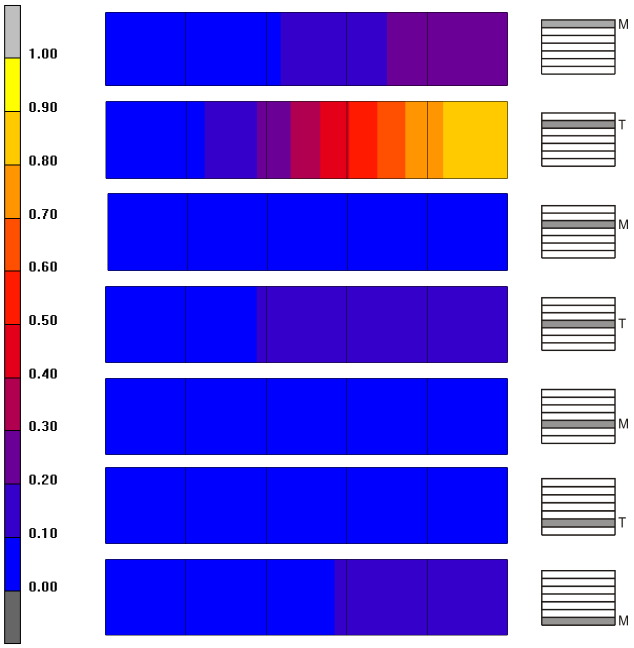

Fig. 14. Contours of the 2nd failure index closely before progressive damage initiation in subsequent laminas (a top view onto the beam quarter)

Simulations of processes using advanced CAE systems have practically unlimited possibilities in tracking the process at any point of the system. This is the basic advantage of numerical research over experimental research. Representative results illustrating simulation of the 3-point bending test for an MT composite beam are presented in Figs. 12–14.

Fig. 12 shows vertical displacement contours of the beam quarter (a side view) for the selected displacements of the punch. These contours are very close to respective experimental displacements (not presented in this study) of the bent specimens.

Failure indices defined in Eqns. (12, 13) are commonly used as measures of material effort in subsequent laminas. Contours of the 1st and 2nd failure indices in subsequent laminas before catastrophic–progressive damage initiation, corresponding to different failure mechanisms for M and T laminas, are collected in Figs. 13 and 14. As observed in the experimental tests, destruction of the MT laminate beam is mainly determined by longitudinal normal strains in M-laminas and by longitudinal normal stresses in T-laminas.

4. FINAL CONCLUSIONS

The study develops FE modelling and simulation of static processes, including progressive failure, in beam/plate/shell structures made of GFRP mixed laminates, using FE code MSC.Marc. The standard 3-point bending test of a GFRP mixed laminate beam has been conducted experimentally and numerically. The following extended numerical tests have been performed:

1. tests on selected finite elements allowable in MSC.Marc system for modelling of laminates;
2. tests on mesh density;
3. tests on strain quantity;
4. tests on the residual stiffness factor;
5. tests on a time step.

Based on these tests, a set of options/values of the numerical modelling and simulation parameters, recommended in engineering

calculations, has been determined. The experimental verification of numerical modelling and simulation of the bending test performed on GFRP laminate beams is positive in both the quasi-linear and the catastrophic – progressive failure zones.

REFERENCES

1. ASTM D5379 / D5379M - 98 (1998), *Standard Test Method for Shear Properties of Composite Materials by the V-Natched Beam Method*.
2. *Covering Systems – Technical Concept* (2006), C.F. Maier Europlast GmbH & Co KG, Königsbronn, Germany.
3. *Product Catalogue* (2010), P.T. Glaplast, Kielce (in Polish).
4. LS-DYNA (2009), *Keyword User's Manual*, Version 971/ Release 4 Beta, LSTC, Livermore, CA, USA.
5. Marc 2008 r1 (2008), *User's Guide*, MSC.Software Co., Santa Ana, CA, USA.
6. Marc 2008 r1 (2008), *Theory and User Information*, MSC.Software Co., Vol. A, Santa Ana, CA, USA.
7. Marc 2008 r1 (2008), *Element Library*, MSC. Software Co., Vol. B, Santa Ana, CA, USA.
8. PN-EN ISO 14129 (1997), Fibre-reinforced structural composites. Determination of shear strain and stress, shear modulus and strength at tension at angle ±45° (in Polish).
9. PN-EN ISO 527 (2000), Plastics. Deterniation of mechanical properties at static tension. Test conditions for isotropic/orthotropic fibre-reinforced polymer-matrix composites (in Polish).
10. PN-EN ISO 14125 (2001), Fibre-reinforced structural composites. Determination of properties at bending (in Polish).
11. PN-EN ISO 14130 (2001), Fibre-reinforced structural composites. Determination of nominal interlaminar shear strength using the short beam method (in Polish).
12. PN-EN ISO 14126 (2002), Fibre-reinforced structural composites. Determination of properties at in-plane compression (in Polish).
13. **Vacĭk J., Lašovă V., Kosnar M., Janda P., Kottner R.** (2010), Selection of optimum type FEM model for hybrid composite structure, *Advanced Engineering*, 4.
14. **Zemčĭk R., Laš V., Kroupa T., Purš H.** (2011), *Identification of material characteristics of sandwich panels*, University of West Bohemia in Pilsen, Czech Republik.
15. *Polyester resins* (2008), Engineers' Handbook, Organika-Sarzyna Chemical Plant (in Polish).

The study has been supported by National Centre of Science, Poland as a part of a research project No N506 1228 40, realized in the period 2011-2013. This support is gratefully acknowledged.

ROTARY HEAD KINEMATICS DURING CLEANING OF FLAT SURFACES

Grzegorz CHOMKA*, Jerzy CHUDY*

*Faculty of Mechanical Engineering, Koszalin University of Technology, ul. Racławicka 15-17, 75-620 Koszalin, Poland

grzegorz.chomka@tu.koszalin.pl, jerzy.chudy@tu.koszalin.pl

Abstract: The present article covers the problem of a mathematical description of the trajectory of those postprocessing traces that occur in the process of hydro jet cleaning of flat surfaces with the use of a rotary head. An analysis was conducted of postprocessing traces taking into consideration the provision of their uniform distribution. The determination of the conditions of an effective cleaning will allow such a selection of the working parameters of the head when a surface is obtained of a high quality, i.e. with a uniform degree of the removal of impurities.

Key words: Rotary Head, Prolate Cycloid, Cleaning, Postprocessing Traces

1. INTRODUCTION

High-pressure water jet machining is being more and more extensively applied. Recently, research has been conducted among others concerning the use of this technology for the cutting (Sharma et al., 2011) and breaking up of coal (Borkowski et al., 2012). Also, the possibilities of the use of a high-pressure water jet for the renovation of concrete structures (Bodnarova et al., 2011) have been investigated. Interesting results were obtained while cleaning grinding discs with a water jet with the use of various types of nozzles (Heinzel and Antsupov, 2012). Owing to the development of the technology of the generation of water jets, ultra-high pressures (600 MPa) can be used now. These are used among others in the machining of titanium alloys (Huang et al., 2012) and austenitic steel (Azhari et al., 2012) as well as in the preparation and finishing of metal surfaces (Chillman et al., 2007).

Seeking of new technologies to allow an optimization of cleaning processes has led to the development of a technology that uses water under a high pressure. It facilitates both accurate washing of the surface and a preparation of the base for painting, or a removal of old coats, rust, deposits and impurities.

The precision of cleaning of a surface with water under a high pressure is yet another important issue. Until recently, abrasive jet cleaning, most frequently realized as sand blast cleaning, was considered to be the only method that offers the highest degree of surface cleaning. In this process, the removal of impurities produces a good geometrical structure required for the anchoring of the coating. Nevertheless, the investigations that have been conducted in the recent years concerning the influence of the ion purity of the surface on the durability of paint coatings somehow undermined this view. Abrasive jet methods fail to remove salts that are set on the surface; furthermore, a "salted" abrasive may even increase the quantity of chemical compounds in the base.

Doping of a high-pressure water jet with an abrasive material yields promising results in the machining of titanium alloys (Kong and Axinte, 2011), laminar composites (Shanmugam and Masood, 2009) and concrete (Kim Jung-Gyu et al., 2012). Furthermore, work is conducted aimed at a prediction of the roughness of the surface that is obtained as a result of machining with an abrasive water jet with the use of artificial neural networks (Caydas and Hascalik, 2008).

The high-pressure hydro jet technology is widely used for the purpose of a removal of sediments. They occur in practically every industry branch. They may form in natural processes (e.g. corrosion or boiler scale) and during technological processes (e.g. a sedimentation of materials or their fractions). Another group includes sediments that occur in food industry and those that form during the operation of various machinery, such as ships, mechanical vehicles, hardware and construction or road machinery, carriages etc. Corrosive layers of metals, concrete, plastics etc. constitute a particular type of sediments. When cleaning the surface of an object, its superfluous surface layer can be considered as a sediment. Therefore, those coatings that have lost their properties for various reasons are considered to be sediments.

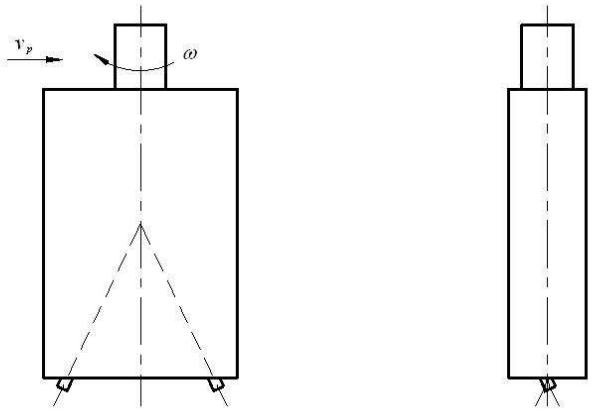

Fig. 1. Rotary head for the cleaning of flat surfaces

Working heads are used for the purpose of cleaning of flat surfaces, tanks of various shapes and pipelines. A head with specific parameters is selected depending from the type of the surface to be cleaned. Owing to an analysis of those postprocessing traces that are formed, it is possible to determine a num-

ber of quantities related to the cleaning process. These include the processing efficiency, which is obtained when a fairly uniform distribution of postprocessing traces is ensured (Frenzel, 2007; Gałecki and Mazurkiewicz, 1987).

The body of a head for the cleaning of flat surfaces (Fig. 1) possesses a grip for the connection of a gun with high-pressure conduits as well as channels that supply water to nozzles. These nozzles produce high-pressure water jets that constitute the cleaning tool. Owing to the adequate arrangements of the nozzles in the head, the head is provided with a rotational speed. When an additional plane motion is imparted to a head that rotates in this manner, cleaning of the entire surface is obtained.

2. PROLATE CYCLOID

If point *P* is moving with a resultant motion that consists of a uniform motion over a circle with radius *r* and velocity ω and a uniform linear motion with drift velocity v_p in a direction that is parallel to the plane of the motion over a circle, this point circumscribes a prolate cycloid (Fig. 2). In a Cartesian coordinate system, it is described with two equations in a parametric form:

$$\begin{aligned} x &= r\cos(\varphi_0 - \varphi) + v_p t = r\cos(\varphi_0 - \omega t) + v_p t \\ y &= r\sin(\varphi_0 - \varphi) = r\sin(\varphi_0 - \omega t) \end{aligned} \tag{1}$$

where: *r* –radius of circle, φ_0 – initial angle of the location of point P for *t=0*, ω – angular velocity of the head, v_p – axial velocity of the head, *t* – time, *t>0*.

A cycloid pitch is a shift of the point along axis *x* that corresponds to its full rotation in relation to the centre of the circle. It is as follows:

$$h = 2\pi\frac{v_p}{\omega}, \tag{2}$$

where: v_p – axial velocity of the point, ω – angular velocity of the point.

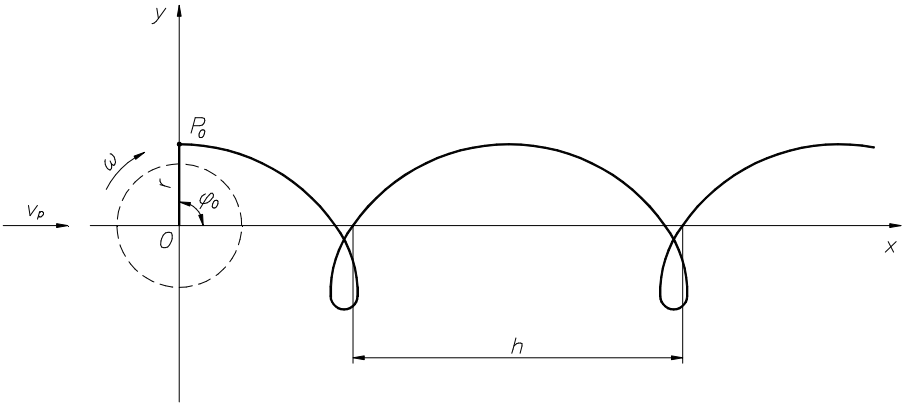

Fig. 2. Prolate cycloid

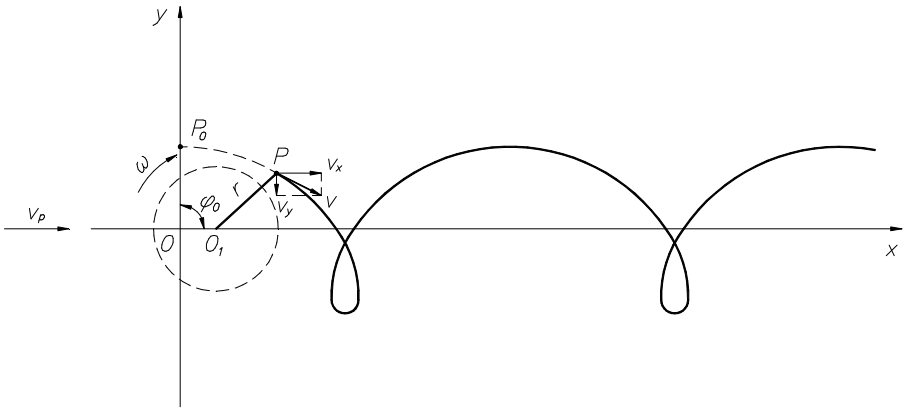

Fig. 3. Distribution of velocity vectors

3. MOTION OF THE POINT

In a Cartesian coordinate system, the equations of motion for a point that is moving along a prolate cycloid path have the form of Equation (1):

$$\begin{aligned} x &= r\cos(\varphi_0 - \omega t) + v_p t \\ y &= r\sin(\varphi_0 - \omega t) \end{aligned} \tag{3}$$

The velocity in this motion has two components, which are the derivatives of the path (Fig. 3):

$$\begin{aligned} v_x &= x' = r\omega\sin(\varphi_0 - \omega t) + v_p \\ v_y &= y' = -r\omega\cos(\varphi_0 - \omega t) \end{aligned} \tag{4}$$

The absolute value of velocity *v* is calculated from the following formula:

$$v = \sqrt{v_x^2 + v_y^2}, \tag{5}$$

considering that:

$$\begin{aligned} v_x^2 + v_y^2 &= r^2\omega^2 \sin^2(\varphi_0 - \omega t) + \\ &+ 2r\omega v_p \sin(\varphi_0 - \omega t) + v_p^2 + r^2\omega^2 \cos^2(\varphi_0 - \omega t) = \\ &= r^2\omega^2 + 2r\omega v_p \sin(\varphi_0 - \omega t) + v_p^2. \end{aligned} \tag{6}$$

Therefore, Formula (5) takes on the following form:

$$v = \sqrt{r^2\omega^2 + 2r\omega v_p \sin(\varphi_0 - \omega t) + v_p^2}, \tag{7}$$

r – radius along which the point is moving, ω – angular velocity of the motion of the point, v_p – axial velocity of the motion of the point along axis x, t – time.

4. DETERMINATION OF THE JET LENGTH

In order to guarantee the efficiency of the cleaning of the entire flat surface, the water jet is to be directed under small angle α in relation to the surface being cleaned. Furthermore, a deflection of the jet under angle β is to be provided so as to set the working head in a rotary motion (Fig. 4).

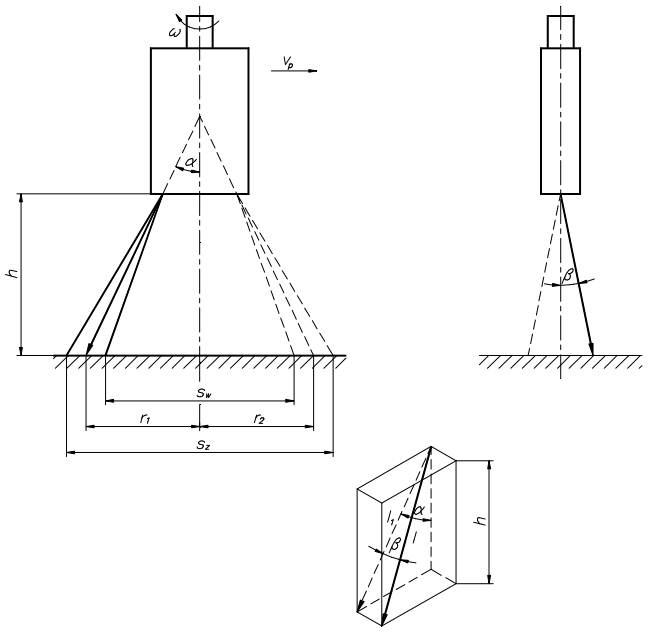

Fig. 4. Diagram of geometric dependences that occur when cleaning flat surfaces with a rotary head

Taking the above into consideration as well the real length of the jet in air, from its point of departure from the nozzle to the contact point with the surface being cleaned, one can determine the following from the dependences presented below:

$$\frac{l_1}{l} = cos\beta \quad \Rightarrow \quad l = \frac{l_1}{cos\beta}, \tag{8}$$

$$\frac{h}{l_1} = cos\alpha \quad \Rightarrow \quad l_1 = \frac{h}{cos\alpha}. \tag{9}$$

By converting Equations (8, 9), the final formula is obtained for the real jet length in the following form:

$$l = \frac{h}{cos\alpha \cdot cos\beta}, \tag{10}$$

h – distance between the head's face and the surface being cleaned, α – angle in the front projection contained between the rotation axis of the head and the projection of the jet flowing out onto the vertical plane, β – angle in the side projection contained between the rotation axis of the head and the projection of the jet flowing out onto the vertical plane.

5. DETERMINATION OF THE LOCATION OF POSTPROCESSING TRACES

The quality of the surface being cleaned, that is the ability to uniformly remove impurities, is a parameter which is of a key importance for the usefulness of a given method to various applications. The distance between postprocessing trances is the quantity that is decisive for the effects of cleaning. A mathematical analysis needs to be conducted in order to determine these quantities.

When a working head that possesses two nozzles is making a uniform motion over a circle with velocity ω and a uniform linear motion with drift velocity v_p in a direction that is parallel to the plane of the motion over a circle, it leaves traces on the surface being cleaned in the form of two prolate cycloids (Fig. 5).

It was accepted that φ_0, i.e. the initial angle of the location of point P_1 for $t=0$ is π. In view of the fact that the nozzles are arranged symmetrically in the nozzle in relation to the rotational axis, the initial angle φ_0 of the location of point P_{11} for $t=0$ is 0. The distances between the centre of the rotation of the head and points P_1 and P_{11} are equal, hence according to Fig. 5 $r_1=r_2=r$. The distance between points P_1 and P_{11} is $2r$ and, what follows from that, $h_4=2r$. The pitch of the prolate cycloid is the parameter that characterizes it. According to Equation (2), it is as follows: $h = 2\pi\frac{v_p}{\omega}$. If one wants to determine distance h_1, one needs to subtract coordinate x for point P_3 from coordinate x for point P_2. Hence, the following dependence is obtained:

$$\begin{aligned} h_1 &= x_2 - x_3 = \left[r\cos(\varphi_0 - \varphi_2) + v_p t_2\right] + \\ &- \left[r\cos(\varphi_0 - \varphi_3) + v_p t_3\right] = \\ &= r\cos(\pi - \pi) - r\cos(\pi - 2\pi) + v_p(t_2 - t_3) = \\ &= r + r + v_p(t_2 - t_3) = 2r + v_p(t_2 - t_3). \end{aligned} \tag{11}$$

Considering that:

$$t_3 - t_2 = \frac{\pi}{\omega}, \tag{12}$$

and by making adequate transformations:

$$t_3 - t_2 = \frac{\pi}{\omega}\Big/(-1), \tag{13}$$

$$t_2 - t_3 = -\frac{\pi}{\omega}\Big/v_p, \tag{14}$$

$$v_p(t_2 - t_3) = -\pi\frac{v_p}{\omega}, \tag{15}$$

the following dependence is finally obtained:

$$h_1 = 2r - \pi\frac{v_p}{\omega}. \tag{16}$$

In order to determine the remaining quantities that occur between the postprocessing traces, one needs to perform several transformations:

$$h = h_1 + h_3, \tag{17}$$

hence:

$$h_3 = h - h_1 = 2\pi\frac{v_p}{\omega} - 2r + \pi\frac{v_p}{\omega} = 3\pi\frac{v_p}{\omega} - 2r, \tag{18}$$

$$h_2 = h + h_1 = 2\pi\frac{v_p}{\omega} + 2r - \pi\frac{v_p}{\omega} = 2r + \pi\frac{v_p}{\omega}, \tag{19}$$

$$h_5 = h - h_4 = 2\pi\frac{v_p}{\omega} - 2r. \tag{20}$$

The dependence that is described with Equation (20) is true, if $h_4<h$, and in so far as v_p fulfills the following inequality:

$$v_p > \frac{r\omega}{\pi}. \tag{21}$$

If:

$$v_p < \frac{r\omega}{\pi}, \tag{22}$$

formula (20) takes on the following form:

$$h_5 = h_4 - h = 2r - 2\pi\frac{v_p}{\omega}. \tag{23}$$

The remaining dependences are legitimate for this case, as well, and their graphical presentation is to be found in Fig. 6.

Apart from the two cases that are described above, there may also occur a situation when $h_4=h$, hence:

$$v_p = \frac{r\omega}{\pi}, \tag{24}$$

then:

$$h_5 = h_4 - h = 0, \tag{25}$$

and so both cycloids cross axis *x* at one point. This particular case is presented in Fig. 7.

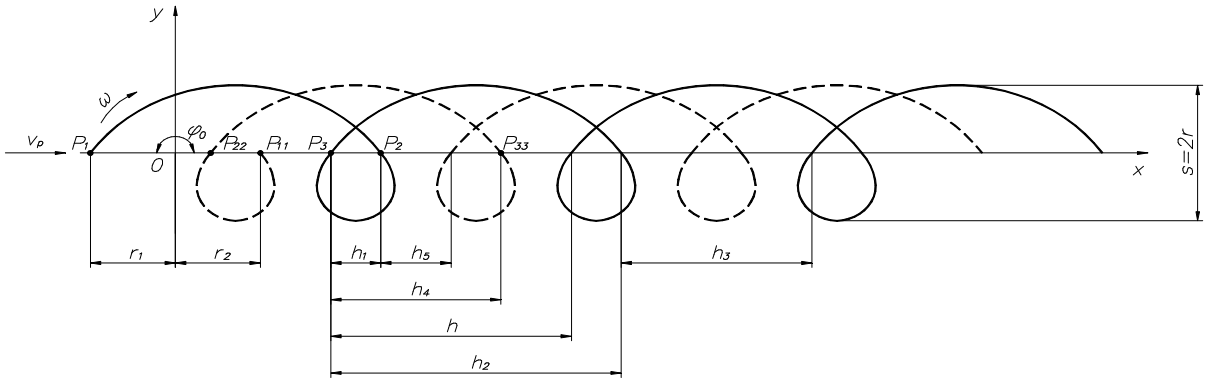

Fig. 5. Traces that are generated when cleaning with a rotary head with two nozzles

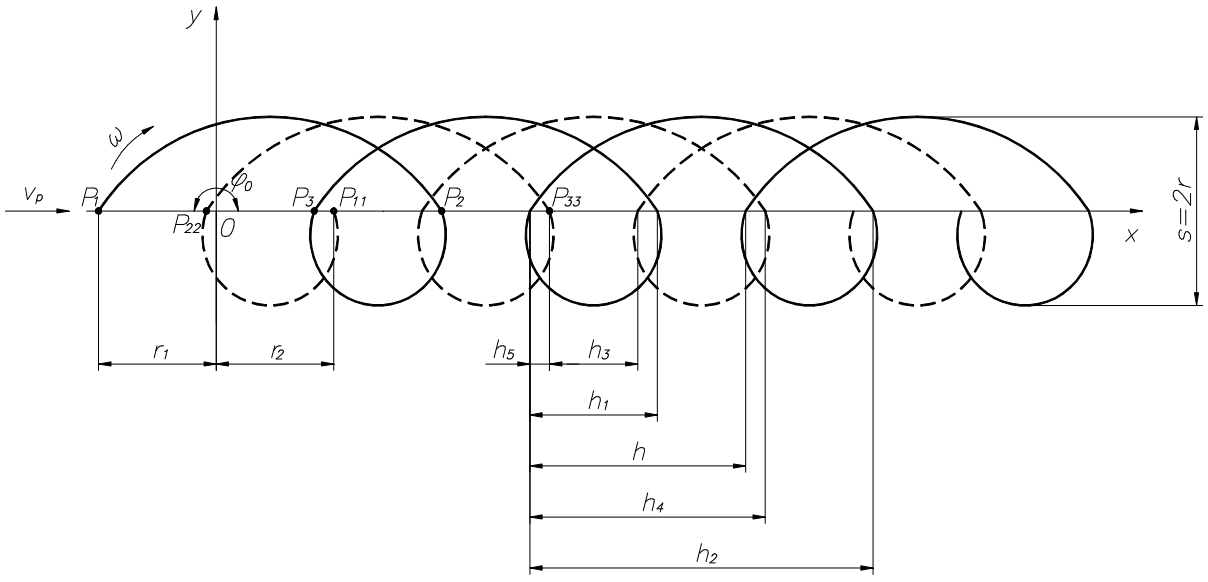

Fig. 6. Distribution of those prolate cycloids that fulfill condition $v_p < \frac{r\omega}{\pi}$

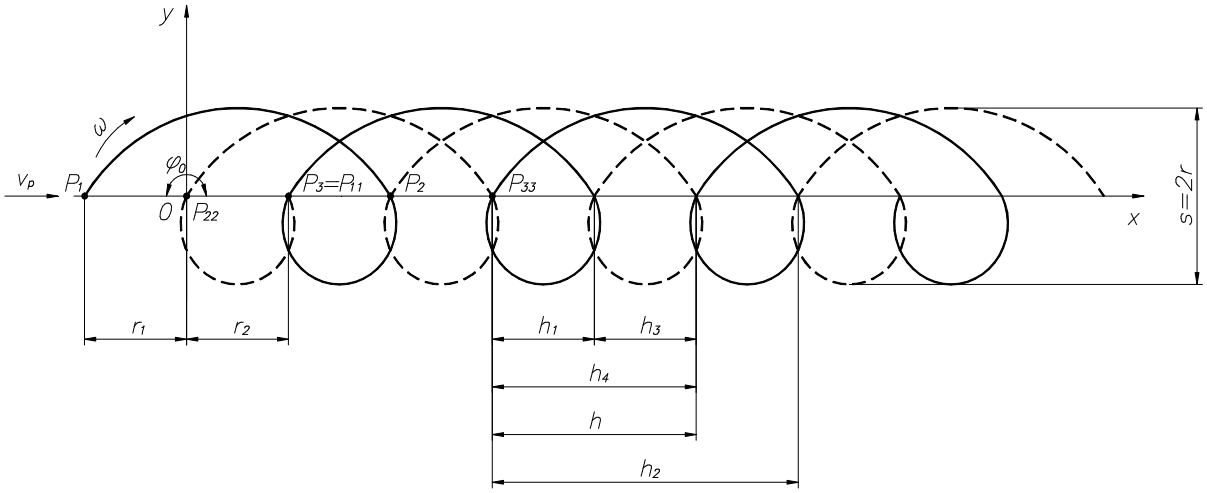

Fig. 7. Distribution of those prolate cycloids that fulfill condition $v_p = \frac{r\omega}{\pi}$

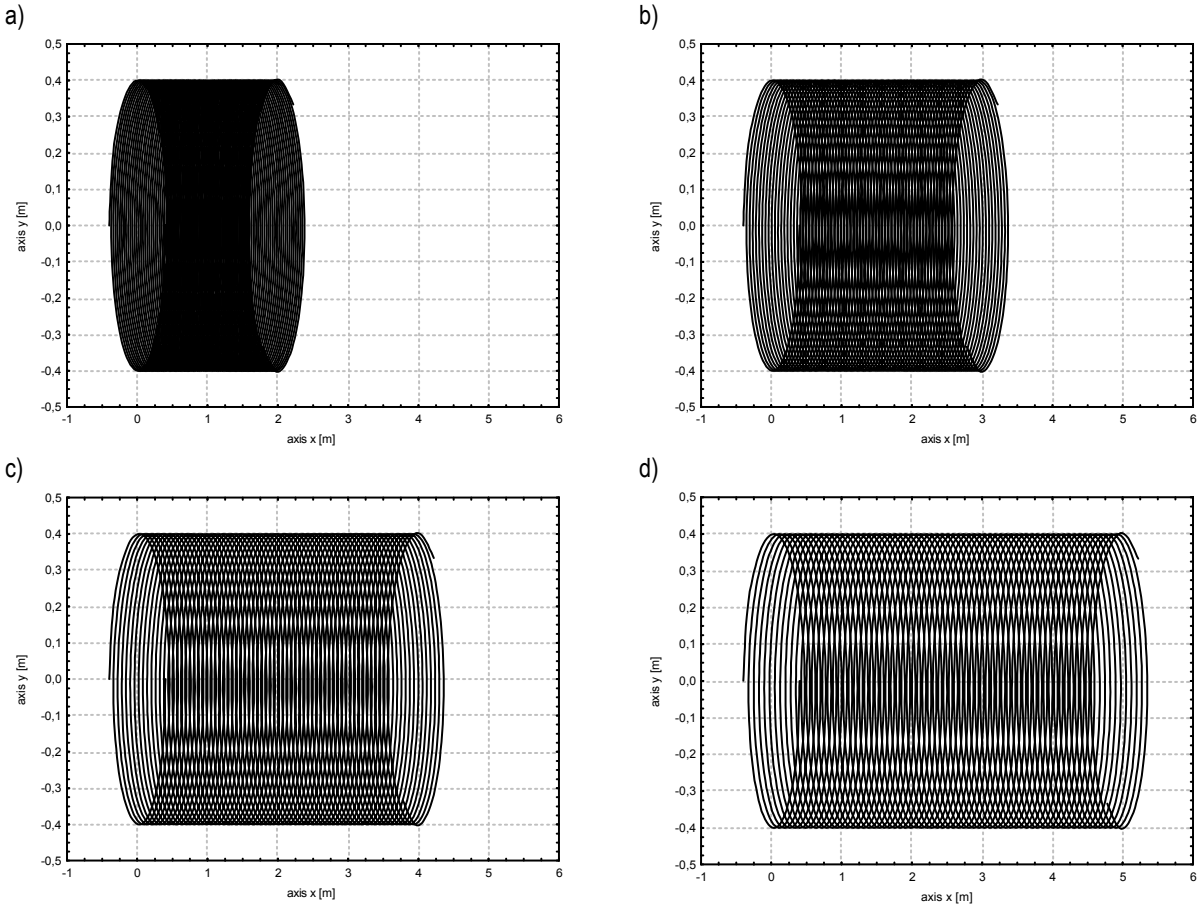

Fig. 8. The distribution of the processing traces for ω=*41.9* 1/s: a) v_p=*0.4* m/s, b) v_p=*0.6* m/s, c) v_p=*0.8* m/s, d) v_p=*1* m/s

For a surface that is being cleaned to be uniformly cleaned, the distances between the postprocessing traces need to be smaller or at the most equal to the jet width. According to this condition, in the case when $v_p > \frac{r\omega}{\pi}$, the following dependences must be fulfilled:

$$h_1 \le \frac{s_z - s_w}{2}, \tag{26}$$

$$h_5 \le \frac{s_z - s_w}{2}. \tag{27}$$

If $v_p < \frac{r\omega}{\pi}$, the conditions of a uniform cleaning of the surface take on the following form:

$$h_3 \le \frac{s_z - s_w}{2}, \tag{28}$$

$$h_5 \le \frac{s_z - s_w}{2}. \tag{29}$$

If $v_p = \frac{r\omega}{\pi}$, the following condition is to be fulfilled:

$$h_1 \leq \frac{s_z - s_w}{2}. \tag{30}$$

Nevertheless, in this case one needs to take into account the fact that the intersection points of the cycloid with axis *x* are the common points of the intersection of the two cycloids. Hence, this may lead to a local erosion of the surface being cleaned, and this is not desirable. Therefore, one needs to focus on using such parameters in practice that will allow one to obtain those cleaning effects that are analyzed in the two remaining cases.

However, the conditions presented above of uniform cleaning of flat surfaces with a rotary head and that are described with Inequalities 26÷30 are approximate conditions, as according to Fig. 4:

$$\frac{s_z}{2} - r_1 \neq r_1 - \frac{s_w}{2}. \tag{31}$$

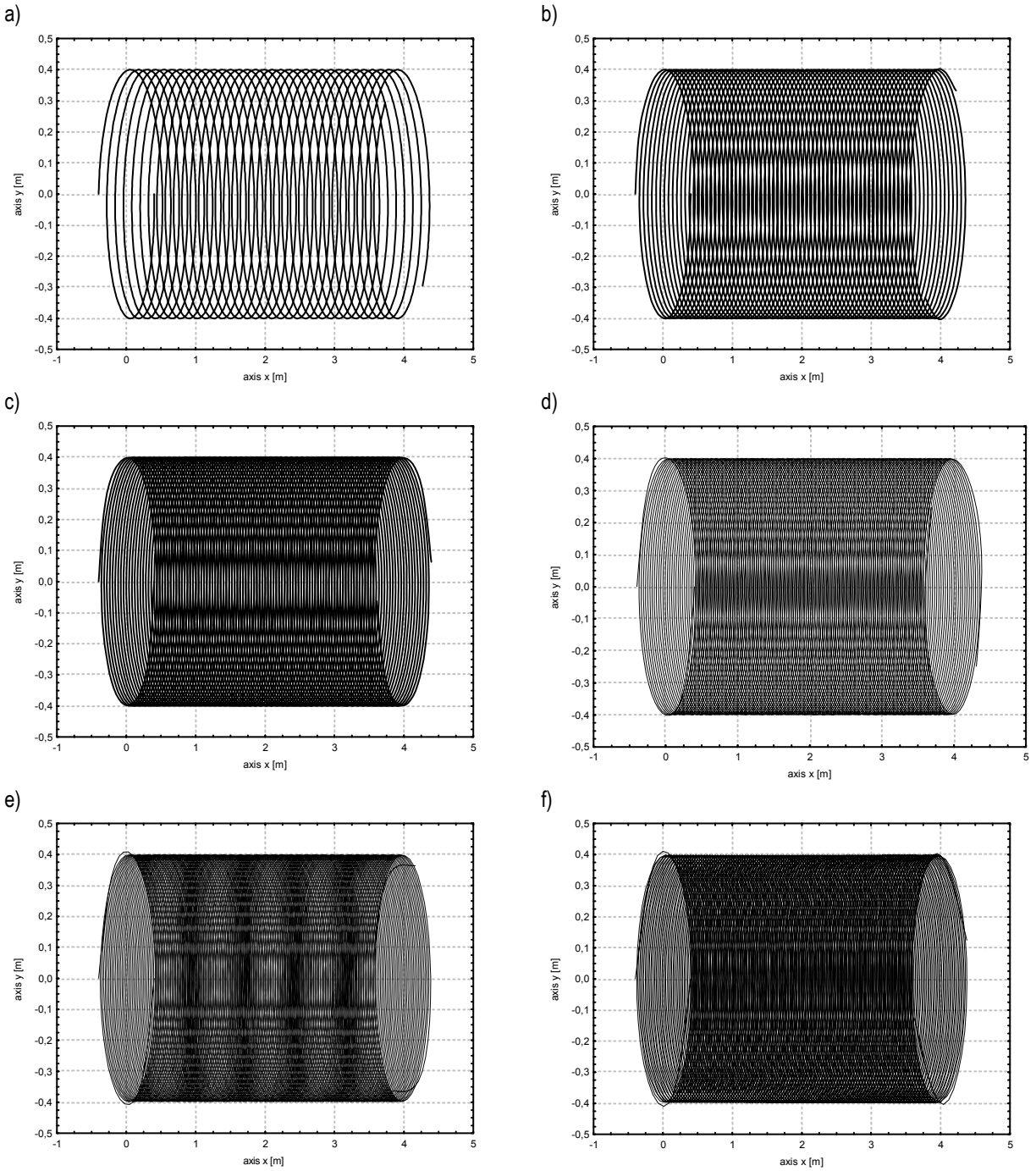

Fig. 9. The distribution of the processing traces for v_p=*0.8* m/s: a) ω=*20.9* 1/s, b) ω=*41.9* 1/s, c) ω=*62.8* 1/s, d) ω=*83.7* 1/s, e) ω=*104.7* 1/s, f) ω=*125.6* 1/s

Nevertheless, the generalizations applied have no influence on the quality of the surface obtained, and the differences between dimension $\frac{s_z}{2} - r_1$ and dimension $r_1 - \frac{s_w}{2}$ can be treated as being negligibly small.

The determination of the optimal working conditions of a rotary head is a complex issue, one which requires an analysis of numerous aspects including the following: the influence of the axial velocity, the influence of the angular velocity, the distribution of energy in the cross-section of the jet, the possibility of the use of additional nozzles that are arranged at smaller distances from the rotational axis of the head as compared with the distances between the main nozzles, etc.

In the present study, attention was paid to the selection of the operational parameters of processing for a double hole nozzle. The influence was determined of the axial velocity of v_p of the head (Fig. 8) and the influence of angular velocity ω (Fig. 9) on the distribution of the processing traces. The following parameters were accepted: $r=0.4$ m; $\varphi_{01}=\pi$ rad; $\varphi_{02}=0$ rad; $t=5$ s. The uniformity of the distribution of the postprocessing traces was visually assessed.

It is evident from the figures above that axial velocity v_p has an influence on the length of the surface cleaned in a time unit. The result of an increase of velocity v_p is a greater length being obtained of the surface cleaned; at the same time, it has an influence on an increase of the distances between postprocessing traces. It can be seen in each case that the middle section of the surface under consideration is cleaned most poorly, whereas the largest amounts of postprocessing traces are to be found on the edges. The most uniform distribution of the traces of cleaning can be observed for axial velocity v_p: from 0.6 to 1.2 m/s. It can be clearly seen with lower velocities that the edges of the surface are cleaned very strongly, which involves a risk of an erosion of the base material.

The angular velocity of the head ω has an influence on the quantity of the postprocessing traces obtained. It was found that an increase of the angular velocity results in an increased amount of postprocessing traces, the consequence being a reduced distance between them. The result of an angular velocity that is too low is the surface being non-uniformly cleaned (Fig. 9a). The traces of processing are located too far from one another. The impact time of the jet is longer as compared to processing with greater rotational velocities; thus, it can be stated that impurities will be removed at the location of the impact of the jet. At the same time, an angular velocity that is too great (Fig. 9f) causes a fairly uniform distribution of the processing traces, yet the time of an impact on the base is too short for a total cleaning of the surface to take place. It was found that the extreme edges that are far away from the central axis of the collective processing trace are cleaned best, whereas the central area is cleaned the least. This is so because the jet traces on the edges are located almost in parallel to the feed direction of the head, and the intersection angles of the jet trajectories are great. For such parameters, an optimal head angular velocity is within the range of $\omega=62.8\div83.7$ 1/s.

The use of a head that is provided with two nozzles (known as external ones) does not ensure a uniform cleaning of the whole surface (Fig. 10a). As a result, two additional nozzles (known as internal ones) were introduced. The purpose of these is to increase the number of postprocessing traces in the central area, which so far has not been sufficiently cleaned. Four traces in the form of prolate cycloids (Fig. 10b) are formed on the surface being cleaned, whereas the external cycloids are the result of the operation of the external nozzles, and internal (smaller) cycloids are the effect of the operation of the internal nozzles.

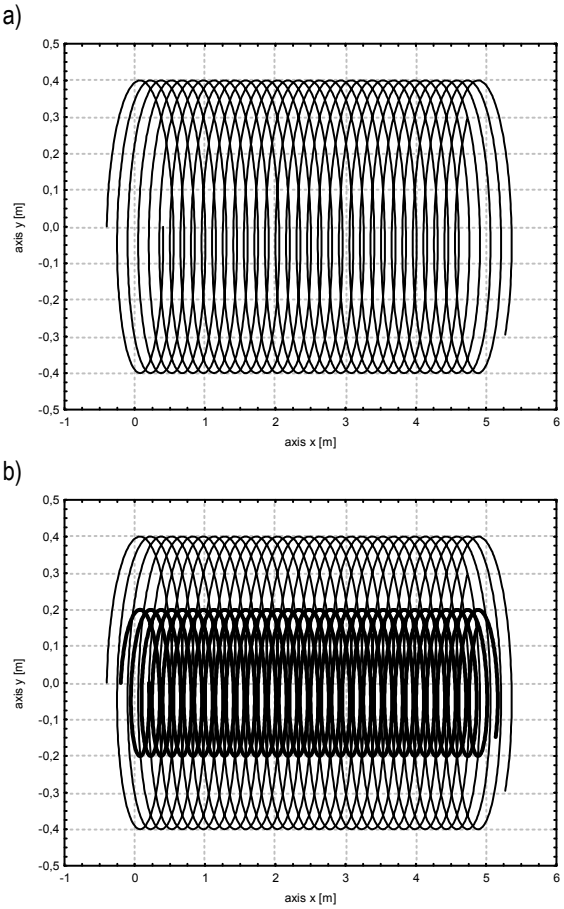

Fig. 10. The distribution of the processing traces for $v_p=1$ m/s and $\omega=20.9$ 1/s: a) head with two nozzles $r_1=r_2=0.4$ m, b) head with four nozzles $r_1=r_2=0.4$ m $r_3=r_4=0.2$ m

The nozzles are located in such a way that the contact point of the jet that flows out of the internal jet is located at a half of the distance between the rotational axis and the contact point of the jet that flows out from the external jet with the surface being cleaned. The use of a rotational axis with four nozzles offers better cleaning effects of a flat surface as compared with processing with the aid of a double hole nozzle. Nevertheless, it is to be observed that the impact time of the jet that flows out of the external jets on the surface being processed is longer than that of the jet from external jets; hence, there occurs a stronger erosion of impurities there. Consequently, adequate processing parameters need to be selected in order to obtain a uniform removal of sediments from the entire surface.

6. CONCLUSION

A uniform removal of impurities from the surface is obtained when the distances between the postprocessing traces are smaller, or when they are at the most equal to the jet trace width.

The most uniform distribution of the cleaning traces of flat surfaces with the use of a rotary double hole head is obtained is obtained for axial velocity v_p within the range of 0.6÷1.2 m/s and angular velocity ω within the range of 62.8÷83.7 1/s.

It was established that in all the cases analyzed, the central area is always cleaned the least, while the edges of the surface being cleaned are densely covered with postprocessing traces. Thus, it can be supposed that better effects of cleaning are to be obtained when additionally using two nozzles that are located between the rotational axis of the head and the external nozzles.

REFERENCES

1. **Azhari A., Schindler Ch., Kerscher E., Grad P.** (2012), Improving surface hardness of austenitic stainless steel using waterjet peening process. *The International Journal of Advanced Manufacturing Technology*, DOI: 10.1007/s00170-012-3962-1.
2. **Bodnárová L., Sitek L., Hela R., Foldyna J.** (2011), New potential of highspeed water jet technology for renovating concrete structures. *Slovak Journal of Civil Engineering*, Vol. XIX, No. 2, 1 – 7.
3. **Borkowski P., Borkowski J., Bielecki M.** (2012), Technical aspects of coal disintegration using high pressure water jet. *Journal of Machine Engineering*, Vol. 12, No. 2, 7-19.
4. **Caydas¸ U., Hascalik A**. (2008), A study on surface roughness in abrasive waterjet machining process using artificial neural networks and regression analysis method. *Journal of materials processing technology* 202, 574–582.
5. **Chillman A., Ramulu M., Hashish M.** (2007), Waterjet peening and surface preparation at 600 MPa: A preliminary experimental study. *Journal of Fluids Engineering, Transactions of the ASME*, Vol. 129, Issue 4, 485-490.
6. **Frenzel L.** (2007), What effect does waterjet clearing have on the surface and surface preparation? *American WJTA Conference and Expo.* Houston, Texas,.
7. **Gałecki G., Mazurkiewicz M.** (1987), Trepanate drilling of deep and large diameter holes In hard rock – conceptual study. *3rd Inter. Conf. on Innovative Mining systems*. Rolla, Missouri, 245-252.
8. **Heinzel C., Antsupov G.** (2012),Prevention of wheel clogging in creep feed grinding by efficient tool clearing. *CIRP Annals - Manufacturing Technology*, Vol. 61, 323–326.
9. **Huang L., Folkes J., Kinnell P., Shipway P. H.** (2012), Mechanisms of damage initiation in a titanium alloy subjected to water droplet impact during ultra-high pressure plain waterjet erosion. *Journal of Materials Processing Technology*, Vol. 212, 1906– 1915.
10. **Kim Jung-Gyu, Song Jae-Joon, Han Song Soo, Lee Chung-In** (2012), Slotting of concrete and rock using an abrasive suspension waterjet system. *KSCE Journal of Civil Engineering*, Vol. 16, No. 4, 571-578.
11. **Kong M. C., Axinte D. A.** (2011), Capability of Advanced Abrasive Waterjet Machining and its Applications. *Applied Mechanics and Materials* (Volumes 110 - 116), Mechanical and Aerospace Engineering, 1674-1682.
12. **Shanmugam D. K., Masood S. H.** (2009) An investigation on kerf characteristics in abrasive waterjet cutting of layered composites. *Journal of materials processing technology* 209, 3887–3893.
13. **Sharma V., Chattopadhyaya S., Hloch S.** (2011), Multi response optimization of process parameters based on Taguchi—Fuzzy model for coal cutting by water jet technology. *Int J Adv Manuf Technol*, Vol. 56, 1019–1025.

APPLICABILITY OF INDICATORS OF TRABECULAR BONE STRUCTURE FOR EVALUATION OF ITS MECHANICAL PROPERTIES

Artur CICHAŃSKI*, Krzysztof NOWICKI*, Adam MAZURKIEWICZ*, Tomasz TOPOLIŃSKI*

*Faculty of Mechanical Engineering, University of Technology and Life Sciences,
ul. Kaliskiego 7, 85-789 Bydgoszcz, Poland

artur.cichanski@utp.edu.pl, krzysztof.nowicki@utp.edu.pl, adam.mazurkiewicz@utp.edu.pl, tomasz.topolinski@utp.edu.pl

Abstract: The paper presents the results of examination of relations between indicators describing trabecular bone structure and its static and cyclic compressive strength. Samples of human trabecular bone were subject to microtomographic tests in order to specify indicators describing its structure. Part of the samples was subject to static compression tests, part to cyclic compressing loads with stepwise increasing amplitude. Evaluation of a degree of applicability level of estimation of bone compressive strength properties was conducted based upon values of structure indicators. Evaluation was performed based upon values of obtained determination coefficients R2 for linear regression. Obtained R2 values were within the range of 0.30-0.51 for relations between examined indicators and static compressive strength within the range of 0.47-0.69 for relations with the results of cyclic test with stepwise increasing amplitude.

Key words: Trabecular Bone, Testing Method, Bone Structure Indicators

1. INTRODUCTION

Structure of human bone is subject to constant changes depending on various factors e.g. human activity, type of work performed etc. After 20-30 year of age a process of decreasing of bone mass commences. It results in the change of bone structure describing indicators and decrease of compressive strength properties of bone tissue (Biewener, 1993; Taylor and Tanner, 1997; Warden et al., 2006). If, with age diseases impairing bone metabolism occur, such as e.g. osteoporosis, dynamics of such changes increases (Rapillard et al., 2006).

Typical bone load is the compressing load applied to e.g. long bones of lower limbs or spine. It is a cyclic load e.g. during walking, thus behaviour under such load is the fatigue behavior (Warden et al., 2006; Keaveny et al., 1993; Martin, 2003).

The target of the hereby paper is to specify applicability of indicators describing trabecular bone structure for the description of its compressive strength properties specified in static compression test and cyclic compression test under loads with stepwiseincreasing amplitude.

2. MATERIAL AND METHODS

For static tests 42 and for cyclic tests 62 samples of human trabecular bone were used, taken from human femur head. The samples were not divided into sub-groups acc. To e.g. age, sex, type of disease or any other factors. Preparations the samples were made of were obtained as a result of implantation of femoral joint.

Samples were in the shape of a cylinder of diameter of 10mm and height of 8.5mm. Sample taking manner is presented on Fig. 1. A slice of 8.5mm thickness was cut from the head base perpendicularly to neck axis, then a cylinder of 10mm diameter and 8.5mm height was cut from central part of the slice.

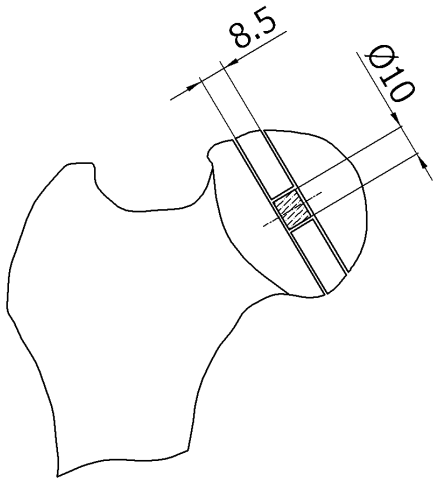

Fig. 1. Manner of taking samples for tests

All samples were tested at micro-tomograph µCT80 at separation of 36µm between subsequent scans for the following parameters: 70kV, 114µA, 500 projections/180°, and 300ms integration time. Upon scanning, as standard, values of 5 bone structure indicators were obtained: average constant trabecular number per sample volume – Trabecular Number Tb.N, average trabecular thickness in a sample – Trabecular Thickness Tb.Th, average trabecular separation in a sample - Trabecular Separation Tb.Sp, quotient of tissue volume vs. volume of the whole sample – Bone Volume Fraction BV/TV, and quotient of tissue surface field in a sample vs. its volume – Bone Surface Ratio BS/BV (Parfitt et al., 1987).

Static compression test was made on strength testing machine MiniBionix 858. The test defined compression strength of samples indicated as US (Ultimate Strength).

In the first part of a test five cycles of loading and relieving for deformation value from ε=0 to ε=0.8% were performed. Initial load, for which ε=0 was assumed, was specified as 50N. Intervals between cycles were five seconds. The cycles were made to stabilize contact surfaces of sample-machine. Test program is presented at Fig. 2.

At the next stage the test was performed until obtaining of compression strength value i.e. obtaining the first maximum at compression curve. From the specified curve compression strength value US was calculated, i.e. stress value at the first curve maximum point.

Static test was performed at room ambient temperature.

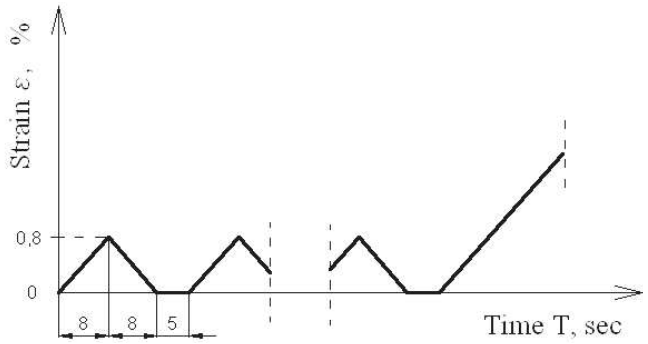

Fig. 2. Static compression test program

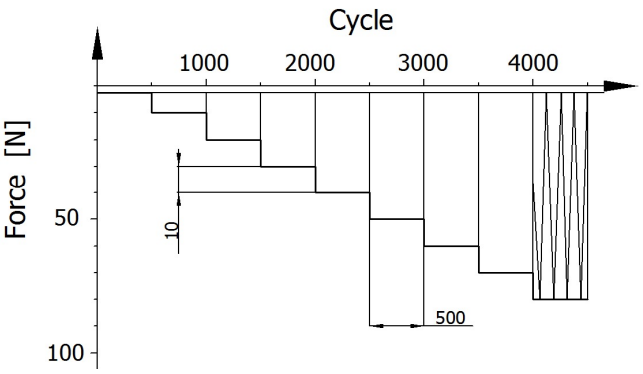

Fig. 3. Cyclic test with stepwise increasing amplitude program

Cyclic tests of bone samples were performed in the conditions of compression upon stepwise increasing load at strength testing machine INSTRON 8874. Frequency of changes of sinusoidal load was 1 Hz. Minimum load for all load levels was 5N. Maximum load started at 20N with 10N increments at subsequent stages. Volume of stages is 500 cycles realized in fixed amplitude conditions. The test program is presented at Fig. 3. During every tests 10 cycles recording of sample load and deformations was made with 100 Hz sampling. Measuring signal from strength testing machine processed with low-pass filter cutting off frequencies exceeding 10Hz in order to equalize current interferences and the noise of measuring devices (dynamometer).

In order to identify fatigue life median of values of deformations increments was specified; then, the first loop, was identified as the value of fatigue life N, for which deformation increment exceeded the value of the specified median by 10%.

Cyclic tests were performed in controlled environment – 0.9% solution of NaCl at temperature of 37±2°C.

3. TEST RESULTS

Tables 1-2 present ranges, average values and standard deviations, relative RSD values of structure indicators obtained from microtomographic tests for groups of samples subject to static compression and cyclic test. Tab. 3 presents analogical values achieved for US compressive strength and fatigue life N obtained in static compression test and in cyclic test with stepwise increasing load.

Tab. 1. Ranges, average values and standard deviations relative values of structure indicators obtained from microtomographic tests for samples subject to static compression

	BS/BV, 1/mm	BV/TV, -	Tb.N, 1/mm	Tb.Th, mm	Tb.Sp, mm
Min.	7.737	0.068	0.76	0.089	0.331
Max.	22.505	0.392	1.958	0.259	1.223
Average	13.903	0.222	1.436	0.151	0.572
RSD, %	22	36	19	24	32

Tab. 2. Ranges, average values and standard deviations relative values of structure indicators obtained from microtomographic tests for samples subject to cyclic test

	BS/BV, 1/mm	BV/TV, -	Tb.N, 1/mm	Tb.Th, mm	Tb.Sp, mm
Min.	5.206	0.066	0.511	0.105	0.424
Max.	18.995	0.459	1.543	0.384	1.829
Average	11.998	0.204	1.1329	0.176	0.749
RSD, %	23	37	20	26	34

Tab. 3. Ranges, average values and standard deviations relative values of US compressive strength and fatigue life N, obtained in static compression test and cyclic test with stepwise increasing load

	US, MPa	N, number of cycles
Min.	1.678	$9.75 \cdot 10^3$
Max.	36.143	$3.52 \cdot 10^4$
Average	12.675	$20.73 \cdot 10^3$
RSD	55%	55%

Tab. 4. Values of R2 determination coefficients for relations between bone structure indicators and its static compressive strength and cyclic strength

Indicator	Static compressive strength US, MPa	Fatigue life N, number of cycles
BS/BV, 1/mm	0.44	0.50
BV/TV, -	0.51	0.69
Tb.N, 1/mm	0.30	0.50
Tb.Sp, mm	0.36	0.47
Tb.Th, mm	0.48	0.50

Tab. 4 presents values of R^2 determination coefficients, obtained with application of linear regression for relations between

bone structure indicators and its static compressive strength and fatigue life.

Figs. 4-5 present dependencies between BV/TV and Tb.Th and static compressive strength US

Figs. 6-7, on the other hand, present dependencies between BV/TV and Tb.Th and fatigue life obtained during the test with stepwise increasing amplitude.

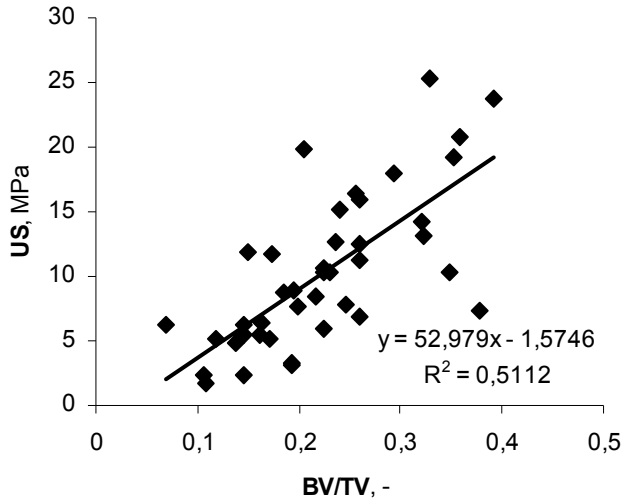

Fig. 4. Relation between BV/TV and static compressive strength US

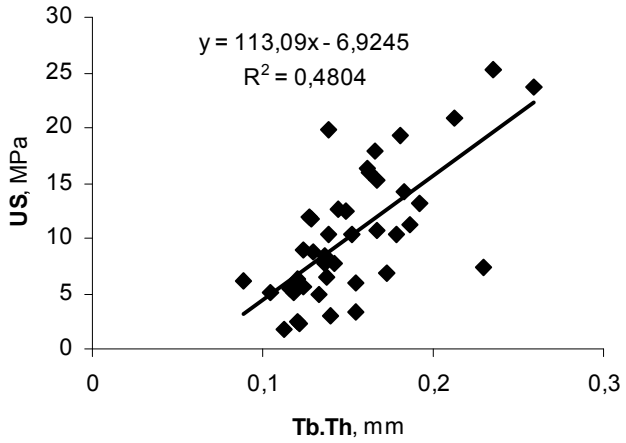

Fig. 5. Relation between Tb.Th value and static compressive strength US

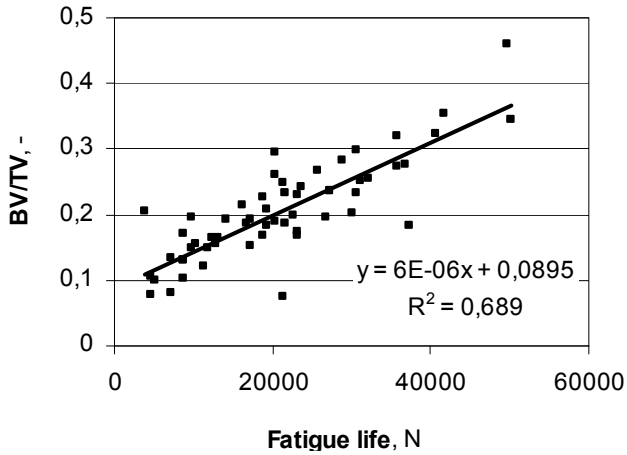

Fig. 6. Relation between BV/TV value and fatigue life obtained during the test with stepwise increasing amplitude

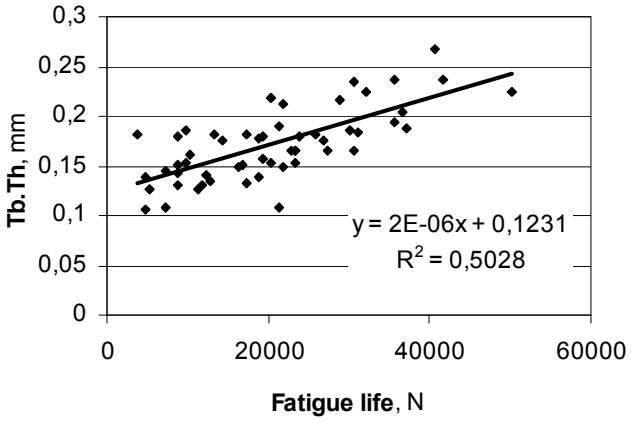

Fig. 7. Relation between Tb.Th value and fatigue life obtained during the test with stepwise increasing amplitude

4. DISCUSION

Performed tests refer to samples from over 100 donors thus on relatively big population. Usually (Rapillard at al., 2006; Haddock et al., 2004; Zioupos et al., 2008) tests refer to no more than 10 donors and the samples are multiplied by taking of more than a single sample from each donor. Thus, we are dealing with significant variability of sample structures resulting from individual properties and pathological properties (osteoporosis, coxarthrosis**).** If the structure was described with variability of relative BV / TV volume coefficient, it would be 36-37%, which is close to maximum values of variability quoted in literature (Haddock et al., 2004). Both performed tests are statistically homogenous – examined relative structure indicators differ maximally by 2%.

The measure of strength of connection of two independent factors in functional description of regression is R^2 determination coefficient. Referring the results obtained from structure tests for first group to static compressive strength determination coefficient R^2 for tested indicators was specified up to the value of 0.5 – the highest value for BV/TV. For the second group the same value, but for fatigue life, is 0.69 which can be considered high for this variability. Also, for all other structure indicators with respect to fatigue life, determination coefficient value is significantly higher. It indicates that examinations of bone fracture risk testing method with stepwise increasing amplitude allows for obtaining better correlation with bone structure, in particular with BV/TV indicator.

REFERENCES

1. **Biewener A.A.** (1993), Safety factors in bone strength, *Calcified Tissue International*, Vol. 53, Suppl. 1, 68-74.
2. **Taylor M., Tanner K.E.** (1997), Fatigue failure of cancellous bone: a possible cause of implant migration and loosening, *The Journal of Bone and Joint Surgery*, Vol. 79-B, 181-182.
3. **Warden S.J., Burr D.B., Brukner P.D. (2006),** Stress fractures: pathophysiology, epidemiology, and risk factors, *Current Osteoporosis Reports*, Vol. 4, No. 3, 103-109.
4. **Rapillard L., Charlebois M., Zysset P.K.** (2006), Compressive fatigue behavior of human vertebral trabecular bone, *Journal of Biomechanics*, Vol. 39, No. 11, 2133-2139.
5. **Keaveny T.M., Borchers R.E., Gibson L.J., Hayes W.C.** (1993), Technical Note: Theoretical analysis of the experimental artifact in trabecular bone compressive modulus, *Journal of Biomechanics*, Vol. 26, 599-607.

6. **Martin, R.B.** (2003), Fatigue Microdamage as an Essential Element of Bone Mechanics and Biology, *Calcified Tissue International*, Vol. 73, 101-107.
7. **Parfitt A.M., Drezner M.K., Glorieux F.H., et. al.** (1987), Bone histomorphometry: standardization of nomenclature, symbols, and units. Report of the ASBMR Histomorphometry Nomenclature Committee, *Journal of Bone Mineral Research*, Vol. 2, 595-610.
8. **Haddock S.M., Yeh O.C., Mummaneni P.V., Rosenberg W.S., Keaveny T.M.** (2004), Similarity in the fatigue behavior of trabecular bone across site and species, *Journal of Biomechanics*, Vol. 37, No. 2, 181-187.
9. **Zioupos P., Gresle M., Winwood K.** (2008), Fatigue strength of human cortical bone: Age, physical, and material heterogeneity effects, *Journal of Biomedical Materials Research*, Vol. 86A, No. 3, 627-636.

Acknowledgement: This work by supported by The State Committee for Scientific Research (KBN) under grant No. N N501 308934.

THE DYNAMICS OF LIQUID MOVEMENT INSIDE THE NOZZLE DURING THE BUBBLE DEPARTURES FOR LOW AIR VOLUME FLOW RATE

Paweł DZIENIS*, Romuald MOSDORF*, Tomasz WYSZKOWSKI*

*Białystok University of Technology, Faculty of Mechanical Engineering, Department of Mechanics and Applied Computer Science.
ul. Wiejska 45C, 15-351 Białystok, Poland

dzienis.pawel@gmail.com, mosdorf@gmail.com, wyszkowski.tomasz@gmail.com

Abstract: The main aim of investigation was to analyze the influence of liquid movement inside the nozzle on the dynamics of bubble departure. Dynamics of such process decides about the periodic and aperiodic bubble departures. During the experiment it has been simultaneously recorded: changes of the depth of the nozzle penetration by liquid, air pressure and shape of bubble trajectory directly over the nozzle (in the length of 30 mm). The air volume flow rate was in the range 0.00632 - 0.0381 l/min. There has been shown that for all air volume flow rates the time periods with periodic and aperiodic bubble departures have been occurred. Duration of these intervals varies with the air volume flow rate. It has been found that the aperiodic bubble departures begin when the time of bubble growth increases. The changes of maximum values of liquid position inside the nozzle are associated with changes of the shape of bubble trajectories. There has been shown that straightens of the trajectory precedes the appearance of periodical or aperiodic time period of bubble departures. The aperiodic bubble departures are accompanied by a significant deviation of bubble trajectory from a straight line. The correlation dimension analysis shown that three independent variables are enough to describe the behaviour of liquid movement inside the nozzle. These independent variables may be: liquid velocity, liquid position in the nozzle and gas pressure in the nozzle.

Keywords: Bubbles, Nonlinear Analysis

1. INTRODUCTION

The time period between two subsequent bubbles departing from the nozzle may be divided into two periods: waiting time and time of the bubble growth. During the waiting time for the low frequency of bubble departures the nozzle is flooded by liquid. Then, the liquid is removed from the nozzle, because the gas pressure inside a gas supply system increases (Koval'chuk et al., 1999). Dynamics of such process decides about the periodic and aperiodic bubble departures.

There are a lot of papers reporting the non-linear behaviours of the bubbling process. It has been found that the meniscus oscillations in orifice strongly affect the subsequent bubble cycles (Ruzicka et al., 2009a, b). The analyses carried out in (Ruzicka et al., 2009a) show that ways of chaos appearance in bubbling depend on the nozzle or orifice diameter (Stanovsky et al., 2011; Cieslinski and Mosdorf, 2005; Mosdorf and Shoji, 2003; Koval'chuk et al., 1999; Zang and Shoji, 2001). The influence of: plate thickness, surface tension, viscosity of the liquid and the height of liquid column on the length of liquid penetration inside the nozzle have been reported in the papers (Ruzicka et al., 2009a, b; Dukhin et al., 1998a, b; Koval'chuk et al., 1999). In Stanovsky et al. (2011) the influence of orifice diameter on the depth of liquid penetration inside the orifice has been investigated. In Stanovsky et al. (2011) the influence of chamber volume and the height of the liquid over the orifice outlet on frequency of bubble departure have been investigated. There has been observed that increase of the chamber volume increases the time period between two subsequent bubbles. The increase in height of the liquid over the orifice outlet leads also to the increase of time period between the subsequent bubbles. In Ruzicka et al. (2009a) for investigation of bubble formation and liquid movement inside the orifice the high-speed photography and video techniques have been used. The oscillations of the gas-liquid interface inside the orifice have been analyzed. It has been shown that the gas-liquid interface inside the orifice modifies the duration of time periods between subsequent bubbles. Time period between subsequent bubbles decreases when the number of gas-liquid interface oscillations decreases.

The phenomena of liquid movement inside the orifice or nozzle have been modelled by many researches (Ruzicka et al. (2009b), Dukhin et al. (1998a), Koval'chuk et al., 1999). In Ruzicka et al. (2009b) the gas-liquid interface oscillations inside the orifice, during the waiting time, have been investigated. The process was divided into two phases. The first phase was the bubble growth and the second phase was the liquid flow inside the orifice. The liquid flow has been described by the equation of motion of mass centre of the liquid filling the orifice. Results obtained from the model have been compared with the experimental results presented in Ruzicka et al. (2009a). In Dukhin et al. (1998b) a model describing the changes of pressure distribution along the capillary and its impact on the time of liquid movement inside the nozzle has been proposed. The model takes into account the Hagen-Poiseuille equation describing the relationship between the liquid flow rate and its viscosity, pressure gradient and the nozzle geometry (length and diameter). There has been found that the maximum liquid penetration of the nozzle is dependent on the capillary pressure. The increase in gas pressure supplied to the nozzle causes the removing of liquid from the nozzle. It was also found that the time of the interface motion is longer than the time of gas pressure growth in the gas supply system. In Dukhin et al. (1998a) a model describing the gas pressure changes in the nozzle during the bubbles detachment

and gas - liquid interface position inside the nozzle has been proposed. The model is based on the simplified Navier-Stokes equations (it includes the liquid mass and momentum conservation equations). Gas was supplied to the system in periodic and aperiodic way. In the paper a relationship between the amplitude and frequency of liquid movement in the nozzle and gas pressure changes have been proposed. There has been shown that when the amplitude of pressure oscillations decreases the frequency of these oscillations increases. It was also found that the length of liquid penetration inside the nozzle decreases when the gas pressure increases. The model based on the capillary equation and equation of pressure changes in the capillary has been presented in (Koval'chuk et al., 1999). A capillary equation was based on Newton's second law for the motion of the mass centre of the liquid inside the capillary. The depth of liquid penetration inside the nozzle and duration of this process have been analyzed.

In the present study the dynamics of the liquid flow inside the glass nozzle in the process of subsequent bubble departures has been investigated experimentally. The impact of the dynamics of changes of the depth of nozzle penetration by the liquid on the process of bubbles detachment has been analyzed. During the experiment it has been simultaneously recorded: changes of the depth of the nozzle penetration by the liquid, air pressure, and shape of bubble trajectory directly over the nozzle (in the distance of 30 mm). The air volume flow rate was in the range 0.00632 - 0.0381 l/min. For such volume flow rates the bubbles do not coalesce.

2. EXPERIMENTAL SETUP AND MEASUREMENT TECHNIQUE

In the experiment bubbles were generated in tank (300x150x700 mm) - from glass nozzle with inner diameter equal to 1 mm. The experimental setup has been shown in Fig.1.

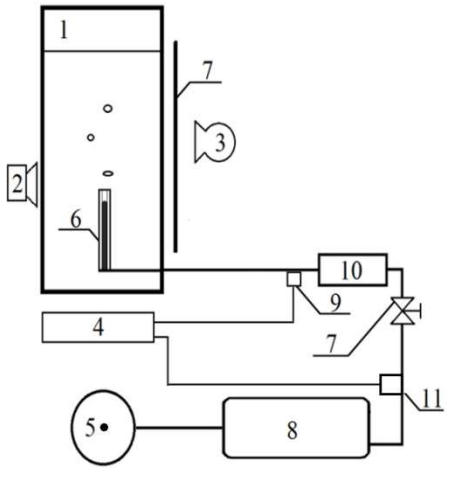

Fig. 1. Experimental setup: 1 – glass tank, 2 – camera, 3 – light source, 4 – computer acquisition system, 5 – air pump, 6 – glass nozzle, 7 - air valve, 8 – air tank, 9, 11 – pressure sensor, 10 – flow meter

The nozzle was placed at the bottom of the tank. The tank was filled with distilled water, with temperature about $20\,^{o}\mathrm{C}$. The temperature was constant during the experiment. The air pressure fluctuations have been measured using the silicon pressure sensor MPX12DP. The air volume flow rate was measured using the flow meter and was changed from 0.00632 to 0.0381 l/min. For such volume flow range the bubbles do not coalesce and the maximum depth of liquid penetration inside the nozzle was in the range between 2 mm and 20 mm. The pressure was recorded using the data acquisition system DT9800 series USB Function Modules for Data Acquisition Systems with sampling frequency of 2 kHz.

The bubble departures and liquid movement inside the nozzle were recorded with a high – speed camera – CASIO EX FX 1. The duration of each video was 20s. The recorded videos (600 fps) in gray scale have been divided into frames (Fig.2). The depth of liquid penetration inside the nozzle was measured using a computer program. The program counts on each frame the number of pixels with high brightness. The brightness threshold was different for each video. The calibration has been done by multiplication of all elements of time series by coefficient which value has been estimated using the detailed analysis of subsequent frames during the first cycle of nozzle penetration by liquid. For the selected gas flow rate, the length of the each time series was about 12 000 samples. In Fig. 2 the length of liquid penetration inside the nozzle and the bubble departures are shown. In order to better illustrate the length of liquid nozzle penetration the part of nozzle filled with a gas has been marked by continue black line. In the frames 1-6 it is visible the decrease of the length of liquid penetration inside the nozzle - the liquid is removed from the nozzle. Frames 7-12 show the bubble growth process, at frame 12 it is shown a moment of bubble departure. The frames 13 - 19 show the increase of the length of liquid penetration inside the nozzle. Above the nozzle it is visible the bubble movement. The maximum length of liquid penetration inside the nozzle in frame 19 is equal to 10 mm.

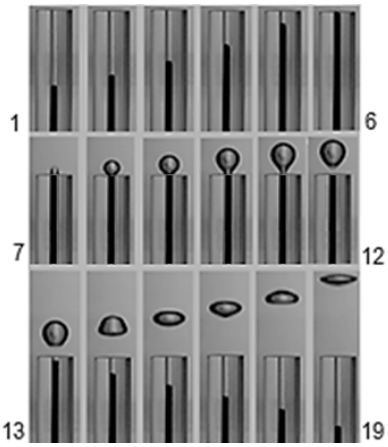

Fig. 2. The length of liquid penetration inside the nozzle and the bubble departures for air volume flow rate q = 0.0085 l/min

The example of recorded time series of changes of the length of liquid penetration inside the nozzle is shown in Fig. 3. In the time series the two time periods may be distinguished. These periods have been marked with 'I' and 'II' symbols. In the first period, the oscillations are periodic or quasi periodic. The amplitude of changes of the length of liquid penetration inside the nozzle is approximately the same for subsequent departing bubbles. In the second period (II in Fig.3), the amplitude of changes of the length of liquid penetration inside the nozzle significant varies for subsequent departing bubbles.

Time series of the length of liquid penetration inside the nozzle were obtained with using a high speed camera (600 fps) but the air pressure changes have been recorded using a data acquisition system (2 kHz). For synchronization of such recorded time series an additional system laser - phototransistor connected to data acquisition station has been used. The moment of appearance of the laser beam on the recorded film and increase of the voltage on the phototransistor was treated as the beginning of synchronized time series (the changes of pressure and the length of liquid penetration inside the nozzle).

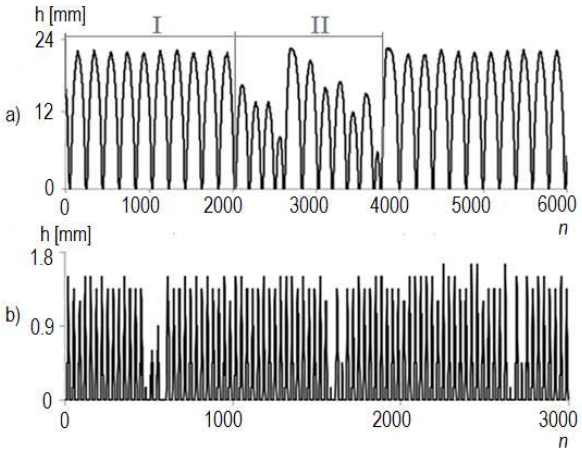

Fig. 3. Time series of changes in the position of air-liquid interface inside the glass nozzle for two gas volume flow rates, a) q = 0.0063 l/min, b) q = 0.0381 l/min

The trajectories of departing bubbles were reconstructed by computer program from recorded video. The Sobel filter has been used to identify the bubbles on the frames. Because the Sobel algorithm identifies only the boundary of the bubble, therefore the additional algorithm to fill interior of the detected bubble by black pixels has been used. This program marked the mass centre of bubble and recorded the changes of its position. The mass centre has been calculated according to the following formula:

$$x_c = \frac{\Sigma_i \ \Sigma_j \ k}{s}, \text{ where k} = \begin{cases} i \text{ for black pixels} \\ 0 \text{ for otherwise} \end{cases} \quad (1)$$

$$y_c = \frac{\Sigma_i \ \Sigma_j \ k}{s}, \text{ where k} = \begin{cases} j \text{ for black pixels} \\ 0 \text{ for otherwise} \end{cases} \quad (2)$$

where: s denotes the area of the bubble picture, x_c, y_c coordinates of the centre of mass

The example of obtained trajectories is shown in Fig. 4.

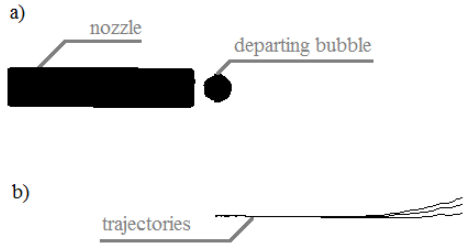

Fig. 4. Technique of bubble trajectories reconstruction: a) the black and white image of nozzle and departing bubble; b) the trajectories of three subsequent bubbles for air volume flow rate q = 0.00632 l/min

3. DATA ANALYSIS

The frequency of bubble departures has been estimated using the FFT method. The results of analysis are shown in Fig. 5. The dominant frequency of power spectrum is equal to the mean frequency of bubble departures. For q = 0.00632 l/min (Fig. 5a) the ratio between first dominate frequency and the second one is greater than in case presented in Fig. 5b. It means that when the air volume flow rate increases, the bubble departure becomes more non periodic (more chaotic).

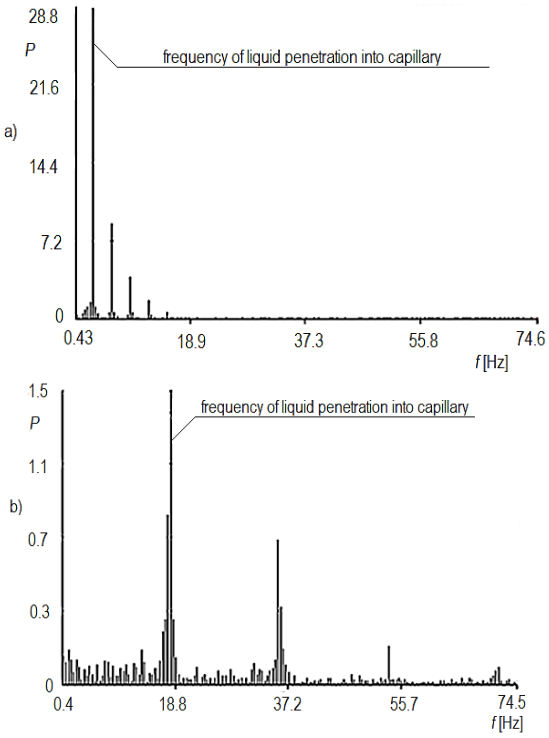

Fig. 5. Power spectrums P of time series changes in the position of air-liquid interface inside the glass nozzle: a) q = 0.00632 l/min, b) q = 0.0381 l/min (Dzienis P. et al.)

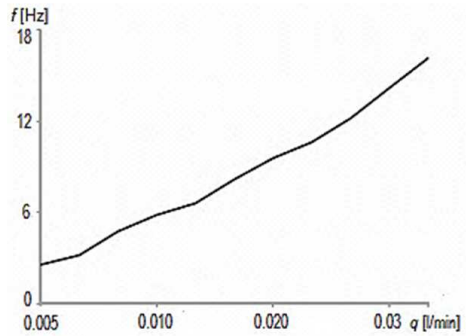

Fig. 6. The mean frequency of bubble departures f for different gas volume flow rates

Using the FTT method the mean frequency of bubble departures, f, for different air volume flow rates, q, has been determined. The results are presented in Fig.6.

In time series of the length of liquid penetration inside the nozzle the number of bubbles in two periods shown in Fig.3 and maximum value of length of liquid penetration inside the nozzle change with increase of the air volume flow rate. Typical

changes of maximum value of length of liquid penetration inside the nozzle and number of bubbles in periods I and II (Fig. 3) are shown in Fig. 7. The number of bubbles departing periodically and aperiodically, for various air volume flow rates are shown. The black bar represents the number of bubbles departing periodically in the area I (Fig. 3). The gray bar shows the number of bubbles departing aperiodically in the area marked with the symbol II in Fig. 3. The line represents the maximum length of liquid penetration inside the nozzle.

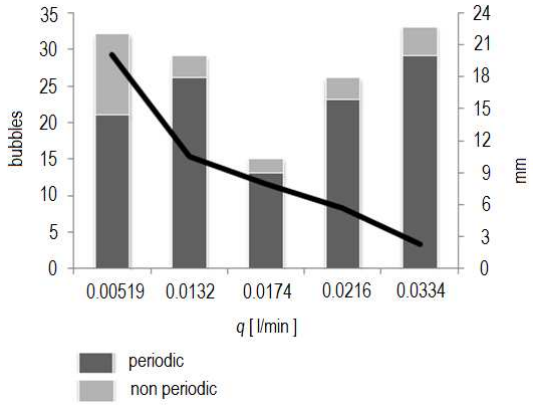

Fig. 7. Typical number of periodic and aperiodic bubbles in the time periods I and II (Fig.3) and the maximum value of length of liquid penetration inside nozzle

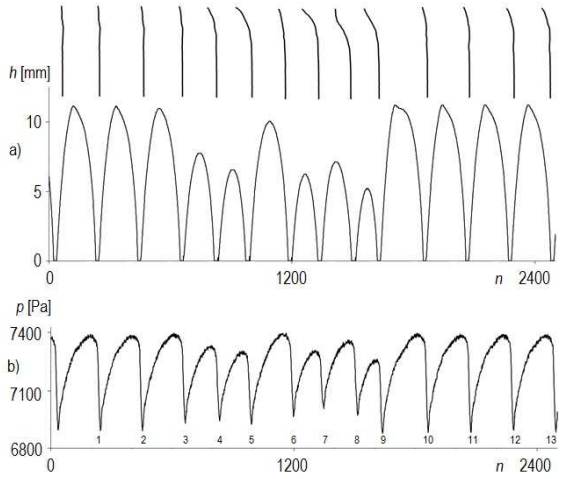

Fig. 8. Synchronized data concerning the series of bubble departures: a) the amplitude of changes in the position of air-liquid interface *h* inside the glass nozzle and the trajectories of departing bubbles for *q* = 0.0063 l/min b) the air pressure changes *p* for *q* = 0.0063 l/min

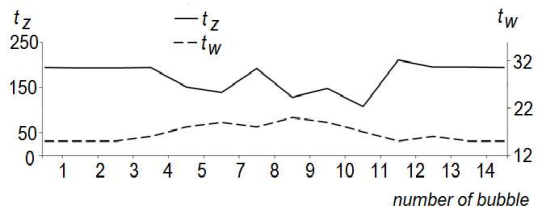

Fig. 9. The time of the growth of vapour bubbles, t_w, and the waiting time, t_z, for bubbles series presented in Fig. 8

For air flow rate, *q* = 0.00519 l/min the 21 bubbles departing periodically but 11 aperiodically. The ratio between number of aperiodically and periodically departing bubbles decreases while the air volume flow rate increases. For air volume flow rate *q* = 0.0132 l/min 26 bubbles departing periodically, and only three bubbles aperiodically. The lowest ratio between number of aperiodically and periodically departing bubbles occurs for *q* = 0.0216 l/min. For *q* = 0.0334 l/min, the ratio between number of aperiodically and periodically departing bubbles increases.

We can conclude that in the range of the air volume flow rate between 0.00519 and 0.0174 l/min, the increase of air volume flow rate is accompanied by decrease of the number of aperiodically departing bubbles. The opposite situation occurs in the range of the air volume flow rate between 0.0174 – 0.0334 l/min.

The maximum depth of liquid penetration inside the nozzle decreases while the air volume flow rate increases (Fig. 7). For *q* = 0.0334 l/min the maximum length of liquid penetration inside the nozzle was about 2 mm.

In Fig. 8 the time series representing the changes in time of the position of liquid-gas interface inside the glass nozzle (Fig. 8a), for *q* = 0.0132 l/min is shown. Above the chart the reconstruction of subsequent bubble trajectories are presented. The length of trajectories is equal to about 30 mm. In Fig. 8b the air pressure changes in gas supply system are presented. In Fig. 9 there has been shown the changes of subsequent times of: growth of bubbles and liquid movement inside the nozzle. The calculation has been made using the recorded video. The data presented in Fig. 8 and 9 refer to the same bubble series, all data are synchronized.

For the first three bubbles (Fig. 8) the time changes of the gas-liquid interface position inside the nozzles after subsequent bubble departures are similar to a periodic function. For these bubbles the maximum value of air pressure in the subsequent cycles are similar. The minimum value of air pressure reached in the subsequent cycles are similar only for the first two bubbles. Liquid flow in nozzle after third bubble begins at higher pressure, in comparison with the previous (second) bubble. Trajectories of bubbles 1-3 are similar to straight lines. For the third bubble, its growth time is longer in comparison with previous bubbles. The beginning of aperiodic bubble departures is accompanied with the rise of the time of growth bubble. For the bubbles 4, 5 (Fig. 8) the maximums of length of liquid penetration inside the nozzle and amplitudes of air pressure changes are smaller than for the previous bubbles. The liquid penetration inside the nozzle and bubble growth begins at lower air pressure. The shape of the trajectories of the bubbles 4, 5 deviates from the straight line. The time of liquid penetration inside the nozzle and bubble growth changes for subsequent cycles of growth bubbles. Bubble growth time is longer but the time of liquid penetration inside the nozzle is smaller in comparison with periodically departing bubbles (1 and 2, Fig. 8). After departure of bubble 5 the maximum value of liquid penetration depth inside the nozzle and amplitude of pressure changes increase. The liquid penetration inside the nozzle starts at higher pressure than for bubbles 4 and 5 and is close to the pressure obtained for bubbles 1-3. The trajectory of the bubble 6 is similar to the trajectory of bubbles 1-3 – it is similar to straight line. The time of liquid penetration inside the nozzle increases and is close to the times characteristic for cycles 1-3. Bubble growth time becomes smaller in comparison with bubbles 4 and 5, but it is still higher than for bubbles 1-3. The maximum value of liquid penetration inside the nozzle and amplitude of air pressure changes for bubbles 7-9 are smaller than for previous bubbles. The bubbles 7 and 8 depart at higher pressure, while the liquid penetration inside the nozzle starts at pressure lower than for bubble 6. For the bubble 9, the minimum value of air pressure

reaches the lowest value. The trajectories of bubbles 7-9 are not similar to straight lines. Times of liquid penetration inside the nozzle are lower than for bubbles 1-3 and 6. But times of growth of bubbles (7-9) are longer than for previous bubbles. The maximum value of liquid penetration inside the nozzle appearing before the bubble 10 is the lowest in analyzed time series. For the bubbles 11-13 are similar for values appearing for bubbles 1-3. The amplitudes of air pressure changes are greater than the amplitude of pressure changes for the previous bubbles, and are similar to these ones reached for bubbles 1-3. Reconstructions of bubble trajectories for these bubbles are more different from straight line in comparison with the previous bubbles. The time of liquid penetration inside the nozzle after the bubble 10 is the longest and the time of bubble growth is the smallest in bubbles time series under consideration. For bubbles 11 -13 the times of bubble growth and times of liquid penetration inside the nozzle are similar to times characteristic for bubbles 1-2. The periodic bubble departures begin when the duration of liquid penetration inside the nozzle increases and time of bubble growth decreases (bubble 11, Fig. 10).

We can conclude that the shapes of the trajectories of the departing bubbles are correlated with the maximum values of liquid penetration inside the nozzle. Straightening the trajectories of bubbles precedes the appearance of aperiodical bubble departures. Aperiodic changes of the maximum values of liquid penetration inside the nozzle appear together with significant deviations of the bubble trajectories. The periodic bubble departures lead to straightening the trajectories of bubbles.

The result presented in Fig. 10 shows that the maximum value of liquid penetration inside the nozzle is determined by highest value of air pressure changes. The time of bubble growth is determined by the minimum value of air pressure changes during the cycle of the bubble growth.

4. NONLINEAR ANALYSIS

The results presented in Fig. 7 show that increase of the air volume flow rate causes the changes of the ratio between number of bubbles in periods I and II (in Fig.3). In the period I the bubbles depart periodically, but in the period II the bubbles depart aperiodically. In order to evaluate the periodicity of bubble departures, the nonlinear analysis of time series of changes of the length of liquid penetration inside the nozzle in periods I and II has been carried out. The following elements of nonlinear analysis: attractor reconstruction, autocorrelation correlation function, correlation dimension and the largest Lyapunov exponent have been used.

The trajectories of nonlinear dynamic system in the phase space form objects called strange attractors of the structure resembling a fractal (Otto, 19978; Wolf et al., 1985). The analysis of strange attractor gives information about the properties of dynamic system such as system complexity and its stability. In nonlinear analysis the reconstruction of attractor in a certain embedding dimension has been carried out using the stroboscope coordination. In this method subsequent co-ordinates of attractor points have been calculated basing on the subsequent samples, between which the distance is equal to time delay τ. The nonlinear analysis of the experimental data is initiated by determining the time delay τ. For that purpose, the autocorrelation function, C, is usually calculated. The value of the time delay τ is determined from the condition $C(\tau)\sim 0.5*C(0)$ (Schuster H.G., Otto E.).

In Fig. 10 are shown the examples of 3D attractors reconstructions. The values of τ have been calculated using the autocorrelation function.

The correlation dimension D_2 is one of the characteristics of attractors, which allows to identify the structure of attractors. It is defined by the following expression (Schuster, 1993; Otto, 1997):

$$D_2 = \lim_{d\to 0} \frac{1}{\ln(d)} lnC^2(d) \tag{3}$$

where: $C^2(d) = \frac{1}{N}\sum_i \left[\frac{1}{N}\sum_j \theta\left(d - |x_i - x_j|\right)\right]$, d – distance in embedding space, N – number of points, θ – Heaviside's step function that determines the number of attractor point pairs of the distance shorter than d.

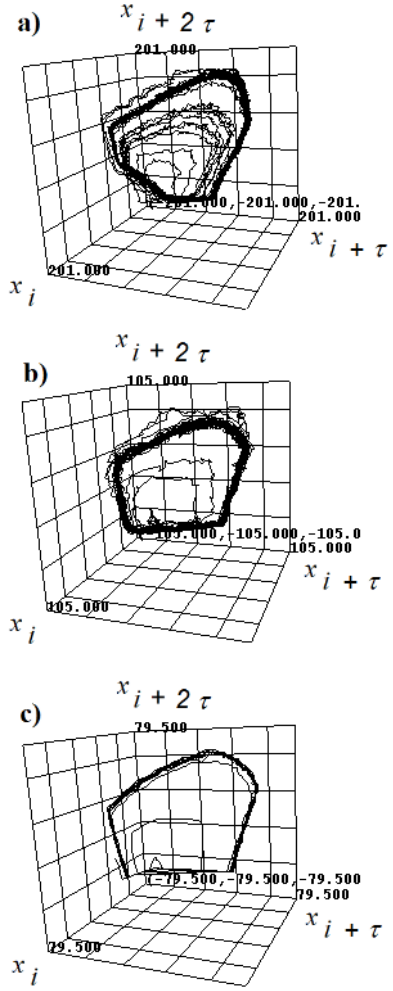

Fig. 10. 3D attractors for liquid penetration inside the nozzle time series: a) q = 0.00519 l/min and τ = 30, b) q = 0.0132 l/min and τ = 16, c) q = 0.0174 l/min and τ = 12

The correlation dimension allows to estimate the number of independent variables describing the phenomenon under consideration. This number is estimated as the lowest integer number greater than the correlation dimension. In Fig.11 the results of calculation of correlation dimension are presented. Obtained results show that correlation dimension of all time series is less than three. It means that three independent variables are enough to describe the behaviour of liquid movement inside the nozzle.

The another important characteristics of attractors is the largest Lyapunov exponent. In this case two points on the attractor immersed in M dimensional space have been selected. The distance between these points $d(x_j)$ is at least the one orbiting period.

After the passage of certain time the distance between the selected points has been calculated again and denoted as $d(x_{j+1})$. The largest Lyapunov exponent has been calculated according to the following formula:

$$L = \frac{1}{t}\sum_{j=1}^{m} \log \frac{d(x_{j+1})}{d(x_j)} \quad (4)$$

where: m – number of examined points, t – time of evolution.

The largest Lyapunov exponent allows calculation of time period $(1/L)$ of long time memory in the system in which the process of stability loss occurs. The comparison between the value of long time memory calculated from the largest Lyapunov exponent and the average time of the single bubble growth ($1/f$) is presented in Fig.10 ($(1/L)/(1/f) = f/L$).

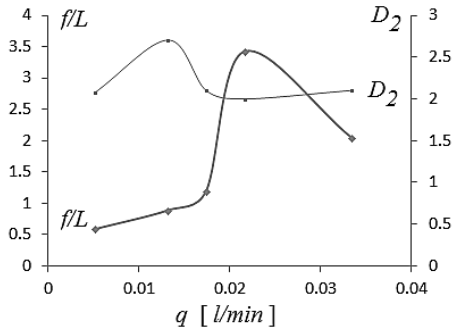

Fig. 11. The correlation dimension and largest Lyapunov exponent of changes in the position of air-liquid interface in glass nozzle versus air volume flow rate

The ratio f/L (f – the frequency of bubble departures, L – largest Lyapunov exponent) specifies the number of bubbles in which the stability of system is lose. For air volume flow rate q = 0.00519 l/min and q = 0.0132 l/min the ratio f/L has a value below 1. Because in case under consideration the time of bubble growth is about 10 times smaller in comparison with the duration of liquid penetration inside the nozzle, therefore results can be concluded that the aperiodical bubble departures are caused by the sensitivity to initial and boundary conditions of the liquid movement inside the nozzle.

5. CONCLUSIONS

The main aim of investigation was to analyze the influence of dynamics of liquid movement inside the nozzle on the dynamics of bubble departure. It has been analyzed: the liquid penetration inside the nozzle, air pressure changes in gas supply system and bubble trajectories shape. The results of analysis can be summarized as follows:

- increase of air volume flow rate is accompanied by increase of frequency of bubble departures and decrease of maximum values of liquid penetration (during the single bubble cycle) inside the nozzle;
- for all air volume flow rates (in the experiment) the time periods with periodic and aperiodic bubble departures appeared. The duration of these intervals varies with air volume flow rate;
- changes of maximum values of liquid position inside the nozzle are associated with changes of the bubble trajectories. Straightening the trajectory precedes the appearance of periodical and aperiodical time periods of bubble departures. The aperiodic bubble departures are accompanied by a significant deviation of bubbles trajectory from a straight line;
- changes of the amplitudes of air pressure (during the single bubble cycles) are correlated with the duration of liquid penetration inside the nozzle and times of the bubble growth. The maximum values of liquid penetration inside the nozzle are determined by highest value of air pressure changes. The times of bubble growths are correlated with the minimum values of air pressure changes;
- the aperiodic bubble departures begin when the time of bubble growth increased;
- the periodic bubble departures begin when the duration of liquid penetration inside the nozzle increase and time of bubble growth decreased;
- the aperiodical bubble departures are caused by the sensitivity to initial and boundary conditions of the liquid movement inside the nozzle;
- the correlation dimension analysis showed that three independent variables are enough to describe the behaviour of liquid movement inside the nozzle. These independent variables can be: liquid velocity, liquid position in nozzle and gas pressure in the nozzle.

REFERENCES

1. **Cieslinski J.T., Mosdorf R.** (2005), Gas bubble dynamics experiment and fractal analysis, *Int. J. Heat Mass Transfer*, Vol. 48, No. 9, 1808–1818.
2. **Dukhin S.S., Koval'chuk V.I., Fainerman V.B., Miller R**. (1998a), Hydrodynamic processes in dynamic bubble pressure experiments Part 3. Oscillatory and aperiodic modes of pressure variation in the capillary, Colloids and Surfaces A, *Physicochemical and Engineering Aspects*, Vol. 141, 253–267.
3. **Dukhin S.S., Mishchuk N.A., Fainerman V.B., Miller R.** (1998b), Hydrodynamic processes in dynamic bubble pressure experiments 2. Slow meniscus oscillations, Colloids and Surfaces A: *Physicochemical and Engineering Aspects*, Vol. 138, 51–63.
4. **Dzienis P., Wyszkowski T., Mosdorf R.** (2012), Nonlinear analysis of liquid movement inside the glass nozzle during air bubble departures in water, *Advances in Chemical and Mechanical engineering*, 133-137.
5. **Koval'chuk V.I., Dukhin S.S., Fainerman V.B., Miller R.** (1999), Hydrodynamic processes in dynamic bubble pressure experiments, 4. Calculation of magnitude and time of liquid penetration into capillaries, Colloids and Surfaces A: *Physicochemical and Engineering Aspects*, Vol. 151, 525–536.
6. **Mosdorf R., Shoji M.** (2003), Chaos in bubbling - nonlinear analysis and modelling, Chem. Eng. Sci., Vol. 58, 3837–3846.
7. **Otto E.,** (1997), *Chaos in Dynamical Systems*. WNT (in Polish).
8. **Ruzicka M.C., R. Bunganic R., Drahos J.** (2009b) , Meniscus dynamics in bubble formation. Part II: *Model, Chemical Engineering Research and Design*, Vol. 87, 1357–1365.
9. **Ruzicka, M.C., Bunganic, R. Drahos, J.** (2009a), *Meniscus dynamics in bubble formation*, Part I: *Experiment. Chem. Eng. Res. Des.,* Vol. 87, 1349–1356.
10. **Schuster H.G.** (1993), *Deterministic Chaos. An Introduction*, PWN, Warszawa 1993 (in Polish).
11. **Stanovsky P., Ruzicka M.C., Martins A., Teixeira J.A** (2011), Meniscus dynamics in bubble formation: A parametric study, *Chemical Engineering Science*, Vol. 66, 3258–3267.
12. **Wolf A., Swift J.B., Swinney H.L., Vastano J.A.** (1985) Determining Lyapunov Exponent from a Time series, *Physica-D*, Vol. 16, 285-317.
13. **Zang L., Shoji M.,** (2001), Aperiodic bubble formation from a submerged orifice, *Chemical Engineering Science*, Vol. 56, 5371-5381.

ANALYSIS OF THE STRUCTURE AND MECHANISM OF WING FOLDING AND FLEXION IN XYLOTRUPES GIDEON BEETLE (L. 1767) (COLOPTERA, SCARABAEIDAE)

Tomasz GEISLER*

*Institute of Mechanics and Machine Design Foundations, Department of Mechanical Engineering and Computer Science, Częstochowa University of Technology, ul. J. H. Dąbrowskiego 73, 42-201 Częstochowa, Poland

geisler@imipkm.pcz.czest.pl

Abstract: This study presents the structure and functions of flying wings in beetles (Coloptera). Structural analysis and function of multi-planar flexion and the structure of the wings in selected beetles were also carried out. The author developed a method of determination of points, structures and surfaces on the wing in folding and flexing motions. The paper describes the system of veins, foils and folds in the wing. Photographs of the wing in different phases of folding and flexion are presented in the paper. The paper emphasizes practical applications of the method of analysis in bionic mechanisms.

Key words: Hind Wings, Structure, Mechanism, Folding and Flexion of Wings

1. INTRODUCTION

The aim of the present paper is to analyse the structure of flying wings in beetles which at rest are folded and tucked under the wing case (elytra). Spread wings represent a drive for an insect for moving in aerospace. Research into real systems regarding structural analysis of mechanisms and application of bionic modelling encounters difficulties at the stage of determination of system structures and their performance. The discussed subject area is contained in the field of entomology and bionics.

As a field of knowledge, bionics encompasses research and cognition of the principles for living organisms. This research is often applied in practical mechanical solutions. Observations and investigations of animal morphology, including insects, have been the focus of numerous researchers for a long time and inspire a variety of researcher. Leonardo da Vinci and Pettigrew's studies (1891, 1908) are the examples of fascination with flying nature, similar to the investigations by other authors, listed in Samko's publications (2010).

The function and mechanical mapping of insect wings has been extensively researched in the field of bionics. There are studies in the literature that focus on the analysis of the structure and wing folding patterns in beetles and other insects. Studies by Bhayu et al., (2010) and Nguyen et al., (2010) are the examples of application of wing design in bionics. In these publications, the shape of beetle wings was used to build a macro model of a flying object which simulates wing movements.

The study (Muhammad et al., 2010) analysed folding and spreading of wings and the structure of an artificial wing in a beetle made of metals with shape memory. Wings in this study were based on a simplified model of bending joint with a system of one-point hinges, without considering folding of wing foil in hind folds. In the study (Jin et al., 2010), the method of finite elements was employed for simplified modelling and examination of beetle wing flexion.

Application of modern composite materials in construction of flying models of wings in bats, butterflies, crickets, dragonflies and beetles was presented in the study by Pornsin-sirirak et al., (2001). Closing functions of the first pair of wings were discussed in a study by Frantsevich (2012).

The use of wings is a form of adaptation of beetles and other insects to their environment. It is connected with evolution and further specialization to prevent from extinction through searching for food and colonization of new terrains. The wings can be hidden under the first pair wings (elytra). The hiding motion is composed of the main movements of folding and flexion of wing components. Connection of these movements causes that the wings are completely tucked under the elytra.

Bionic structure of the wing results from very long evolution and it meets the optimal functional demands, without unnecessary additional components.

In order to examine the wing in the beetle analysed in this study, the analysis focused on hind wings of Xylotrupes gideon beetle that belongs to Coloptera family, which is characterized by high activity in flight.

Microscopic examinations provided the basis for the development of the methodology of structural analysis and for dimensioning of the analysed wing. The structural analysis involved determination of points, regions and planes in flexion joint and folding the components of the internal structure of the wing.

2. MORPHOLOGY AND FUNCTIONS OF FLYING BEETLE WINGS

Presence of wings and ability to fly are most unique properties of insects. Flight of beetles is possible due to complex movement of mostly hind wings around an axis close to the long axis of the body and axis of the wing.

Complex movement consists of ascendant and drive movement. Wing movement in different planes is possible due to a mechanically complicated mechanism. The wing motion is generated by the work of trunk muscles and elastic deformation of the thorax by means of thoracic and abdominal muscles, de-

scribed in the studies by Szwanwicz (1956) and Hass (2001). The study by Dudley (2002) contains a description of the flight evolution and biomechanics, structure of wings in different insects and their kinematic and aerodynamic properties.

A wing, as a bulging part of a body, is attached flexibly by means of an articular membrane. The main elements of the wing described in the studies by Szwanwicz (1956) and Pławilszczikow (1968) are foils, veins, nerves and hemolymph. The hemolymph circulates in veins which are formed in the locations of the nerves and tracheae. It is a mixture of water, organic and inorganic matter. The hemolymph contains the suspension of blood cells, haemocytes and other components, such as proteins, amino acids and cations (sodium, potassium, calcium and magnesium) or anions.

The main component in morphology of skeletal parts of insect's body and wings is chitin. Chitin is numbered among polysaccharides from the group of natural polymers. They include e.g. collagens, casein, wool, natural silk, spider's web, cellulose and its derivatives, starch, gum Arabic, lignin and natural rubber. Natural polymers are produced by living organisms as structural components of tissues. Chitin is a material that reinforces insects' skeletons. It is white, hard and little elastics substance. Chitin exhibits hydrophobic properties, high strength and is poorly soluble in water and the most of the solvents. Chitosan, obtained synthetically, is a derivative of chitin. These biopolymers can form different morphological structures used in medicine.

Veins are chitinized pipes and provide a scaffold for the wings. They cover an insignificant part of the wing, but are a basic component to support the stiff, double-layer wing membrane. The spaces between the veins are termed cells or segments.

The photograph below (Fig. 1) presents a male beetle Xylotrupes gideon (Linnaeus, 1767) belonging to the family Scarabaeidae and subfamily Dynastinae.

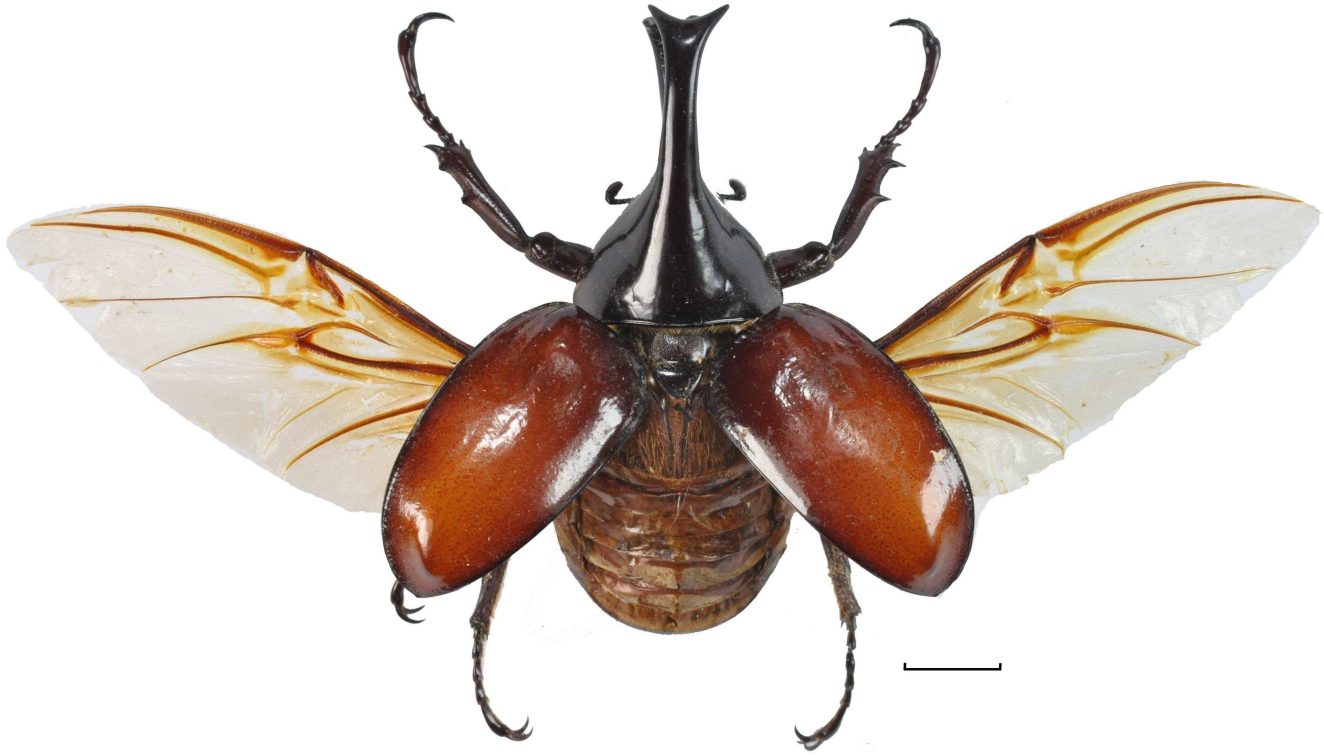

Fig. 1. Xylotrupes gideon (L.)

The main surface area of the wing is taken by a flexible and strong layered system of two foils that form a membrane with veins. Connections of the veins and foils allow for great lifting surface at minimum weight.

Mass of hind wings of different beetles described in a study by Geisler (2011) ranges from 1 to 2.5% of body mass of the insects, whereas the elytra mass accounts for 3 to 8% of the total mass.

Movable wings area connected with musculoskeletal system of the insect. They are attached to mesothorax and metathorax by means of wing joints.

In beetles, the first pair of wings (elytra) is typically transformed into sclerotized hard wing case which in the most of species are used to protect the second pair of wings (alae) tucked under the elytra when unused. They have a spatial and complex structure that provides them with great strength. The morphology and composite microstructure of elytra have been presented in the studies by Chen et al., 2007a, 2007b).

When not in flight, these covers protect folded wings, abdomen, mesothorax and metathorax. In flight, the elytra are either raised totally or only lifted a little to enable spreading out the hind wings. These covers are also equipped with a specific system of interlocks to ensure a strong connection with abdomen and thorax when unused.

The main propulsion in beetles is produced by the motion of hind wings. However, the forewings (elytra) have also some effect on generation of propulsive forces, which was demonstrated in the study (Sitorus et al., 2010).

A study by Jaroszewicz (2009) presents the analysis of aerodynamic forces that act on a miniature wing of a flying object, named entomopter.

Hind wings in beetles are usually much longer than the elytra. In order not to be damaged they must be capable of reducing the dimensions and be tucked under the covers. This is enabled by folding them along the body and flexing under the elytra.

The reduction in dimensions is also possible through internal folding the wing's membrane along folds. Studies by Bethoux (2005) and Wootton (1979) describe the system of veins and folds used for folding wings in insects that belong to different orders.

The chitin of foils and veins is broken in locations of folds. The study by Hass (2000) found the content and presence of resilin in folds on wing membrane in a Pachnoda marginata beetle. Resilin is a protein (polymer) with irregular structure, present in nature in jumping (e.g. flea, Aphaniptera) and flying insects. The insects frequently use its elasticity and capacity to be deformed repeatedly (e.g. flexion) and store energy very efficiently.

Folding a two-part wing is composed of the motion of its main part in the wing joint and folding in the bending joint in the wing's plane. Flexion might occur once into two parts or twice into three parts.

Wing connection with the insect's body is supposed to provide it with highest possible frequency of movements while maintaining the relative motion in specific planes. Motion planes result from muscle movements, movements of insects' abdomen and the elasticity of the wing.

Functionality of the wing largely depends on its activation during motion (flight) and the ability to fold and bend it in order to protect the wing when unused.

The photograph below (Fig. 2) presents an abdomen of a beetle with the left wing positioned in resting state and a distinct sulcus (marked as br in the picture) on the abdomen to fit the veins C+Sc+R1 of the right wing.

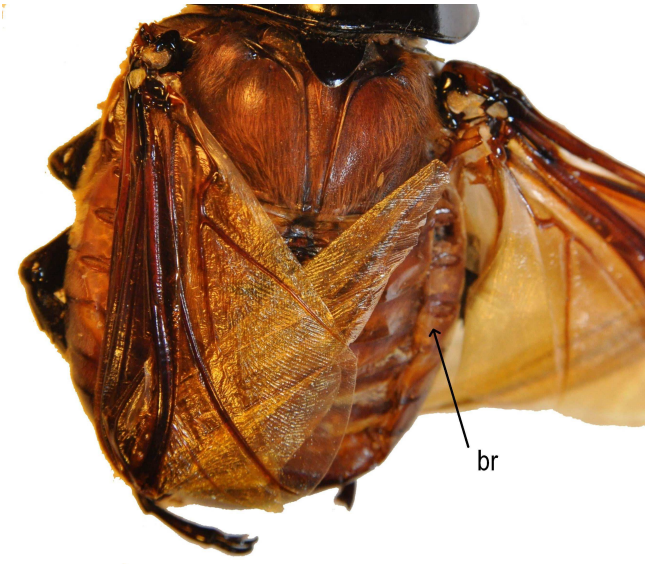

Fig. 2. Wing in resting state

Shape of the wing must meet its aerodynamic demands and allow the wing to change the shape in upward and downward motion both in vertical and horizontal planes. These demands are satisfied by elastic foil in wings and the related changes in shape around the long axis.

Changes in wings' shape are connected with muscular and articular activity. A wing is maintained outstretched through contraction in the muscular system. When the muscles are relaxed, the wing stops to be tight and moves partially towards the hind part of the body. Further motion of the wing towards the hind side results from the contraction of a muscle in one of axillary plates and its rotation. The work of this muscle plays the main role in folding the wing.

One of the axillary plates locks and determines the motion of a part of the wing (RA). Mutual movement of axillary plates can be viewed as a lever mechanism motion.

Changes in shape and dimensions are necessary to fold the wing and hide it under the covers. The wings might be tucked under the elytra which are totally open or only lifted a little (Cetonidae). Folding and drawing the wing in is facilitated by the indentation in lateral edge of the covers.

In order to classify and provide taxonomy for beetles, a special nomenclature of veins has been used in the literature. There are longitudinal veins along the wings that include: costal vein, subcostal vein, radial vein, medial vein, cubital vein, axillary vein and jugal vein. All the veins, apart from the first one, might be branched. Besides the longitudinal veins, there are also transversal veins.

Description of venation used in entomology was presented in the studies by Pławilszczikow (1968), Razowski (1987, 1996), Stebnicka (1978) and Szwanwicz (1956). The study by Stank (1974) termed bending joint as radial sector root (RSR).

3. FLEXION AND FOLDING OF INTERNAL STRUCTURES OF BEETLE WINGS

In mechanical terms, the wings, folded and bent at rest, are a complex structure. Connection of the wing with the body by means of the wing joint and connection in the bending joint are regarded to be some of the most complicated mechanisms in the insect's body.

The many-level mechanism of flexion makes a structure of an insect wing very complex and has more components than uniform wings.

The structure of the spread-out and folded wing is not a flat plane. Insect adopt the shape of the wing so that it is the most aerodynamic.

A wing is composed of two (or more) main parts. The base part is attached to the thorax with the wing joint, whereas the second part is connected to the base part in the bending joint. An important function of hiding the hind wing under the elytron results from its arrangement in horizontal plane and is associated with bending the wing.

Movement of the second part of the wing in bending joint might occur in the direction which is consistent with the main direction (rotation) of folding for a single bending. In double folding, the direction of the movement of this part might be opposite or complex for the last bent part of the wing.

Proportions in wing flexion depend on the ratio of wing length to cover length. They vary and depend on the family a beetle belongs to. Folding of the wing membrane occurs in a fan pattern in specific planes, alternately along the folds that are formed in the wing's membrane.

Mutual arrangement of folds in wings has been broadly discussed in studies by Szwanwicz (1956) and Hamilton (1971, 1972). When folding the wing membrane, the jugal part (Ju,

Fig. 6) of the membrane folds along the jugal fold (fj) and is placed under the anal part (Fig. 6) in a complex motion on the abdomen.

The system of wing folding is capable of increasing the lifting surface with the least possible surface (dimensions) of the wing when at rest. Apart from folding alone, the dimensions are also reduced by an accordion-like folding of wing membrane.

Arrangement of the wings under the elytra must take into account the limited space and the bigger wings must be overlapped. The degree of overlapping of the foil in the two wings under the elytra varies depending on the family and was presented for selected families of beetles in a study by Geisler (2011).

The figure below presents a wing of the analysed beetle in the phase of unfolding.

Fig. 3. Right wing in the phase of unfolding

4. STRUCTURAL ANALYSIS OF WINGS

Structural analysis of a wing necessitates the knowledge of connecting the parts into the kinematic pairs, determination of the degrees of freedom and the mobility of mechanisms.

Structural analysis of the wing mechanism involves selecting and determination of the elements of the wing which allow for folding. A beetle wing represents a complex system of the main components such as veins, foil and folds.

The figure below presents a beetle wing with distinct spatial bending joint (Fig. 4).

Fig. 4. Spatial structure of wing flexion

Wings from several initially analysed families of beetles were selected for the examinations. Kinematic pairs and internal nodes were also separated. The criterion for searching for the points was their location at the intersection of the folds where a change in the shape of the wing membrane surface was observed. Deformations of the membrane caused creation of the rigid structures (areas). These structures typically took the shape of triangles, quadrilaterals and complex spatial shapes (Fig. 6).

The figure below presents the right wing of a beetle in flexed state (at rest) (Fig. 5).

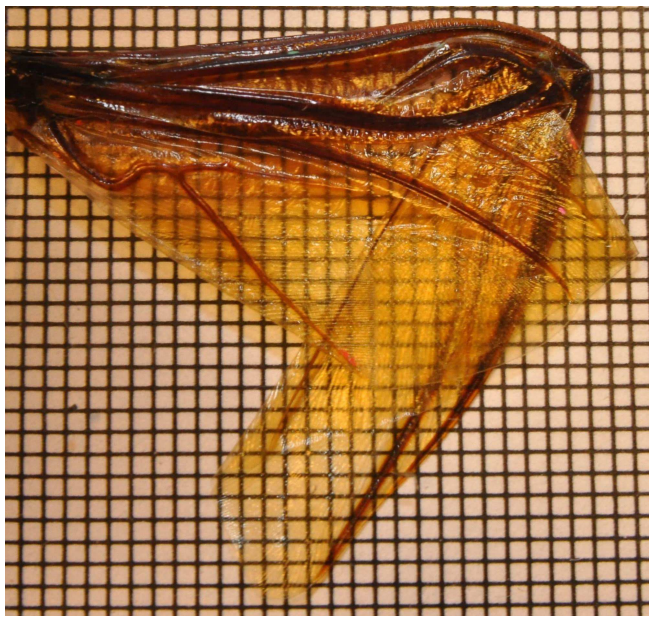

Fig. 5. Flexed (resting) position of the right wing

A precondition for adopting the structure as constant (rigid) was invariability of its shape in movement phases when bending and folding the wing membrane. When moving the structures, the folds were formed at the surface of the wing.

The folds between the points formed lines. The folds contain the ridges (g.) and valleys (d.). It was adopted that a ridge moves towards the upper surface of the wing and a valley moves in opposite direction.

The folds were marked with symbols denoting ridges and valley (e.g. g. 1-4, d. 10-11), and, additionally fa, fj,..... (Fig. 6) and the structures (e.g. s. 1-2-3), containing the adopted numbering of points. For essential points located at the lower edge of the wing, the authors adopted the following symbols: b1, b2,… . For selected points located in the area of wing joint the adopted symbols were ps1, ps2.

Wing flexion is possible only as a result of changes in position of the planes which contain rigid structures.

Analysis of multiplanar mechanism of wing flexion and folding revealed that arranging and folding the structures with respect to each other might be total or partial.

Selected folds in the wing, such as ridges and valleys maintain their positions with respect to each other that do not form flat surfaces, with planes positioned at different angles. It was assumed that the structures form the U shape.

The structure of a wing also contains V-shaped triangular rigid structures. Folding the structures along the folds might be either total or partial.

Combination of the U-shaped and V-shaped structures naturally stiffens the structure when the wing is unfolded and folded.

The U structure is maintained in e.g.: rigid structure s. 18-26-29-ps4-ps5-14-18 with valley d. 18-ps4, structure s. 1-2-24-14-1 with valley d. 14-24-2-1.

When determining the structure of the wing, the author analysed dislocations (rotation) of the defined points and structures with respect to each other.

The photograph below (Fig. 6) presents the right wing of the analysed beetle with the marked points and structural diagram and symbols for folds, veins (ż) and thickness zones (h).

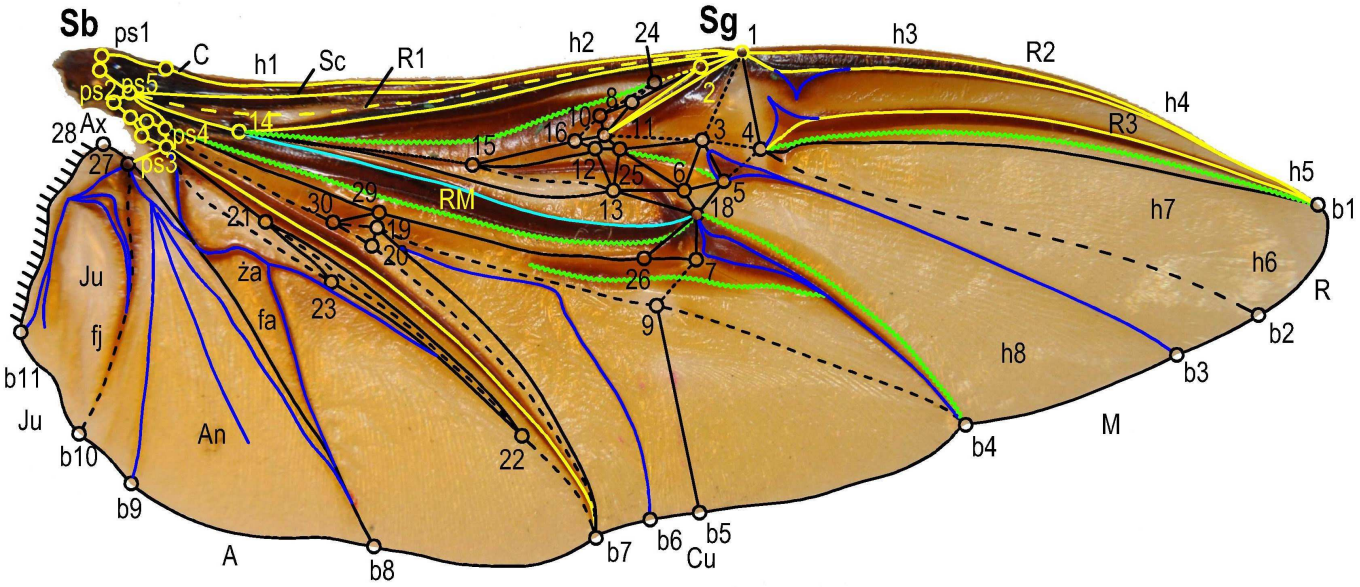

Fig. 6. A beetle wing: Xylotrupes gideon (L.) with the assumed structural components

The photograph of the wing (Fig. 6) presents the description of veins, structures and areas: R – area of radial veins, (R1, R2, ...), M – area of medial veins, Cu – area of cubital veins, A – area of anal veins, An – anal area of the wing, Ju – jugal part of the wing, Ax – area of axillary veins, C – costal vein, Sc – subcostal, Sb – wing joint, Sg – bending joint.

Figure below presents magnification of the diagram of rigid structures in the bending joint (Fig. 7).

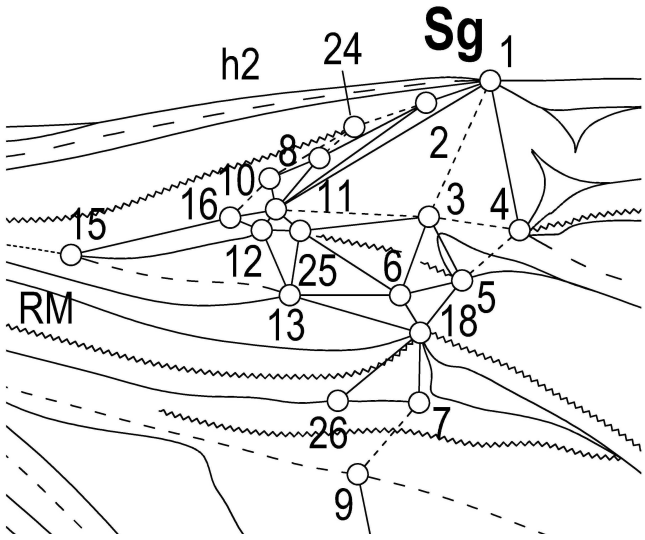

Fig. 7. Magnification of the diagram of points and structures in the bending joint

The following rigid structures and their component movements:

- system C+Sc+R1, (s. 1-14-ps5-ps1) forms a structure with symbol of (RA);
- U-structure: s. R3 (4-b1)-4-b1 z d. 4-b1 (zigzag);
- solid: s. 18-26-29-ps4-ps5-14-18, forms a system (vein) with symbol (RM);
- solid: s. b8-ps3-21-23-22-b7;
- structure s. 21-22-23 forms an internal V system with d. 21-22;
- solid: s. 1-b1-b2-4;
- solid: s. 1-4-3, including g. 1-4 folds into the fold d. 4-5, and, simultaneously, s. 1-4-3 bends (rotates) around g. 1-3;
- within the macrostructure of the wing, the section of the ridge g. 5-6 remains vertical after folding,;
- solid s. 8-11-10 and s. 10-11-16 are arranged vertically with g. 10-11 perpendicular to the wing surface;
- solid s. 1-11-2, s. 2-11-8, s. 2-8-24, s. 24-2-8 form a complex system which folds in V system along d. 1-2-24-10-16;
- structures: s. 19-b7-20 and 19-20-30 form the V system with g. b7-ps3 and fold totally along f. b7-20-30-ps4 on s. b7-ps3-ps4;
- solid s. 7-9-19-29-26-7 and s. 19-30-29 form the V system with 9-b7-19 and fold under the solid s. 18-26-29-ps4-ps5-14-18 along d. 9-19-ps4;
- the fold g. 9-b5 folds with d. 7-9 (significant);
- solid s. 19-30-29 and s. 19-20-30 fold with respect to each other along d. 19-30;
- split vein (ża) provides a reinforcement for the structure s. b7-b8-ps3-ps4;
- after wing folding, the structure b2-b3-b4-18-5-4-b2 forms one plane in consideration of folding d. 4-5 and g. 5-18 with folds g. 18-7 and d. 7-9.

When marking the points of structures, the author adopted the right hand rule. Moreover, the locations of the selected reinforcing veins were also marked ż1, ż2, ... (Fig. 6).

The main fold for folding the wing membrane outside the rigid structures in bending is the fold g. 9-b5.

When folding the hind part of the wing it is essential to fold the jugal part along the fold: d. b10-27-28, in conjunction with folding the anal part around the fold: g. b8-27. The fold f. b11-28

is connected with the insect abdomen (Fig. 6).

Locking the open wing is possible through contraction of a system of muscles that unfold and drive the wing motion.

The motion (opening) of the second part of the wing in bending joint occurs without using muscles because they do not exist in the main wing membrane.

This is possible through changes in the structures that form the U shape. These include the external structures: s. 1-14-ps5-ps2-ps1-1 (RA) and 18-ps4-ps5-14-18 (RM) and the structures between them.

Structures (Ra, RM, Fig. 6) perform a relative (scissors-pattern) motion that is formed by a complex dislocations in the wing joint. It is essential for this motion to maintain the chain marked with points: 1-4-5-18.

When bending and folding the wing, some local structures and folds occur. Their existence is necessary as they allow wing to fold and bend and the surfaces to overlap. One of these fold is: f. b4-9.

The analysis assumed that the veins in the wing are elastically arranged in bending planes, maintaining the global flatness of the wing which is an elastic membrane.

Classical kinematic pairs with one degree of freedom (rotating pair) are present in binding joint in certain places (e.g. 1, Fig. 6) and in wing joint. Descriptions of kinematic pairs have been presented in example studies by Artobolewski (1988) and Miller (1996).

In the system of C+Sc+R1 (RA) (Fig. 6), vein R1 has special 'ribs' perpendicular to the wing surface. It contains elastic structure in the area of bending joint and allows for rotation of the R2 vein, only in the wing plane.

A substantial majority of the wing planes when at rest are parallel to each other. Hence, the flatness of the wing can be assumed for the resting state.

The obtained form of the wing corresponds to the requirements of minimal dimensions in the plane which is perpendicular to the flat surface of folding and bending. Interfolding of ridges and internal folding of folds is an element that stabilized the wing.

The components of the wing adopt a spatial structure within certain borders (dimensions of the macrostructure determined by the thickness of the wing.

Basic parameters of the beetle and its wings analysed in the study included: total length of the beetle (70 mm), wingspan (135 mm) and parameters of a single wing: mass (~0.09 g), length (60 mm), width (23 mm), section 10 mm (Fig. 1).

The dimensions of the folded wing are presented in the photograph (Fig. 5) against the background of a graph paper. The smallest distances between the points and the internal structures have dimensions of 0.5-1.5 [mm].

The thickness of the components of the wing was also determined. It accounted respectively for the areas: h1-0.35, h2-0.34, h3-0.20, h4-0.13, h5-0.07, h6-0.025, h7-0.09, h8-0.015 mm (Fig. 6). The thickness of the structure of the wing in the binding joint ranged from 0.6 to 1.6 [mm].

Tucking the wings under the elytra is a combined effect of several factors. It was observed during the study that arrangement of wings under the wing case is facilitated by the indentation in the beginning and at the end of the elytra that perfectly fit the natural curvature of wing and bending joints. Stabilization of the folded wings and abdomen is ensured by a sulcus profile (br) where the MA structure is arranged (Fig. 2, 3).

It was also observed that when the folded wing is arranged, the final arrangement of the wing on the abdomen occurs as a result of pressing it with the wing case. This mainly concerns the structure s. 18-26-29-ps4-ps5-14-18. Closing the wing case causes the deeper interfolding of the rigid structures and final arrangement of the wing.

Furthermore, wing folding is supported by interrelated 'sliding' motions of the segments of abdomen and a possible additional motion of hind legs in selected families of beetles.

An essential factor for the function of wing flexion is the constitution and stiffness of the vein Cu/b7-ps3, and cutting it weakens the mechanism of opening of the second part of the wing.

The microscopic examinations were carried out by means of a technical stereoscopic microscope PZO Warszawa with magnification of 4/100x with special sectional diode light source. Photographs and films were recorded by Nikon D90 (12.3 MPx) with macro lens and equipment.

5. ANALYSIS OF LOCAL DEGREES OF FREEDOM IN THE STRUCTURES

Beetle wings have varied structure and constitution. In order to determine this differentiation, a method of calculation of local mobility in internal structures was employed.

An example structure with a determined degree of local mobility in internal structures is presented below. The simplified method of calculation takes into consideration the presence of kinematic pairs of I class defined in fundamental studies on the theory of machines and mechanisms by Artobolewski (1988) and Miller (1996).

The calculations assumed mutual spatial displacement of the structures reduced to one plane. The mobility formula was: R=3n-2p1, where: n- number of movable parts, p1-rotary connections along the lines between the structures.

The following pairs were determined in the system of structures presented in Fig. 8: 1-2, 1-3, 2-4, 3-5, 4-6, 5-6, 5-7, 6-8, 7-8. The calculated mobility amounts to R=3

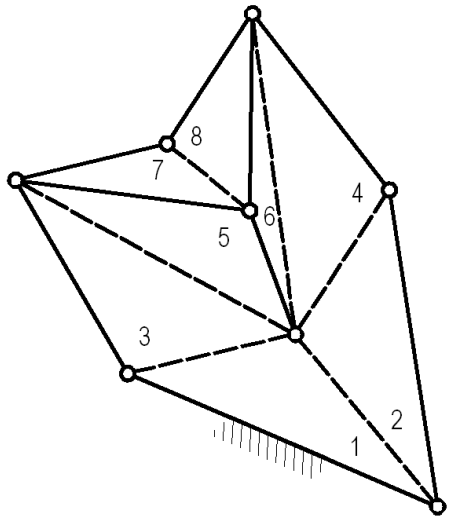

Fig. 8. System of internal folding of the structures

The number of local degrees of mobility increases with the level of complexity and the number of folding of triangular and other structures that represent the components in the wing structure.

In order to use the above method, it is necessary to conduct the analysis of the component lengths of the structures. The relations between the lengths of the sides in the analysed structures determine the internal angle of folding and the adopted position of the plane with the structure in the wing space.

Local degrees of mobility necessitate consideration for the principles of formation of folds on flat surfaces with respect to each other, similar to paper surfaces used in Japanese origami.

The method of determination of local mobility is used for evaluation of the level of complexity in wings and will be used for further research. It can help introduction of necessary simplifications in the structure of modelled wings.

6. CONCLUSIONS

The biological and mechanical structure of a wing is very complex. Analysis of the structure of the wing in different beetles points to a variety of structures, morphologies and wing folding and flexion patterns in this family of insects.

This study presented the analysis of selected mechanisms of flexing the wing in its articulation (wing joint) and internal folding of the wing structures. Some simplifications can be employed in wing design, which result from the properties of modern materials while maintaining their functions. The structure of the beetle wing presented in this study meets the requirement of continuity of wing surface throughout all the motion phases.

It was demonstrated that the motion of the second part of the wing in bending joint is affected by several factors, of which the most important is the change in position of specific U-shaped structures with variable parameters. It is essential that the most components in wing structure, including a part of vein systems connected with the structures discussed in this study fits the described U and V shapes. There are some common elements of the wing structure in beetles and other insects which can be used for further analyses and designs.

Further research should focus on the analysis of all the wing motions, including the motion of axillary plates in the wing joint, regarded to be a complex lever mechanism motion as well as flat and spatial mechanisms of different classes.

There are a number of patterns for folding and bending of insect wings. It is necessary to analyse greater number of structures typical of different families of beetles, including the bending joint. Other structures of wings exhibit different number of points and rigid structures and differ in functions of folding and flexion.

The analysis presented in this study can be used for designing and building the wings for bionic applications, using the necessary simplifications. It is also possible to use the analysed properties of the structure and modelling the wings in the design of flying macro-mechanisms (entomopter) which meet the demands of minimization of geometrical dimensions and using modern materials. The materials used for wing modelling should meet the following requirements: light structure, high strength, low costs and easiness of connecting both in construction and during repair works.

Analysis of differentiation in structural properties of wings, their proportions and methods of wing folding and bending might help develop the methods of optimization of the structure and constitution of wings in flying models.

The methodology of wing structure analysis developed in this study might facilitate modelling and designing the flying machines that mimic complex functions performed by the insects which are so far unattainable for other machines. Further analysis will include the insects from several tens of families, types and species of beetles from the collections owned by the author.

REFERENCES

1. **Artobolewski J. J.** (1988), *Theory of mechanisms and machines*, Moscov, 1988, (in Polish).
2. **Bethoux O.** (2005), Wing venation pattern of Plecoptera (Insecta: Neoptera), *Illisia*, Vol. 1, number 9, 52-81.
3. **Bhayu P. R., Nguyen Q. V., Park H. C., Goo N. S., Byun D.** (2010), Artifical Cambrered-Wing for a Beetle-Mimicking Flaper, *Journal of Bionic Engineering*, Vol. 7, 130-136.
4. **Chen J., Dai G., Xu Y., Iwamoto M.** (2007), Optimal composite structures in the forewings of beatles, *Composite Structures*, Vol. 81, 432-437.
5. **Chen J., Ni Q. Q., Xu Y., Iwamoto M**. (2007), Lightweight composite structures in the forewings of beetles, *Composite Structures*, Vol. 79, 331-337.
6. **Frantsevich L.** (2012), Indirect closing of elytra by the prothorax in beetles (Coleoptera): general observations and exceptions, *Zoology*, Vol. 115, 12-21.
7. **Geisler T.** (2011), Structure and wing folding of beetles from the chosen families (Coloptera), *Biuletyn Częstochowskiego Koła Entomologicznego*, Częstochowa, Nr 10, 12-21, (in Polish).
8. **Haas F., Beutel R. G.** (2001), Wing folding and the functional morphology of the wing base in Coleoptera, *Zoology*, Vol. 104, 123-141.
9. **Haas F., Gorb S., Blickhan R.** (2000), The function of resilin in beetle wings, Proceedings of the Royal Society B: *Biological Sciences*, Vol. 267, 1451, 1375-1381.
10. **Hamilton A. K. G.** (1971), The insect wing, Part I. Origin and Development of Wings from Notal Lobes, *Kansas Entomological Society*, Vol. 44, No 4, 421-433.
11. **Hamilton A. K. G.** (1972), The insect wing, Part III. Venation of the orders, *Kansas Entomological Society*, Vol. 45, No 2, 145-162.
12. **Jaroszewicz A.** (2009), Modeling and simulation of flight dynamics of an entomopter, *Modelowanie inżynierskie*, vol. 38, 77-85.
13. **Jin T., Goo N. S., Park H. C.** (2010), Finite Element Modeling of a Beetle Wing, *Journal of Bionic Engineering*, vol 7, 145-149.
14. **Miller S.** (1996), *Theory of machines and mechanisms - Analysis of kinematic structures*, Politechnika Wrocławska, Wrocław, (in Polish).
15. **Muhammad A., Nguyen Q. V., Park H. C, Hwang D. Y., Byun D., Goo S. G.** (2010), Improvement of Artificial Foldable Wing Models by Mimicking the Unfolding/Folding Mechanism of a Beetle Hind Wing, *Journal of Bionic Engineering*, Vol. 7, 134-141.
16. **Nguyen Q. V., Park H. C, Goo S. G., Byun D.** (2010), Characteristics of a Beetle's Free Flight and a Flapping-Wing. System that Mimics Beetle Flight, *Journal of Bionic Engineering*, Vol. 7, 77-86.
17. **Pettigrew J. B.** (1891), *Animal Locomotion or Walking, Swimming, and Flying*, Kegan Paul, Trench, Trubner & Co., London.
18. **Pettigrew J. B.** (1908), *Design in Nature*, Longmans, Green, and Co., London.
19. **Pławilszczikow N.** (1968), *Marking key of insects*, PWRiL, Warszawa, (in Polish).
20. **Pornsin-sirirak T. N., Tai Y. C., Nassef H., Ho C. M.** (2001), Titanium-alloy MEMS wing technology for a micro aerial vehicle application, *Sensors and Actuators,* Vol. 89, 95-103.
21. **Razowski J.** (1987), *Entomological dictionary*, PWN, Warszawa, (in Polish).
22. **Razowski J.** (1996), *Dictionary of insect morphology*, PWN, Warszawa-Kraków, (in Polish).
23. **Samek A.** (1994), *Bionics: the natural knowledge for engineers*, Uczelniane Wydaw. Nauk. - Dydakt., AGH im. S. Staszica, Kraków, (in Polish).

24. **Sitorus P. E., Park H. C., Byun D., Goo N. S., Han C. H.** (2010), The Role of Elytra in Beetle Flight: I. Generation of Quasi-Static Aerodynamic Forces, *Journal of Bionic Engineering*, Vol. 7, 354-363.
25. **Stanek V. J.** (1994), *Encyclopedia of insects, Beetles*, Delta W-Z, Warszawa, (in Polish).
26. **Stebnicka A.** (1978), Marking keys of Polish insects, Beetles - Coloptera, PWN, Warszawa, Nr 100, Cz. XIX, Zeszyt 28b, (in Polish).
27. **Szwanwicz B**. (1956), *General Entomology*, PWRiL, Warszawa, (in Polish).
28. **Wootton R. J.** (1979), Function, homology and terminology in insect wings, *Systematic Entomology*, Vol. 4, 81-93.

This study is supported by the Polish Ministry of Science and Higher Education in 2012.

MODELLING OF PRESSURE-DROP INSTABILITY IN SINGLE AND MULTI MICROCHANNELS

Hubert GRZYBOWSKI*, Romuald MOSDORF*

*Department of Mechanics and Applied Computer Science, Faculty of Mechanical Engineering,
Bialystok University of Technology, ul. Wiejska 45 C, 15-351 Białystok, Poland

r.mosdorf@pb.edu.pl, grzybowskihubert@wp.pl

Abstract: In the paper the model of pressure-drop oscillations has been proposed. The model was based on the iterative solution to equations. The dynamics of pressure-drop oscillations in a single channel and in two neighbouring channels have been analyzed. There has been assumed that the pressure-drop oscillations in the system are caused by interactions between the heat supply system and liquid supply system. These interactions influence the heat and mass transfer inside the microchannel. Obtained results indicate that the shape of pressure drop curve has a significant influence on the system stability. When the slope of curve $\Delta p = f(G)$ in the region between function extremes increases then the pressure oscillations become chaotic. In case of multichannel system the thermal interactions (occurring through the channel walls) and hydrodynamic interactions (occurring inside the common channels outlet) have been considered. Four types of two-phase flow behaviours in parallel channels have been observed depending on the intensity of interactions: alternate oscillations, consistent oscillations, periodic oscillations and completely synchronized oscillations. Obtained qualitative results have been compared with conclusions of experimental results reported by other researches. The good qualitative agreement with experimental results has been obtained.

Key words: Two-Phase Flow Instabilities, Microchannels, Pressure Drop, Flow Oscillations

1. INTRODUCTION

During two-phase flow in microchannel system different types of instabilities may occur. The classification of two-phase flow instabilities was discussed in papers (Kakac and Bon, 2008; Boure et al., 1973). In general they identify two types of instabilities: static and dynamic. The process when the existing state of equilibrium after some disturbance tends to a new different state is called the static instability. The following static instabilities are identified in two-phase flow in microchannels: Ledinegg instability, boiling crisis, flow pattern transition instability, bumping, geysering or chugging. The Ledinegg instability occurs when channel pressure-drop curve versus flow rate has a negative slope and its slope is greater than the slope of liquid supply system curve. When two-phase flow in microchannel cannot absorb the heat supplied to the system then boiling crisis appears. Flow pattern transition instability is connected with oscillations between the bubbly and annular flow regimes (Boure et al., 1973). Bumping, Geysering and Chugging are also considered as static instability and are associated with the process of violent liquid evaporation (Kakac and Bon, 2008).

Dynamic instabilities occur when the disturbed flow cannot reach a new equilibrium point because of complex mechanism of multiple feedbacks occurring in the system. Generally, four types of dynamic instabilities can be distinguished (Kakac and Bon, 2008):

- density-wave oscillations;
- pressure-drop oscillations;
- acoustic oscillations;
- thermal oscillations.

Multiple feedbacks between the mass flow rate, steam generation and pressure drop in the channel are responsible for density-wave oscillations. Density-wave oscillations have low frequency and large amplitudes. The pressure-drop oscillations are connected with existence of compressible volume in the system. The compressible volume amplifies the interaction between microchannel and liquid supply system. Pressure-drop instability causes long period oscillations. The formation of acoustic oscillations is related to the speed of the pressure waves in the system which causes high frequency oscillations. The thermal oscillations of heating surface temperature are connected with transitions between different boiling regimes.

In multi microchannels the channel walls are very thin and the channels interact through the conduction. Other interactions occur in common liquid inlet and outlet. The spatial non-uniform distribution of heat flux density supplied to the multi channel system appears for example in computer systems where the single heat exchanger is installed on the many processors. Dynamics of work of microprocessors causes the changes of spatial distribution of heat flux supplied to the heat exchanger. Such changes finally influence the structure of two-phase flow in neighbouring channels.

In the paper the iterative solution to equations have been used to model the pressure-drop oscillations. The dynamics of pressure-drop oscillations in a single channel and in two neighbouring channels have been analyzed. The thermal and hydrodynamic interactions between channels have been considered. There has been considered the thermal interactions occurring through the channel walls and the hydrodynamic interactions occurring inside the common outlet of channels. The obtained qualitative results have been compared with conclusions of experimental results reported by other researches.

2. MECHANISM OF PRESSURE-DROP OSCILLATIONS

Mechanism of pressure-drop instability was discussed in papers (Liu et al.,1995, Kakac, Bon, 2008). The two conditions must

be fulfilled so that this type of oscillations occur: the curve of channel pressure drop versus mass flow rate must have negative slope region and the compressible volume must be in the system. Existence of compressible volume in the system amplifies the interaction between microchannel and liquid supply system. Pressure-drop instability causes long period oscillations (period oscillations is equal about 20 sec, Kakac, Bon, 2008) with high amplitude of pressure, temperature and mass flow rate fluctuations.

During these oscillations the sudden flow changes between subcooled and superheated operating conditions are observed (Liu et al., 1995). In Fig. 1 the example of cycle of pressure-drop oscillations has been presented. The chart has been prepared basing on data presented in (Zhang et al., 2010). Sudden flow change is shown by two line segments: D-A and B-C. The mechanism of pressure-drop oscillations is as follows. When boiling is initiated in microchannel, then more vapour appears in two-phase flow. It causes the increase in pressure drop. Compressible volume (surge tank) starts to accumulate the liquid because the channel exit is blocked by vapour. The system pressure drop increases until it reaches the peak (point D, Fig. 1). Accumulated liquid in surge tank is now released - vapour is being pushed out from the channel and system moves to point A (Fig. 1). At this point the amount of liquid leaving the surge tank is greater than the entering liquid. Pressure in the surge tank is decreasing until the point B is reached. In this stage the pressure in the surge tank is too low to prevent the boiling in microchannel and system moves to point C (Fig. 1). Now the channel exit is being blocked by vapour which causes that the liquid is accumulated in the surge tank and the system pressure drop is increasing until it reaches the point D. Now the cycle repeats again. Between points A-B and C-D the stable flows in microchannel are observed.

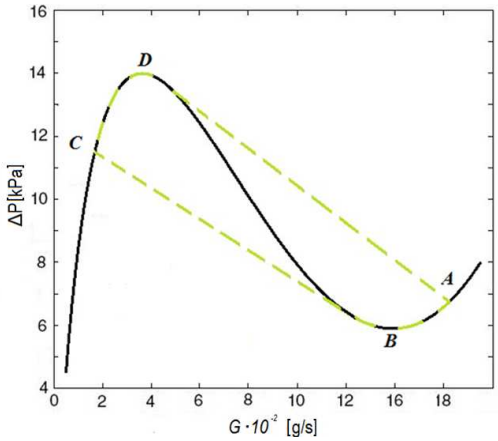

Fig. 1. The curve of pressure drop vs. mass flow rate. The dashed line shows the cycle of pressure-drop oscillations. The chart has been prepared based on data presented in Zhang et al., (2010)

The process of the sudden changes between two operating conditions very often has periodic character but the chaotic changes are also reported in papers (Hardt et al.,2007).

3. MODELLING OF HEAT AND MASS TRANSFER IN MICROCHANNEL

To describe the heat and mass transfer in microchannel the mass, momentum and energy balance equations inside the micro channel should be considered. This set of equations should be supplemented by relationships describing the mechanism of phase change, interactions between phases and equations describing the behaviours of liquid and heat supply systems.

In modelling of heat and mass transfer in microchannel system the many assumptions are usually considered. Different types of models are used to describe the behaviour of two-phase flow in microchannel. The most commonly used models are: homogeneous flow, separated flow and drift flux (Kakac and Bon, 2008; Awad and Muzychka, 2008; Kocamustafaogullari, 1971; Ishii, 1977).

In pressure-drop oscillations the system state oscillates between two kinds of stable two-phase flows. Because the duration of stable two-phase flow regimes is relatively long (e.g. 20 s) therefore, such two-phase flows can be treated in the paper as quasi-steady states. Thus, we can assume that the pressure-drop oscillations occur between two quasi-steady states. This allows us to model the dynamics of such oscillations using the iterative equations, which determines the successive values of the parameters characterizing the quasi-steady states. Such model has a qualitative character, but due to its low mathematical complexity it allows us in easy way to estimate the complexity of the system dynamics. It also allows for the identification of processes responsible for the stability loss.

3.1. Model of a single channel system

In Fig. 2a it has been shown the schema of microchannel system with two systems supplying heat and liquid to the microchannel. The heat supply system consists of the heat source (generating the constant heat flux (q_d)) and the heating surface whose temperature varies in time. The liquid supply system consists of compressible volume (surge tank) which may accumulate the liquid when the channel exit is blocked by vapour. The surge tank is supplied by constant liquid mass flux (G_d). It has been assumed that each steady state of heat and mass transfer in microchannel can be clearly identified by the following parameters: heating surface temperature (T_w), thermodynamic vapour quality (X), liquid mass flux (G), pressure drop (Δp) and heat flux absorbed by boiling liquid (q_b).

It has been assumed that the pressure-drop oscillations in the system are caused by interactions between the heat supply system and liquid supply system. These interactions influence the heat and mass transfer inside the microchannel. In Fig. 2b it has been shown the schema of mutual relationships between two supply systems and heat and mass transfer inside the microchannel. Changes of the value of heat absorbed by boiling liquid in the microchannel cause the changes of heating surface temperature (*I*, Fig. 2b). Such changes (in our model will be described by function f_1) influence the heat and mass transfer inside the microchannel (1, Fig. 2b) and reduce the boiling intensity. Finally, the vapour quality (*II*, Fig. 2b) decreases. In our model these changes will be described by function f_2. The changes influence the liquid supply system (2, Fig. 2b) and modify the pressure drop and mass flux (*III*, Fig. 2b). In our model such changes will be described by functions f_3 and f_4. Such new conditions influence the heat and mass transfer inside the microchannel (3, Fig. 2b). The new liquid flow inside the microchannel modifies the value of heat flux absorbed by boiling liquid (*IV*, Fig. 2b). In our model such changes will be described by function f_5. This new value of heat flux absorbed by boiling liquid influence on the

heat supply system (4, Fig. 2b) and the new cycle start again (new quasi-steady state appears inside the microchannel system). The time of one cycle, Δt, corresponds with the duration of quasi-steady state. For example in the paper (Zhang et al., 2010) such time is about 20 s. In our model this time period is constant. To complete the model knowledge about five functions, *f*, shown in the Fig. 2b is required.

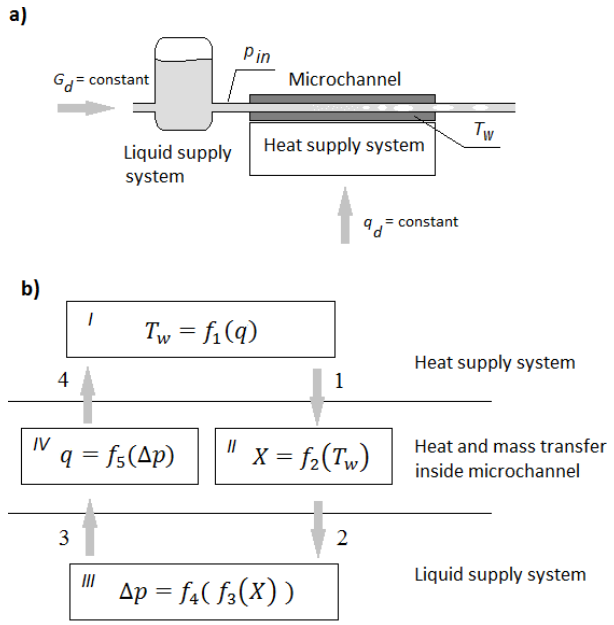

Fig. 2. Model of heat and mass transfer during the pressure-drop oscillations: a) schema of microchannel system. b) schema of algorithm of calculations of the quasi-steady states parameters. 1. Influence of heat supply system on the two phase flow in microchannel, 2. Influence of two phase flow in microchannel on the liquid supply system. 3. Influence of liquid supply system on the two phase flow in microchannel. 4. Influence of two phase flow in microchannel on the heat supply system.

In the paper (Wang et al., 2008) it has been noted that flow instabilities cause oscillates between two quasi-steady states which correspond with minimal and maximal values of wall temperature or pressure drop in microchannel. In the present model it has been used normalized values of parameters describing the heat and mass transfer inside the microchannel. For example the heating surface temperature has been described as follows:

$$T_w = \hat{T}_w\left(T_{w,max} - T_{w,min}\right) + T_{w,min} \tag{1}$$

where $\hat{T}_w$ is normalized value of heating surface temperature.

According to Warrier's for the narrow rectangular channel the heat transfer coefficient can be expressed by the following correlation (Warrier et al.2002):

$$\alpha_{tp} = \frac{Nu_3}{Nu_4}\left(E\alpha_{sp}\right) \tag{2}$$

where: $\alpha_{sp} = Nu_4 \frac{k_f}{d_h}$

$E = 1.0 + 6Bo^{\frac{1}{16}} - 5.3(1 - 855Bo)X^{0.65}$; $Nu_3 = 8.235(1 - 1.883\beta + 3.767\beta^2 - 5.814\beta^3 + 5.361\beta^4 - 2.0\beta^5)$; $Nu_4 = 8.235(1 - 2.042\beta + 3.085\beta^2 - 2.477\beta^3 + 1.058\beta^4 - 0.186\beta^5)$; $Bo = q/G \cdot h_{lv}$ – boiling number, α_{sp} – heat transfer coefficient (*sp* – single-phase, *tp* – two-phase), Nu – Nusselt Number, X – thermodynamic vapour quality, β – aspect ratio, k_f – thermal conductivity, h_{lv} – latent heat of vaporization, d_h – hydraulic diameter.

Considering that:

$$\alpha_{tp} = \frac{q}{(T_w - T_{sat})} \tag{3}$$

The equation (2) allows us to calculate the value of function $X(T_w)$. In Fig. 3 the function $X(T_w)$ obtained for constant q and *G* is presented.

In Fig. 3 it has been also shown the example of chart of function $\hat{X}\left(\hat{T}_w\right)$ prepared for the exemplary oscillations occurring in the rectangular area. For simplifying the future consideration it has been assumed that function $\hat{X}\left(\hat{T}_w\right)$ is linear and its values change as it has been shown in Fig. 3.

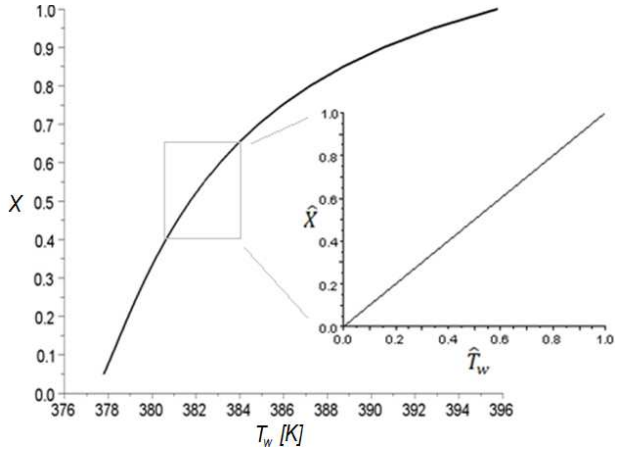

Fig. 3. Vapour quality vs. heating surface temperature. q = 8.5 W/cm^2, G = 200 kgm^{-2}s^{-1}, d_h = 100 μm

The thermodynamic vapour quality is defined as follows (Wang et al., 2008):

$$X = \frac{h_{in} - h_{l,sat}}{h_{lv}} + \frac{A_w Bo}{A_c} \tag{4}$$

where: Bo – Boiling Number, h_{in} – inlet enthalpy, $h_{l,sat}$ – enthalpy of saturated liquid, h_{lv} – latent heat of evaporation, A_w – cross-sectional flow area of each microchannel, A_c – area of microchannel bottom wall and side walls.

In Fig. 4 it has been shown the function $G(X)$ based on equation (4).

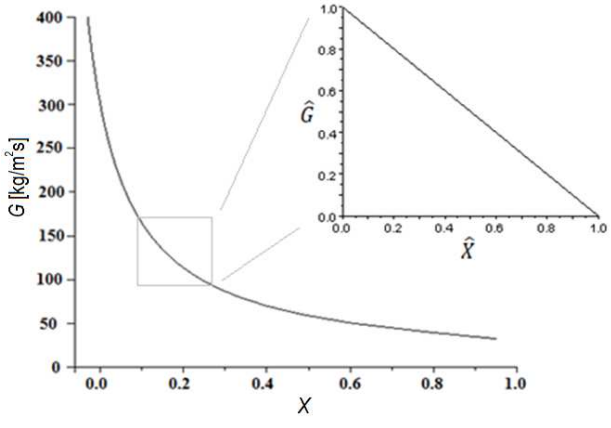

Fig. 4. Function *G*(*X*) according to the Eq.4 for d_h = 100 μm, q = 8.5 W/cm^2

Fig. 4 presents the example of chart of function $\hat{G}\ (\hat{X})$ prepared for the exemplary oscillations occurring in the rectangular area. For simplifying the future consideration it has been assumed that function $\hat{G}\ (\hat{X})$ is linear and its values change as it has been shown in Fig. 4.

Pressure drop vs. heat flux is presented in Fig. 5. The chart has been prepared based on data presented in (Weilin, Issam, 2004).

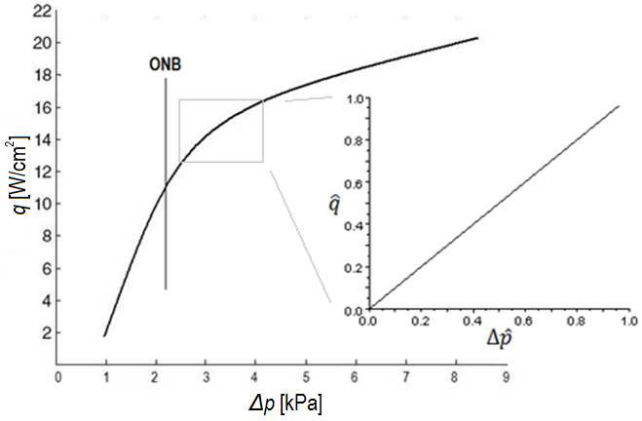

Fig. 5. Heat flux vs. pressure drop. The chart has been prepared based on data presented in (Weilin and Issam, 2004)

In Fig. 5 it has been also shown the example of chart of function $\hat{q}\ (\Delta\hat{p})$ prepared for the exemplary oscillations occurring in the rectangular area. For simplifying the future consideration it has been assumed that function $\hat{q}\ (\Delta\hat{p})$ is linear and its values change as it has been shown in Fig. 5.

Energy balance in time Δt, in a small element of the heating surface with linear dimension δ, leads to the following equation:

$$q_d - q_b = \frac{\delta \cdot \rho \cdot c \cdot (T_{w_{t+\Delta t}} - T_{w_t})}{\Delta t} \tag{5}$$

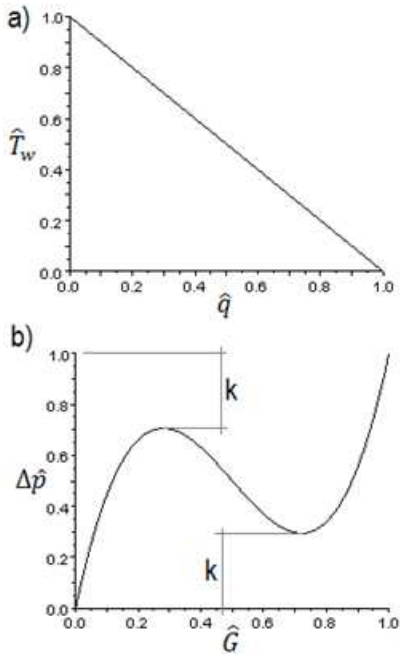

Fig. 6. The functions: f_1 and f_2. a) $\hat{T}_w = f_1(\hat{q}_b)$, b) $\hat{q}_b = f_5(\Delta\hat{p})$

Increase of q_b with constant q_d leads to decrease of T_w. Therefore, the function $\hat{T}_w = f_1(\hat{q})$ has been described by the linear function (with negative slope). The function $\Delta\hat{p} = f_4(\hat{G})$ has a minimum and maximum. It has been considered normalized function where both function values and function arguments are in the range (0, 1). The simulations were carried out for different values of negative slop of function $\Delta\hat{p} = f_4(\hat{G})$. The function has been modified by changing the function values for $G = 0.25$ and $G = 0.75$. It has been assumed that $f_4(0.25) = 1 - k$ and $f_4(0.75) = k$. The modification of value of coefficient k modifies the value of negative slope of function $\Delta\hat{p} = f_4(\hat{G})$. In Fig. 6 there has been shown functions: $\hat{T}_w = f_1(\hat{q})$ and $\Delta\hat{p} = f_4(\hat{G})$.

Finally, the system behaviours (Fig. 2a) have been described by the following five functions:

$$\begin{aligned} \hat{T}_w &= f_1(\hat{q}) \\ \hat{X} &= f_2(\hat{T}_w) \\ \hat{G} &= f_3(\hat{X}) \\ \Delta\hat{p} &= f_4(\hat{G}) \\ \hat{q} &= f_5(\Delta\hat{p}) \end{aligned} \tag{6}$$

where: $\hat{T}_w$ – normalized heating surface temperature, $\hat{X}$ – normalized vapour quality, $\hat{G}$ – normalized liquid mass flux, $\Delta\hat{p}$ – normalized pressure drop in microchannels, $\hat{q}$ – normalized heat flux absorbed by boiling liquid.

Zhang et al., (2010) studied pressure-drop oscillations in parallel-channel system with compressible volumes. They reported oscillations in range from 4 to 14 kPa. Obtained from the model pressure changes were rescaled to values obtained during the experiment. In Fig. 7 there has been shown the examples of function $\Delta p = f_4(G)$ obtained for different values of coefficient k. For $k = 0.38$ the subsequent iterations of set of equations (5) lead to reaching the single stable state in the system. The parameters of such state are shown in Fig. 7a by black dot. For $k = 0.2$, when the value of negative slope increases, the subsequent iterations of set of equations (6) create the periodic cycle between two quasi-steady states marked with black dots in Fig. 7b. The line segment which connects these points is the trajectory of the system. Further increase of the value of negative slope of function $\Delta p = f_4(G)$ (for $k = 0.097$) causes that the subsequent iterations of set of equations (6) create the chaotic time series. Finally, oscillations appear between two sets of quasi-steady states characteristic for subcooled and superheated operating conditions (Fig. 7c). In the right side of the charts (Fig. 7) the schematic picture of flow patterns appearing in the microchannel has been presented.

In Fig. 8 it has been shown the bifurcation diagram of iterations of set of equations (6) for different values of coefficient k. The pressure-drop oscillations starts for the critical value of $k = 0.35$. The chaotic pressure-drop oscillations starts for $k = 0.15$. In the right side of bifurcation diagram the schematic pictures of flow patterns in microchannel characteristic for different value of Δp have been presented.

Obtained results (Fig. 7) indicate that the shape of pressure drop curve has a significant influence on the system stability. When the slope of curve $\Delta p = f_4(G)$ in the region between function extremes increases the pressure oscillations become chaotic. Kakac (Kakac, Bon, 2008) noted that the higher heat flux supplied to the system moves the maximum of pressure drop curve to higher value which causes the increase of the slope

of curve $\Delta p = f_4(G)$ in the region between function extremes. Therefore, we can assume that the value of coefficient *k* corresponds to the amount of heat supplied to the system. Kakac noted also that the increase of the slope of curve $\Delta p = f_4(G)$ in the region between function extremes causes the bigger instability and oscillations become chaotic.

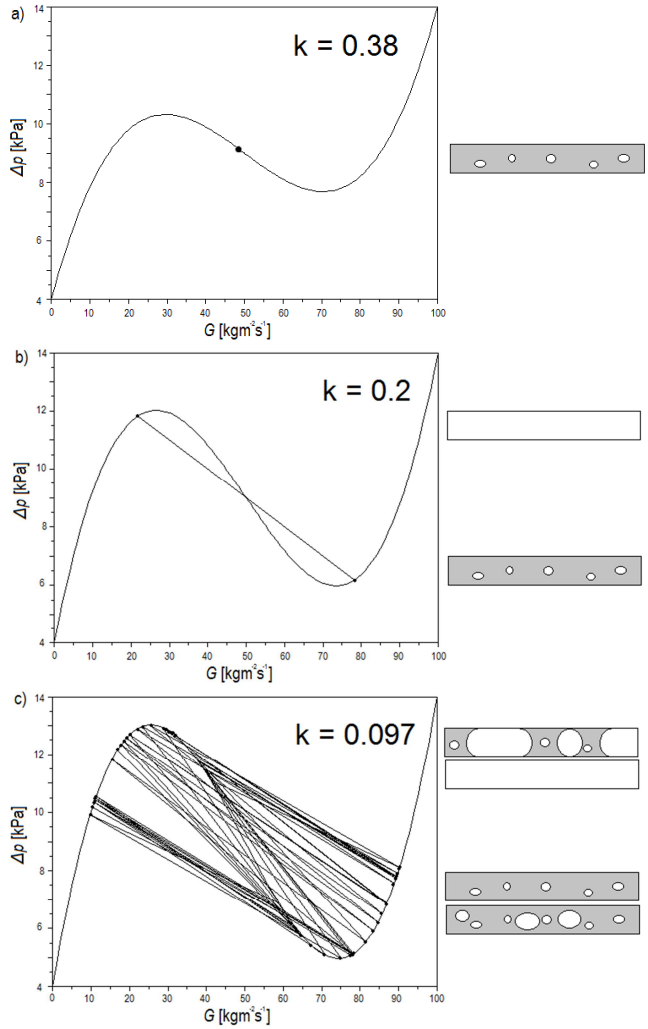

Fig. 7. The examples of subsequent iterations of function $\Delta p = f_4(G)$ for different values of coefficient *k*. a) *k* = 0.38, b) *k* = 0.2, c) *k* = 0.097

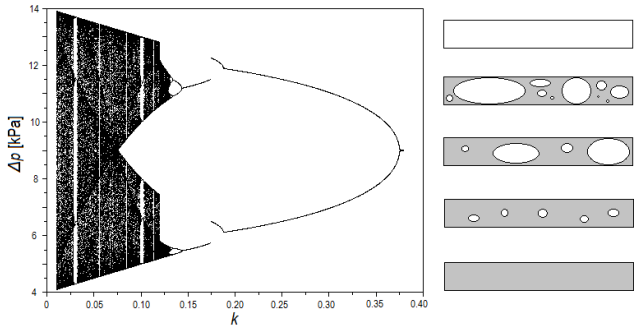

Fig. 8. The bifurcation diagram of iteration of set of equations (5) for different values of coefficient *k*

From this point of view the qualitative model properties are consistent with experimental results presented in the paper (Kakac, Bon, 2008).

3.2. Two neighbouring parallel microchannels

In case of multi channels system the channel-to-channel interactions may cause the synchronization of heat and mass transfer in neighbouring channels (Chen, 2004).

It the present paper it has been considered two neighbouring microchannels. The two kinds of interactions between channels have been considered:

- thermal (heat transfer between channels q^T);
- hydrodynamic (flow disturbance because of common channels outlet).

In Fig. 9 it has been schematically shown the section of microchannels perpendicular to axis of channels. The heat flux, q_n^T, (where *n* is a moment of time) modifies the temperature of heating surfaces of microchannels, marked adequately with $T_{w_n}^{\ 1}$ and $T_{w_n}^{\ 2}$. The heat flux, q_n^T, is proportional to difference between heating surface temperatures of each channel $q_n^T \sim T_{w_n}^{\ 2} - T_{w_n}^{\ 1}$. The heating surface temperature changes in time period, Δt, are proportional to the heat flux, q_n^T. For channel 1 there is $T_{w_{n+1}}^{\ 1} - T_{w_n}^{\ 2} \sim q_n^T$. It allows us to estimate the heating surface temperature after time period Δt as follows:

$$\hat{T}_{w_{n+1}}^{\ 1} = \hat{T}_{w_n}^{\ 1} + A_T\left(\hat{T}_{w_n}^{\ 2} - \hat{T}_{w_n}^{\ 1}\right) \qquad (7)$$
$$\hat{T}_{w_{n+1}}^{\ 2} = \hat{T}_{w_n}^{\ 2} + A_T\left(\hat{T}_{w_n}^{\ 1} - \hat{T}_{w_n}^{\ 2}\right)$$

The coefficient A_T describes the intensity of heat transfer between the channels. Its value depends on the distance between channels, their geometry and material of heating surface.

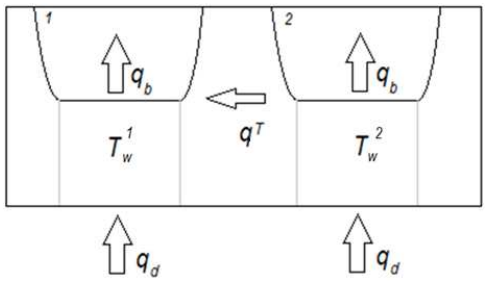

Fig. 9. Schema of heat transfer between two neighbouring channels

Common channels outlet has significant influence on the two-phase flow in neighbouring channels. Changes of kind of two-phase flow in one of microchannel cause the pressure changes in outlet of channels. Such process causes the appearance of pressure difference between neighbouring channel outlets. It causes the flow disturbance, ΔG_n, in each channel. The flow disturbance has been defined as follows: $\Delta G_n \sim G_n^2 - G_n^1$. The flow disturbance, ΔG_n, in each channel is proportional to difference between pressure drop in neighbouring microchannels ($\Delta G_n^1 \sim \Delta p_n^2 - \Delta p_n^1$). Finally, in time period of Δt the pressure drops in neighbouring microchannels vary. The pressure drops after time period of Δt can be estimated as follows:

$$\Delta\hat{p}_{n+1}^1 = \Delta\hat{p}_n^1 + A_p(\Delta\hat{p}_n^2 - \Delta\hat{p}_n^1) \qquad (8)$$
$$\Delta\hat{p}_{n+1}^2 = \Delta\hat{p}_n^2 + A_p(\Delta\hat{p}_n^1 - \Delta\hat{p}_n^2)$$

The coefficient A_p describes the intensity of influence of the pressure drop in neighbouring channels on the two-phase flow. Its value depends on the distance between channels and outlet geometry.

Finally, in subsequent time periods the parameters describing the quasi-steady states are described by the following set of equations.

$$\hat{T}^1_{w,n} = f_1(\hat{q}^1_n) + A_T \cdot [f_1(\hat{q}^1_n) - f_1(\hat{q}^2_n)]$$
$$\hat{T}^2_{w,n} = f_1(\hat{q}^2_n) + A_T \cdot [f_1(\hat{q}^2_n) - f_1(\hat{q}^1_n)]$$
$$\hat{X}^1_n = f_2(\hat{T}^1_{w,n}),\ \hat{X}^2_n = f_2(\hat{T}^2_{w,n})$$
$$\hat{G}^1_n = f_3(\hat{X}^1_n),\ \hat{G}^2_n = f_3(\hat{X}^2_n) \quad (9)$$
$$\Delta\hat{p}^1_n = f_4(\hat{g}^1_n) + A_p \cdot [f_4(\hat{g}^1_n) - f_4(\hat{g}^2_n)]$$
$$\Delta\hat{p}^2_n = f_4(\hat{g}^2_n) + A_p \cdot [f_4(\hat{g}^2_n) - f_4(\hat{g}^1_n)]$$
$$\hat{q}^1_{n+1} = f_5(\Delta\hat{p}^1_n),\ \hat{G}^2_{n+1} = f_5(\Delta\hat{p}^2_n)$$

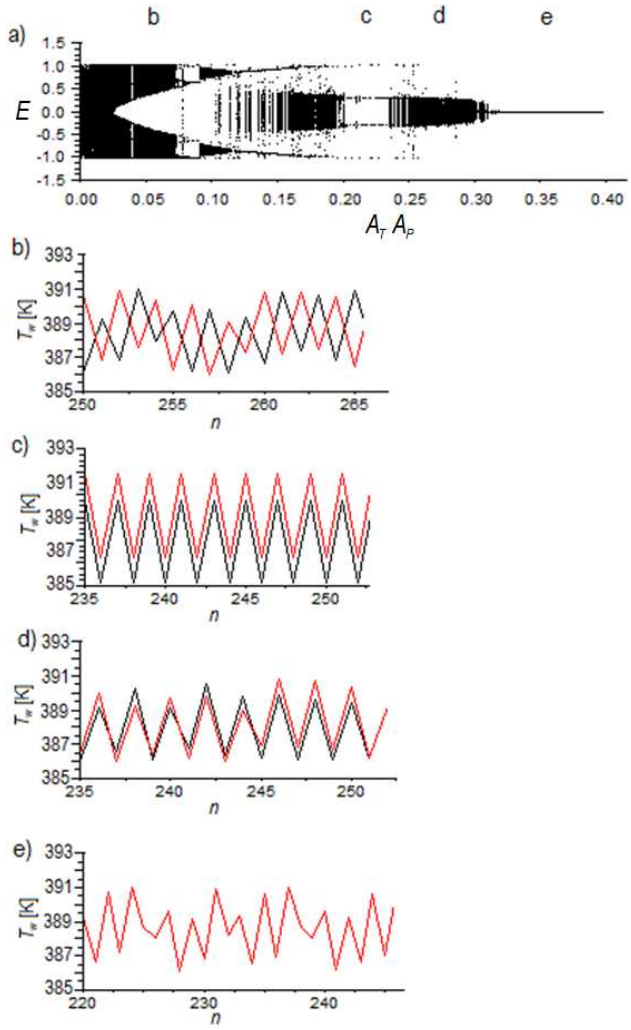

Fig. 10. Examples of simulations results for different values of coefficient A_T *and* A_P. a) changes of synchronization error for different values of coefficients A_T and A_P b) temperature changes for A_T, A_P *= 0.05 c)* temperature changes for A_T, A_P *= 0.22 d)* temperature changes for A_T, A_P *= 0.28 e)* temperature changes for A_T, A_P *= 0.35*

Synchronization error is a parameter which describes the level of synchronization. It is defined as difference between values of parameters characterising the synchronized systems. For example, for heating surface temperature the synchronization error is as follows:

$$E^T = T_{w_n}{}^1 - T_{w_n}{}^2 \quad (10)$$

In Fig. 10 it has been shown the examples of simulation results obtained for different values of coefficient A_T and A_P. During the simulations the coefficient A_T was equal to A_P.

The changes of synchronization error for different A_T and A_P coefficients have been shown in Fig. 10a. Normalized values of $\hat{T}_{w_n}$ were converted to values observed in experimental results (Wang et al.,2007). Obtained results indicates that for $A_T > 0.32$ and $A_P > 0.32$ *the* synchronization between channels appears even when pressure-drop oscillations in both channels are chaotic (Fig. 10e). Hardt et al. also reported synchronization between parallel channels (Hardt et al, 2007). For A_T and $A_P < 0.32$ different scenarios of channel-to-channel interaction can appear. For A_T and A_P equal to 0.05 the temperature alternately oscillates in the neighbouring channels (Fig. 11b). Synchronization between channels is low and temperature oscillations are chaotic. Similar regime of working the system of microchannels was reported in paper (Hardt et al, 2007). For A_T and A_P equal to 0.22 periodic oscillations in microchannels are observed (Fig. 11c). Synchronization error has a constant value. Wang et al. reported similar instability regime in the paper (Wang et al., 2007). For A_T and A_P equal to 0.35 (Fig. 11d) temperature oscillations are chaotic but the synchronization error, E^T, is equal to zero – the heat and mass transfer in neighbouring microchannels are completely synchronized.

4. CONCLUSION

In the paper the dynamics of pressure-drop oscillations in a single channel and in two neighbouring channels have been analyzed. The thermal and hydrodynamic interactions between the channels have been considered.

Obtained results indicate that the shape of pressure drop curve has significant influence on the stability of the system. When the slope of curve $\Delta p = f_4(G)$ in the region between function extremes increases then the pressure oscillations become chaotic.

Four types of two-phase behaviours in parallel channels have been observed depending on the intensity of interactions.

- two-phase flow parameters oscillate alternately in the neighbouring channels but synchronization between channels is low and oscillations of two-phase flow parameters are chaotic;
- two-phase flow parameters oscillate consistently in the neighbouring channels but synchronization between channels is low and oscillations of two-phase flow parameters are chaotic;
- two-phase flow parameters oscillate periodically;
- oscillations of two-phase flow parameters in both channels are chaotic but the synchronization error is equal to zero – the heat and mass transfers in neighbouring microchannels are completely synchronized.

Obtained qualitative results have been compared with conclusions of experimental results reported by other researches (Kakac, Bon, 2008, Hardt et al, 2007, Wang et al., 2007). The qualitative model properties are consistent with experimental results.

REFERENCES

1. **Awad M.M., Muzychka Y.S**. (2008), Effective property models for homogeneous two-phase flows, *Experimental Thermal and Fluid Science*, Vol. 33, No. 1, 106–113.

2. **Boure J.A., Bergles A.E.,Tong L.S**. (1973), Review of two-phase flow instability, *Nuclear Engineering and Design*, Vol. 25, No. 2, 165–192.
3. **Hardt S., Schilder B., Tiemann D., Kolb G., Hessel V., Stephan P.** (2007), Analysis of flow patterns emerging during evaporation in parallel microchannels, *International Journal of Heat and Mass Transfer*, Vol. 50, No. 1–2, 226-239.
4. **Ishii M.** (1977), *Drift-flux model and derivation of kinematic constitutive laws*, in: S. Kakac, F. Mayinger, T.N. Veziroglu (Eds.), Two-Phase Flows and Heat Transfer, Hemisphere, Washington, DC,
5. **Kakac S., Bon B**. (2008), A Review of two-phase flow dynamic instabilities in tube boiling systems, *International Journal of Heat and Mass Transfer*, Vol. 51 No: 3-4, 399-433.
6. **Kocamustafaogullari G**. (1971), *Thermo-fluid dynamics of separated twophase flow*, Ph.D. Thesis, School of Mechanical Engineering, Georgia Institute of Technology, Atlanta, Georgia.
7. **Li-Qun Chen** (2004a), *A general formalism for synchronization in finite dimensional dynamical systems*, Chaos, Solitons & Fractals, Vol. 19, No. 5, 1239-1242.
8. **Liu H.T., Koçak H., Kakaç S**. (1995), Dynamical analysis of pressure-drop type oscillations with a planar model, *International Journal of Multiphase Flow*, Vol. 21, No. 5, 851-859.
9. **Wang G, Cheng P., Bergles A.E.** (2008), Effects of inlet/outlet configurations on flow boiling instability in parallel microchannels, *International Journal of Heat and Mass Transfer*, Vol. 51, No. 9-10, 2267-2281.
10. **Wang G., Cheng P., Wu H.** (2007), Unstable and stable flow boiling in parallel microchannels and in a single microchannel, *International Journal of Heat and Mass Transfer*, Vol. 50, No.21-22, 4297-4310.
11. **Warrier G.R., Dhir V.K., Momoda L.A.** (2002), Heat transfer and pressure drop in narrow rectangular channels, *Exp. Therm. Fluid Sci*., Vol. 26, No. 1, 53–64.
12. **Weilin Q., Issam M.** (2004), Transport Phenomena in Two-Phase Micro-Channel Heat Sinks, *Journal of Electronic Packaging*, Vol. 126, No. 2, 213-224.
13. **Zhang T, Peles Y., Wen J T., Tong T., Chang J, Prasher R,. Jensen M. K.** (2010), Analysis and active control of pressure-drop flow instabilities in boiling microchannel systems, International *Journal of Heat and Mass Transfer*, Vol. 53, No. 11–12, 2347-2360.
14. **Zhang T., Tong T., Chang J., Peles Y., Prasher R., Jensen M., Wen J.T., Phelan P.** (2009), Ledinegg instability in microchannels, *International Journal of Heat and Mass Transfer*, Vol. 52, No.25-26 5661–5674.

FAST AND ENERGY EFFICIENT LEARNING ALGORITHM FOR KOHONEN NEURAL NETWORK REALIZED IN HARDWARE

Marta KOLASA*

*Institute of Electrical Engineering, Faculty of Telecommunication and Electrical Engineering, University of Technology and Life Sciences, ul. Kaliskiego 7, 85-796, Bydgoszcz, Poland

markol@utp.edu.pl

Abstract: A new fast energy efficient learning algorithm suitable for hardware implemented Kohonen Self-Organizing Map (SOM) is proposed in the paper. The new technique is based on a multistage filtering of the quantization error. The algorithm detects such periods in the learning process, in which the quantization error is decreasing (the 'activity' phases), which can be interpreted as a progress in training, as well as the 'stagnation' phases, in which the error does not decrease. The neighborhood radius is reduced by 1 always just after the training process enters one of the 'stagnation' phases, thus shortening this phase. The comprehensive simulations on the software model (in C++) have been carried out to investigate the influence of the proposed algorithm on the learning process. The learning process has been assessed by the used of five criteria, which allow assessing the learning algorithm in two different ways i.e., by expressing the quality of the vector quantization, as well as the topographic mapping. The new algorithm is able to shorten the overall training process by more than 90% thus reducing the energy consumed by the SOM also by 90%. The proposed training algorithm is to be used in a new high performance Neuroprocessor that will find a broad application in a new generation of Wireless Body Area Networks (WBAN) used in the monitoring of the biomedical signals like, for example, the Electrocardiogram (ECG) signals.

Keywords: Kohonen Neural Network, CMOS Implementation, WBAN, Optimized Learning Process, Low Energy Consumption

1. INTRODUCTION

In the literature one can notice many attempts to employ artificial neural networks (ANNs) in the analysis of biomedical signals, including ECG signals (Chudáček et al., 2009; Fernández et al., 2001; Lagerholm and Peterson, 2000; Leite et al., 2010; Osowski and Linh, 2001; Talbi et al., 2010; Tighiouart et al., 2003; Valenza et al., 2008; Wen et al., 2009). These attempts aim to develop such methods and tools that will enable automatic analysis of the biomedical signals thus aiding medical staff in their work. One of the significant directions is to enable a quick detection of atypical sequences in such signals that usually indicate various problems. One of the main problems encountered in this area is that all applications of the ANNs involve PC computers or other programmable devices and as such are not suitable for the application in the Wireless Body Area Networks (WBAN).

The author of the paper is going to develop a new ultra-low energy consumption ANN realized as a specialized CMOS chip – a Neuroprocessor. The proposed chip will find the application in modern medical diagnostics tools based on WBAN systems. The chip will offer advanced data processing and analysis abilities directly in particular sensors (nodes) of the WBAN. As a result, instead of using a battery that enlarges the sizes of the sensor, an alternative supply source based on the energy scavenged from the environment (e.g. the body heat) will be used. This, in turn, will allow miniaturization of the sensors, making the overall wearable system much more convenient for the patients than the systems offered on the market today.

Due to the rapid growth in this research area a variety of learning algorithms and the architectures of the ANNs have been invented. Looking from the hardware realization point of view of such networks the most interesting solutions are those offering relatively simple learning algorithms. In this case, as simple arithmetic operations are being used, the algorithms require significantly less hardware resources. The resultant chips dissipate less power and occupy less chip area and thus are much more suitable for the application in the WBAN. A very simple and simultaneously fast learning algorithm is offered by the Kohonen Self-Organizing Map (SOM). This algorithm requires only basic arithmetic operations like addition, subtraction and multiplication. The Kohonen SOM is commonly used in the analysis and classification of the ECG signals (Leite et al., 2010; Tighiouart et al., 2003; Valenza et al., 2008; Wen et al., 2009). In case of the classification tasks, the reported results for this type of the ANN are comparable or even better than the results achieved in the case of using other algorithms (Chudáček et al., 2009; Fernández et al., 2001; Lagerholm and Peterson, 2000; Osowski and Linh, 2001; Talbi et al., 2010; Tighiouart et al., 2003; Valenza et al., 2008). In case of the analysis of the ECG signals the reported efficiency of even 97% is possible for the number of neurons not exceeding 150.

The Kohonen SOM already found the application in a wearable system that enables analysis of the acquired data in the real-time (Valenza et al., 2008). This system is able to recognize most significant cardiac arrythmias. The system is based on the Master Processing Unit (MPU) realized as the off-the-shelf SoC with the analog ECG signal conditioning circuit. The efficiency and sensitivity reported in (Valenza et al., 2008) are at high level of up to 99 %.

The author of the paper recently designed programmable architecture of the SOM that is able to operate with different topologies of the SOM and different neighborhood functions on a single

chip. The author proposed a fully parallel and asynchronous neighborhood mechanism that independently on the sizes of the map, allows for determining the distances from the winning neuron to all neighboring neurons in the period less than 11 ns. The adaptation is then performed also in parallel in all neurons covered by the neighborhood range in a given learning cycle (Długosz et al., 2011; Kolasa et al., 2012).

This paper presents one of the very important steps in the overall design process of the new chip - a new learning algorithm suitable for low power ANNs realized in hardware. The new algorithm enables shortening the overall learning process of the SOM even by 90% thus reducing the energy consumption also by 90%.

2. KOHONEN NEURAL NETWORK

Teuvo Kohonen in 1975 proposed a new class of neural networks that use competitive unsupervised learning algorithms (Kohonen, 2001). His neural networks (KNNs) in their classical approach, also called self-organized map (SOM), contain one layer of neurons that form a map. The number of the outputs of the network equals the number of neurons, while all neurons have common inputs, whose number depending on the application can vary in-between two and even several dozen. SOMs are used in data visualization and analysis (Boniecki, 2005; Brocki, 2007; Mokriš and Forgáč, 2004).

The competitive unsupervised learning in KNNs relies on presenting the network with the learning vectors X in order to make the neurons' weight vectors W resemble presented data. For each training vector X KNN determines Euclidean distances (d_{EUC}) between this vector and the weights vectors W in each neuron, which for n network's inputs are calculated using the following formula:

$$d_{\mathrm{EUC}}(X, W_i) = \sqrt{\sum_{l=1}^{n}\left(x_l - w_{i,l}\right)^2} \tag{1}$$

The neuron, whose weights are the most similar to the training vector X becomes a winner and is allowed to adapt own weights. Two general types of such networks can be distinguished. In the Winner Takes All (WTA) approach only the winning neuron is allowed to adapt the weight, while in the Winner Takes Most (WTM) algorithm also neurons that belong to the winner's neighborhood are allowed to adapt the weights, according to the following formula:

$$W_j(l+1) = W_j(l) + \eta(k)G\big(R, d(i,j)\big)[X(l) - W_j(l)] \tag{2}$$

where η is a learning rate that control strength of the learning algorithm, W_j denotes the weights' vector of a given j^{th}, neuron, and $X(l)$ is a given input pattern in the l^{th} cycle. Particular neurons that belong to the winner's neighborhood are adapted with different intensities, whose values depend on the neighborhood function $G()$. The commonly used neighborhood functions are: rectangular and Gaussian neighborhood function. Different neighborhood functions were defined by the author in (Kolasa, 2012).

One of the important parameters is the network topology, which can be defined as a grid of neurons. This feature determines which neurons belong to the winner's neighborhood for a given value of the radius R (Boniecki, 2005; Kohonen, 2001; Mokriš and Forgáč, 2004). The commonly used topologies are: a hexagonal one (Hex) in which particular neurons have maximum six neighbors and a rectangular with four (Rect4) and eight (Rect8) neighbors.

The quality of the learning process can be evaluated by means of the quantization error (Q_{err}) and the topographic error (E_{T1}), which are a commonly used criterias in such cases. In this paper the effectiveness of the learning process of the SOM is evaluated on the basis of five criteria described in (Lee and Verleysen, 2002). The quantization error is defined as:

$$Q_{\mathrm{err}} = \frac{\sum_{j=1}^{m}\sqrt{\sum_{l=1}^{n}(x_{j,l} - w_{i,l})}}{m} \tag{3}$$

where m is the number of learning patterns in the input data set, n *is* the number of the network inputs, while i identify the winning neuron. This criterion illustrates a way of fitting of the map to input data (Uriarte and Martin, 2005). A second measure used to assess the quantization quality is the percentage of dead neurons (PDN), which tells us about the ratio of inactive (dead) neurons versus all neurons. Dead neurons are those neurons that never won the competition and as such have not become representatives of any input data. These errors are detrimental to the assessment of the topological order of the map.

The quality of the topographic mapping is assessed using three measures (Lee and Verleysen, 2002). The first one is the Topographic Error E_{T1}, which is defined as follows:

$$E_{\mathrm{T1}} = 1 - \frac{1}{m}\sum_{h=1}^{m}\lambda(X_{\mathrm{h}}) \tag{4}$$

This is one of the measures proposed by Kohonen (Kohonen, 2001; Uriarte E. and Martin F., 2005). The value of $\lambda(X_{\mathrm{h}})$ equals 1 when for a given pattern X two neurons whose weight vectors that resemble this pattern to the highest extent are also direct neighbors in the map. Otherwise the value of $\lambda(X_{\mathrm{h}})$ equals 0. The lower the value of E_{T1} is, the better the SOM preserves the topology (Beaton et al., 2010; Uriarte and Martin, 2005). In an ideal case, the optimal value of E_{T1} equals 0.

The remaining two measures of the quality of the topographic mapping do not require the knowledge of the input data. In the second criterion, in the first step, the Euclidean distances between the weights of an ρ^{th} neuron and the weights of all other neurons are calculated. In the second step, it has to be check if all p direct neighbors of neuron ρ are also the nearest ones to this neuron in the sense of the Euclidean distance measured in the future space. To express this requirement in a formal manner, let us assume that neuron ρ has $p = |N(\rho)|$ direct neighbors, where p depends on type of the map topology. Let us also assume that function $g(\rho)$ returns the value equal to the number of the direct neighbors that are also the closest to neuron ρ in the feature space. As a result, the E_{T2} criterion for P neurons in the map can be defined as follows:

$$E_{\mathrm{T2}} = \frac{1}{P}\sum_{\rho=1}^{P}\frac{g(\rho)}{|N(\rho)|} \tag{5}$$

The optimal value of E_{T2} equals 1. Considering the third criterion, it is built around each neuron ρ a neighborhood in the feature space (Euclidean neighborhood) defined as a sphere with the radius:

$$R(\rho) = \max_{s\epsilon N(\rho)}\left\|W_\rho - W_s\right\| \tag{6}$$

where W_ρ are the weights of a given neurons ρ, while W_S are the weights of its particular direct neighbors. Then it is necessary to count those neurons, which are not the closest neighbors of the neuron ρ, but are located inside $R(\rho)$. The E_{T3} criterion, with the optimal value equal to 0, is defined as follows:

$$E_{\mathrm{T3}} = \frac{1}{P}\sum_{\rho=1}^{P}\left|\{s | s \neq \rho, s \notin N(\rho), \left\|W_\rho - W_s\right\| < R(\rho)\}\right| \tag{7}$$

3. THE PROPOSED ALGORITHM

In the Kohonen learning algorithm it is often assumed that the neighborhood range $R_{max,}$ which is the maximal neighborhood range R set up before starting the learning process, should cover at least half of the map (Kohonen, 2001) and then gradually decrease to zero. The reduction of the value of this parameter can be realized in the following manner:

$$R_k = 1.00001 + (R_{\max} - 1) \cdot (1 - \frac{k}{l_{\max}}) \quad (8)$$

where k stands for the k^{th} iteration, l_{max} is the total number of the iterations in the ordering phase of the learning process.

In practice, as number of iterations usually is much larger than the maximum value (R_{max}) of the neighborhood radius R, therefore the radius decreases always by '1' after the number of iterations equals to:

$$l = \text{round}(\frac{l_{\max}}{R_{\max}}) \quad (9)$$

Value of the l parameter usually is in the range in-between 20 and 200, depending on dimensions of the map. In case of an example map with 15x15 neurons, R_{max} equals 29 or 14, for Rect4 and Rect8 topologies, respectively.

3.1. Applied methodology

The author completed a series of simulations using the software model (in C++) of the map to verify the commonly used 'linear' approach. Simulations have been carried out for all three topologies (Hex, Rect4 and Rect8), sizes of the map varying in-between 4x4 and 64x64 neurons, different numbers of inputs, different values of the initial neighborhood size, R_{max}, different neighborhood functions (rectangular, triangular and Gaussian) and different training sets. The network was trained with 2D and 3D data regularly placed in the input space, as well as with data randomly distributed in this space. Here the author reports on some selected results which can be regarded as being representative to the overall suite of experiments. The author presents results for 8x8 and 16x16 neurons for two example 2D data sets. The results for 2D sets have been selected for a better illustration (Lee et al., 2001; Lee and Verleysen, 2002; Su, 2002; Uriarte and Martin, 2005). In the first data set, data are divided into P classes (centers), where P equals the number of neurons in the map. Each center is represented by an equal number of learning patterns. The centers are placed uniformly in the input data space, as shown in Fig. 1a. This data set is in the paper called CREG. To achieved comparable results in this case, the input space was fitted to input data. For example, for the map with 8x8 neurons the values of the input signals were in the range of 0 to 1, while for 16x16 neurons the values was in the range of 0 to 2. As a result, in all cases the optimal value of Q_{err} equals 16.2e-3, while the optimal values of the remaining parameters (PDN/E_{T1}/E_{T2}/E_{T3}) are equal to 0/0/1/0, respectively. The optimal nonzero value of Q_{err} results from the arrangement of data. The regular arrangement allows for ideal distribution of all neurons over the input data space, assuming the training process was optimal. This approach facilitates a direct comparison of the results for different combinations of particular parameters mentioned above (Li, 2009).

Second data set was composed of 1000 patterns randomly distributed over the selected region, as shown in Fig. 1b. This data set is called SQUARE in the paper. In this case input data are in the constant range, independently from the size of the map. As a result, for larger maps the Q_{err} achieves smaller values.

3.2. Selected simulation results

Selected simulation results illustrating an example learning process are shown in Fig. 2. The Figure presents example illustrative waveforms of the Q_{err} over time i.e. for particular iterations. The results are shown for example maps with 8x8 and 16x16 neurons, the triangular neighborhood function and Rect8 topology, but similar results were commonly observed for different input data, network topologies and neighborhood functions.

Observing the quantization error in time domain one can notice that the 'linear' approach is not optimal.

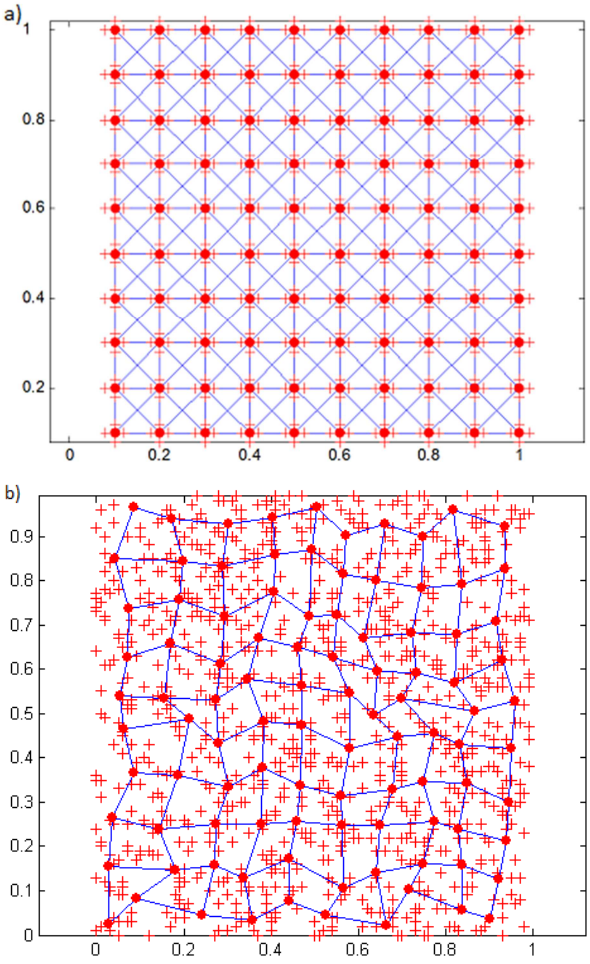

Fig. 1. Input data sets and the final placement of neurons for: 2D data a) regularly; b) randomly distributed in the input space

The first important observation is that when the neighborhood radius R is larger than some *critical* value, the quantization error does not decrease, so in this period the network does not make any progress in training. For example, in diagram (b), for R_{max}=6, the Q_{err} starts decreasing only around the 800th iteration, for R = 2 i.e. for about 1/3 of the map size. So the conclusion is that the learning process may start with the value of the radius R, which

is smaller than the maximal value R_{max}. This significantly shorts the overall training process.

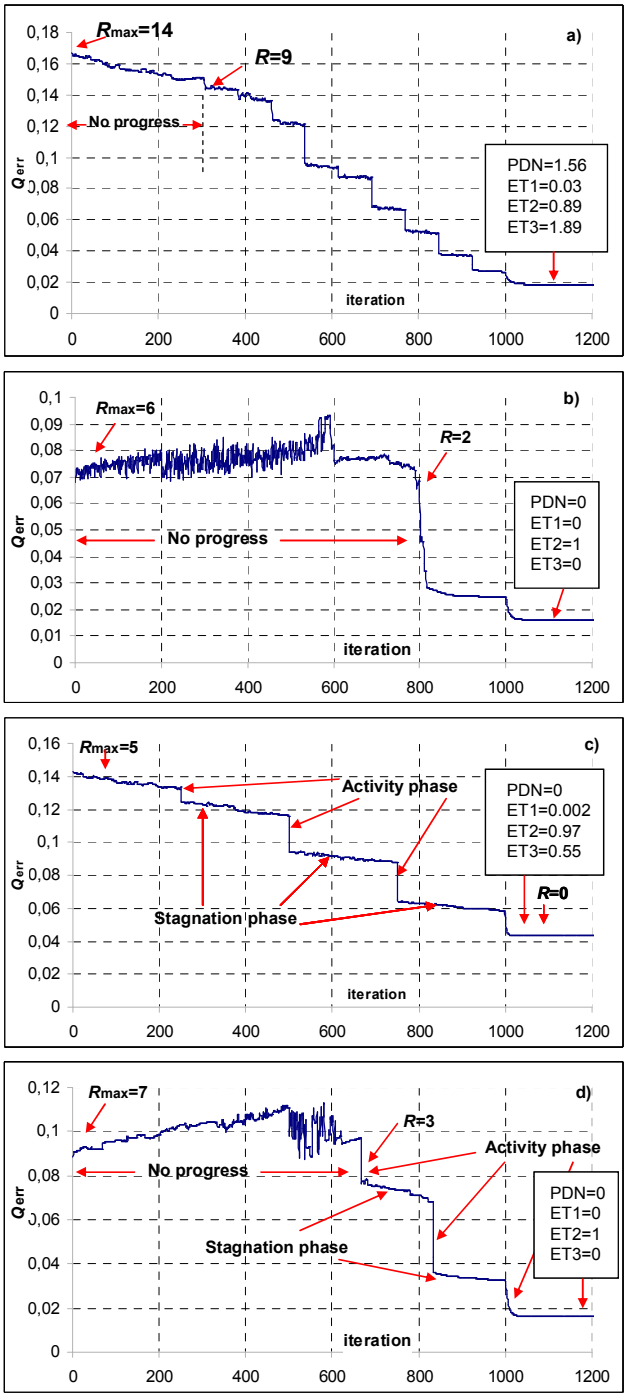

Fig. 2. The quantization error as a function of the number of iterations, for: a) 16x16 SQUARE; b) 16x16 CREG2D; c) 8x8 SQUARE; d) 8x8 CREG2D data file

The main observation is that the quantization error Q_{err} does not decrease monotonically during the overall learning process. One can notice some distinct 'activity' phases, in which the error decreases rapidly and then the 'stagnation' phases, in which the value of the error remains almost constant. The activity phases take place immediately after the radius R is switched to a smaller value. Note that the stagnation phases usually are much longer than the activity phases, which in practice means that the network makes a progress in training only in short periods of the overall process.

The algorithm proposed in this paper relies on shortening the stagnation phases. First it is necessary to detect automatically the activity and the stagnation phases, which is performed by the use of a set of linear and nonlinear filters. Such a multistage filtering of the quantization error detects the activity phases and controls the neighborhood radius R in such a way to significantly shorten the stagnation phases.

This technique uses a special decision mechanism that automatically switches over the radius R just after a given activity phase is finished. This starts a new activity phase, but for the new, smaller value of the radius R. As a result, the learning process may be even 90% faster than in the classic approach, in which the radius R decreases linearly.

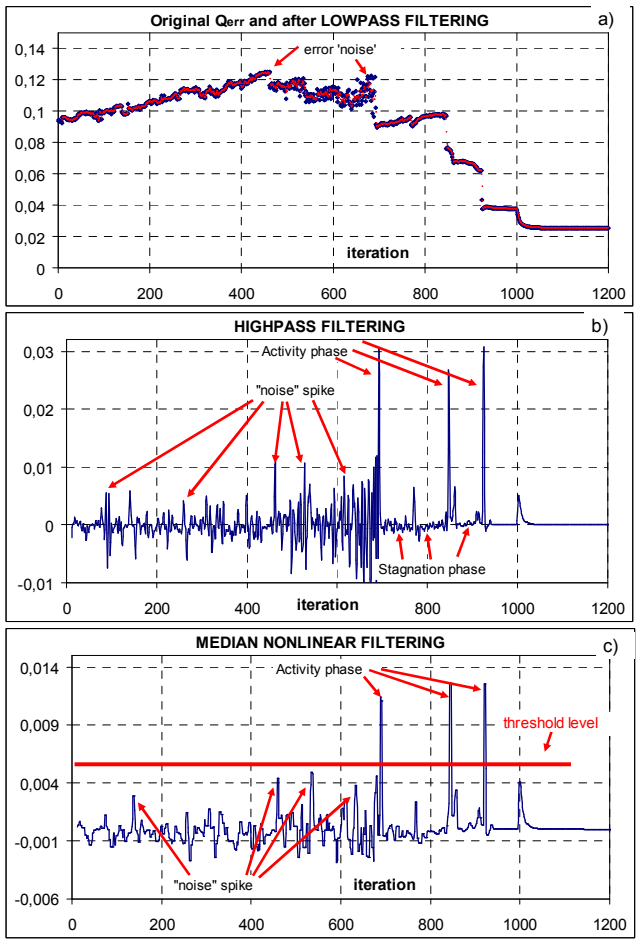

Fig. 3. Proposed 3-stage error filtering: a) the original waveform and the lowpass, b) the highpass, c) the nonlinear median filtering for 16x16 CREG2D data file

3.3. The proposed technique

The proposed 3-stage filtering of the error is presented in Fig. 3 for an example map with 16x16 neurons, triangular neighborhood function, Rect8 topology and CREG data base. In this case three filters have been used. The process of detection of the activity phases starts with a lowpass finite impulse response (FIR) filtering that removes the "noise" from the initial error waveform. This process is shown in Fig. 3a. In this case a simple

Butterworth flat filter has been used with the following coefficients: h_{LPi} = {0.125, 0.375, 0.375, 0.125}.

The next step is the highpass filtering operation that detects edges in the smoothed error waveform. This filter can be very simple, with the length not exceeding 4. In presented example a filter with the coefficients h_{HPi} = {1, 1, -1, -1} has been employed. The resultant waveform is illustrated in Fig. 3b. The spikes in this waveform indicate the activity phases. The problem here is that the "noise" present in the initial error waveform is a source of additional undesired spikes, which often are as high as the 'activity' spikes, although usually are narrower than the 'activity' spikes. To overcome this problem a nonlinear median filter has been additionally applied. The length of this filter has been selected in such a way to even the height of the 'activity' spikes and to eliminate the 'noise' spikes. An example median filter of the length 5 allows to eliminate the 'noise' spikes with the width equal or smaller than 2, as illustrated in Fig. 3c.

The output signals of the highpass and the median filters are used by a decision mechanism that automatically switches over the radius R to smaller values. This procedure starts when the value at the output of the median filter becomes larger than a selected threshold value, which must be high enough to exclude the 'noise' spikes. Switching of the R parameter is performed when the signal at the output of the highpass filter starts falling that means that the training process is just entering the stagnation phase.

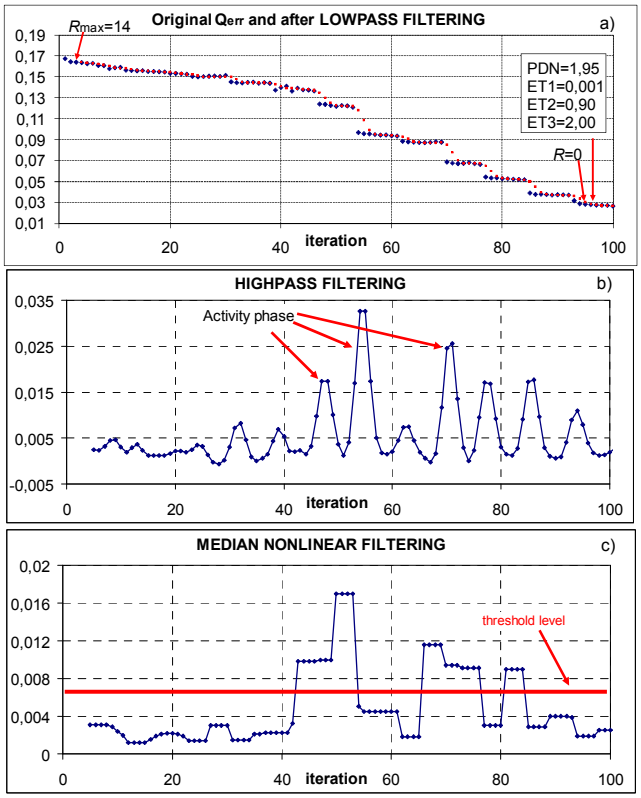

Fig. 4. Proposed 3-stage error filtering for the training process after optimization: a) the original waveform and the lowpass, b) the highpass, c) the nonlinear median filtering for 16x16 SQUARE data file

The proposed algorithm work good with all investigated cases of neighborhood functions and network topologies. It is worth noticing that the proposed algorithm must cooperate with the classic 'linear' method. This is necessary in a situation, in which an 'activity' spike at the output of the median filter would be to small to activate the decision procedure. In this case the 'linear' method will switch over the radius R after I iterations that will stop a given stagnation phase.

3.4. Performance analysis of the proposed solution

Illustrative simulation results in case of the optimized training process are shown in Fig. 4 for an example network with 16x16 neurons for SQUARE data set. In this case the entire training process has been shorten 10 times from initial 1000 iterations to 100 iterations.

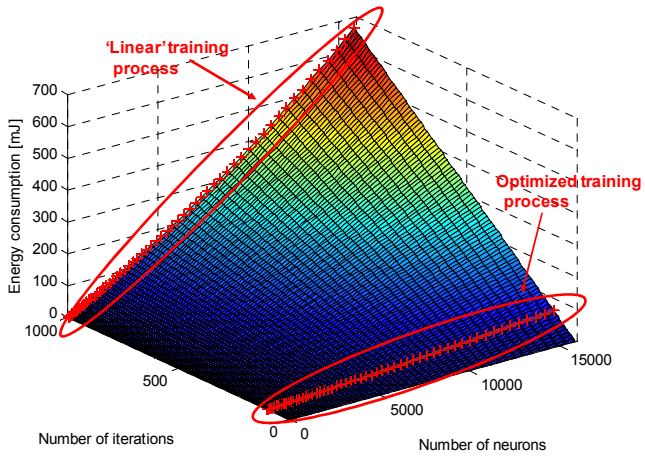

Fig. 5. Estimated energy consumption regarded as a function of the number of neurons and the number of learning iterations

An important parameter is also the energy consumption of a neuron. The simulations of the overall SOM performed in Hspice environment show that a single neuron consumes 25–30 pJ per a single pattern $X(l)$ for the CMOS 0.18µm process (Długosz R. et al., 2011). Fig. 5 shows the estimated energy consumption as a function of the number of neurons and the number of learning iterations for data set comprised of 1000 learning patterns in the worst case scenario, i.e. for the neighborhood range R covering the entire map. In practice, as the values of R are usually small, the energy consumption will be smaller. For an example map with 16x16 neurons the energy consumption is equal to 7.7nJ during presentation of a single input pattern. When the number of iteration is equal 1000 and data set is composed of 1000 patterns, the energy consumption will be equal to 7.7mJ. In case when the overall training process will be shorten 10 times from initial 1000 iterations to 100 iterations the energy consumption wil be equal to 0.77mW. So in case of the optimized training process the energy consumption will be also 10 times smaller. As we can see, one of the main advantages of hardware implemented network is a very low energy consumption. For the comparison, a single software-model test during which the SOM processes 2 million input patterns takes about 20 minutes. Based on the assumption that the power dissipation of a PC computer equals 250W, the energy consumption will equal 300kJ in this case. As a result, the achieved energy consumption in case of hardware implemented neural network is more than eight orders of magnitude smaller than in case of a similar network realized on PC.

Note that these results have been obtained for the CMOS 0.18µm process. For the latest technologies below 65nm, the author expects a substantial improvement of the results.

4. CONCLUSIONS

A new simple learning algorithm for the WTM Kohonen SOM designed for low-power devices has been described in the paper. The proposed technique bases on the observation that the quantization error does not decrease monotonically during the learning process, but there are some activity phases, in which this error decreases very fast and then the stagnation phases, in which the error does not decrease.

The proposed technique using a set of linear and nonlinear filters detects the activity phases and controls the neighborhood *R* in such a way to shorten the stagnation phases. As a result, the learning process may be more than 10 times faster and more than 10 times energy efficient than in the classic approach, in which the radius *R* decreases linearly.

The intended application of the proposed solution will be in Wireless Body Area Networks in the classification and analysis of the EMG and the ECG biomedical signals.

REFERENCES

1. **Beaton D., Valova I., MacLean D.** (2010), CQoCO: A measure for comparative quality of coverage and organization for self-organizing maps, *Neurocomputing*, Vol. 73, 2147–2159.
2. **Bolkowski S., Stabrowski M., Skoczylas J., Sroka J., Sikora J., Wincenciak S.** (1993), *Computer analysis methods of electro-magnetic field*, WNT, Warsaw.
3. **Boniecki P.** (2005), The Kohonen neural network in classification problems solving in agricultural engineering, *Journal of Research and Applications in Agricultural Engineering*, Vol. 50, No. 1, 37-40.
4. **Brocki L.** (2007), *Recent Advances in Mechatronics*, Springer Berlin-Heidelberg.
5. **Chudáček V., Georgoulas G., Lhotská L., Stylios C., Petrík M., Čepek M.** (2009), Examining cross-database global training to evaluate five different methods for ventricular beat classification, *Physiological Measurem,* Vol. 30, No. 7, 661-677.
6. **Długosz R., Kolasa M., Pedrycz W., Szulc M.** (2011), Parallel Programmable Asynchronous Neighborhood Mechanism for Kohonen SOM Implemented in CMOS Technology, *IEEE Transactions on Neural Networks*, Vol. 22, No. 12, 2091-2104.
7. **Fernández E.A., Willshaw P., Perazzo C.A., Presedo R.J., Barro S.** (2001), Detection of abnormality in the electrocardiogram without prior knowledge by using the quantisation error of a self-organising map, tested on the European ischaemia database, *Medical and Biological Engineering and Computing*, Vol. 39, No. 3, 330-337.
8. **Kohonen T.** (2001), *Self-Organizing Maps*, third ed. Springer, Berlin.
9. **Kolasa M., Długosz R., Pedrycz W., Szulc M.** (2012), A programmable triangular neighborhood function for a Kohonen self-organizing map implemented on chip, *Neural Networks* ,Vol. 25, 146-160.
10. **Lagerholm M., Peterson G.** (2000), Clustering ECG complexes using hermite functions and self-organizing maps, *IEEE Transactions on Biomedical Engineering*, Vol. 47, No. 7, 838-848.
11. **Lee J. A., Donckers N., Verleysen M.**, (2001), Recursive learning rules for SOMs, *Workshop on Self-Organizing Maps, ser. Advances in Self-Organising Maps*, Springer Verlag, 67–72.
12. **Lee J., Verleysen M.** (2002), Self-organizing maps with recursive neighborhood adaptation, *Neural Networks*, Vol. 15, No. 8-9, 993–1003.
13. **Leite C.R., Martin D.L., Sizilio G.R., Dos Santos K.E., de Araujo B.G., Valentim R.A., Neto A.D., de Melo J.D., Guerreiro A.M.** (2010), Classification of cardiac arrhythmias using competitive networks, *2010 Annual International Conference of the IEEE Engineering in Medicine and Biology Society*, 1386-1389.
14. **Li F., Chang C.-H., Siek L.** (2009), A compact current mode neuron circuit with Gaussian taper learning capability, *IEEE Int. Symp. Circuits and Systems*, 2129–2132.
15. **Mokriš, Forgáč R.** (2004), Decreasing the Feature Space Dimension by Kohonen Self-Orgaizing Maps, *2nd Slovakian – Hungarian Joint Symposium on Applied Machine Intelligence*, Herľany, Slovakia.
16. **Osowski S., Linh T.H.** (2001), ECG beat recognition using fuzzy hybrid neural network, *IEEE Transactions on Biomedical Engineering*, Vol. 48, No. 11, 1265-1271.
17. **Su M.-C., Chang H.-T., Chou C.-H.** (2002), A novel measure for quantifying the topology preservation of self-organizing feature maps, *Neural Process. Lett.*, Vol. 15, No. 2,137–145.
18. **Talbi M. L., Charef A., Ravier P.** (2010), Arrhythmias classification using the fractal behavior of the power spectrum density of the QRS complex and ANN, *International Conference on High Performance Computing and Simulation*, 399-404.
19. **Tighiouart B., Rubel P., Bedda M.** (2003), Improvement of QRS boundary recognition by means of unsupervised learning, *Computers in Cardiology*, Vol. 30, 49-52.
20. **Uriarte E., Martin F.** (2005), Topology Preservation in SOM, *Int. J. of Math. and Comput. Sci.*, Vol. 1, No. 1, 19–22.
21. **Valenza G., Lanata A., Ferro M., Scilingo E.P.** (2008), Real-time discrimination of multiple cardiac arrhythmias for wearable systems based on neural networks, *Computers in Cardiology*, Vol. 35, 1053-1056.
22. **Wen C., Lin T.-C., Chang K.-C., Huang C.-H.** (2009), Classification of ECG complexes using self-organizing CMAC, *Measurement: Journal of the International Measurement Confederation,* Vol. 42, No. 3, 399-407.

FRETTING WEAR OF MATERIALS – METHODOLOGICAL ASPECTS OF RESEARCH

Ewa KULESZA[*], Jan Ryszard DĄBROWSKI[*], Jarosław SIDUN[*], Antoni NEYMAN[**], Jarosław MIZERA[***]

[*]Faculty of Mechanical Engineering, Chair of Materials and Biomedical Engineering, Bialystok University of Technology,
ul. Wiejska 45 C, 15-351 Bialystok, Poland
[**]Faculty of Mechanical Engineering, Machine Design Department and Maintenance Technology, Gdansk University of Technology,
ul. Narutowicza 11/12, 80-233 Gdansk, Poland
[***]Faculty of Materials Engineering, Division of Materials Design, Warsaw University of Technology,
Pl. Politechniki 1, 00-661 Warszawa, Poland

ewa.kulesza1@gmail.com, j.dabrowski@pb.edu.pl, j.sidun@pb.edu.pl, aneyman@pg.gda.pl, jmizera@inmat.pw.edu.pl

Abstract: In this article, methodical aspects of studies on material fretting wear have been presented. The results of studies conducted on a "pin on disc" type device made at the Department of Materials and Biomedical Engineering of the Bialystok University of Technology confirmed the decisive influence of the amplitude of oscillations and the load value on the course and nature of the process. At a constant value of load, the course of resistance to motion was dependent on the amplitude. Increasing the amplitude of oscillations caused a change in friction conditions: from static friction (elastic deformation of formed adhesive connections, without dislocation of cooperating elements) to kinetic friction (breaking of adhesive bridges and displacement with sliding). The increase of the load value at a constant amplitude value caused a change in the course and nature of resistance to motion from sliding friction to friction at-rest.

Key words: Fretting, Wear, Stainless Steel, Ferrite

1. INTRODUCTION

Fretting is the complex process of destruction of surface layers of cooperating elements having a normal force applied to them as load, moving relative to each other with tangential low-amplitude oscillatory motion. The complexity of fretting wear processes is the result of many interconnected physical and chemical phenomena occurring at points of contact of the cooperating surfaces. Among the many significant factors influencing the intensity and nature of fretting wear, the most important are: load, amplitude, duration, geometry of the contact area, properties of contacting elements (adhesive properties, resistance to corrosion, hardness, tensile strength, yield point, fatigue strength), as well as environmental conditions. There are several definitions of fretting which distinguish the term by specifying the course of the process or its effects. The Glossary of Terms and Definitions in the Field of Friction, Wear, and Lubrication (1969) define fretting as the phenomenon of wear present between two surfaces where there is a relative reciprocating sliding motion of a small amplitude.

The definition of fretting proposed by professor M. Hebda is as follows:

„(…) Fretting is a type of wear occurring during slight (on the order of a fraction of a mm) mutual movement of bodies that are in contact with each other. In its broad sense, the word fretting denotes the group of mechanical, thermal, chemical, and electric phenomena taking place at the places of contact of bodies that are moving slightly relative to each other with rotational or reciprocating motion as a result of vibrations, load pulsation, etc. Thus, this is wear occurring at places that are "nominally" immobile connections. (…)" (Hebda and Wachal, 1980).

The terms fretting and fretting corrosion were used for the first time in 1927 by G.A. Tomlinson (Tomlinson, 1927) in order to specify characteristic damage to steel surfaces.

According to other definitions, fretting is also considered to be a special type of friction occurring under conditions of movement on the micro scale (Smith, 1998). Thus, it is justified to distinguish subordinate terms relative to fretting that are used in the literature. These are: fretting wear, fretting corrosion, fretting fatigue. Fretting wear is the change in mass or volume of the surface layer as a result of a process. Destruction that is mostly caused by the process of oxidation of the surface layer is called fretting corrosion. However, in the case of fretting on the surfaces of elements with applied variable loads, the influence of fretting is decisive for fatigue strength – fretting fatigue (Neyman, 2003).

Destruction of material surface layers through fretting takes place, e.g.: in close-fitted elements (e.g. axles of vehicle axle sets (Guzowski, 2003)); in joints that are screwed, keyed, riveted, or pinned; in non-operating rolling bearings, gear wheels; on the surfaces of electrical contacts in airplane elements, and also in biomedical implants (Guzowski, 2003; Hannel et al. 2001; Hoppner et al. 1994; Neale, 1995; Shanshan, 2010; Tristani et al., 2001; Waterhouse, 1972; Wierzcholski et al. 1999; Young et al. 2010).

1.1. Devices for fretting studies

Four basic systems can be distinguished among the devices for fretting studies:

- a fastening system for studied samples;
- a system for inducing relative oscillatory motion of samples;
- a system for applying load;
- a system for measuring displacements and resistance to motion (Neyman, 1993).

A basic property of the testing station is the type of sample contact. Focused contact is used most often: cylinder – cylinder, sphere – plane, cylinder - plane (Fig. 1 a, b, d). Such a type of contact facilitates identification and measurement of wear due to the existence of a single, central area of wear. In the case of distributed contact, e.g. two flat elements (Fig. 1 c), the wear areas are located at random on the nominal contact surface. This creates significant difficulties during wear measurement. Furthermore, the power of the device must be greater due to the much higher load necessary for creating the appropriately high contact stresses. Ensuring correct contact of cooperating surfaces is a significant problem in these types of stations.

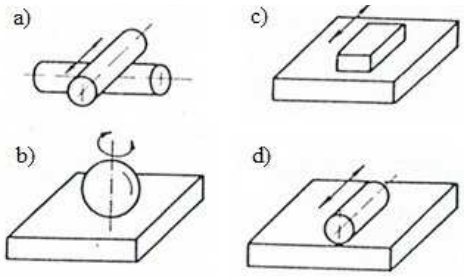

Fig. 1. Configurations of samples most often used in testing stations: a) cylinder - cylinder, b) sphere – flat element, c) flat element – flat element, d) cylinder – flat element (Neyman, 1993)

In testing stations, oscillatory motion can be induced by devices of the following types:

- Mechanical;
- Electromagnetic;
- Piezoelectric;
- hydraulic.

Each of these types of devices is characterized by specific pros as well as cons in terms of their fulfillment of the requirements of conducted tests.

The advantages of mechanical devices, usually operating on the principle of eccentricity, are: easy regulation of oscillation frequency and a constant value of the amplitude of oscillations. A disadvantage is the necessity of replacing the circular cam upon changing the amplitude of oscillations.

Electromagnetic devices ensure achievement of high frequencies and easy regulation of frequency and amplitude. The limitations in achievable values of frequency and amplitude are due to the lower power of these types of devices in comparison with mechanical devices.

Piezoelectric devices are characterized by easy and precise regulation of frequency and oscillation amplitude but have a significantly limited amplitude value.

The greatest load values can be obtained by using hydraulic devices, however they are decidedly the most expensive.

Analysis of contact conditions in a dependency on load and tangent displacements has been conducted by several authors, including O'Connor J. (1981). In the case of a sphere-sphere or sphere-flat element association, the contact area is a circle with radius a (Fig. 2).

If, during loading of the cooperating pair with normal force *N*, the applied, cyclically variable force *T* is not sufficiently large to cause relative sliding, then the conditions presented on Fig. 2 will be present. The normal force between spheres with a radius of *R* and an applied force of *N*, designated p, reaches its maximum in the center of the circular contact area and decreases to zero on the edge of the contact area. If a tangential force of *T* is applied to one of the spheres, in parallel to the contact surface, unit tangential forces „τ" will be present. Unit tangential forces reach a minimum at the center of the contact area and increase in the direction of the boundary of the contact area, approaching infinity under the assumption that sliding in the macro scale is not present. Everywhere that elementary friction forces "μp" are greater than "τ", local slipping (micro slips) does not occur, however where they are lesser, slipping does take place. Thus, the entire contact area is divided into two sub-areas: without slipping (a circle with a radius of a') and with slipping (a ring with an outside radius of a and an internal radius of a').

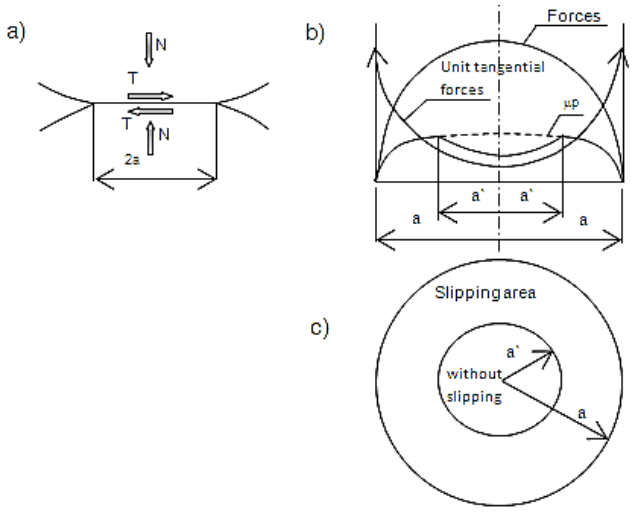

Fig. 2. Conditions of contact for a sphere-sphere association with a lack of full sliding according to (O`Connor, 1981)

Depending on the ratio of radius a' to a, three intervales of contact conditions are distinguished:

- a`/a = 1, a limit instance, contact without slipping (stick regime);
- a`<a, contact with slipping onto parts of the contact area (with micro slips) (partial slip regime);
- a`= 0, a limit instance between contact with slipping onto parts of the contact area and contact with slipping over the entire contact area (gross slip regime).

2. OWN PROPOSITION FOR RESEARCH METHODOLOGY

A prototype device for fretting studies with an eccentric oscillation inducer has been made at the Department of Materials and Biomedical Engineering (Fig. 3, currently in the process of patent application). Samples are applied in the pin on disc configuration, with a flat contact surface.

A series of experiments with various materials used in associations were conducted on this device. The influence of oscillation amplitude on the course of friction and wear processes was studied. Analysis of the obtained results made it possible to confirm the influence of load and amplitude described in the literature on the change in the nature of contact made apparent by a change in the course of friction forces.

The following association was subjected to tests: disc – H18N9T steel, pin – 315 steel. Contact surface *S*=2 mm2. Applied loads had a value of 14 N and the amplitude of oscillations

for instance a) 107 μm (Fig. 4a), and in instance b) 64 μm (Fig. 4b). The results of the courses of friction forces, displacements, and pressure forces after one hour of testing have been presented.

Fig. 3. Prototype of the device with an eccentric oscillation inducer

a)

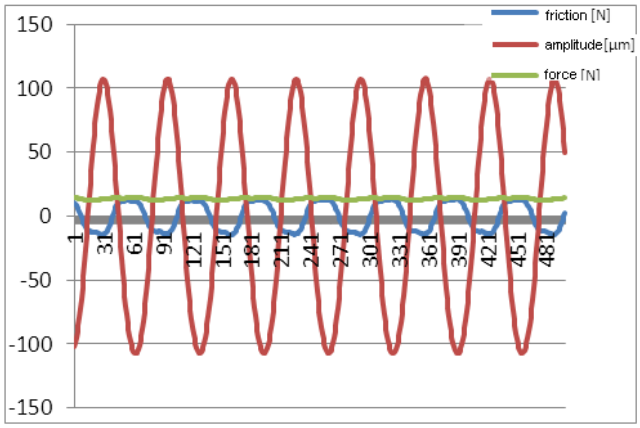

b)

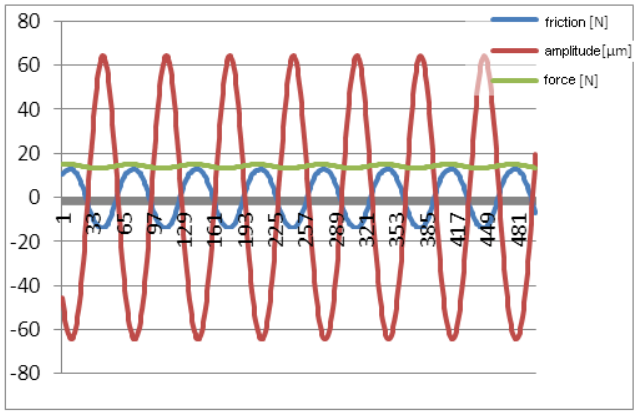

Fig. 4. Charts of the courses of friction forces, displacements, and pressure forces. Pressure force 14 N amplitude, a) 107 μm, b) 64 μm

From the presented photographs (Fig. 5) and on the basis of observations of the nature of the friction forces (Fig. 4), the following conclusions can be made: in the case of a greater amplitude of oscillations, adhesive connections are broken and sliding of contacting surfaces takes place. The material is subject to plastic deformation, and delamination and flaking of fragments of the surface layer occur. On the photograph shown on Fig. 5a, successive stages of surface destruction during fretting are visible: plastic deformation of the material and material delamination, causing detachment of material fragments at places of material discontinuity and creating free wear products. At this time, kinetic friction conditions between contacting surfaces are present, and friction force courses have a trapezoidal nature (Fig. 4a and 5a-b).

a)

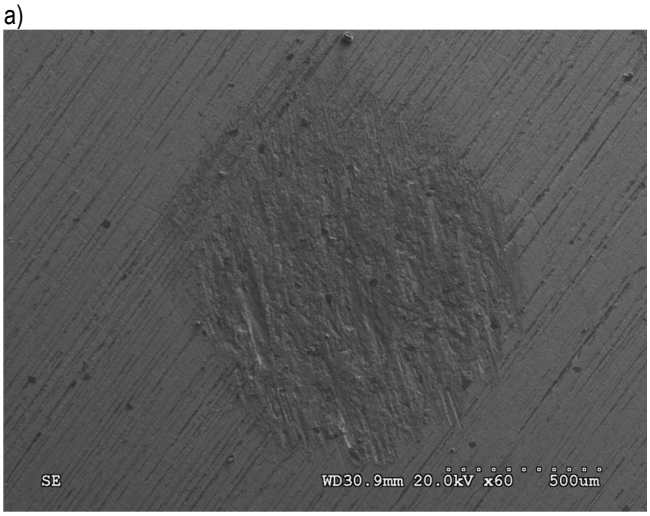

b)

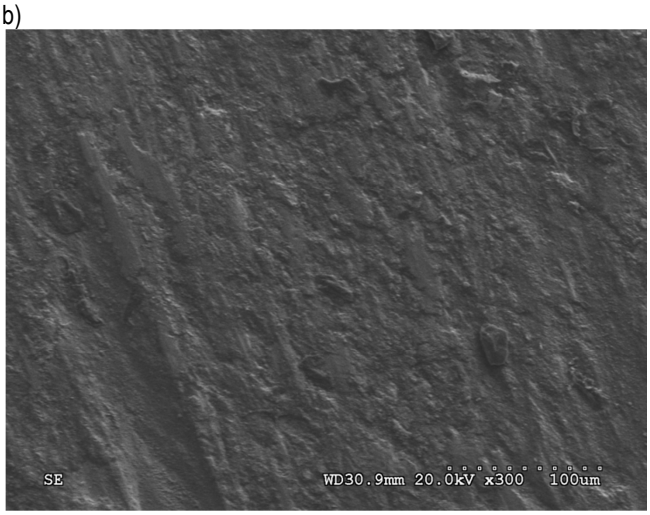

c)

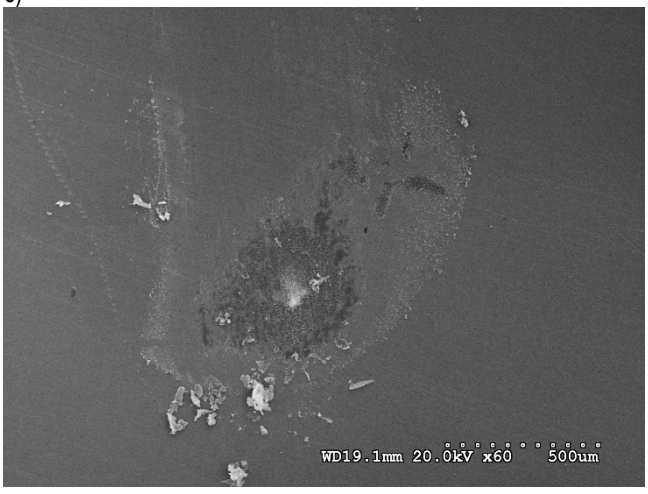

Fig. 5. Photographs from electron microscope. Pressure force 14 N amplitude, a) 107 μm, b) 107 μm, c) 64 μm

However, for smaller amplitude values, adhesive connections and compensations of tangential displacements through elastic deformation of connected peaks of surface irregularities take place. Friction has a static nature and the courses of friction forces have a sinusoidal nature (Fig. 4b).

3. CONCLUSIONS

Analysis of the results of tests confirms the decisive influence of the value of applied load and tangential displacement amplitude on the nature of contact and courses of friction forces. In the pin on disc sample configuration with two flat surfaces, for a constant value of applied load, the value of the amplitude of oscillations was decisive to the nature of friction forces. Increasing the amplitude value caused a change in friction conditions: from static friction (elastic deformation of formed adhesive connections, without dislocation of cooperating elements) to kinetic friction (breaking of adhesive connections and dislocation with sliding).

REFERENCES

1. *Glossary of Terms and Definitions In the Field of Friction, Wear and Lubrication*, (1969) OECD Publications, Paris
2. **Guzowski S.** (2003), *Analiza zużycia frettingowego w połączeniach wciskowych na przykładzie osi zestawów kołowych pojazdów szynowych*, Wydawnictwo PK, Kraków.
3. **Hannel S., Fouvry S., Kapsa Ph., Vincent L.** (2001), The fretting sliding transition as a criterion for electrical contact performance, *Wear*, Vol. 249, 761-770.
4. **Hebda M., Wachał A.** (1980), *Trybologia*, WNT Warszawa.
5. **Hoppner D., Chandrasekoron V.** (1994), Fretting in orthopaedic implants; a review. *Wear*, Vol. 173, 189-197.
6. **Neale M. J.** (1995), *The tribology handbook*, Elsevier, Oxford.
7. **Neyman A**. (1993), Studia nad frettingiem. Wpływ struktury węzła styku na zużycie, *Zeszyt Naukowy Politechniki Gdańskiej, Mechanika* No. 501, Gdańsk.
8. **Neyman A.** (2003), *Fretting w elementach maszyn*, Wydawnictwo PG. Gdańsk.
9. **O`Connor J.J.** (1981), The role of elastic stress analysis in the interpretation of fretting fatigue failures. *In Waterhouse R.B. ed. Fretting Fatigue, London*: Applied Science Publishers.
10. **Shanshan G., Zhenbing C., Huixin Q., Minhao Z., Haiyang Y.** (2010), Comparison between radial fretting and dual-motion fretting features of cortical bone, *Tribology International,* Vol. 43, 440-446.
11. **Smith E.H.** (1998), *Mechanical Engineer's Reference Book*, Elsevier.
12. **Tomlinson G.A.** (1927) The Rusing of steel surfaces *In contact. Proc. Roy. Soc*. No 115A, 427.
13. **Tristani L., Zindine E.M., Boyer L., Klimek G.** (2001), Mechanical modeling of fretting cycles in electrical contacts, *Wear*, Vol. 249, 12-19.
14. **Waterhouse R.B.,** (1972), *Fretting corrosion*, Pergamon Press Ltd., Oxford.
15. **Wierzcholski K., Czajkowski A.A.** (1999), Procesy zużycia biotribologicznego. *Mat. Konferencyjne XXIII Jesiennej Szkoły Tribologicznej, Zielona Góra Lubiatów*, Wrzesień 1999, 247-252.
16. **Young W.P., Hyung G.J., Kang Y.L.** (2010), Effect of intermittent fretting on corrosion behavior in electrical contact, *Wear*, Vol. 268, 353-360.

This work was supported by the National Centre for Research and Development under research project No. N R15 0117 10/NCBR.

THE EFFECTS OF TEMPERATURE ON THE STRENGTH PROPERTIES OF ALUMINIUM ALLOY 2024-T3

Adam LIPSKI*, Stanisław MROZIŃSKI*

*Department Laboratory for Research on Materials and Structures, Department of Mechanics and Mechanical Design
Faculty of Mechanical Engineering, University of Technology and Life Sciences in Bydgoszcz
Al. Prof. Sylwestra Kaliskiego 7, 85-789 Bydgoszcz, Poland

adam.lipski@utp.edu.pl, stanislaw.mrozinski@utp.edu.pl

Abstract: This paper presents results of monotonous tensile tests of 0.16" thick samples made of non-clad plates of aluminium alloy for aircraft purposes 2024-T3. Tests were performed for samples cut out from a sheet plate in two different directions: in the parallel and perpendicular direction to sheet plate rolling direction, for eight different temperature values from the range 25°C – 200°C. The tests were performed using the hydraulic-drive testing machine INSTRON 8502 equipped with thermal chamber. The analysis of results included changes of basic strength-related parameters depending on temperature. It was also observed that the intensity of Portevin-Le Châtelier (PLC) effect depends on the temperature.

Key words: Aluminium Alloy 2024-T3, Monotonous Tensile Tests, Elevated Temperature, Portevin-Le Châtelier Effect

1. INTRODUCTION

Aircraft structures are particularly sensitive to damage, which may significantly reduce flight safety and, as a consequence, increase probability of a catastrophe posing danger to passenger's and crew's life as well as possible significant material losses. Thus, in that case, it is very important to have the broadest possible knowledge on materials used in such structures, particularly on their strength properties.

Typical materials used for plating of plane and helicopter fuselage, tensioned wing parts, ribs subject to shear as well as any area where appropriate rigidity, high static and fatigue strength is required include aluminium alloy 2024-T3. That alloy may also be used in the area of engines, where high operating temperature occurs – which amounts up to 120°C in case of 2024-T3 alloy – (acc. to ALCOA Alloy 2024 TechSheet). Basic strength properties are determined using tensile test at elevated temperature in accordance with the standard PN EN 10002-5:2002 or ASTM E 21-05.

The aim of this paper is to determine effects of temperature on basic strength properties of aluminium alloy 2024-T3. Due to that aim, authors of this paper presented results of monotonous tensile tests of 0.16" thick standard samples made of non-clad plates of aluminium alloy 2024-T3. The tests were performed for eight different temperatures ranging from 25°C up to 200°C with the step of 25°C. Tests were performed for samples cut out from a sheet plate in two different directions: in the parallel and perpendicular direction to sheet plate rolling direction.

2. TEST STATION

The tests were performed in the Department Laboratory for Research on Materials and Structures (certified by the Polish Centre for Accreditation – PCA AB 372) of the Faculty of Mechanical Engineering at the University of Technology and Life Sciences in Bydgoszcz, using the testing machine INSTRON 8502 (with the following parameters: maximum static force – 300 kN, maximum dynamic force – 250 kN, piston stroke: ±75 mm) fitted with the control system 8500+, and equipped with the heating chamber (Fig. 1).

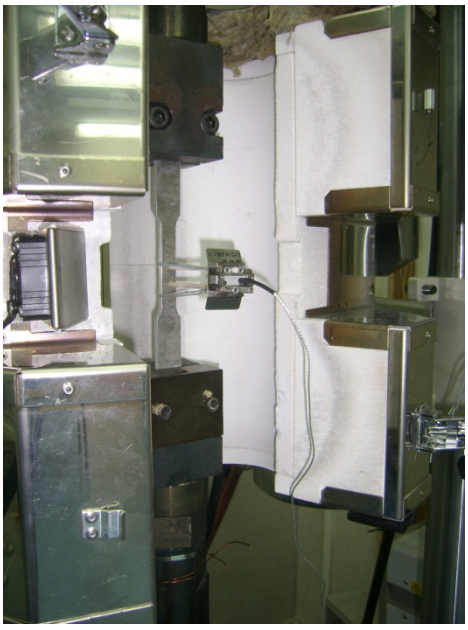

Fig. 1. The test sample and the extensometer installed inside the heating chamber (opened in the presented photo) of the Instron 8502 system

3. THE MATERIAL AND TEST CONDITIONS

Tests were performed using non-clad plates made of aluminium alloy 2024-T3 (AlCu4Mg1 – supersaturated, cold deformed

and naturally aged up to stable condition) in accordance to the American standard AMS-QQ-A-250/4.

The tests were performed in compliance with guidelines of Urząd Lotnictwa Cywilnego (Civil Aviation Office) based on the standard MIL-HDBK-5H (1998) as well as relevant ASTM standards referred to there. Monotonous properties of the alloy 2024-T3 in elevated temperatures were determined in accordance with the standard ASTM E 21-05 (2005).

Design features of the samples are shown in Fig. 2. Samples were cut from plate sheets in two perpendicular directions using *Water Jet* technology:

- parallel to the plate sheet rolling direction;
- perpendicular to the plate sheet rolling direction.

The analysed part of samples was subject to finishing in order to obtain required surface roughness.

Tests were performed at the temperature of 25°C, 50°C, 75°C, 100°C, 125°C, 150°C, 175°C and 200°C. The temperature was measured directly on samples which were heated until their temperature stabilized at the required level. The temperature was maintained at that level for at least 10 minutes before the test start.

During tests, samples were subject to uniaxial monotonously increasing tension up to their damage. During tests, the load force and the displacement of the test machine handle, together with the sample deformation, were recorded using high temperature extensometer with measurement base of 12.5 mm and the measuring range -1.25÷+2.5 mm. The tests were performed with displacement rate of 0,05 mm/s in order to achieve constant sample deformation rate.

4. TEST RESULTS

Selected tension charts obtained from the tests in the direction parallel to the plate rolling direction were provided in Fig. 3a, while for tests in the direction perpendicular to the plate rolling direction - in Fig. 3b.

Based on charts presented in Fig. 3, the authors determined average values of strength parameters:

- elastic (Young's) modulus E;
- yield point R_{eL} or yield strength at non-proportional increment $R_{p0,2}$;
- tensile strength R_m;
- ultimate elongation A_t.

The determined parameters were presented in Tab. 1.

5. ANALYSIS OF TEST RESULTS

5.1. Effects of temperature on strength properties

Based on the obtained results, one can conclude that the tested plate is characterized by significant differences of strength properties depending on the rolling direction. Samples taken parallel to plate rolling direction, regardless of the temperature, are characterized by clear yield point and better strength-related properties (apart from the elongation) than samples taken perpendicular to the rolling direction.

Fig. 4 shows schematically the change of strength properties determined based on the monotonous tensile test of the studied plate depending on temperature.

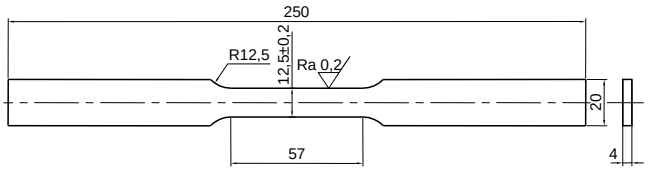

Fig. 2. Sample for monotonous properties tests

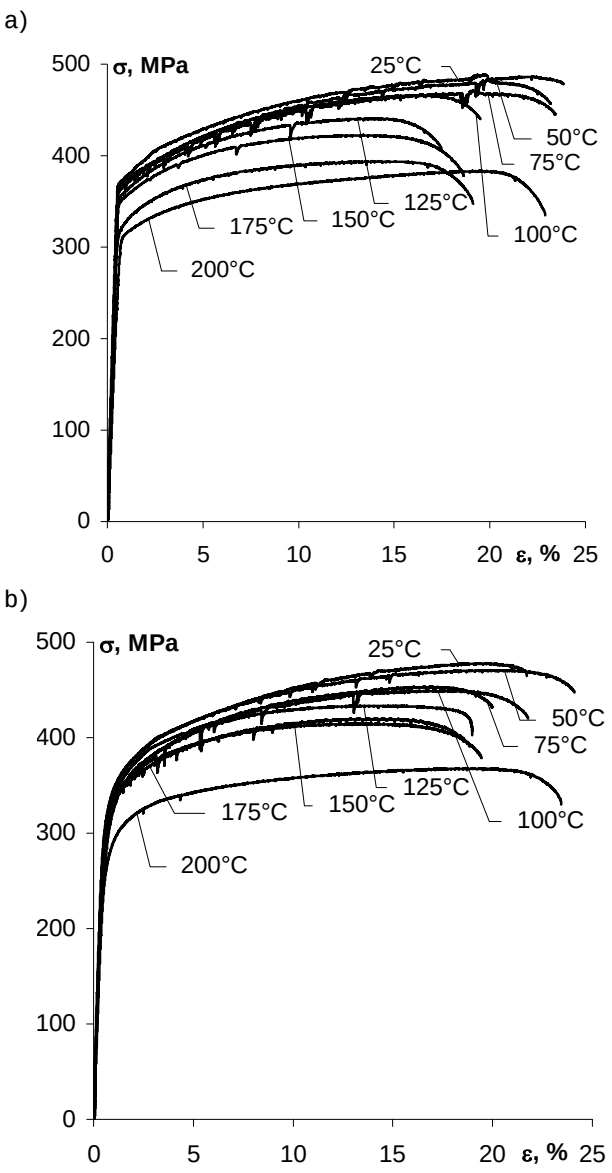

Fig. 3. Charts of monotonous tensile tests of samples made of aluminium alloy 2024-T3 cut parallel (a) to the plate rolling direction and perpendicular (b) to the plate rolling direction for different temperatures

The nature of strength properties change depending on the temperature, presented in Fig. 4, is qualitatively similar for both sampling directions. Either the tensile strength value R_m, as well as yield point R_{eL} (parallel to rolling direction) or the yield strength at non-proportional increment $R_{p0,2}$ (perpendicular to rolling direction) decrease as the temperature rises. The tensile strength in the temperature range from 25°C to 125°C decreases by about 10%, while at the temperature of 200°C it achieves about 75% of R_m value obtained for the temperature 25°C. The decrease is lower for R_{eL} ($R_{p0,2}$), i.e.: at the temperature of 125°C, it drops by about 5%, while at 200°C, by about 15%

as compared to the temperature of 25°C.

Whereas the elastic (Young's) modulus E slightly increases as the temperature rises and achieves the maximum value at about 75°C, and then gradually decreases. For sampling direction parallel to the plate rolling direction, that decrease is significantly higher than for perpendicular direction. At the temperature of 200°C, the modulus drops to about 2/3 of its value at the temperature of 25°C in the former case, and to about 85% in the latter case.

It should be noted that R_m, R_{eL}, $R_{p0,2}$ and E charts presented in Fig. 4 are highly correlated with the results of the experiments. As regards the elongation A_t, charts presented in Fig. 4 show only qualitative nature of the change of its value depending on the temperature. The elongation slightly decreases as the temperature rises and its achieves the minimum value for 125-150°C, and then gradually rises.

Based on presented research results, one can conclude that main strength properties of the plate made of the alloy 2024-T3 may drop by up to 10% for the operating temperature range recommended by the manufacturer (max. 120°C).

5.2. The Portevin - Le Châtelier effect

The analysis of charts obtained from the research (Fig. 5) shows abrupt stress change during tensile test, which is characteristic for the Portevine-Le Châtelier effect (so called PLC effect).

For better image of those changes, Fig. 5 shows selected tension charts for samples cut parallel to the plate rolling direction tested at different temperatures. Those charts were limited only to the range where significant plastic strain occurs. Fig. 6 shows analogous charts obtained for samples cut perpendicular to the plate rolling direction.

Tab. 1. Strength properties determined based on monotonous tensile tests of 0,16" thick samples made of non-clad plates of aluminium alloy 2024−T3

Direction	Temperature	E	R_{eL}	$R_{p0.2}$	R_m	A_t
	°C	MPa				%
Parallel to the plate rolling direction	25	68 563	367.5	-	488.8	23.9
	50	66 879	367.5	-	483.0	23.2
	75	70 403	361.8	-	471.1	23.4
	100	65 564	360.3	-	466.2	18.4
	125	62 863	354.0	-	440.7	16.5
	150	62 082	348.3	-	422.5	17.7
	175	66 814	318.2	-	394.2	19.1
	200	46 624	312.9	-	383.2	22.2
Perpendicular to the plate rolling direction	25	64 456	-	323.6	478.0	21.7
	50	65 674	-	320.4	470.9	24.1
	75	72 926	-	314.4	453.3	20.0
	100	65 965	-	307.4	449.3	21.8
	125	64 721	-	279.8	433.6	21.1
	150	60 858	-	305.7	414.9	19.4
	175	66 886	-	306.7	420.2	18.8
	200	53 675	-	270.0	367.7	23.4

The Portevin-Le Châtelier effect is characteristic, among others, for non-ferrous metal alloys (e.g. brass and aluminium alloys) as well as for iron at elevated temperatures. It manifests on the tensile chart with multiple repeating jumps which result from the fact that atoms of impurities are intercepted by moving dislocations, which are immobilized and then abruptly released. Stopping dislocation movement results in stress increase, while release of dislocation in stress reduction. As a result, dislocation movement speed changes between extreme values. At low speed, the strain progress caused by stress increase is slow and once it achieves sufficient value for dislocation release, the fast plastic flow phase starts, causing stress decrease. Released dislocations intercept atoms of impurities on their way again, which results in dislocation slowing down and that cycle repeats again (Przybyłowicz (1999, 2002)). It should be noted that PLC effect occurs only within a certain limited strain speed range. If the strain rate is sufficiently high, the flow stress is always higher than the dislocation release stress and, as a result, the abrupt strain change is unnoticeable (Courtney (2000)).

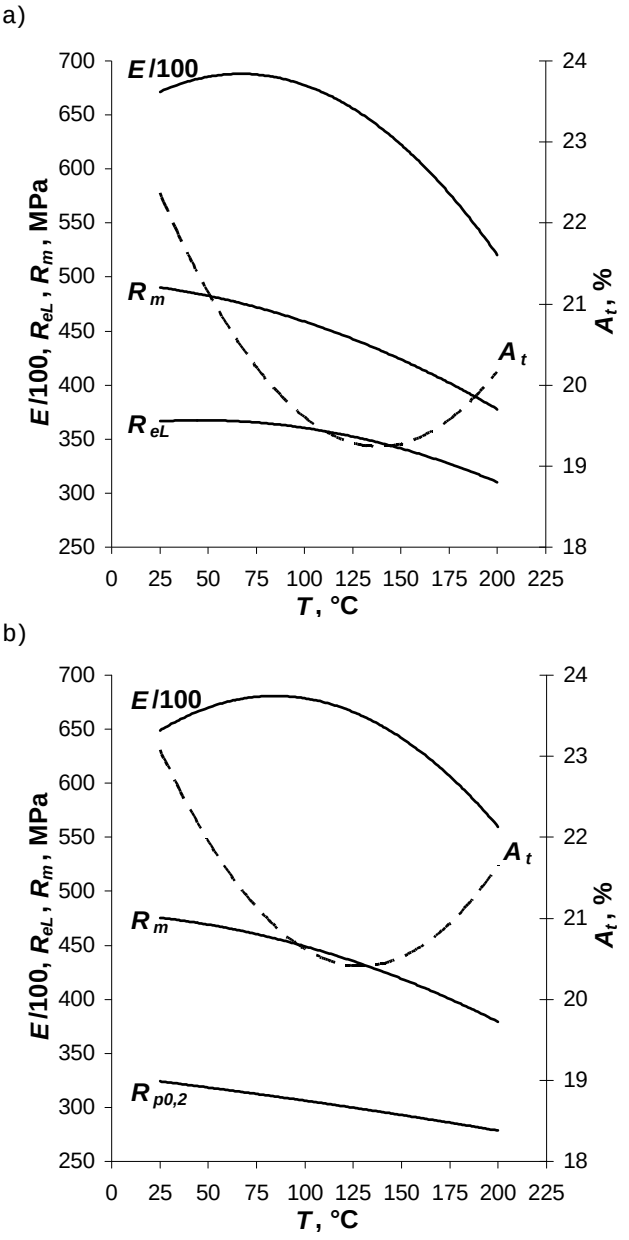

Fig. 4. Changes of strength properties determined based on monotonous tensile tests of samples made of aluminium alloy 2024-T3 cut parallel (a) to the plate rolling direction and perpendicular (b) to the plate rolling direction, depending on the test temperature

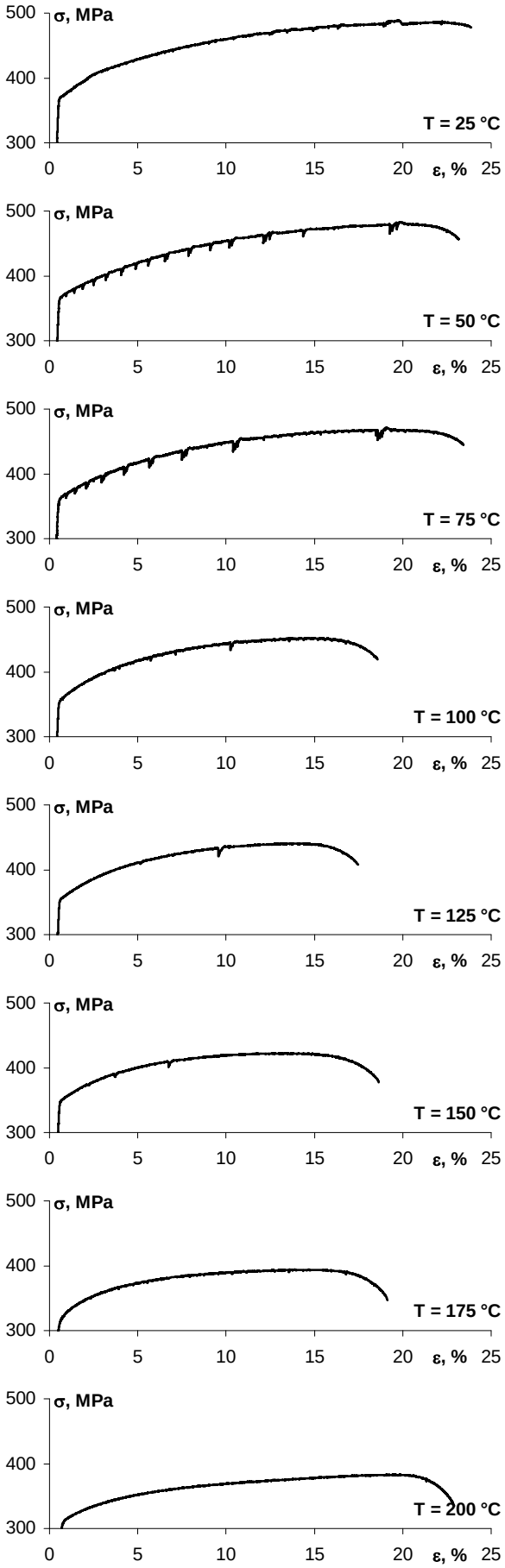

Fig. 5. Tensile tests charts for samples made of aluminium alloy 2024-T3 cut parallel to the plate rolling direction for different temperature values

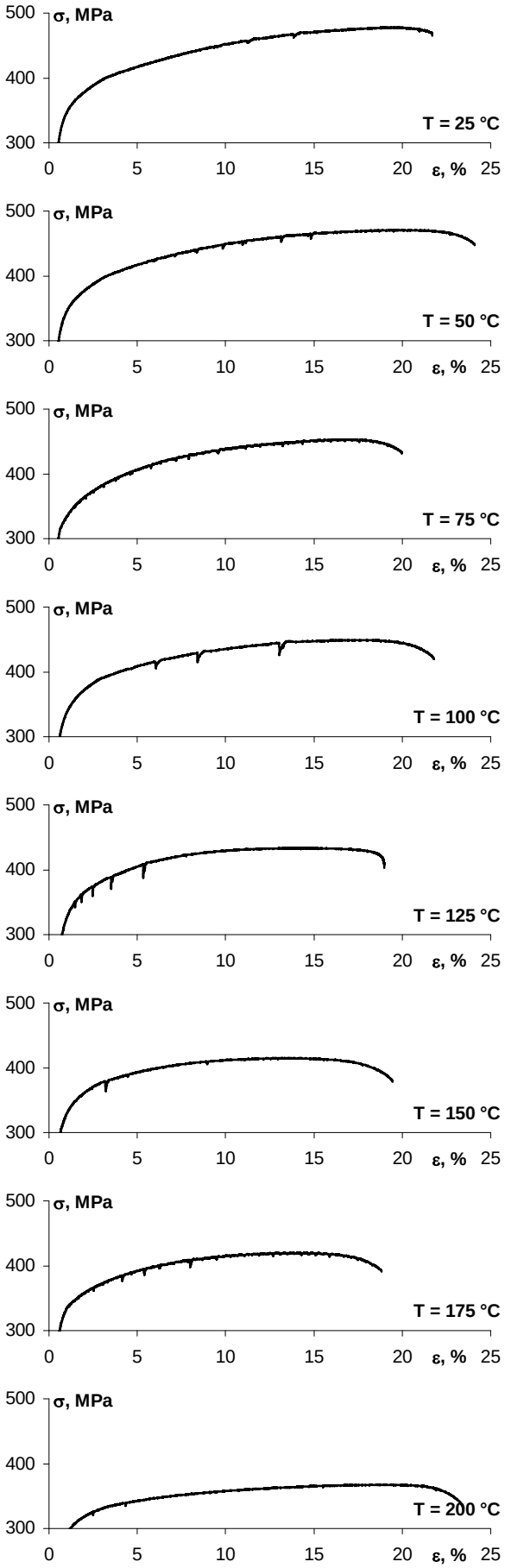

Fig. 6. Tensile tests charts for samples made of aluminium alloy 2024-T3 cut perpendicular to the plate rolling direction for different temperature values

There are also more mechanisms of PLC effect presented in professional literature, other than the aforementioned one. Other descriptions of the effect can be found, e.g. in the papers by Courtney (2000), Bharathi et al. (2003), by Huifeng et al. (2007) and by Ho (2000) and Klose (2004).

In case of the discussed tests results obtained for samples made of aluminium alloy 2024-T3, one can notice, that PLC effect is more intense for samples cut parallel to the plate rolling direction (Fig. 5). The amplitude and frequency of those noticeable stress jumps are higher than in case of samples cut perpendicular to the rolling direction (Fig. 6).

PLC effect was noticeable even at such low temperature as 25°C. Stress fluctuations were most intense within the temperature range from 50 to 75°C. In case of samples cut parallel to rolling direction, those fluctuations gradually fade out as the temperature rises and they are virtually unnoticeable at the temperature of 200°C. While for samples cut perpendicular to the rolling direction, stress jumps become less intense as the temperature rises, however their value increases.

6. SUMMARY

Plates made of aluminium alloy 2024-T3, which is the successor of duralumin, belong to the group of materials widely used in aircraft industry. Due to their functional properties, they may operate in elevated temperatures up to 120°C.

The research results presented in this paper indicate to orthotropic strength properties of the plate associated with the plate rolling direction and to gradual reduction of mechanical properties for the temperature increase from 25°C to 125°C.

The PLC effect occurring at the conditions of the performed tensile tests, depends on the temperature and the direction of sampling with respect to the plate rolling direction. The effect occurs even at such low temperature as 25°C, and is most intense in the temperature range 50-75°C, and then it gradually decreases as the temperature rises. The PLC effect is more distinct is case of sampling parallel to the plate sheet rolling direction.

REFERENCES

1. **ALCOA**, Alloy 2024. Sheet and Plate, *ALCOA TechSheet*, ALCOA Mill Production, Inc.
2. **ASTM E 21 – 05 (2005)**, Standard Test Methods for Elevated Temperature Tension Tests of Metallic Materials, *ASTM International*.
3. **Bharathi M.S., Rajesh S., Ananthakrishna G.** (2003), A dynamical model for the Portevin–Le Chatelier bands, *Scripta Materialia*, Vol. 48,1355–1360.
4. **Courtney T.H.** (2000), *Mechanical Behavior of Materials*, McGraw-Hill International Editions.
5. **Ho K., Krempl E.** (2000), Modeling of Positive, Negative and Zero Rate Sensitivity by Using the Viscoplasticity Theory Based on Overstress (VBO), *Mechanics of Time-Dependent Materials*, Vol. 4, 21–42.
6. **Huifeng J., Qingchuan Z., Xuedong Ch., Zhongjia Ch., Zhenyu J., Xiaoping W., Jinghong F.** (2007), Three types of Portevin–Le Chatelier effects: Experiment and modeling, *Acta Materialia*, Vol. 55, 2219–2228.
7. **Klose F.B.** (2004), Experimental and numerical studies on the Portevin-LeChâtelier effect in Cu-Al and Al-Mg in strain and stress controlled tensile tests, *Dissertation*, Technischen Uniwersität Carolo-Wilhelmina, Braunschweig.
8. *MIL-HDBK-5H* (1998), Military Handbook: Metallic Materials and Elements for Aerospace Vehicle Structures, *Department of Defense*, USA.
9. **PN-EN 10002-5:2002** (2002), *Metallic materials. Tensile testing. Method of test at elevated temperature*, Polish Committee for Standardization (in Polish).
10. **Przybyłowicz K.** (1999), *Theoretical basics of physical metallurgy,* Wydawnictwa Naukowo-Techniczne, Warszawa (in Polish).
11. **Przybyłowicz K.** (2002), *The structural aspects of the deformation of metallic materials*, Wydawnictwa Naukowo-Techniczne, Warszawa (in Polish).

The scientific research was supported by the scientific funds for the years 2011-2013, identified as the research project no. 1215/B/T02/2011/40.

MODERNISATION OF TESTING MODULES AND PROCEDURES IN AN AUTOMATED ASSEMBLY LINE

Bartłomiej MACIEJEWSKI*, Jan ŻUREK*

*Faculty of Mechanical Engineering and Management, Poznan University of Technology,
Pl. M. Skłodowskiej-Curie 5, 60-965 Poznań, Poland

bartek.maciejewski@gmail.com , jan.zurek@put.poznan.pl

Abstract: This dissertation discusses the issue of modernisation of testing modules and procedures in an automated assembly line adapted to manufacture medical pressure transducers in Aesculap Chifa company. The manufactured transducer is used for invasive measurement of patient's physiological pressure, and, therefore, must not pose any threat either to patient's health or life. This is the reason why the operation of the assembly line has been identified, testing modules and procedures have been evaluated and the construction modifications have been suggested. During the research, the influence of suggested construction modifications, enhanced with procedure changes, has been verified.The suggested adjustments have enabled, as required, to improve the operation of automated assembly line adapted to manufacture medical pressure transducers.

Key words: Modernisation, Assembly Line, Medical Pressure Transducer

1. INTRODUCTION

Nowadays, "modern semiconductor sensors, the so-called silicon pressure sensors" (Tietze and Schenk, 2009) are used to measure the pressure. They can be divided into two main groups: piezoresistive sensors and capacitive sensors.

Piezoresistive pressure sensors register membrane deflection triggered by pressure. A tensometric bridge is placed on the membrane. Depending on the accuracy needed, piezoresistors can be arranged in a quarter-bridge, half-bridge or full-bridge circuit (full-bridge circuit guarantees highest accuracy). The pressure applied to the membrane strains and presses the piezoresistors. Then, in accordance with the piezoelectric effect, they change their resistance (piezoresistors deflected in the same direction are located at the opposite legs of the bridge).

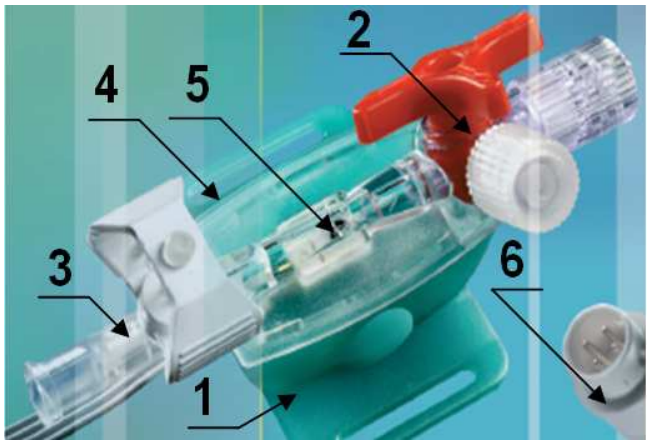

Fig. 1. Combitrans transducer 3 (Maciejewski, 2012)

Piezoresistors fitted in the silicon base which constitutes the membrane are used for the measurements where a great sensor sensitivity is necessary. Sensors produced in such a way are cheaper than those manufactured by means of the "evaporation of the constantan or platinum and iridium layer" technique (Tietze and Schenk, 2009). They are also above ten times more sensitive but they have a higher temperature coefficient.

Combitrans 3 transducer illustrated in Fig. 1 is made up of a lower housing (1), a stopcock (2), a flush device (3), but most of all of a piezoelectric pressure sensor (MPX2300DT1)-(5) fitted in the upper housing (4). The way of combining the elements complies with the ISO 594/1-1986 (E) norm. We differentiate between two types of Lauer-Lock (LL) connection fittings: male and female ones. Sensor pins are soldered to the cable with a plug (6) at its end.

MPX2300DT1 series pressure sensor produced by Motorola company is a miniature integrated circuit plated with a thermoplastic polymer material – a white polysulfone used for medical purposes. A non-toxic, non-allergic, dielectric silicon gel covers the piezoresistive element. Thanks to the gel's distinctive characteristics the separating membrane which is generated does not attenuate stress. It also prevents the piezoresistor and its elements from corrosion in the Ringer's solution chemical environment. Furthermore, the characteristics of silicon guarantee such a level of electrical insulation that both the operation and the lifespan of the sensor are not threatened even in the event of a patient's defibrillation. The sensor has been also equipped with a temperature compensating circuit.

A manufactured transducer is connected to patient circuits and, hence, it must not be either life- or health-threatening. The elements of the machine which are not separated from it during the production have to be made of the materials which do not react with its component parts.

AB08024 machine (Fig. 2) was designed with a view to automated assembly and Combitrans 3 testing. It is made up of three, properly robotised, production units (Żurek et al., 2011). The role of the first one is to link the upper housing to the stopcock and the flush device. The second one is supposed to solder the pressure sensor with the cable and to assess the quality of the connection formed. Production units 1 and 2 which work together with the

main transport unit fit the sensor into the upper housing. The assembly of the lower housing and the transducer testing is done by the third production unit.

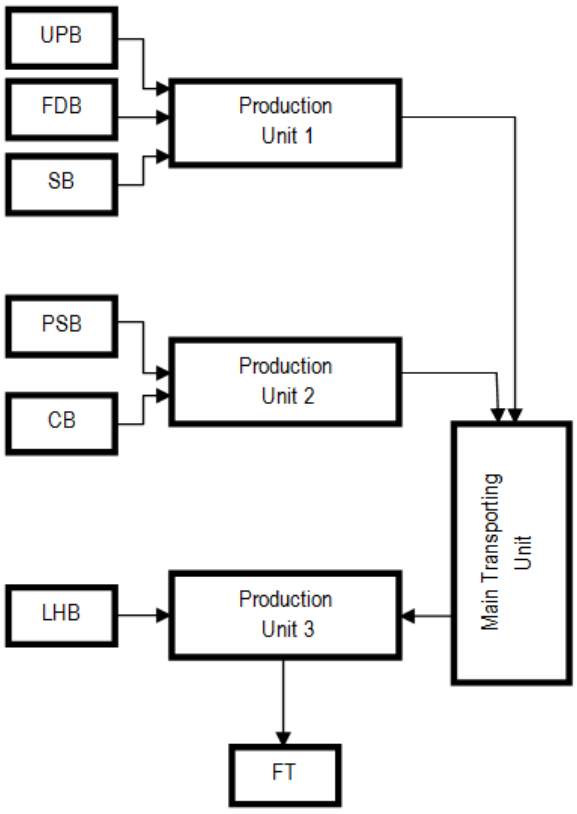

Fig. 2. Flow chart of the AB08024 machine: UPB – upper housing batcher, FDB – flush device batcher, SB – stopcock batcher, PSB – pressure sensor batcher, CB – cable batcher, LHB – lower housing batcher, FT – finished transducer (Maciejewski, 2012)

Automated line to produce the AB08024 machine is equipped with two testing modules. The first one makes it possible to control the quality of the connection between the sensor and the cable to which it has been soldered. The second one measures the quality of the assembly of component parts and the features of the transducer (tightness, flush device flow rate). Based on the procedures agreed upon in the company, a sensor soldered to the cable (or a transducer) is rejected or accepted and delivered to further assembly.

The first module is an electrical tester pulled by a pneumatic actuator to the cable plug. The quality of the cable plug-electrical tester socket connection has a bearing on the voltage values which can be read on pins 2 and 3 of the sensor. Due to problems with access to electrical connection as many as 50 component parts out of the 100 properly assembled ones were classified as faulty.

The testing module 2 consists of the electrical tester, transducer's sealing mandrel, the engine which makes it possible to change the position of the stopcock and the station pumping the air into the transducer. Sealing mandrel and electrical tester change their positions using the pneumatic actuators.

Acceptance or rejection of a transducer being assembled is governed by a multistage testing procedure for module 2 (Fig. 3).

The operation of the automated assembly line has manifested that there are difficulties tightening the Combitrans 3 transducer during the filling, stability and tightness tests. Plastic deformations of the element responsible for closing the tip of the flush device were reported. Similarly to module 1, the quality of the cable plug-electrical tester socket connection made it impossible for the machine to operate properly. Lower voltage values visible on pins 2 and 3 decreased the value of the actual pressure in the transducer. As a result, transducers were classified as faulty (around 23% of production volume). Those transducers which were accepted during the filling test were rejected during the tightness test. In the end, every manufactured transducer was rejected, despite the product assembly sequence being correct (Bourne et al., 2011; Martinez et al., 2009; Suszyński et al., 2009).

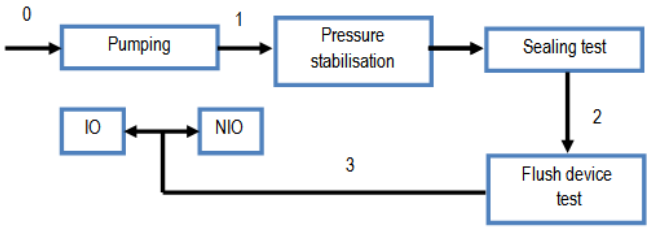

Fig. 3. Flow chart of testing procedure for module 2; 0 – placing the transducer; pulling the station pumping the air, sealing mandrel, electrical tester; solenoid valve opening; 1 – closing the stopcock; solenoid valve closing; 2 – pulling the sealing mandrel back; 3 – lower housing assembly; opening the stopcock; rejection (NIO) or acceptance of the transducer (IO) (Maciejewski, 2012)

The aim of the modern automated assembly line is that out of 100 properly manufactured transducers only one sensor-cable link (module 1) and 5 finished transducers (module 2) could be classified as faulty.

2. THE ASSESMENT OF TESTING MODULES AND PROCEDURES

The advantage of the construction of testing module 1 is that it is possible within a short period of time to get electrical connection between the plug pins and the electrical tester socket, whereas the quality of this connection constitutes its drawback. It stems from the differences in the conductivity of materials used to produce the transducer. Nickel, which forms the upper layer of the pins has a low value of electrical conductivity – 14.3×10^6 S/m, silver, material used to produce the tester socket – $61.39\text{x}10^6$ S/m, whereas copper – $58.0\text{x}10^6$ S/m (Collective work, Industrial Metrology Laboratory, 2002).

Quality control of the connection being soldered is exercised by measuring voltage values on individual pins. If these values exceed tolerance range, the sensor with the cable will be classified as faulty. Tab. 1 presents the required voltage values (amplified sound) when the sensor is supplied with alternating voltage of the value of 6 V.

Tab. 1. Testing procedure parameters – module 1 (Maciejewski, 2012)

Pin no.	Voltage value [V]	Voltage value tolerance [V]
2	2.98	+/- 0.02
3	2.98	+/- 0.02

The control procedure of solder quality is properly exercised if it leads to a good electrical connection between the cable pins and the electrical tester socket. Otherwise, suitable component parts are classified as faulty and rejected automatically.

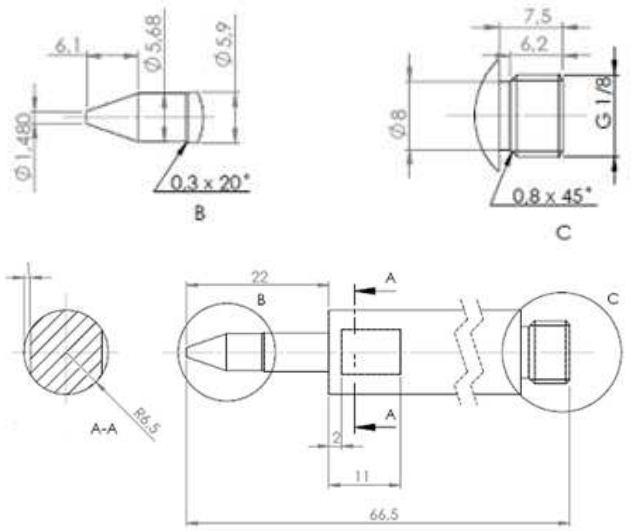

Fig. 4. Sealing mandrel construction 1 (Maciejewski, 2012)

Fig. 4 presents a conical element with the flare angle of α = 40°, responsible for tightening the transducer during the test. The manufacturer of the assembly line did not take into account the flare angle of the cone for the male LauerLock connection fitting of the approximate value of 3.44°. As a result, the connection between the flush device and the cone was not on its surface but around the mandrel's periphery. This resulted in undesirable plastic stress (Connolly, 2009).

The transducer is filled with air to a required pressure value by means of an EVT307-5DO-01F-Q solenoid valve, which works in the open-loop mode. When the transducer is not being filled with air, voltage is supplied to the coil. Current flow increases the temperature of the solenoid valve, the elements to which it is connected and the air in the solenoid valve. The values of the temperature of the elements of module 2 were 46°C, 27°C, 21°C for the solenoid vale, the station filling the transducer with air and the sealing mandrel, respectively.

In the circuit in question the air warmed by the solenoid valve is pumped into the transducer, where it cools down. The relationship between the temperature, pressure, and ideal gas volume is perfectly explained in the Clapeyron equation.

Having assumed that the individual gas content does not change and having transformed the Clapeyron equation we got (1) and (2):

$$\frac{p}{T} = \frac{mR}{V} = const \quad (1)$$

$$\frac{p_1}{T_1} = \frac{p_2}{T_2} = const \quad (2)$$

Equation (2) means that the relationship between pressure and the temperature of the air before and after pumping is constant. Hence, the air cooling down in Combitrans 3 transducer has an influence on its tightness test result.

Testing procedure for module 2 was presented on the flow chart (Fig. 2). It includes: filling test, pressure stability test, tightness test and flush device test. Parameters for separate tests were given in Tab. 2.

It should be noticed that the testing time plays a vital role, influencing the average production cycle time. Particular attention should be paid to the pressure stabilisation time, which needs to be prolonged due to the pumped air being of higher temperature than the transducer's one. This increased labour consumption makes new solutions necessary to be found for economical reasons (Chen et al., 2012; Żurek at al., 2010, 2012).

Tab. 2. Testing procedure parameters – module 2 (Maciejewski, 2012)

Stage no.		
1	Filling time [ms]	800
	PA3027 sensor max/min pressure after filling [mmHg]	330.00
		260.00
	MPX2300DT1 sensor pressure tolerance in comparison to PA3027 sensor pressure [mmHg]	12.00
		12.00
2	Stabilisation time [ms]	1.200
	MPX2300DT1 sensor max/min pressure difference, with reference to the previous stage [mmHg]	25.00
		-10.00
3	Sealing test time [ms]	1.000
	MPX2300DT1 sensor max/min pressure difference, with reference to the previous stage [mmHg]	0.25
		-2.50
4	Flush device testing time [ms]	800
	MPX2300DT1 sensor max/min pressure difference, with reference to the previous stage [mmHg]	140.00
		90.00
Testing procedure duration time [ms]		3.800

In the case of the sealing test, time, as well as minimum and maximum values of the transducer's pressure difference at the end of the sealing test and stabilisation can be modified. The pressure values should be observed during the production process, in order for the difference tolerance to be changed. Similarly to the previous tests, the flush device test consists in measuring the pressure value at the end of the test and comparing it with the value from the previous examination.

3. PROPOSALS FOR CONSTRUCTION CHANGES IN THE ASSEMBLY LINE

A proper material for the cable plug pins was needed to create an electrical connection of good electrical conductivity. The pins were nickel-plated copper rods before the tests. As copper has autopassivating properties, it was proposed to make silver-plated pins which would guarantee the lack of electric tension falls where the plug is connected to the socket.

Constructional changes proposed in the second testing module refer to the mandrel that seals the transducer. A new version of the sealing mandrel (Fig. 5) was designed, on the basis of ISO 594/1-1986 (E) and the original mandrel structure (Fig. 4).

The modernised structure 2 (Fig. 5) has one of its parts shortened, with a diameter of less than 5 mm, which, together with a proper curvature added, allowed for greater stiffness and facilitated the mandrel production (smaller deflection of the rod treated). The conical surface was designed according to ISO 594/1-1986 (E).

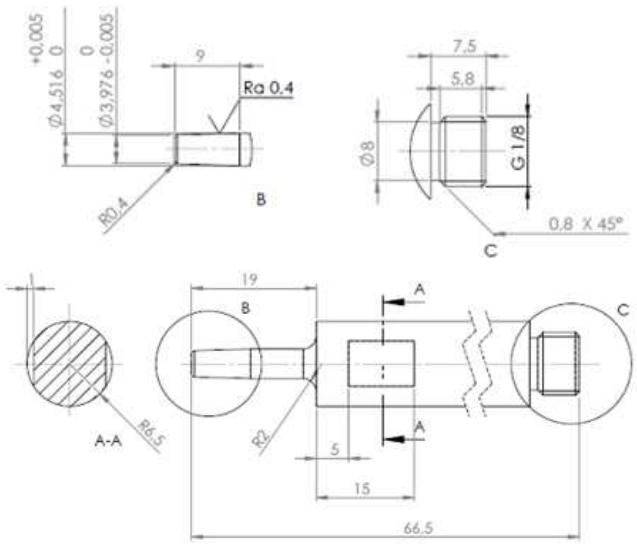

Fig. 5. Sealing mandrel construction 2 (Maciejewski, 2012)

4. VERIFICATION TESTS

Checking whether the first testing module operates properly consisted in the visual control of the rejected soldered connections. The quality of the accepted components' connections was inspected when the second testing module's functioning was being verified (the automatic machine accepted 525 connections of the sensor and the cable).

The automated assembly line rejected 7 connections of soldered component parts out of 525 transducers manufactured, while the visual control proved a bad solder quality in 6 cases and no faults were found in one case.

The quotient of the number of suitable components' connections and the number of good transducers was less than 1 per mil, which proves that the modernisation proposed and conducted on the testing module 1 one was correct.

Pressure transducers' user properties were verified by means of manually operated stationary testers. Air flow volume was measured using the MPS 5 device, and the sealing test was conducted by means of the MPS40 device by JW FROEHLICH company. The flush rate of the flush device was not tested when a given transducer proved not to be tight.

As it has already been stated, 525 Combitrans 3 transducers produced by the modernised automated machine underwent the verification tests. The testing procedure parameters were changed in their production process. Tab. 3 includes the chosen parameters and the results of the 0, 1 and 12 verification tests.

Testing procedure parameters of the 0 verification test are consistent with the ones proposed by the manufacturer of the automated machine. The results of this test reflect the influence of the changes proposed on the automated machine's operation. As it has already been stated, 100% of suitable transducers were wrongly qualified. This value decreased to 60.61% after the testing modules' modernisation. This proves that there is a need for procedural changes that would allow for balancing the assembly line (Corominas et al., 2011; Martinez ate al., 2009).

The results of the 1 and 12 verification tests are consistent with the requirements established at the beginning. Respectively, 4.08% and 2.50% of the transducers are wrongly qualified. The testing time of the 12 examination is more than 3 times shorter than the 1 test's time.

Tab. 3. 0, 1 and 12 verification tests' results (Maciejewski, 2012)

Stage no.	Procedure	Test 0	Test 1	Test 12
1	Filling time [ms]	800	800	800
	PA3027 sensor max/min pressure after filling [mmHg]	330.00	330.00	330.00
		260.00	260.00	260,00
	MPX2300DT1 sensor pressure tolerance in comparison to PA3027 sensor pressure [mmHg]	12.00	12.00	12.00
		12.00	12.00	12.00
2	Stabilisation time [ms]	1.200	4.000	1.200
	MPX2300DT1 sensor max/min pressure difference, with reference to the previous stage [mmHg]	25.00	25.00	25.00
		-10.00	-10.00	-10.00
3	Sealing test time [ms]	1.000	4.000	1.000
	MPX2300DT1 sensor max/min pressure difference, with reference to the previous stage [mmHg]	0.25	0.25	0.50
		-2.50	-2.50	-2.50
4	Flush device testing time [ms]	800	4.000	800
	MPX2300DT1 sensor max/min pressure difference, with reference to the previous stage [mmHg]	140.00	140.00	140.00
		90.00	90.00	90.00
Testing procedure duration time [ms]		3.800	12.800	3.800
Number of manufactured transducers		140	55	42
Number of accepted transducers (IO)		52	47	39
Manual control	Sealing test IO	52	47	39
	Flush rate test IO	52	47	39
	Total IO	52	47	39
Number of rejected transducers (NIO)		88	8	3
Manual control	Sealing test	80 IO 8 NIO	2 IO 6 NIO	1 IO 2 NIO
	Flush rate test IO	80	2	1
	Total IO	80	2	1
Number of suitable transducers produced		132	49	40

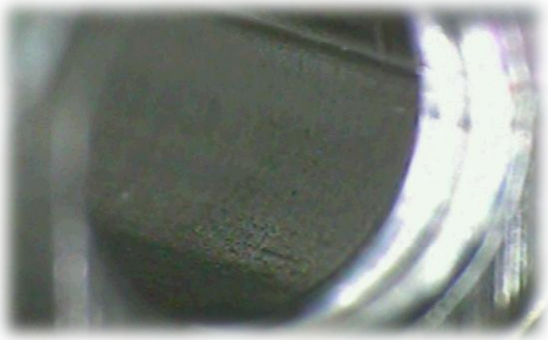

Fig. 6. Surface of a randomly chosen flush device (Maciejewski, 2012)

The visual control of the transducers produced referred to the inner surface of the flush device. The aim of the control was to check if the polymer structure could be damaged in any way. The control was led by means of the Heidenhain ND 1300 Quadra Chek device, compatible with the Lynx microscope. Visual assessment of randomly chosen transducers did not reveal any damages in the flush device's inner layer (Fig. 6), and the presence of the sealing mandrel's material was also not detected.

5. CONCLUSION

Functioning assessment of the automated assembly line to manufacture medical pressure transducers revealed a number of problems related to their assembly quality control. The reservations referred to the 1 and 2 testing modules' construction and the parameters of the testing procedure 2.

Bad quality of the electrical connection between the transducer examined and the electric tester had a negative influence on the testing procedure. Wrong Combitrans 3 sealing mandrel construction, in turn, caused the occurrence of plastic stresses during the production cycle.

Automated assembly line modernisation referred to the materials used to produce elements of the electrical connection between the pressure transducer and module of the automated machine. Silver was used as the material for cable pins. Due to this, only one good solder connection out of 525 was rejected.

The mandrels sealing the transducer (Fig. 4) during the tests were produced in the Division of Technology Machines of the Poznan University of Technology. The quality of shape and volume of the elements produced allowed for the automated machine's functioning assessment after its modernisation.

The duration of the testing procedure was taken into account while choosing the best parameters for it. The production costs increase together with the rise in average production time. While the testing procedure of the test 1 takes 12.8 s, it is only 4 s in the case of the test 12. What is crucial, is that all the transducers accepted by the automated machine fulfil the conditions of being allowed for use.

During the verification tests a slight wear of the sealing mandrel's conical surface was noticed, which was the result of the surface not being heat-treated. The mandrel's resistance to abrasive wear increased after the material's hardening and tempering, as well as controlling the shape and volume accuracy.

The testing modules and procedures modernisation proposed allowed for the fulfilment of requirements established for the functioning of the automated assembly line to manufacture medical pressure transducers.

REFERENCES

1. **Bourne D**., **Corney J**., **Gupta S.K**. (2011), Recent advances and future challenges in automated manufacturing planning, *Journal of Computing and Information Science in Engineering*, Vol. 11, No. 2.
2. **Chen K.M**., **Chen J.C**., **Cox R.A**. (2012), Real time facility performance monitoring system using RFID technology, *Assembly Automation*, Vol. 32, No. 2, 185-196.
3. Collective work, *Industrial Metrology Laboratory: Automated tests of sensors and pressure transducers* (in Polish) *(ed. J. Żelezik)* (2002), Wydawnictwo Politechniki Śląskiej, Gliwice.
4. **Connolly C**. (2009), Precision assembly systems for medical devices, *Assembly Automation*, Vol. 29, No. 4, 326-331
5. **Corominas A**., **Ferrer L**., **Pastor R**. (2011), Assembly line balancing: General resource-constrained case, *International Journal of Production Research*, Vol. 49, No. 12, 3527-3542.
6. ISO 594/1-1986 (E).
7. **Maciejewski B.** (2012), *Modernization of testing modules and procedures in an automatic assembly line adapted for medical pressure transducers manufacture* (in Polish), Politechnika Poznańska.
8. **Martinez M**., **Pham V.H**., **Favrel J**. (2009), Optimal assembly plan generation: A simplifying approach, *Journal of Intelligent Manufacturing*, Vol. 20, No. 1, 15-27.
9. **Nearchou A.C.** (2011), Maximizing production rate and workload smoothing in assembly lines using particle swarm optimization, *International Journal of Production Economics*, Vol. 129, No. 2, 242-250.
10. **Suszyński M**., **Ciszak O**., **Żurek J.** (2009), Methodology for assembly sequence planning with application of hypergraph, directed graph and state matrix (in Polish), *Archiwum Technologii Maszyn I Automatyzacji*, Vol. 29, No. 4, 103-111.
11. **Tietze U., Schenk Ch.** (2009), *Semiconductor systems* (in Polish), Wydawnictwo Naukowo-Techniczne, Warszawa.
12. **Żurek J.**, **Cieślak R**., **Suszyński M**. (2012), A study on assembly technological process labour production, by means of the ChronFoto_RC method (in Polish), *Archiwum Technologii Maszyn I Automatyzacji*, Vol. 32, No. 2, 61-68, 123-130.
13. **Żurek J.**, **Ciszak O**., **Cieślak R**. (2010), The labour-consumption in the process of assembly in the real world and in virtual reality analysed with the use of MTM method (in Polish), *Technologia i Automatyzacja Montażu*, No. 2, 29-34.
14. **Żurek J.**, **Ciszak O**., **Cieślak R**., **Suszyński M**. (2011) The choice and assessment of an industrial robot by means of the AHP method (in Polish), *Archiwum Technologii Maszyn i Automatyzacji*, Vol. 31, No. 2, 201-211.

.

ENERGY SAVING ROBUST CONTROL OF ACTIVE MAGNETIC BEARINGS IN FLYWHEEL

Arkadiusz MYSTKOWSKI*

*Bialystok University of Technology, Faculty of Mechanical Engineering, Wiejska 45C, 15-351 Bialystok, Poland

a.mystkowski@pb.edu.pl

Abstract: The paper reports on the investigation and development of the flywheel device as a energy storage system (FESS). The FESS is designed to operate in a vacuum and is supported on a low energy controlled active magnetic bearings (AMBs). The goal was to design and experimentally test the self integrated flywheel conception with a smart control of the flywheel rotor magnetic suspension. The low power control approach, with the reduced bias current, of the flywheel active magnetic bearings is used. The weighting functions are designed in order to meet robust control conditions. The laboratory investigations of the flywheel with high gyroscopic effect operated at low speed met the control and energy performances requirements.

Key words: Flywheel, Active Magnetic Bearings, Weighting Functions, Singular Control

1. INTRODUCTION

Many conventional power backup or energy storage systems have been developed over the last decade. A several of them are modern and are characterized by immediate delivery of energy and high power density. The fast progress of material science offers advanced technologies as composite flywheels [5], superconductors, supercooled electromagnets, hybrid-fuel cells, hydraulic and pneumatic energy storages and electrochemical batteries. The wide overview of flywheel technology, its applications and resent development is presented in the work Bolund et al., (2007).The high energy density lead electric batteries are commonly used in many devices/applications and their number is still increasing. But this type of storage energy is not "clean", and causes environmental problems.

The alternative solution of the "clean energy storage system" are flywheels (Kameno et al., 2003; Nathan and Jeremiah, 2002; Norman, 2002; Ward, 2005). The traditional (low speed) Flywheel Energy Storage System (FESS) has a steel wheel supported by the mechanical contact bearings and coupled with motor/generator, such that they increase moment of inertia and limit rotational speed. The traditional FESS are capable of delivering approximately 70% of the flywheel's energy as usable. Thus, they have many disadvantages such as low power density, high mechanical friction and aerodynamic losses and noise. The power consumption is optimized by hardware and software development. In many applications the IGBTs power control technology are used. The IGBT is a switch device with ability to handle voltages up to 6.7 kV, currents up to 1.2 kA and most important high switching frequencies (www.igbt-driver.com/ english/news/scale _hvi.shtml, www.pwrx.com).

The modern compact high speed flywheels have a rotor supported magnetically (non-contact) with composite wheel and bearingless motor. These rotating parts are located in a vacuum chamber. Therefore, the applications achieve a high storage energy capacity, high power density, low current and aerodynamics losses. These systems take advantages of a modern materials, electronics technologies and optimal control strategies (Charara et al., 1996; Kubo, 2003; Larsonneor, 1990; Lottin et al., 1994). The active or passive magnetic bearings is a way to stabilize the end of the flywheel axle, possible since the configuration of the electromagnetic coils or permanent magnet levitates the flywheel, and thus, reduce the mechanical friction (Fremery, 1992; Swedish patent Nr 508 442, 1998).The main disadvantage of the active magnetic bearings (AMBs) flywheels are demanding additional control and supply units. Also the active magnetic bearings are nonlinear systems itself, therefore their modelling is complicated (Gosiewski and Mystkowski, 2006, 2008; Tomczuk et al., 2011; Tomczuk and Zimon, 2009).

A purpose of this research is development of the flywheel energy storage system which can replace the conventional battery without maintenance and environment degradation. The flywheel is supported magnetically in the radial and axial directions. The position control of the 5 DOF (degree of freedom) flywheel is realized by active magnetic bearings in the closed-loop feedback configuration. The low-bias current and non-linear control algorithms are used. Thus, the energy saving AMBs flywheel is developed and presented via calculations and experimental investigations.

2. ENERGY SAVE APPROACH

Many conventional magnetic bearings systems are controlled by the control current or flux with a bias current. This method is much easier than control without a bias, but has many disadvantages. First, the bias current causes a negative stiffness of AMBs, which has to be compensated by the control current. Second, the AMBs with control method based on the bias current consume energy even if the rotor is controlled at the equilibrium point. Third, the control with both bias and control currents often requires a additional feedback loop for bias current control. Finally, in high rotational speed the bias current causes an eddy current losses. Several nonlinear methods have been investigated for the zero-bias AMB problem (Sivrioglu et al., 2003; Zhang and

Nonami, 2002). Input-output linearization has been studied in Charara and Caron (1992); Fremery (1992); Larsonneur (1990); Lottin et al. (1994); Smith and Weldon (1995). Sliding mode controllers have been investigated in Torries et al., (1999). The rotating flywheel stable position is controlled by the AMBs. In order to save energy, the low-bias current control method is used (Hu et al., 2004; Sivrioglu and Nonami; 2003; Sivrioglu et al., 2003).

The reduction of energy losses is very important especially in energy storage AMBs flywheel systems. In order to eliminate eddy current losses the synchronous motors and magnetic bearings are performed with thin lamination sheets. The control energy of the AMBs must compensate any disturbances e.g. rotating unbalance forces and losses e.g. hysteresis, eddy current, etc. In the electromagnetic AMBs circuit the losses are divided into: ohmic loss ($\approx I^2$), rotating hysteresis loss ($\approx I$) and eddy current loss ($\approx I^2$). So the energy is used to fix the bias point, to stabilize the unstable rotor, and to increase the level of the vibration damping. The reduction of the magnetic flux in the magnetic bearing circuits can be done by both control/software and hardware optimization (Maslen et al., 1989; Schweitzer, 2002).

In the paper, the displacement control of the vertical 5-DoF (degree of freedom) rotor flywheel supported magnetically with low-bias current control based on the optimal nonlinear robust control strategy is proposed. The optimal robust controller has been designed using weighting functions to optimize the energy consumptions and signals limits with respect to the desirable performances of closed-loop system (Gosiewski and Mystkowski, 2006, 2008). The bias current was limited to reduce the negative stiffness of the bearings controlled by the robust control system. In this approach, the control current is switched between two opposite magnetic actuators generating the attractive electromagnetic forces in each of two perpendicular directions. Thus, at any time only the one coil is activated in each of two control axes. The rotor displacement (x) control law is given by (see Fig. 1):

$$u = -\mathbf{sgn}(K)x \tag{1}$$

The control algorithm function K is operated in negative feedback loop. From optimal energy control point of view the rotor displacement and control signals have to be limited. The output displacement signal is limited by robustness weighting function W_y which was selected based on the complementary sensitivity function given by transfer function (Zhou and Doyle, 1998):

$$T(s) = L(s)S(s) \tag{2}$$

where: L – open-loop function, S – sensitivity function denoted here $S=(1+L)^{-1}$.

The control signal u is limited by the control weighting function W_u which was assigned based on the control function given by Zhou and Doyle (1998):

$$R(s) = K(s)(I + L(s))^{-1} \tag{3}$$

The performances of the closed-loop system strongly depend on the properties of chosen weighting functions (Zhou and Doyle, 1998). The signal limits have to pass the stability conditions given by inequality (Zhou and Doyle, 1998):

$$\left\| \begin{matrix} R(s)W_u(s) \\ T(s)W_y(s) \end{matrix} \right\|_\infty \leq 1. \tag{4}$$

If the influence of the power amplifier dynamics can be neglected (flat Bode plot), then the electromagnetic coil control current depends only of the coils dynamics (R-L curve) $i_s=u\times$(coil dynamics) [6, 7]. The total current in upper and lower coils equals:

$$i_{1,2} = i_0 \pm i_{s1,2} \tag{5}$$

The static bias current i_0 is limited due to performance given by (4). Additional bias and control currents control sequence was used due to over-ranged signals. Therefore, the singular switching control function was used. The value and sign of the control law function depends on the system conditions described above. These one degree of freedom AMB control system is presented in Fig. 1.

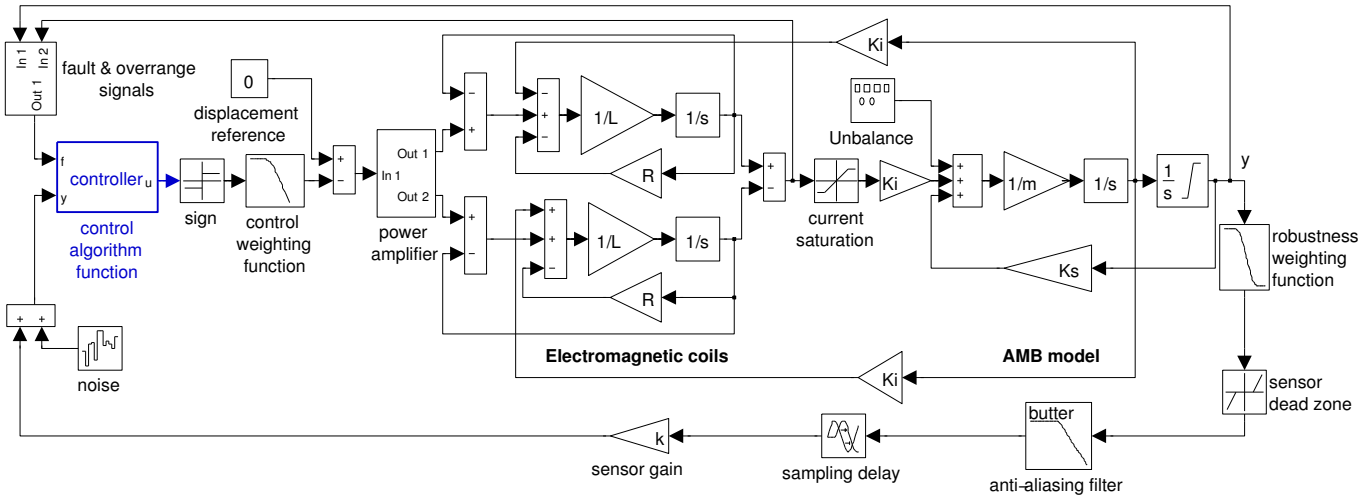

Fig. 1. Single degree of freedom AMB control system

In this application actively controlled digital power amplifiers are used based on the pulse width modulation (PWM) technology. The PWM amplifiers are bipolar, where the switching frequency equals to 18 kHz, voltage ±180 V and a maximal current is up to 10 A. The measured power consumption of the magnetic suspension of the flywheel system, where the radial and axial magnetic

bearings are supplied by the 10 channels of the PWM amplifiers, equals to 480 W. The 480 W is a nominal power to compensate the flywheel weight, unbalance forces and other external/internal disturbances, in case of PID control. By using optimal singular control, the power consumption was reduced to 380W. Moreover, the other energy losses could arise during flywheel loading/unloading. The position controller bandwidth is over 4kHz. Meanwhile, the bandwidth of the whole closed-loop system is limited by the power amplifier to 1kHz.

3. EXPERIMENTAL SET-UP

The composite steel flywheel assembled on the high strength steel rotor is used as electromechanical energy accumulator. The total kinetic energy storage capacity is ~10 MJ, where the maximal power equals to 100 kW at the maximal rotational speed of 40 000 rpm. Meanwhile, for presented system the maximal achieved rotational speed was limited to 2000 rpm. The flywheel outer diameter is 0.47 m and main shaft length is 1.12 m. The total mass of the flywheel with rotor is over 150 kg. The energy-absorbing composite rotor is driven by two motors/generators of 50 kW power each. The synchronous motors (3 pole pairs, 3 phases) are performed with lamination sheets and permanent magnets mounted on outer rotor. The motors/generators are controlled by electronic inverters. The two radial and one axial active magnetic bearings are applied to 5 DOF rotor position control. The axial bearing (thrust bearing) carriers the weight of the rotor. The force disturbances in axial direction for the thrust bearing are small, where the radial disturbing forces (mainly due to unbalance) are quite strong. Each of the radial magnetic bearing has 8 electromagnets which are connected to 4 pairs in serial configuration (see Fig. 2). The magnetic bearings parameters are presented in Tab. 1.

Tab. 1. Parameters of the AMBs

	radial AMB	axial AMB
nominal air gap	$0.4 \cdot 10^{-3}$ m	$0.7 \cdot 10^{-3}$ m
bias current	5 A	5 A
maximal current	10 A	10 A
number of coils	8	2
displacement stiffness	$2.6 \cdot 10^{6}$ N/m	$9.1 \cdot 10^{6}$ N/m
current stiffness	$0.2 \cdot 10^{3}$ N/A	$1.2 \cdot 10^{3}$ N/A

The rotor radial and axial displacements are measured by using 5 eddy current proximity sensors. The radial and axial AMBs are supplied by controlled 10-chanells current PWM amplifiers.

Fig. 2. Heteropolar radial active magnetic bearing

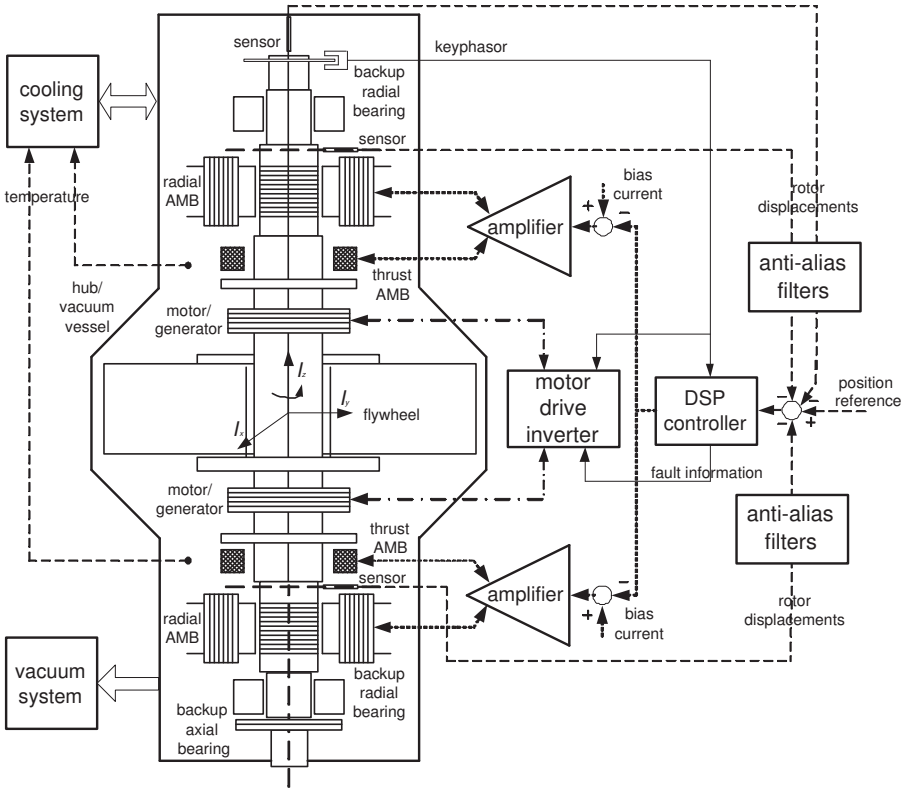

Fig. 3. Flywheel with control, cooling and vacuum system

The maximum current does not exceed 10 A for each of the active magnetic bearing electromagnets. The control of the rotor/flywheel position is fully digital in the real time. The control algorithm was implemented in digital signal processor (DSP). The sampling frequency of the AMBs controller equals to 10 kHz. To ensure a stable operation at high rotor speed, the PWM amplifiers must have a wide bandwidth of 2 kHz. The flywheel set-up configuration is presented in Fig. 3. The ratio of the moments of inertia I_z/I_x is 2.28/5.75 kgm^2, thus the influence of the gyroscopic effect is quite strong and could case stability problems.

Fig. 4. Flywheel supported by active magnetic bearings during assembling

It is important for the flywheel system to keep electrical power for many hours, thus any energy losses should be taken into account. Therefore, the flywheel is suspended without mechanical contact by AMBs and is located in a vacuum chamber. The low pressure system (under-pressure of about 1 Pa) is used to reduce aerodynamic friction losses and overhead power consumption. The fluid cooling system is applied to reduce a temperature of the motor and AMBs. In case of current supply failure or the AMBs stability loss, the critical touch-down (backup) radial and axial bearings are designed. The backup bearings are used to rotor emergency slow down and stop in a controlled way. Finally, the flywheel construction is characterized by high energy density, low maintenance, wide operating temperature range and very long cycle life (see Fig. 4).

4. SPEED TESTS

A stable levitation and low control current of the FESS rotor was achieved. For example, the measured results of total currents and rotor displacements are shown in Fig. 5 and Fig. 6.

The rotor speed equals to 1 000 rpm, the mean value of the radial AMB currents was below 2 A, where for the axial AMB upper coil was over 5 A. Thus, these values do not extend 50 % of amplifiers ability. The rotor displacements in radial directions (x-y) do not extend $0.08 \cdot 10^{-3}$ m. The investigated low-bias control approach is verified during experimental rotational tests. The initial rotational tests confirmed that:

- by using optimal control algorithm, the AMB currents are lower (about 15%) than in case of full bias standard control (not presented here);
- stable rotor operation and fast compensation of the external disturbances was achieved by using limited control signal;
- future reduction of AMBs power consumption need a hardware optimization.

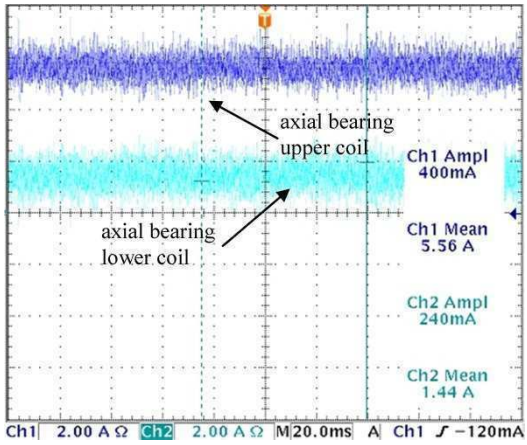

Fig. 5. Measured results of currents for low energy control

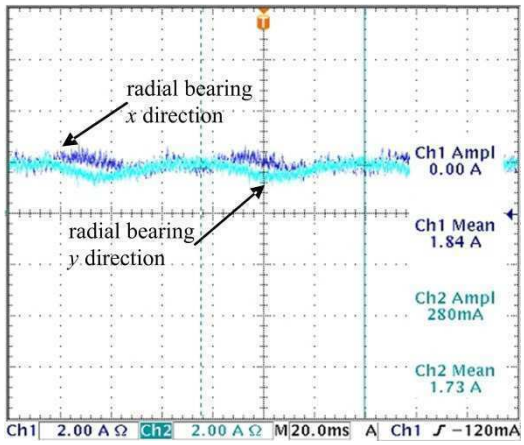

Fig. 6. Measured results of rotor displacements for low energy control

The critically important further task of the rotational tests will be verification of the control algorithm which should ensure the robust stability in spite of unstable phenomena which could occurs at higher rotational speeds.

5. SUMMARY

The magnetic bearings FESS prototype was described and the optimal robust feedback control law with the low energy consumption was proposed. The low-bias control approach to stabilize the rotor supported by active radial/thrust magnetic bearings are presented via experimental investigations. The parameters of the magnetic bearings flywheel and test rig setup were described. The speed test results were presented. The energy saving active magnetic bearings controlled by the nonlinear control algorithm with the low-bias control current was successfully applied in the flywheel.

REFERENCES

1. **Bolund B., Bernhoff H., Leijon M.** (2007), *Flywheel energy and power storage systems*, Elsevier, Vol. 11, 235-258.
2. **Charara A., Caron B.** (1992), Magnetic Bearing: Comparison Between Linear And Nonlinear Functioning, *Proc. of the 3rd Int. Symposium on Magnetic Bearings*, 451-463.
3. **Charara A., Miras J., Caron B.** (1996), Nonlinear Control of a Magnetic Levitation System Without Premagetization, *IEEE TraNo. Control Sys. Tech.*, Vol. 4, No. 5, 513–523.
4. **Fremery J. K.** (1992), *Axially stabilized magnetic bearing having a permanently magnetized radial bearing*, US patent No. 5,126,610; 30.
5. **Gabrys C. W.** (2001), *High Performance Composite Flywheel*, US patent Pub. No.: US 2001/0054856 A1.
6. **Gosiewski Z., Mystkowski A.** (2006), The Robust Control of Magnetic Bearings for Rotating Machinery, *Solid State Phenomena*, VOL. 113, 125-130.
7. **Gosiewski Z., Mystkowski A.** (2008), Robust Control of Active Magnetic Suspension: Analytical and Experimental Results, *Mechanical Systems & Signal Processing*., Vol. 22, No. 6, 1297-1303.
8. **Hu T., Lin Z., Allaire P. E.** (2004), Reducing Power Loss in Magnetic Bearings by Optimizing Current Allocation, *IEEE TraNo. on Magnetics*, Vol. 40, No. 3, 1625-1635.
9. **Kameno H, Kubo A., Takahata R.** (2003), Basic Design of 1 kWh Class Compact Flywheel Energy Storage System, *Koyo Engineering Journal*, No.163, 44-48.
10. **Kubo A., et al.** (2003), Dynamic Analysis And Levitation Test in 1kWh Class Flywheel Energy Storage System, *Proc. of 7th Int. Symposium on Magnetics Tech.*, 144-149.
11. **Larsonneur R.** (1990), *Design and Control of Active Magnetic Bearing System For High Speed Rotation*, Diss. Eth, Zurich No.. 9140.
12. **Lottin J., Mouille P., Ponsart J. C.** (1994), Nonlinear Control of Active Magnetic Bearings, *Proc. of the 4th Int. Symposium on Magnetic Bearings*, Eth Zurich, 101-106.
13. **Maslen E. Hermann P., Scott M.** (1989), Practical Limits to the Performance of Magnetic Bearings: Peak Force, Slew Rate And Displacement Sensitivity, *ASME Journal on Tribology*, Vol. 111, 331-336.
14. **Nathan G. W., Jeremiah I. R.** (2002), *Flywheel System With Parallel Pumping Arrangement*, U.S. Pat. 6 347 925 B1.
15. **Norman C. B.** (2002), *Stiff Metal Hub for an Energy Storage Rotor*, U.S. Pat. 6 817 266.
16. **Schweitzer G.** (2002), Active Magnetic Bearings – Chances and Limitations, *8th Int. Symposium on Magnetic Bearings*, Mito JapaNo.
17. **Sivrioglu S., Nonami K., et al**., (2002), Nonlinear Adaptive Control For a Flywheel Rotor AMB System with Unknown Parameter, *Proc. of 8th International Symposium on Magnetic Bearings*, ISMB-8, 593-598.
18. **Sivrioglu S., Nonami K., Takahata R., Kubo A.** (2003), Adaptive Output Backstepping Control of a Flywheel Zero-Power AMB System With Parameter Uncertainty, *Proc. of 42nd IEEE Conference on Decision and Control (CDC)*, 3942-3947.
19. **Smith R. D., Weldon W. F.** (1995), Nonlinear Control of a Rigid Rotor MBS: Modeling and Simulation With Full State Feedback, *IEEE TraNo. on Mag.*, Vol. 31, 973-980.
20. **Swedish patent,** (1998), No. 508 442, *Elektrodynamiskt magnetlager*.
21. **Tomczuk B., Wajnert D., Zimon J.** (2011), Modelling of control system for an active magnetic bearing, *Proc. of Electrotechnical Institute*, No. 252, 1-14.
22. **Tomczuk B., Zimon J.** (2009), Filed Determination and Calculation of Stiffness Parameters in an Active Magnetic Bearing (AMB), *Solid State Phenomena*, Vol. 147-149, 125-130.
23. **Torries M. Sira-Ramirez H., Escobr G.** (1999), Sliding Mode Nonlinear Control of Magnetic Bearings, *Proc. of the IEEE Int. Conference on Control Applications*, 743-748.
24. **Ward R. S.** (2005), *Composite Flywheel Rim With Co-Mingled Fiber Layers And Methods Of Determining The Same*, U.S. Pat. 6 884 039 B2.
25. www.igbt-driver.com/english/news/scale_hvi.shtml, CT-Concept Tech. Ltd, homepage accessed Nov 2004
26. www.pwrx.com, Powerex, Inc., homepage accessed Nov 2004,
27. **Zhang Y., Nonami K.** (2002), Zero Power Control of 0.5KWh Class Flywheel System Using Magnetic Bearing with Gyroscopic Effect, *Proc. of 8th International Symposium on Magnetic Bearings ISMB-8*, 587-592.
28. **Zhou K., Doyle J.** (1998), *Essentials of Robust Control*, Prentice Hall.

NUMERICAL MODELLING, SIMULATION AND VALIDATION OF THE SPS AND PS SYSTEMS UNDER 6 KG TNT BLAST SHOCK WAVE

Marek ŚWIERCZEWSKI*, Marian KLASZTORNY*, Paweł DZIEWULSKI*, Paweł GOTOWICKI*

*Department of Mechanics and Applied Computer Science, Faculty of Mechanical Engineering, Military University of Technology, ul. Gen. S. Kaliskiego 2, 00-908 Warszawa, Poland

mswierczewski@wat.edu.pl, mklasztorny@wat.edu.pl, pdziewulski@wat.edu.pl, pgotowicki@wat.edu.pl

Abstract: The paper develops a new methodology of FE modelling and simulation of the SPS and SP systems under 6 kg TNT blast shock wave. SPS code refers to the range stand – protected plate – protective shield ALF system, while PS code refers to the range stand – protected plate system. The multiple – use portable range stand for testing protective shields against blast loadings was developed under Research and Development Project No. O 0062 R00 06. System SPS uses high strength M20 erection bolts to connect the protective shield to the protected plate. In reference to the SPS system, validation explosion test was performed. It has pointed out that the developed methodology of numerical modelling and simulation of SPS and PS systems, using CATIA , HyperMesh, LS-Dyna, and LS-PrePost software, is correct and the ALF protective shield panels have increased blast resistance and high energy – absorption capability.

Key words: Military Vehicle, Passive Shield, Range Stand, Protected Plate, Blast Shock Wave, Numerical Modelling, Simulation, Range Tests, Validation

1. INTRODUCTION

Within the framework of Research and Development Project No. O 0062 R00 06 (Klasztorny, 2010a) the authors' team has designed the ALF energy-absorbing shield and the portable range stand for testing protective shields against shock wave loading induced by blast of a spherical charge up to 6 kg of TNT. The ALF shield is purposed for protection of crew-occupants of military vehicles against blast and fragmentation of AT mines and IED devices for selected protection levels. Papers (Klasztorny, 2010b, c) present numerical modeling, simulations and experimental validation of the SPS and PS systems loaded by 2 kg TNT blast shock wave. The SPS code is referred to as the range stand – protected plate – ALF shield system while the PS code denotes the range stand – protected plate system. In the case of 2 kg of TNT charge the ALF square segment was glued to the protected plate. At larger HE charges erection bolts must be applied.

The paper develops a new methodology of FE modelling and simulation of SPS and SP systems under 6 kg TNT blast shock wave. In SPS system four bolt connections were used to join the energy-absorbing shield to the protected plate. In reference to the SPS system the validation range test is presented. The parameter modification of laminas of the hybrid laminates has been examined in order to eliminate non-physic erosion of the composite finite elements. The physic damping has been limited to the protected plate in order to achieve better convergence of the explicit algorithm (Hallquist, 2009). The literature review has been presented in (Klasztorny, 2010b).

2. DESCRIPTION OF THE SPS SYSTEM

The ALF energy-absorbing shield is purposed for protection of crew-occupants of logistic vehicles (LV) and light armoured vehicles (LAV) against blast and fragmentation of AT mines and IED devices under the vehicle body shell.

The tactical – technological assumptions related to the ALF shield, formulated according to standards (AEP, STANAG), are collected below:

- the shield is purposed to modernize serviced LV and LAV vehicles (without any modifications of the vehicle body bottom) and to design new types of military vehicles;
- the shield has modular structure;
- structural layers of the shield panels have plate shape and are joined together with glue;
- the shield is non-flammable, resistant to atmospherical and chemical factors;
- the shield thickness does not exceed 76 mm;
- the maximum shield mass per unit area equals 50 kg/m^2;
- thickness of the protected steel plate modelling the vehicle body bottom plate equals 5÷8 mm;
- high energy-absorbing materials are applied as components of the shield;
- the maximum overall dimensions of the shield panels amount to 700×700 mm;
- the shield panels are exchangeable directly on the vehicle using bolt connections;
- a simple manufacturing, assembly and disassembly technology in reference to the shield panels must be developed;
- the shield is characterised by long durability and low material – production costs;
- the layered structure of the shield must be developed in such a way to achieve the highest protection level of crew-occupants of LV and LAV vehicles against blast and fragmentation of AT mines and IED devices under the vehicle body shell.

The ALF shield has sandwich structure with cover shells made of hybrid laminate in the form of special combination of uniform

laminates. The latter are manufactured using the following components:

- incombustible VE 11-M vinylester resin matrix produced by Organika-Sarzyna Chemical Plant, Poland;
- Style 430 / Tenax HTA40 6K plain weave carbon fabric, 300 g/m^2 substance, 400/400 tex warp/weft, 3,7/3,7 strand/cm, produced by C. Cramer GmbH & Co. KG Division ECC;
- Style 328 / Kevlar 49 T 968 / T 968 TG aramid plain weave fabric, 230 g/m^2 substance, 158/158 tex warp/weft, 7/7 strand/cm, produced by C. Cramer GmbH & Co. KG Division ECC;
- S SWR 800 glass plain weave fabric, 800 g/m^2 substance, produced by Hongming Composites CO., Ltd.

Useful properties of VE 11-M vinylester resin matrix corresponding to the adopted assumptions, are as follows:

- neutral resin with good moulding properties;
- good saturatability of fibres;
- high elasticity;
- incombustibility;
- high chemical and thermal resistance;
- high relative tensile strength;
- high relative stiffness;
- high resistance to atmospheric factors and service pollutants,
- long durability;
- anti-vibrating resistance.

The following uniform laminates have been designed and used in hybrid laminates (Klasztorny, 2010a):

- the vinylester–carbon regular cross–ply laminate (C/VE); laminas composed of VE 11-M resin and Style 430 carbon fabric with fibre volume/mass fraction f_V=54,4%, f_m=68,0%,
- the vinylester–aramid regular cross–ply laminate (A/VE); laminas composed of VE 11-M resin and Style 328 aramid fabric with fibre volume/mass fraction f_V=48,3%, f_m=57,5%,
- the vinylester–glass regular cross–ply laminate (S/VE); laminas composed of VE 11-M resin and SWR800 S glass fabric with fibre volume/mass fraction f_V=53,5%, f_m=73,7%.

Hybrid laminate plates, manufactured using the vacuum technology, are 24-ply composites with the specified sequence of GFRP, CFRP and KFRP laminates. Based on the preliminary ballistic tests, performed on selected configurations of uniform laminates (Klasztorny, 2010a), the final symmetric SCACS hybrid laminate has been designed to apply it in ALF protective shields, with the ply sequence of:

$$\{[(0/90)_{SF}]_2\,[(0/90)_{CF}]_4\,[(0/90)_{AF}]_6\,\}_S \qquad (1)$$

where: SF – SWR800 S glass fabric, CF – Style 430 carbon fabric, AF – Style 328 aramid fabric. Thicknesses of uniform laminate components respectively are equal to 1,3; 1,3; 3,8; 1,3; 1,3 mm (9 mm in total).

The following properties of hybrid laminate components have been utilized:

- high tensile strength of Carbon 6K (Style 430, ECC) fibres;
- high elasticity of Kevlar 49 T 968 aramid fibres;
- high impact resistance SWR800 S glass fibres;
- high elasticity of VE 11-M vinylester resin;
- maximum ballistic resistance of the SCACS stacking configuration;
- fire resistance, chemical resistance and resistance to atmospheric factors of VE 11-M vinylester resin.

Semi-finished products of SCACS hybrid laminates have been manufactured using the vacuum technology by ROMA Ltd. Grabowiec, Poland. The vacuum pressing technology developed by ROMA Ltd. is described below:

- stacking of reinforcement and resin layers (50% gravimetrically);
- pressing in the closed mould with Vacuum connected;
- air removing and pressure on the mould through partial vacuum -0.03/-0.04 MPa;
- the composite curing;
- seasoning over 24 hours;
- removing the composite from the mould;
- mechanical working (cutting off technological allowances);
- after stove at 70°C over 3 hours.

The parameters for curing and after stove of VE 11-M resin matrix were compatible with Material Card published by the producer (Organika-Sarzyna Chemical Plant, Sarzyna, Poland).

Taking into consideration the tactical – technological assumptions for the layered shield and the literature review results, Authors' team has designed the shield having the stacking structure set up in Tab. 1 and illustrated in Figs. 1 and 2. The shield has bestowed the ALF code (Aluminium – Laminate – Foam protective panel). The mass per unit area equals 50 kg/m^2, and the thickness equals 76 mm including glue joining layers.

Tab. 1. The stacking structure of the ALF shield for LV/LAV crew-occupants protection from blast and fragmentation of AT mines/ IED devices (Klasztorny, 2010a)

Layer No.	Specificatio (from the impact side)	thickness [mm]
1	PA11 (EN AW-5754) aluminium	2
2	Soudaseal 2K glue	2
3	SCACS hybrid laminate	9
4	Soudaseal 2K glue	2
5	ALPORAS aluminium foam	50
6	Soudaseal 2K glue	2
7	SCACS hybrid laminate	9
	Total	**76**

The shield components are joined with Soudaseal 2K chemoset glue exhibiting good adherence to metals and composites. It is characterized by high hardness (55 in Shore A scale), good mechanical properties, good resistance to atmospheric factors and limited chemical resistance. This glue is designed to make elastic connections exposed to heavy vibrations which are well damped. The thermal resistance of the glue is close to the VE 11-M resin matrix.

The layer No. 1 (aluminium plate) is the head layer carrying the thermal impact and protecting shield–plate assembling with erection bolts. The layers No. 2, 7 (hybrid laminates) are energy-absorbing resistant layers. The blast impact energy is absorbed utilizing the following progressive failure mechanisms: shear, delamination, bending. The alyer No. 5 (aluminium foam) is the central high energy-absorbing resistant layer. The blast impact energy is absorbed utilizing the following progressive failure mechanisms: compression, disruption, shear. Aluminium foam is the core of the sandwich panel, enabling carrying high bending moments and shear forces. Three glue layers enlarge flexibility of the shield, induce multiple reflected waves when the blast

impact wave crosses the shield. In this way, the protected plate is impacted by the wave of weaker impulse pressure.

The LV/LAV vehicle protective shield is divided into panels shaped and dimensioned according to the shape and dimensions of the vehicle body shell bottom. In the failure case the panels are exchanged. The maximum overall dimensions of the panels are 500×500 mm. The panels are connected to the vehicle bottom plate with erection bolts having increased strength and protection against unbolting. There are used M16 bolts with heads welded point wisely on vehicle bottom plate, from the vehicle body inside and using self-blocking shaped nuts (Figs. 1 and 2).

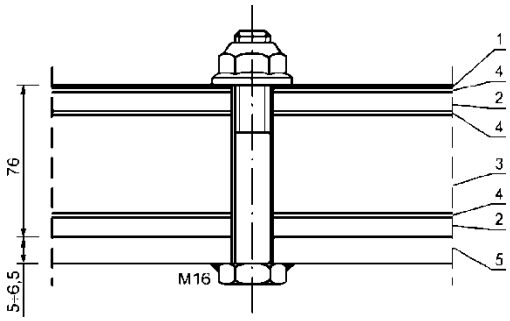

Fig.1. The bolt connection of the ALF shield to the protected plate: 1 – aluminium plate, 2 – hybrid laminate, 3 – aluminium foam, 4 – glue, 5 – protected plate

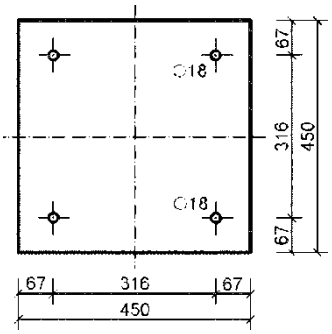

Fig. 2. The top view on the ALF square panel used in range tests (the holes for the erected bolts are depicted)

A multiple-use portable range stand for blast tests up to 6 kg of TNT, named with code BTPS, is shown in Figs. 3 and 4. The stand has the following specification:

- The BTPS stand is composed of three closed, horizontal, steel frames, respectively graded and connected together with six high strength 10.9 M20 erection bolts. Normal washers make possible unbolting after each blast test in order to exchange the tested subsystem (the protective plate or the shield–plate subsystem). The nuts are protected with cups. The holes for bolts are with passage with head blocking in the horizontal recesses in the bottom frame. The holes have 2 mm clearance.
- Each frame has mass ~100 kg. The frames are equipped with carrying handles for four persons (25 kg per person).
- The protected plate, without or with the protective panel, has dimensions 650×650×*h* mm (*h*=5÷6,5 mm) and is put in the 7 mm thick horizontal recess in the central frame. The plate is initially put eccentrically in the recess zone and next shifted into the recess and positioned centrally.
- The protected plate is fixed between two frames with possible travelling and friction. This solution ensures selection of the energy absorbed by the protected plate or the shield–plate subsystem. For the 5 mm thick protected plate the clearance between the protected plate supported strips and the top frame amounts to 2 mm. The friction is repeatable in subsequent tests.
- The width of the supported plate strip equals 90 mm on the whole perimeter of the plate. It protects the plates against line feed from the perimeter gap at HE charges up to 6 kg of TNT.
- The energy-absorbing panel has the overall dimensions 450×450×65 mm. The perimeter clearance between the shield and the top frame equals 10 mm to make the assembly easy and to unblock the panel failure during the blast test.
- There are incorporated plain scarfs on the internal perimeter of the top frame at angle of 26° that protect the tested subsystem from the wave reflected from the top frame.
- The stand frames are dimensioned under condition of elastic strains and small deflections under blast shock waves induced by HE charges up to 6 kg of TNT. The frames are made of 790×650×60 mm St3S steel flats.
- Meshes of the frames have horizontal clearances in order to make the assembly easier.
- The stand rests on the 900×850×20 mm steel plate having the central square hole of dimensions 450×450 mm. Under the plate the 450×450×300 mm central free space in the subsoil is done. The subsoil has increased stiffness.
- The HE charge is hanged centrally over the stand 400 mm from the top surface frame.

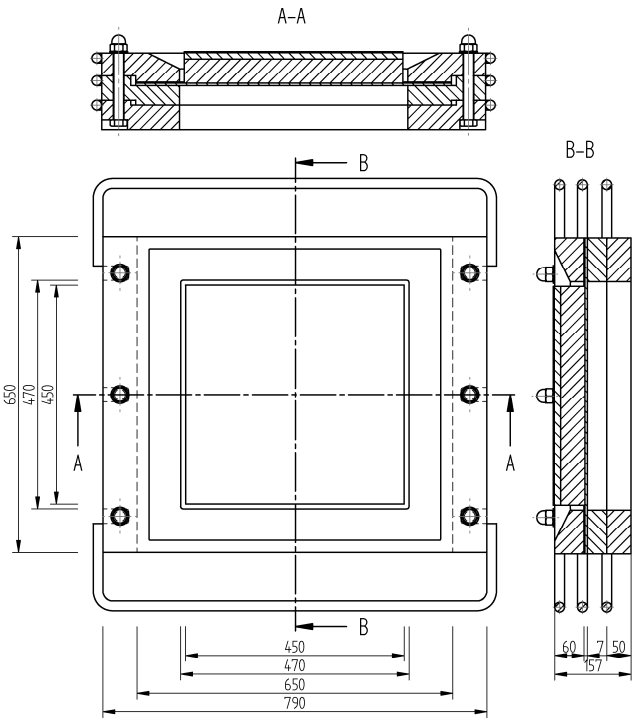

Fig. 3. The basic dimensions and main cross-sections of the BTPS range stand (Klasztorny, 2010a)

The three closed thick frames creating the BTPS stand body, respectively profiled and joined together, make possible performing blast tests up to 6 kg of TNT in such a way that:

- the stand body deforms elastically;
- the protected plate has freedom of movement and strains between the top and central frames;
- the protected plate may deform plastically and the protective

panel may by fully destroyed.

In the simulations and range tests, the 6 kg TNT spherical charge was applied, suspended centrally over the SPS system, distanced by 400 mm from the top frame surface. A detonator was placed centrally inside the sphere. The 5 mm thick protected plate was made of Armox 500T armoured steel.

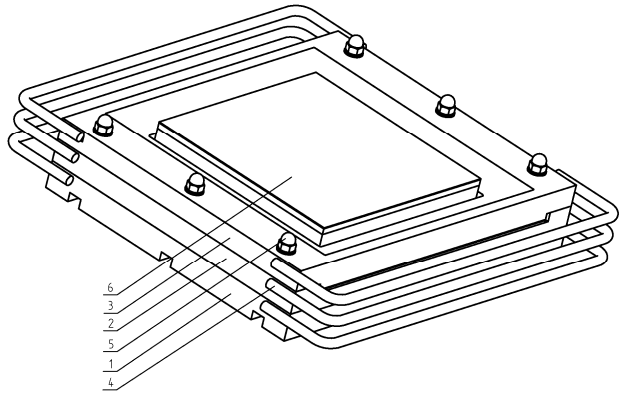

Fig. 4. The assemblied BTPS range stand: 1 – bottom frame, 2 – central frame, 3 – top frame, 4 – handle, 5 – bolt, 6 – protective panel (Klasztorny, 2010a)

3. NUMERICAL MODELLING OF THE PS AND SPS SYSTEMS

The FEM numerical modelling, simulation and postprocessing in reference to the PS and SPS systems under blast shock wave were developed using the following CAE systems: CATIA, HyperMesh, LS-Dyna, LS-PrePost.

The geometrical models of the PS and SPS systems were built using CATIA system. The FE meshing in particular subsystems was generated automatically using HyperMesh platform. LS-PrePost programme was used as a pre-processor to define the boundary conditions, finite elements, material properties, the solution type. Complete FE model was exported as a key file with LS-Dyna preferences. LS-Dyna programme was used as a solver and LS-PrePost programme was applied as the post-processor.

The 8-node 24 DOF brick finite elements were used, taking into account contact and friction phenomena. The FE model of the protected plate – range stand (PS) system has about 98000 DOFs, whereas the FE model of the protective shield – protected plate – range stand (SPS) system has about 282000 DOFs. The FE models are relatively dense and finite elements' dimensions satisfy the aspect ratio condition before and during the blast loading. For the composite layers 1–Gauss point integration (ELFORM 1) and hourglass control were applied. For the remaining structural components 8–Gauss point integration (ELFORM 2) was adopted. The horizontal dimensions of most FEs were 5×5 mm. Thicknesses of FE layers were assumed to satisfy the aspect ratio before and during dynamic process (Hallquist, 2009). Quantities and thicknesses of the FE layers in particular components of the modelled system are collected in Tab. 2.

Uniform laminates S (2 layers), C (4 layers) can be modelled as single equivalent layers since mechanical properties of these laminates were identified experimentally in macroscale (e.g. interlaminar shear strength) and the ply sequences are limited to $[0/90]_n$. The thicker A laminate was reflected by three layers; it means that each FE layer reflects 4 laminate layers. The reasons for such FE meshing given for S and C laminates are also valid for A laminate.

The aluminium foam layer is modelled as equivalent homogenized solid body. The 10 mm thick FE layers protect aspect ratio before and after foam compaction.

Tab. 2. Quantities and thicknesses of the FE layers in particular components of the SPS numerical model

Component of the PS/SPS system	Layers quantity	Layer thickness [mm]
aluminium sheet	1	2
glue	2	1
S laminate	1	1.3
C laminate	1	1.3
A laminate	3	1.27
aluminium foam	5	10
protected plate	3	1.67

The erection bolts in the range stand are designed to work in the elastic range, so they can be modelled approximately as bars with the equivalent square cross-section. The erection bolts in the ALF panels were modelled more accurately, i.e. with circular cross-sections taken into account. The stiffened subsoil was limited to the cubicoidal volume 2000×2000×1000 mm.

Because of bisymmetry of the PS and SPS systems, their numerical models were limited to respective quarters of the global systems. The boundary conditions in the planes of symmetry eliminate displacements perpendicular to these planes. The numerical models of the PS and SPS systems are shown in Figs. 5 and 6.

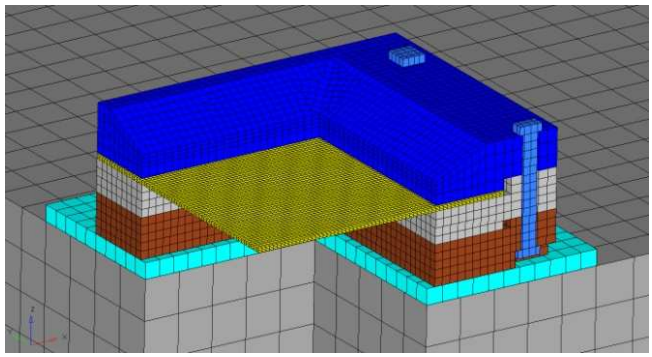

Fig. 5. Components of the PS system resting on the supporting plate and the subsoil (FE mesh of the system quarter)

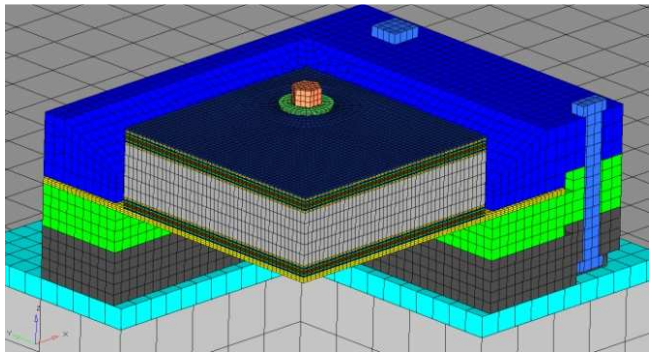

Fig. 6. Components of the SPS system resting on the supporting plate and the subsoil (FE mesh of the system quarter)

Material models for subsequent parts of the SPS system have been assumed from (Klasztorny, 2010a; Hallquist, 2009; Nillson, 2003; STANAG). In the materials' description original notation of input data assumed in FE code LS-Dyna as well as a system of units used in the numerical modelling and simulation (kg, mm, msec, K, GPa, kN) have been saved.

Armox 500T steel and PA11 aluminum
LS-Dyna material type 15: MAT_15
(MAT_JOHNSON_COOK)
Equation-of-state: EOS_GRUNEISEN

This is the Johnson–Cook strain and temperature sensitive plasticity material, used for problems where strain rates vary over a large range and adiabatic temperature increases due to plastic heating cause material softening. The model requires equation-of-state. Material data for Armox 500T steel and PA11 aluminium are collected in Tab. 3.

Tab. 3. Material constants for Armox 500T steel and PA11 aluminium

Parameter	Armox 500T	PA11
Mass density, RO	7.85e-6	2.815e-6
Shear modulus, G	79.6	28.6
Scale yield stress, VP	0	0
Flow stress: A B N C M	0.849 1.34 0.0923 0.00541 0.870	0.369 0.684 0.730 0.00830 1.70
Melt temperature, TM	1800	775
Room temperature, TR	293	293
Quasi-static threshold strain rate, EPSO	0.001	0.01
Specific heat , CP	450	875
Spall type , SPALL	2	2
Plastic strain iter. option, IT	1	1
Failure par.: D1 D2, D3, D4, D5	0.50 0	1.50 0
Intercept C	4570	5328
Slope coeff.: S1 S2, S3	1.49 0	1.338 0
Gruneisen gamma GAMAO	1.93	2.00
First order vol. correction A	0.50	0.48
Initial internal energy E0	0	0
Initial relative volume V0	1	1

Tab. 4. Material constants for components working in the elastic range

parameter	St3 steel	10.9 bolt steel	range subsoil
Mass density, RO	7.85e-6	7.85e-6	1.00e-6
Young's modulus, E	210	210	0.300
Poisson's ratio, PR	0.30	0.30	0.20
Yield stress, SIGY	0.33	0.90	2.5e-4
Tangent modulus, ETAN	1.00	1.00	1e-8
Plastic strain to failure, FAIL	0.50	0.50	1.00

Tab. 5. The average values of material constants for uniform composites S, C, A

Parameter	S	C	A
Mass density, RO	1.81e-6	1.45e-6	1.24e-6
Young's modulus in long. direction, EA	29	60	29
Young's modulus in transverse direction, EB	29	60	29
Young's modulus in through thickness direction, EC	9.8	7.2	3.9
Poisson's ratios: PRBA PRCA=PRCB	0.15 0.22	0.044 0.052	0.08 0.070
Shear moduli: GAB GBC=GCA	4.7 3.8	4.6 3.7	1.4 1.1
Material axes option: globally orthotropic, AOPT	2	2	2
Material axes change flag: no change, MACF	1	1	1
Layer in-plane rotational angle (degrees), BETA	0	0	0
Longitudinal tensile strength, SAT	0.439	0.624	0.579
Longitudinal compressive strength, SAC	0.335	0.580	0.0538
Transverse tensile strength, SBT	0.439	0.624	0.579
Transverse compressive strength, SBC	0.335	0.580	0.538
Trough thickness tensile strength, SCT	0.080	0.080	0.080
Crush strength, SFC	0.335	0.581	0.728
Fibre mode shear strength, SFS	0.056	0.046	0.031
Matrix mode shear strength in principal planes: SAB SBC=SCA	0.040 0.040	0.040 0.040	0.040 0.040
Scale factor for residual compressive strength, SFFC	0.10	0.10	0.10
Material model: fabric layer model, AMODEL	2	2	2
Coulomb friction angle for matrix and delamination failure (degrees), PHIC	14	14	14
Element eroding axial strain, E_LIMIT	0.035	0.035	0.035
Scale factor for delamination criterion, S_DELM	1	1	1
Limit compressive volume strain for element eroding, ECRSH	0.109	0.109	0.109
Limit tensile volume strain for element eroding, EEXPN	0.109	0. 109	0.109
Coefficients for strain rate	0	0	0

St3 steel, 10.9 bolt steel and hardened range subsoil
LS-Dyna material type: MAT_24
(MAT_PIECEWISE_LINEAR_PLASTICITY)

This is an elasto-plastic material with an arbitrary stress vs. strain curve and arbitrary strain rate dependency. St3 steel has been used for manufacturing the range stand and the bottom plate that stiffens the subsoil. The 10.9 steel is used to manufacture

M20 erection bolts. Material data are taken from (Klasztorny, 2010b). Input data for St3 steel, 10.9 bolt steel and hardened range subsoil are set up in Tab. 4. These components work in the elastic range at high margin safety; it explains why the static properties have been taken into account.

Plain weave fabric composites
LS-Dyna material type: MAT_161
(MAT_COMPOSITE_MSC)

This model is used to reflect the progressive failure criteria, including delamination, in composites consisting plain weave fabric layers. The failure criteria have been established by adopting the methodology developed by Hashin. The ply sequence type is $[(0/90)_{WF}]_n$, where subscript WF denotes woven fabric. In-plane principal directions are denoted as A and B, whereas out-of-plane principal direction is C. Material data, based on the standard experiments performed by Authors (average values), are set up in Tab. 5. Part of the material parameters were estimated from the rule of mixtures.

ALPORAS aluminium foam
LS-Dyna material type: MAT_26 (MAT_HONEYCOMB)

This material model is useful for honeycomb and foam materials. A nonlinear elasto-plastic behaviour is defined separately for all normal and shear stresses considered to be fully uncoupled. After homogenization, aluminium foam is modelled as an orthotropic material. The elastic moduli vary from the initial uncompacted values to the fully compacted values. The normal stress vs. volumetric strain load curve in the uniaxial compression test, in the form required by LS-Dyna code, is presented in Fig. 7. Material data are based on the Material Card and on the experiments executed by Authors:

- Mass density RO=0.23e-6;
- Young's modulus for fully compacted material E=70;
- Poisson's ratio for fully compacted material PR=0.30;
- Yield stress for fully compacted material SIGY=0.125;
- Relative volume at which the material is fully compacted VF=0.10;
- Material viscosity coefficient MU=0.05;
- Bulk viscosity flag (bulk viscosity is not used) BULK=0;
- Elastic modules in uncompressed configuration EAAU=EBBU=ECCU=0.075;
- Shear modules in uncompressed configuration GABU=GBCU=GCAU=0.030;
- Material axes option (globally orthotropic) AOPT=2;
- Material axes change flag (no change) MACF=1;
- Tensile strain at element failure (element will erode) TSEF=0.050;

SOUDASEAL 2K glue
LS-Dyna material type: MAT_27
(MAT_MOONEY-RIVLIN_RUBBER)

This is a two-parametric material model for rubber. The axial force vs. actual change in the gauge length, ΔL, in the uniaxial tension test, required by FE code LS-Dyna, is presented in Fig. 8. Material data, based on Material Card and on the experiments performed by Authors, are collected below:

- Mass density RO=1.45e-6;
- Poisson's ratio PR=0.495;
- Specimen gauge length SGL=30;
- Specimen width SW=5.75;
- Specimen thickness ST=2.3;

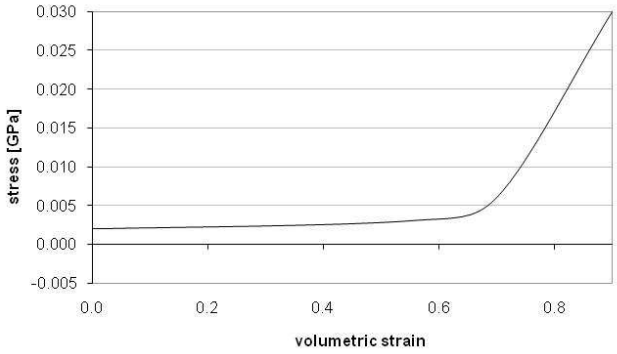

Fig. 7. The normal stress vs. volumetric strain load curve in the uniaxial compression test for ALPORAS aluminium foam

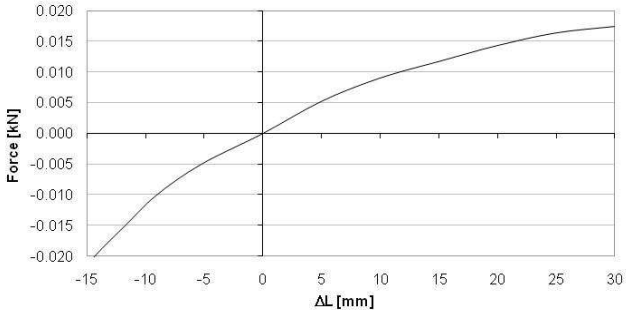

Rys. 8. The axial force vs. the actual change in the gauge length (average experimental data) in the uniaxial tension test for SOUDASEAL 2K glue specimens

The following assumptions are adopted in numerical modelling of the PS and SPS systems loaded by 6 kg TNT blast shock wave (Hallquist, 2009):

- The range stand, erection bolts, the plate stiffening the subsoil and the subsoil work in the linear viscoelastic range. The material models of these components take into account possibility of falling into the plasticity zone. Thus, the assumption related to working range is simply verified during the simulations.
- The external aluminium plate and the protected plate (Armox 500T) work in the elastic–plastic range taking into account high strain rates (the Johnson–Cook model). The plates may be due to large displacements and large plastic deformations.
- Material models corresponding to uniform laminates (S, C, A), ALPORAS aluminium foam, SOUDASEAL 2K glue do not take into account high strain rates, but take into consideration basic failure mechanisms for these materials. The materials undertaken may be due to both large displacements and large deformations.
- Contact and dry friction between respective parts of the PS/SPS systems are taken into account.
- Damping in the protected plate is taken into account according to the constant decrement damping model in the frequency range valuable in the dynamic response of the plate.
- The blast shock wave induced by detonation of HE charge at the central point over the range stand is modelled approximately using the CONWEP model. This model approximates fluid–solid interaction based on the experimental data.
- The initial displacement, strain and stress states induced by the dead load in the PS/SPS systems are neglected.
- The welded joints of erection bolt heads to the protected plate

are reflected approximately by respective constraints.

Blast shock wave was modelled using the LOAD_ BLAST_ENHANCED option offered by LS-Dyna system. This load model defines an airblast function for the application of pressure loads due to explosion of conventional charge, including enhancements for treating reflected waves, moving warheads and multiple blast sources. A type of blast source is spherical free-air burst (BLAST=2).

The exact simulation of the blast/structure interaction using LS-Dyna v971 code requires the use of the burn model described by the velocity of the detonation wave and the thermodynamical parameters on the detonation wave front. This advanced approach is not considered in this study.

The Automatic_Single_Surface steel – steel contact model has been assumed with the static and kinematic friction coefficients equal to 0.10 and 0.05, respectively. In order to minimize penetrations, the Segment_Based_ Contact (SOFT 2) has been selected. The steel – subsoil contact is taken into account with the kinematic friction coefficient equal to 0.20. Moreover, the steel–composite, steel–aluminium foam kinematic friction coefficients are equal to 0.20.

For the protected plate DAMPING_FREQUENCY_ RANGE option has been selected. This option provides approximately constant damping, i.e. frequency independent, over a chosen range of frequencies. The damping parameters amount to (Klasztorny, 2010b): CDAM=0.004 (damping in fraction of critical), FLOW=0.03 (lowest frequency [cycles per ms]), FHIGH=3 (highest frequency [cycles per ms]).

The remaining options in the LS-Dyna solver, selected for blast simulations in the PS and SPS systems, are as follows:

- HOURGLASS control for composites: IHQ-4 CONTACT_ERODING_SINGLE_SURFACE; this is contact taking into account the changes in contacting surfaces resulting from elements erosion;
- FS 2 (DEFINE_FRICTION option);
- VDC 25 (damping in contact);
- SOFT 2 (segment based contact);
- SBOPT 5 (warped segment checking and improved sliding behaviour);
- DEPTH (edge to edge contact);
- CONTROL_TIMESTEP;
- TSSFAC 0.6 (decreasing the time step to 0.6dt);
- ERODE 1 (erosion of the elements for which dt drops below 1% of the initial value; erosion of finite elements with negative volume).

4. RANGE TESTS OF SPS SYSTEM UNDER 6 KG TNT BLAST SHOCK WAVE

The main purposes of experimental – numerical tests performed on energy-absorbing panels ALF joined to the protected plate (Armox 500T) are experimental validation of numerical modelling of the SPS system and assessment of ALF shield effectiveness at 6 kg TNT blast shock wave loading.

The conditions for the experimental test are collected below:

- a spherical charge made of SEMTEX HE material equivalent 6 kg of TNT in reference to the pressure criterion;
- a detonator placed centrally in the sphere;
- central free suspension of HE charge at 400 mm distance from the top surface of the range stand (a typical distance of the vehicle bottom plate from AT mine hidden under the ground surface);
- the range stand resting on the 20 mm thick plate stiffening the subsoil;
- the 450×450×300 mm cubicoidal central hole done under the plate stiffening the subsoil.

Fig. 9. Segment SP with M16 erection bolts before 6 kg g TNT blast test

Fig. 10. The SPS system before 6 kg TNT blast test

Fig. 11. The SPS system after 6 kg TNT blast test

The range experiments were conducted in 2010 on the Navy Academy Range near Strzepcz, Poland. The photo documentation of the experimental blast test is presented in Figs. 9 – 11. Fig. 9 shows the SP segment before 6 kg TNT range test. Figs 10, 11

illustrate the SPS system before and after detonation of 6 kg TNT spherical charge hanged centrally over the stand at the 400 mm vertical distance. High resistance of the stand body is proved experimentally. The erection bolts gave in small plastic deformations. The following damages have been observed:

- valuable plastic deformations and central cracks in the aluminium sheet;
- cracks and delamination of layers in the hybrid laminates,
- failure of glue layers i large areas;
- slight asymmetry of the blast;
- medium plastic deformations and no damages in the protected plate,;
- full compaction and multi-plane breaking of the aluminium foam core.

The deformation contours in reference to the bottom surface of the protected plate in the SPS system after the 6 kg TNT blast, measured using Handyscan scanner are presented in Fig. 12. The plate deformations were quasi-bisymmetric.

5. SIMULATIONS OF DYNAMIC PROCESSES IN THE PS AND SPS SYSTEMS

The simulations correspond to detonation of 6 kg TNT spherical charges in the PS and SPS systems. The results presenting the ALF panel failure picture and plastic deflection of the protected plate in the SPS system have been used to validate experimentally numerical modelling and simulation of the SPS system.

a)

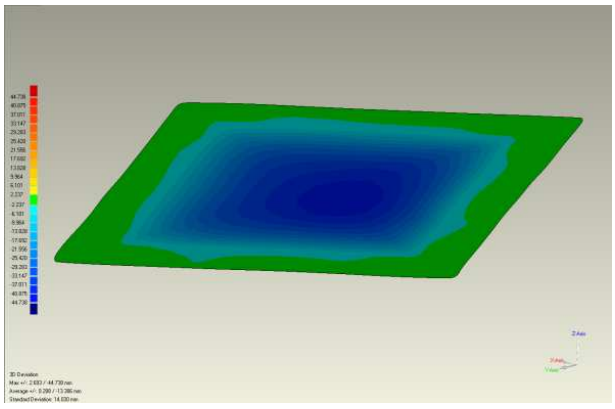

b)

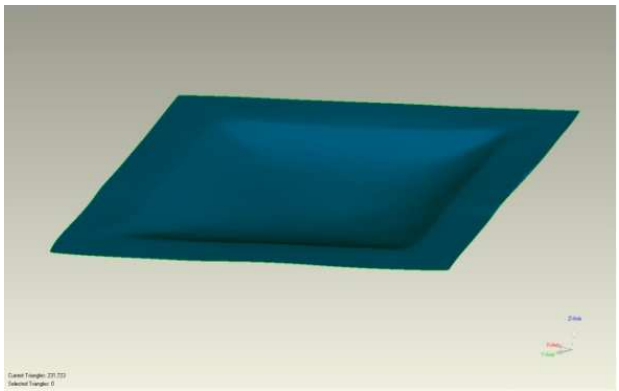

Fig. 12. The plastic deformation 3D scan (performed using Handyscan) for the protected plate removed from SPS system after 6 kg TNT blast: a) the vertical displacement contours; b) the virtual model of the deformed plate

The computations were performed in Department of Mechanics and Applied Computer Science, Military University of Technology, Warsaw, Poland, using LS-Dyna v971 software. The CPU time amounted to ~8 h for the PS system (the real process duration time equals 50 ms), and ~44 h for the SPS system (the real process duration time equals 35 ms). The computations were performed using 8P).

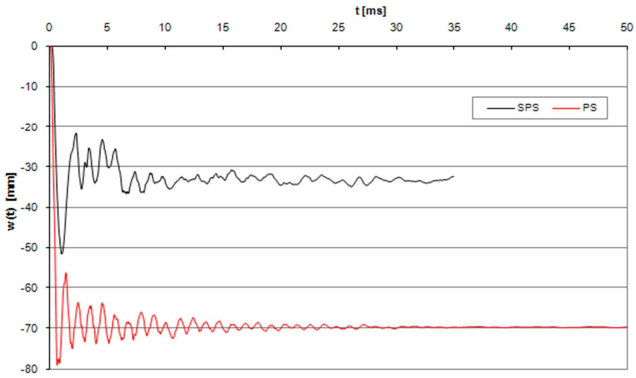

Fig. 13. The SPS and PS systems loaded by 6 kg TNT blast shock wave. Time histories of the relative vertical deflection at the central point of the protected plate

a)

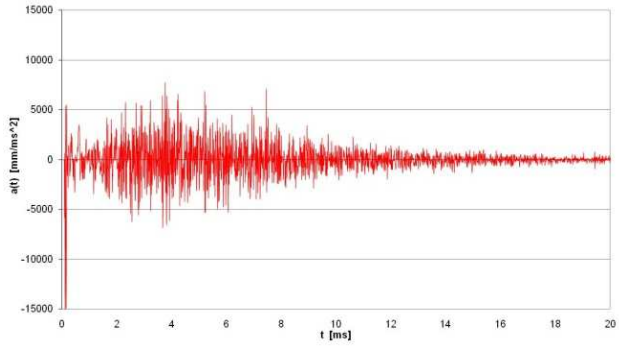

b)

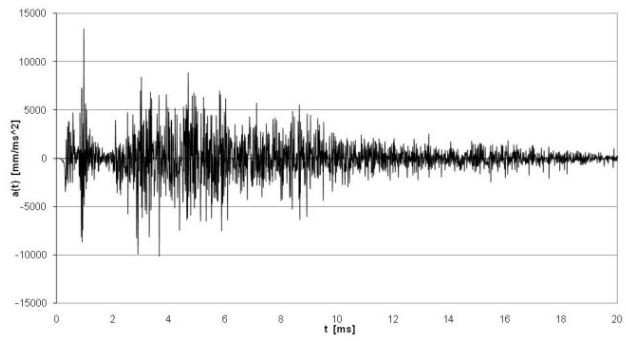

Fig. 14. The PS (a) and SPS (b) systems loaded by 6 kg TNT blast shock wave. Time-histories in the vertical acceeration at the central point of the protected plate

The simulation results are presented in Figs. 12–23. Fig. 13 presents time histories of the relative vertical deflection at the central point of the protected plate in reference to the SPS and PS systems under 6 kg TNT blast. This quantity is understood as the vertical displacement at the midpoint less the vertical displacement at the reference point located in the main cross-section A-A (Fig. 3) at 235 mm distance from the midpoint (at the internal edge

of the central frame). The red line curve, corresponding to the PS system, tends to 70 mm plastic deflection, while the black line curve, related to the SPS system, tends to 33.4 mm plastic deflection. Comparing these deflections enables assessing the effectiveness of the protective panel ALF.

Fig. 14 presents time-histories of the vertical acceleration at the midpoint of the protected plate for the PS system (red line) and the SPS system (black line). The physical correctness of these curves is observed. Small reduction in accelerations at the midpoint of the protected plate is observed. It results from the structural and boundary conditions in both systems. The maximum vertical accelerations overpass time and again the admissible values for a human. Note that the range stand does not reflect LV or LAV vehicle. There are modelled PS and SPS systems and the results cannot be directly interpreted for screw-occupants. One may compare only the maximum values in the PS and SPS systems before developing the algorithm transforming the range results to real vehicles.

Fig. 15 presents the plastically deformed protected plate in the PS system. The next Fig. 16 shows a half of the SPS system in the axonometric view at instant t=1.05 ms corresponding to the maximum vertical deflection in the protected plate. In Fig. 17 one can observe the deformed and partly damaged SP subsystem extracted from the SPS system at the instant corresponding to the maximum vertical deflection in the protected plate.

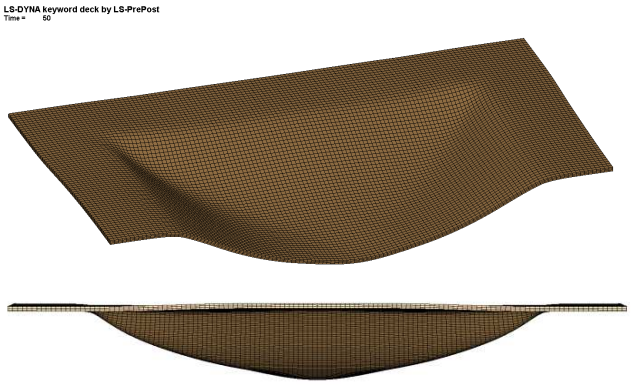

Fig. 15. The deformed protected plate extracted from the PS system after 6 kg TNT blast shock wave. The axonometric view and the side view on the half plate

Fig. 16. The deformed protected plate – ALF panel subsystem extracted from the SPS system loaded by 6 kg TNT blast shock wave. The axonometric view on the half subsystem at t=1.05 sec corresponding to the maximum deflection of the plate

The displacement contours [mm] for the protected plate are presented in Figs. 18 and 19, respectively in the PS and SPS systems under the blast considered. The contours correspond to the instant at which the maximum vertical deflection in the protected plate has occurred. The Huber-Mises-Hencky effective stress contours [GPa] in the protected plate, at the same dynamic conditions, are shown in Figs. 20 and 21. Contours illustrating the effective plastic strains [–] in the protected plate after finishing the dynamic process are presented in Figs. 22, 23 for the PS and SPS systems, respectively.

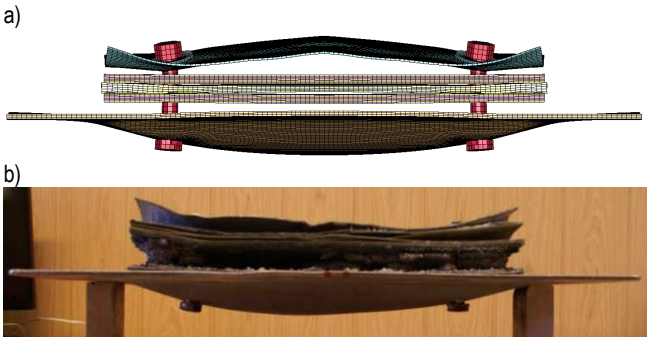

Fig. 17. The SPS system after 6 kg TNT blast shock wave. The side view: a) simulation; b) experiment

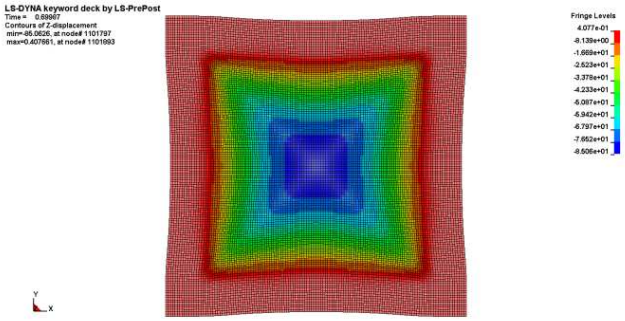

Fig. 18. The PS system loaded by 6 kg TNT blast shock wave. Contours of the vertical displacements [mm] of the protected plate at instant t=0.70 ms (the maximum deflection of the plate)

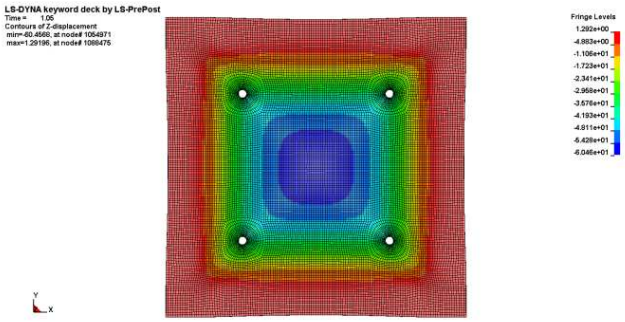

Fig. 19. The SPS system loaded by 6 kg TNT blast shock wave. Contours of the vertical displacements [mm] of the protected plate at instant t=1.05 ms (the maximum deflection of the plate)

The results presented in Figs. 12–23 prove correctness of the physical and numerical modelling as well as simulations of dynamic processes in the PS and SPS systems.

In addition, the internal energy absorbed in the PS and SPS systems, simulated in LS-Dyna, was observed. In the PS system, the absorption amounted to 23.5 kJ; the major part has been absorbed by Armox plate (16.6 kJ), the subsoil absorbed 2.2 kJ, and 4.7 kJ was absorbed by the remaining components, friction

and viscous damping. The SPS system dissipated 53.7 kJ since the vertical distance of the HE charge from the top of the system has been decreased by the ALF panel. The components of the system absorbed the following energies: 34.2 kJ – Alporas foam, 5.3 kJ – Armox plate, 3.9 kJ – Soudaseal glue, 3.4 kJ – hybrid laminates, 3.0 kJ – subsoil, 3.9 kJ – the remaining components, friction and viscous damping.

Impact in the form of the 6 kg TNT blast shock wave induces plastic deformations in the Armox plate in both PS and SPS systems. The plastic deflection can be treated as the measure of these deformations. Respective numerical and experimental values of the plastic deflection are collected in Tab. 6.

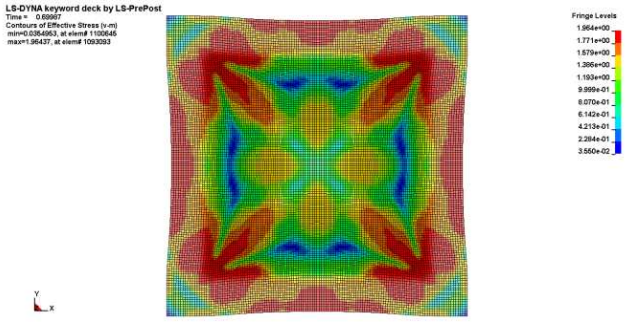

Fig. 20. The PS system loaded by 6 kg TNT blast shock wave. Contours of the Huber-Mises-Hecky effective stresses [GPa] in the protected plate at instant t=0.70 ms (the maximum deflection of the plate)

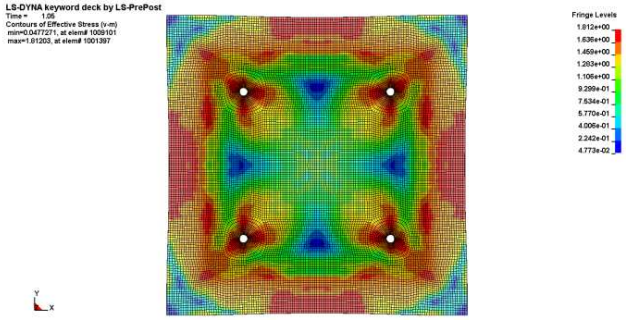

Fig. 21. The SPS system loaded by 6 kg TNT blast shock wave. Contours of the Huber-Mises-Hecky effective stresses [GPa] in the protected plate at instant t=1.05 ms (the maximum deflection of the plate)

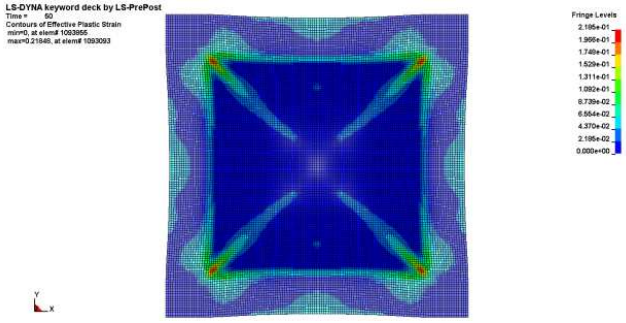

Fig. 22. The PS system after 6 kg TNT blast shock wave. Contours of the effective plastic strains [–] in the protected plate

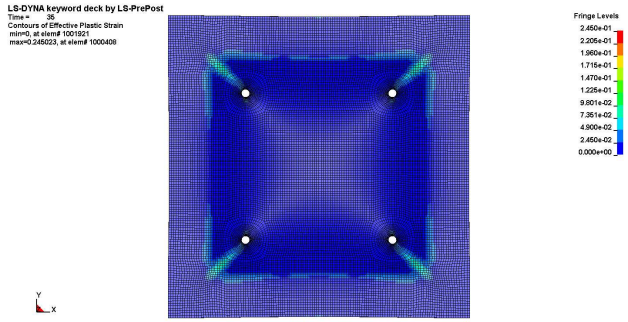

Fig. 23. The SPS system after 6 kg TNT blast shock wave. Contours of the effective plastic strains [–] in the protected plate

Experimental validation of the numerical modelling of the SPS system is measured by the deviation of the numerical plastic deflection from the experimental one. The respective error is defined by the formula:

$$\delta = \frac{|d_N - d_E|}{L} \tag{2}$$

where: d_N – numerical plastic deflection, d_E – experimental plastic deflection, L=470 mm – reference length equal to width of the square hole in the range stand.

Tab. 6. The plastic deflection of the protected plate d [mm] in the PS, SPS systems after 6 kg TNT blast shock wave (N – simulation, E – experiment)

System	6 kg TNT		δ [%]
	N	E	
PS	70.0	–	–
SPS	33.4	38.6	1.1

In reference to the SPS system error is relatively small. Quantitative conformity of the numerical and experimental failure in the ALF shield is assessed positively. Summing up, experimental validation of numerical modelling has been assessed positively with possibility of further improvement of the numerical models. Attention should be put on better modelling of laminate delamination as well as on better modelling of fully compacted aluminium foam at tension. Moreover, the material models describing aluminium foam, hybrid laminates, and glue could be extended on high strain rates.

The effectiveness of the ALF protective shield can be measured by the plastic deflection reduction coefficient defined by the formula

$$\beta = \frac{d_{SPS}}{d_{PS}} \tag{3}$$

where: d_{PS} – plastic deflection in the PS system, d_{SPS} – plastic deflection in the SPS system.

This coefficient is equal to 0.48 for the systems undertaken. Plastic deflection reduction is relatively high and is mainly influenced by the designed stacking structure of the ALF shield as well as by the bolt connections applied in the SPS system.

Within the limits of the Johnson–Cook model the effective stresses in the protected plate reach values 1.96 and 1.81 GPa in the PS and SPS system, respectively. One can observe valuable differences between effective stress contours (in the protected plate) in the PS and SPS systems.

6. CONLUSIONS

Experimental validation of numerical modelling is related to the SPS system loaded by 6 kg TNT blast shock wave. The PS system being the SPS' subsystem does not require separate validation. In the validation, the results of the range test performed in 2010 have been applied. The numerical modelling have been performed for the SPS system (the validation purpose) and for the PS system (the effectiveness assessment purpose). The plastic deflection reduction factor has been calculated.

Based on the numerical – experimental research developed in the study the following final conclusions have been formulated:

- The ALF panels exhibit high relative energy absorption and have the key parameters competitive in the market, i.e. thickness, mass per unit area, protection level, price.
- Experimental validation of numerical modelling of the PS and SPS systems under blast shock waves is positive.
- The design assumptions made for the range stand have been confirmed both experimentally and numerically.

The results corresponding to the selected protective panel and selected HE charge are useful for validation and verification of the numerical model of the protective shield – protected plate – range stand system (SPS). After positive validation and verification one can realize numerical research for other blast conditions or optimize protective panels. Compared to the experiments the simulations are much cheaper and can predict displacement/velocity/ acceleration time-histories, effective stress and plastic strain contours for an arbitrary variants of the SPS/PS systems. Such approach enables fast and cheap design of protective panels for required protection level.

REFERENCES

1. **AEP-55,** *Procedures for Evaluating the Protection Levels of Logistic and Light Armoured Vehicles for KE and Artillery Threats*, NATO/PFP Unclassified, Vol. 1.
2. **AEP-55,** *Procedures for Evaluating the Protection Levels of Logistic and Light Armoured Vehicle Occupants for Grenade and Blast Mine Threats Level*, NATO/PFP Unclassified, Vol. 2.
3. **Bachmann H**. (1995), *Vibration problems in structures. Practical guidelines*, Basel – Boston – Berlin, Birkh User.
4. **Hallquist J.O.** (2009), *LS-DYNA. Keyword User's Manual V971 R4 Beta*, LSTC Co., CA, USA.
5. **Jones R.M**. (1975), *Mechanics of composite materials*, McGraw-Hill BC, New York.
6. **Klasztorny M. *et al.*** (2010a), *Application of composite – foam layers for protection from mins and IED. Vol. 1: Composite – foam shields. Final Report. R&D Project No. O R00 0062 06*, Military Univ. Technol, Warsaw, Poland [in Polish].
7. **Klasztorny M. *et al.*** (2010b), Modelling and numerical simulation of the protective shield – protected plate – test stand system under blast shock wave, *Journal of KONES Powertrain & Transport*, Vol. 17, No. 3, 197 – 204.
8. **Klasztorny M. *et al.*** (2010c), Experimental investigations of the protective shield – protected plate – test stand system under blast shock wave, *Journal of KONES Powertrain & Transport*, Vol. 17, No. 4, 229 – 236.
9. **Nillson, M.** (2003), *Constitutive model for Armox 500T and Armox 600T at low and medium strain rates*, Technical Report F01-R-1068-SE, Swedish Defence Research Agency.
10. **STANAG 4190,** *Test Procedures for Measuring Behind-Armour Effects of Anti-Armour Ammunition*, NATO/PFP Unclassified.
11. **STANAG 4569,** *Protection Levels for Occupants of Logistic and Light Armoured Vehicles*, NATO/PFP Unclassified.
12. **Zduniak B., Morka A., Gieleta R.** (2010), Study of FEM model for tension and compression test for aluminium alloys samples in order to set material data, *J. KONES Powertrain & Transport*, Vol. 17, No. 3.

ABSTRACTS

Jerzy Bajkowski, Paweł Skalski
Analysis of Viscoplastic Properties of a Magnetorheological Fluid in a Damper

The aim of presented paper is a mathematical description and an analysis of viscoplastic properties of a magnetorehological fluid in operational conditions of a damper's work. The authors considers the possibility of use the viscoplastic law, typically for metals, to describe the behaviour of device with a magnethorheological fluid.

Agnieszka Bondyra, Marian Klasztorny, Piotr Szurgott, Paweł Gotowicki
Numerical Modelling and Experimental Verification of Glass-Polyester Mixed Laminate Beam Bending Test

The subject undertaken in the study is a glass (fibre) – polyester (matrix) layered composite, of the mixed sequence, com-posed alternately of laminas reinforced with E-glass plain weave fabric (WR600) and E-glass mat (CSM450). The laminate is manufactured on Polimal 104 polyester matrix. The aim of the study is to determine the options/values of parameters for numerical modelling and simulation of static processes in shell structures made of glass-polyester composites undertaken, in MSC.Marc system, recommended in engineering calculations. The effective elastic and strength constants of homogeneous laminas have been determined experimentally according to the standard procedures. The bending test of composite beams has been conducted experimentally and simulated numerically. Numerical investigations have been focused on selection of options/values of the numerical modelling and simulation parameters. The experimental verification of numerical modelling of the bending test is positive in both the quasi-linear range and in the catastrophic – progressive failure zone.

Grzegorz Chomka, Jerzy Chudy
Rotary Head Kinematics During Cleaning of Flat Surfaces

The present article covers the problem of a mathematical description of the trajectory of those postprocessing traces that occur in the process of hydro jet cleaning of flat surfaces with the use of a rotary head. An analysis was conducted of postprocessing traces taking into consideration the provision of their uniform distribution. The determination of the conditions of an effective cleaning will allow such a selection of the working parameters of the head when a surface is obtained of a high quality, i.e. with a uniform degree of the removal of impurities.

Artur Cichański, Krzysztof Nowicki, Adam Mazurkiewicz, Tomasz Topoliński
Applicability of Indicators of Trabecular Bone Structure for Evaluation of its Mechanical Properties

The paper presents the results of examination of relations between indicators describing trabecular bone structure and its static and cyclic compressive strength. Samples of human trabecular bone were subject to microtomographic tests in order to specify indicators describing its structure. Part of the samples was subject to static compression tests, part to cyclic compressing loads with stepwise increasing amplitude. Evaluation of a degree of applicability level of estimation of bone compressive strength properties was conducted based upon values of structure indicators. Evaluation was performed based upon values of obtained determination coefficients R2 for linear regression. Obtained R2 values were within the range of 0.30-0.51 for relations between examined indicators and static compressive strength within the range of 0.47-0.69 for relations with the results of cyclic test with stepwise increasing amplitude.

Paweł Dzienis, Romuald Mosdorf, Tomasz Wyszkowski
The Dynamics of Liquid Movement Inside the Nozzle During the Bubble Departures for Low Air Volume Flow Rate

The main aim of investigation was to analyze the influence of liquid movement inside the nozzle on the dynamics of bubble departure. Dynamics of such process decides about the periodic and aperiodic bubble departures. During the experiment it has been simultaneously recorded: changes of the depth of the nozzle penetration by liquid, air pressure and shape of bubble trajectory directly over the nozzle (in the length of 30 mm). The air volume flow rate was in the range 0.00632 - 0.0381 l/min. There has been shown that for all air volume flow rates the time periods with periodic and aperiodic bubble departures have been occurred. Duration of these intervals varies with the air volume flow rate. It has been found that the aperiodic bubble departures begin when the time of bubble growth increases. The changes of maximum values of liquid position inside the nozzle are associated with changes of the shape of bubble trajectories. There has been shown that straightens of the trajectory precedes the appearance of periodical or aperiodic time period of bubble departures. The aperiodic bubble departures are accompanied by a significant deviation of bubble trajectory from a straight line. The correlation dimension analysis shown that three independent variables are enough to describe the behaviour of liquid movement inside the nozzle. These independent variables may be: liquid velocity, liquid position in the nozzle and gas pressure in the nozzle.

Tomasz Geisler
Analysis of the Structure and Mechanism of Wing Folding and Flexion in Xylotrupes Gideon Beetle (L. 1767) (Coloptera, Scarabaeidae)

This study presents the structure and functions of flying wings in beetles (Coloptera). Structural analysis and function of multiplanar flexion and the structure of the wings in selected beetles were also carried out. The author developed a method of determination of points, structures and surfaces on the wing in folding and flexing motions. The paper describes the system of veins, foils and folds in the wing. Photographs of the wing in different phases of folding and flexion are presented in the paper. The paper emphasizes practical applications of the method of analysis in bionic mechanisms.

Hubert Grzybowski, Romulad Mosdorf
Modelling of Pressure-Drop Instability in Single and Multi Microchannels System

In the paper the model of pressure-drop oscillations has been proposed. The model was based on the iterative solution to equations. The dynamics of pressure-drop oscillations in a single channel and in two neighbouring channels have been analyzed. There has been assumed that the pressure-drop oscillations in the system are caused by interactions between the heat supply system and liquid supply system. These interactions influence the heat and mass transfer inside the microchannel. Obtained results indicate that the shape of pressure drop curve has a significant influence on the system stability. When the slope of curve $\Delta p=f(G)$ in the region between function extremes increases then the pressure oscillations become chaotic. In case of multichannel system the thermal interactions (occurring through the channel walls) and hydrodynamic interactions (occurring inside the common channels outlet) have been considered. Four types of two-phase flow behaviours in parallel channels have been observed depending on the intensity of interactions: alternate oscillations, consistent oscillations, periodic oscillations and completely synchronized oscillations. Obtained qualitative results have been compared with conclusions of experimental results reported by other researches. The good qualitative agreement with experimental results has been obtained.

Marta Kolasa
Fast and Energy Efficient Learning Algorithm for Kohonen Neural Network Realized in Hardware

A new fast energy efficient learning algorithm suitable for hardware implemented Kohonen Self-Organizing Map (SOM) is proposed in the paper. The new technique is based on a multistage filtering of the quantization error. The algorithm detects such periods in the learning process, in which the quantization error is decreasing (the 'activity' phases), which can be interpreted as a progress in training, as well as the 'stagnation' phases, in which the error does not decrease. The neighborhood radius is reduced by 1 always just after the training process enters one of the 'stagnation' phases, thus shortening this phase. The comprehensive simulations on the software model (in C++) have been carried out to investigate the influence of the proposed algorithm on the learning process. The learning process has been assessed by the used of five criteria, which allow assessing the learning algorithm in two different ways i.e., by expressing the quality of the vector quantization, as well as the topographic mapping. The new algorithm is able to shorten the overall training process by more than 90% thus reducing the energy consumed by the SOM also by 90%. The proposed training algorithm is to be used in a new high performance Neuroprocessor that will find a broad application in a new generation of Wireless Body Area Networks (WBAN) used in the monitoring of the biomedical signals like, for example, the Electrocardiogram (ECG) signals.

Ewa Kulesza, Jan Ryszard Dąbrowski, Jarosław Sidun, Antoni Neyman, Jarosław Mizera
Fretting Wear of Materials – Methodological Aspects of Research

In this article, methodical aspects of studies on material fretting wear have been presented. The results of studies conducted on a "pin on disc" type device made at the Department of Materials and Biomedical Engineering of the Bialystok University of Technology confirmed the decisive influence of the amplitude of oscillations and the load value on the course and nature of the process. At a constant value of load, the course of resistance to motion was dependent on the amplitude. Increasing the amplitude of oscillations caused a change in friction conditions: from static friction (elastic deformation of formed adhesive connections, without dislocation of cooperating elements) to kinetic friction (breaking of adhesive bridges and displacement with sliding). The increase of the load value at a constant amplitude value caused a change in the course and nature of resistance to motion from sliding friction to friction at-rest.

Adam Lipski, Stanisław Mroziński
The Effects of Temperature on the Strength Properties of Aluminium Alloy 2024-T3

This paper presents results of monotonous tensile tests of 0.16" thick samples made of non-clad plates of aluminium alloy for aircraft purposes 2024-T3. Tests were performed for samples cut out from a sheet plate in two different directions: in the parallel and perpendicular direction to sheet plate rolling direction, for eight different temperature values from the range 25°C – 200°C. The tests were performed using the hydraulic-drive testing machine INSTRON 8502 equipped with thermal chamber. The analysis of results included changes of basic strength-related parameters depending on temperature. It was also observed that the intensity of Portevin Le Châtelier (PLC) effect depends on the temperature.

Bartłomiej Maciejewski, Jan Żurek
Modernisation of Testing Modules and Procedures in an Automated Assembly Line

This dissertation discusses the issue of modernisation of testing modules and procedures in an automated assembly line adapted to manufacture medical pressure transducers in Aesculap Chifa company. The manufactured transducer is used for invasive measurement of patient's physiological pressure, and, therefore, must not pose any threat either to patient's health or life. This is the reason why the operation of the assembly line has been identified, testing modules and procedures have been evaluated and the construction modifications have been suggested. During the research, the influence of suggested construction modifications, enhanced with procedure changes, has been verified.The suggested adjustments have enabled, as required, to improve the operation of automated assembly line adapted to manufacture medical pressure transducers.

Arkadiusz Mystkowski
Energy Saving Robust Control of Active Magnetic Bearings in Flywheel

The paper reports on the investigation and development of the flywheel device as a energy storage system (FESS). The FESS is designed to operate in a vacuum and is supported on a low energy controlled active magnetic bearings (AMBs). The goal was to design and experimentally test the self integrated flywheel conception with a smart control of the flywheel rotor magnetic suspension. The low power control approach, with the reduced bias current, of the flywheel active magnetic bearings is used. The weighting functions are designed in order to meet robust control conditions. The laboratory investigations of the flywheel with high gyroscopic effect operated at low speed met the control and energy performances requirements.

Marek Świerczewski, Marian Klasztorny, Paweł Dziewulski, Paweł Gotowicki
Numerical Modelling, Simulation and Validation of the SPS and PS Systems under 6 kg TNT Blast Shock Wave

The paper develops a new methodology of FE modelling and simulation of the SPS and SP systems under 6 kg TNT blast shock wave. SPS code refers to the range stand – protected plate – protective shield ALF system, while PS code refers to the range stand – protected plate system. The multiple – use portable range stand for testing protective shields against blast loadings was developed under Research and Development Project No. O 0062 R00 06. System SPS uses high strength M20 erection bolts to connect the protective shield to the protected plate. In reference to the SPS system, validation explosion test was performed. It has pointed out that the deve-loped methodology of numerical modelling and simulation of SPS and PS systems, using CATIA , HyperMesh, LS-Dyna, and LS-PrePost software, is correct and the ALF protective shield panels have increased blast resistance and high energy – absorption capability.